UNIVERSITY OF LEEDS

Power Electronic-Based Solutions for Transient-Free Energization of Traction Power Transformers

Amir Aghazadeh

University of Leeds

School of Electronic and Electrical Engineering

Submitted in accordance with the requirements for the degree of

Doctor of Philosophy

January, 2025

Intellectual Property Statement

The candidate confirms that the work submitted is his own and that appropriate credit has been given where reference has been made to the work of others. The contribution of the candidate and the other authors to this work has been explicitly indicated below.

The work in Chapter 3 of the thesis has appeared in the following publications:

1. A. Aghazadeh, K. Li, V. Terzija, and S. Azizi, "Pre-Fluxing Method for Energization of Single-Phase Transformers," in 2023 IEEE International Conference on Energy Technologies for Future Grids (ETFG), Wollongong, Australia, 2023, pp. 1-6.

   For this paper, Amir Aghazadeh developed and proposed a novel energization method. Amir Aghazadeh implemented this method using PSCAD/EMTDC to thoroughly test and verify its performance and effectiveness through detailed simulations. Dr Azizi provided valuable support in refining the method and meticulously reviewing its performance to ensure accuracy and reliability. Dr Azizi also contributed significantly to writing the paper. After completing the initial work, Prof Terzija and Prof Li reviewed the manuscript and offered insightful comments and suggestions that enhanced the overall quality of the publication.

2. A. Aghazadeh, K. Li, M. Popov, V. Terzija, and S. Azizi, "A Modified Pre-Fluxing Method for the Energization of Single-Phase Transformers," submitted to *IEEE Transaction on Industrial Applications*.

   Amir Aghazadeh developed and proposed the energization method presented in this paper. He was responsible for the conceptualization, simulation-based verification, experimental validation, and writing of the manuscript. Dr Azizi provided critical support in refining the method and

verifying its performance through additional simulations and experimental testing. Dr Azizi also assisted in building the prototype and contributed to the writing of the paper. Following a thorough review, Prof Popov evaluated the method and results to confirm their validity, and both Prof Popov and Dr Azizi contributed to the manuscript's development. Finally, Prof Terzija and Prof Li reviewed the manuscript, providing valuable feedback and suggestions to further improve the work.

The work in Chapter 4 of the thesis has appeared in the following publication:

1. A. Aghazadeh, E. Hajipour, V. Terzija, and S. Azizi, "A Flux Matching Method for Mitigating the Inrush Current of Single-Phase Transformers," published in *IEEE Transaction on Power Delivery*.

   For this paper, Amir Aghazadeh was responsible for both the conceptualization and verification of the method through simulations and experimental validation. Dr Azizi provided invaluable support in refining the method and meticulously verifying its performance through both simulations and experimental tests. Dr Azizi also assisted in building the prototype and thoroughly reviewed the proposed method to ensure its accuracy and effectiveness. Also, Dr Hajipour evaluated the method and results to confirm their validity. Amir Aghazadeh, Dr Azizi, and Dr Hajipour contributed to writing the paper. Finally, after the work was completed, Prof Terzija reviewed the manuscript, offering comments and suggestions to further enhance it.

The work in Chapter 5 of the thesis has appeared in the following publication:

1. A. Aghazadeh, E. Hajipour, K. Li, and S. Azizi, "Mitigating the Inrush Current of V/V Transformers using Railway Conditioners,"*IEEE Access*, vol. 12, pp. 50885-50897, 2024.

   For this paper, Amir Aghazadeh was responsible for proposing the method and verifying it through both simulations and experiments. Dr Azizi provided valuable assistance in developing the method and carefully verifying its performance through simulations and experimental

tests. Dr Azizi thoroughly reviewed the proposed method to ensure its accuracy and effectiveness. Dr Hajipour also evaluated the method and the results to confirm their validity. Amir Aghazadeh, Dr Azizi, and Dr Hajipour contributed to writing the paper. Finally, after the work was completed, Prof Li reviewed the paper, offering comments and suggestions to further improve it.

Acknowledgements

I would like to express my deepest gratitude to my supervisors, Dr Azizi and Prof Li , for their support, guidance, and encouragement throughout my research. Their profound knowledge, insightful feedback, and patience have been instrumental in shaping this thesis. I am truly fortunate to have had the opportunity to work under their mentorship.

A special thanks to Dr Hajipour, whose valuable help and expertise significantly contributed to the progress and completion of this work. His constructive suggestions and willingness to assist at crucial moments were greatly appreciated.

I am also immensely grateful to my family who deserves so much more than mere words. To my parents, your belief in my abilities and your constant encouragement provided me with the strength to persevere. Thank you for your prayers which have been always my spiritual strength to move forward. To my siblings, Maryam, Leila, and Saeed, your understanding and support were indispensable during this journey. I am always indebted to you because of your relentless support whenever I was in trouble, either in my PhD or in my general life matters. Thanks for sticking by me in the most considerate way possible!

Lastly, to my beloved wife, Mina, your unwavering support, patience, and sacrifices have been my greatest source of strength. Your belief in me, even during the most challenging times, has been a constant source of motivation. Thank you for being my best friend and for listening to my worries, sharing my joys, and reassuring me on tough days. This achievement would not have been possible without you by my side.

Abstract

High-speed electric trains have recently gained significant attention over other modes of transportation due to their lower emissions, reduced initial and maintenance costs, and high efficiency. Traction power supply systems (TPSSs), which supply electric trains, typically include specialized traction transformers that convert three-phase systems into single-phase ones. To mitigate power quality issues in these systems, railway power conditioners (RPCs) are employed alongside traction transformers. Despite extensive research on power quality improvement, the challenge of energizing traction transformers has been largely overlooked in the literature. When a transformer is energized, a high-magnitude asymmetrical current, known as inrush current, can flow into the energized winding while the other winding is open-circuited. This can lead to the malfunction of differential protective relays and generate axial and radial forces that deform transformer windings, potentially causing turn-to-turn faults. These issues not only shorten the transformer's lifespan but also create disturbances in the power grid supplying the transformer. Therefore, this research project seeks to develop methods to reduce or eliminate inrush currents during the energization of traction transformers. It is essential to address inrush currents without depending on the transformer's design information or initial status.

New energization methods are proposed to address the challenges associated with energizing traction transformers, specifically focusing on single-phase and V/V traction transformers, which are the most common types installed in TPSSs. Compared to existing energization techniques, these methods offer several advantages: 1) They do not require knowledge of the initial residual flux density, 2) They are fast, even for high-power transformers, 3) They account for the closing operation of circuit breakers (CBs) and all related uncertainties, minimizing their impact on transformer energization, 4) If they rely on measurement data, they are designed to be immune to errors in the outputs from measurement devices, and 5) They aim to mitigate inrush current (keeping it below the transformer's nominal current) using existing infrastructure or by adding a small device that incurs minimal initial and maintenance costs. To achieve these goals, three energization methods are proposed for single-phase traction transformers, designed to effectively

address inrush current problems while being fast, immune to measurement errors, less sensitive to CB closing operations, and requiring only a small device for flux adjustment. Additionally, two methods are introduced for V/V transformers: one for transformers energized with independent-pole-operated CBs, and the other for those energized with gang-operated CBs, both of which rely on RPCs for flux adjustment.

To assess the proposed methods' performance and compare them with existing energization methods, they are implemented in PSCAD/EMTDC and thoroughly tested under different conditions. Furthermore, a hardware-in-the-loop (HIL) test system is developed, which is composed of transformers, a Typhoon 604 HIL device, and an instantaneous turn-on solid-state relay. This setup facilitates the practical application and validation of the methods on real transformers. The results consistently demonstrate that the proposed methods significantly reduce inrush currents compared to existing energization methods. Specifically, they limit the current magnitude to 70% of the transformer's nominal current (equivalent to more than a 98% reduction compared to the peak inrush current of the worst-case energization scenario), while other methods can result in current magnitudes reaching 200%–300% of the nominal value.

Contents

List of Figures

List of Tables

Abbreviations

ADC	Analog-to-Digital Converter
ANN	Artificial Neural Network
APF	Active Power Filter
APQC	Active Power Quality Compensator
CB	Circuit Breaker
CF	Coefficient
CT	Current Transformer
DC	Direct Current
DFT	Discrete Fourier Transform
EKF	Extended Kalman Filter
FCL	Fault Current Limiter
FFNN	Feed-Forward Neural Network
HAPF	Hybrid Active Power Filter
HB	Half-Bridge
HBRPC	Half-Bridge Railway Power Conditioner
HIL	Hardware-in-the-Loop
HT	Hybrid Transformer
IGBT	Insulated-Gate Bipolar Transistor
IM	Impedance Matching
JA	Jiles-Atherton
MAD	Median Absolute Deviation
MMC	Modular Multi-level Converter
MPFM	Modified Pre-Fluxing Method
NDF	Normalized Difference Function
NS	Neutral Section
POW	Point-on-Wave

PWM	Pulse Width Modulation
RDDS	Rate of Decrease of Dielectric Strength
RPC	Railway Power Conditioner
RS	Residual Signal
RSFCL	Resistive Superconducting Fault Current Limiter
SFCL	Superconducting Fault Current Limiter
STATCOM	Static Synchronous Compensator
TDM	Terminal Duality Model
TPSS	Traction Power Supply System
VSC	Voltage Source Converter
WT	Wavelet Transform
ZSFCL	Impedance Superconducting Fault Current Limiter

Nomenclature

α	JA Model Parameter
ΔI_{DC}	DC Offset of Current Transducer
ΔT_{CB}	Mechanical Scatter
Δt	Time of Change of Current from Zero to I_{ex}
Δt_1	Time Interval of the JA Model
ΔT	Timing Error
ΔV_{DC}	DC Offset of Voltage Transducer
λ	Flux
λ_p	Prospective Flux
λ_r	Residual Flux
λ_r^{ad}	Adjusted Residual Flux
λ_r^{max}	Maximum Feasible Residual Flux
λ^{max}	Maximum Flux
λ_{safe}	Upper Bound of Safe Flux Range
μ	Permeability
μ_0	Free Space Permeability
ω	Angular Frequency
ϕ_0	Voltage Angle
δ	Directional Parameter of the JA model
A	Cross-Section Area
a	JA Model Parameter
$\boldsymbol{A}$	Incidence Matrix
B	Flux Density
B_e	Effective Magnetic Induction
B_{crit}	Upper Limit of Compatibility Flux Density
B^{max}	Maximum Flux Density

B_p	Prospective Flux Density
B_r	Residual Flux Density
B_r^{ad}	Adjusted Residual Flux Density
B_r^{max}	Maximum Feasible Residual Flux Density
B_r^{α}	α-side Transformer's Residual Flux Density
B_r^{β}	β-side Transformer's Residual Flux Density
$B_r^{\alpha,op}$	α-side Transformer's Optimal Residual Flux Density
$B_r^{\beta,op}$	β-side Transformer's Optimal Residual Flux Density
B_{α}^{DC}	α-side Transformer's DC Flux Density
B_{β}^{DC}	β-side Transformer's DC Flux Density
c	JA Model Parameter
f	Power System Frequency
f_r	Frequency of Injected Current
H	Magnetic Field Strength
H_c	Coercive Magnetic Field Strength or Coercive Magnetizing Intensity
H_e	Effective Magnetic Field Strength
$\boldsymbol{I_b}$	Branch Current Vector
I_{ex}	Peak Excitation Current
I_n	Transformer Nominal Current
$\boldsymbol{I_n}$	Nodal Current Vector
I_p	Peak Value of Injected Current
i_{87T}	Current Passing Through Differential Relay
i_{inj}	Injected Current into Transformer
K	Core Material Coefficient
l	Length of the Magnetic Path
$\boldsymbol{L}$	Branch Inductance Matrix
k	JA Model Parameter
L_m	Magnetizing Inductance
$\boldsymbol{L_s}$	Inductance Matrix
m	Slope of Injected Current
M	Magnetization
M_{an}	Anhysteretic Magnetization
M_{irr}	Irreversible Magnetization

M_{rev}	Reversible Magnetization
m_{max}	Maximum Slope of Injected Current
M_s	JA Model Parameter
N	Number of Winding Turns
N_p	Number of Primary Winding Turns
N_s	Number of Secondary Winding Turns
q_1	Lower Bound of Making Interval
q_2	Upper Bound of Making Interval
q_m	Ideal Making Point
q_{tan}	Intersection of the Lower Side of Quadrilateral Region with the Previous Hump
s^{max}	Maximum *RDDS*
s^{mean}	Mean Value of *RDDS*
s^{min}	Minimum *RDDS*
T	Time Period
T_{CB}	Closing Time
T_{min}	Minimum Time of Current Injection
T_r	Time Period of Injected Current
t_0	Energization Instant
t_{ct}	Contact Touch Instant
t_{in}	Closing Operation Initiation Instant
t_m	Making Instant
t_m^{op}	Optimal Making Instant
τ_{ct}	Critical Contact Touch Instant
τ_{in}	Critical Closing Operation Initiation Instant
τ_m	Critical Making Instant
τ_{tan}	Instant of Making on q_{tan}
$\boldsymbol{V_b}$	Branch Voltage Vector
$\boldsymbol{V_n}$	Nodal Voltage Vector
v_p	Primary Winding Voltage
$\hat{B}$	Per-Unit Value of Flux Density Based on Maximum Flux Density
$\boldsymbol{Y_n}$	Nodal Admittance Matrix

$\boldsymbol{Z_b}$ Branch Inductance Matrix

Chapter 1

Introduction

1.1 Background

In response to the growing population and increasing demand for transportation, high-speed electric trains have been recognized as an effective solution to enhance transportation capacity due to their safe, clean, reliable, and efficient performance. To power these trains, various types of traction transformers, including single-phase transformers, Woodbridge transformers, Scott transformers, impedance matching (IM) transformers, and V/V transformers are installed in traction power supply systems (TPSSs). These transformer types are discussed in detail in Section 1.1. Typically, traction transformers are equipped with power conditioners (described further in Section 1.1) to mitigate the harmonic currents generated by electric trains. Additionally, power conditioners are necessary to compensate the negative sequence currents observed in the three-phase network, as electric trains, being single-phase loads, draw these negative sequence currents from the upstream three-phase grid to which the traction transformers are connected.

Despite significant efforts to address the power quality challenges associated with TPSSs, insufficient research has been conducted on the protection of traction transformers, which play a crucial role in supplying high-speed electric trains. Similar to typical three-phase transformers, a differential protection scheme is employed to protect traction transformers against various types of faults. In [1], this scheme is adapted to protect Scott transformers. However, the energization of the traction transformer is not considered in this research. The energization of a traction power transformer, like any other power transformer, can result in the flow of high-magnitude excitation current, known as inrush current [2]. This is due to the ferromagnetic characteristics of the transformer's magnetic core [3].

In most cases, the transient currents and voltages generated by such actions are effectively damped within the power network. However, under certain conditions, inrush current may lead to problems such as protective relay maloperation, power quality degradation, and mechanical stress. In extreme scenarios, this current may lead to surge arrester failure or transformer insulation degradation. Severe cases of energization can even result in transformer insulation damage. In aging power networks, where some components may be nearing the end of their operational life, a key priority is extending transformer lifespan. Effective condition monitoring and aging management require solutions to mitigate transients, such as inrush currents, to minimize mechanical and electrical stresses on equipment [4].

In practice, to improve the performance of protection devices during transformer energization, techniques such as gap detection and second-order harmonic criteria are commonly used, as seen in SIPROTEC 5 protective relays from SIEMENS. A study in [5] explores a differential protection scheme for Scott transformers that utilizes second-order harmonic detection to block protection device operation during energization. However, it is important to note that these criteria do not perform optimally for high-magnitude inrush currents [6]. To address this limitation, various algorithms have been proposed, including those based on artificial neural networks (ANN) and fuzzy logic. For example, a signal-processing-based method is proposed for a TPSS with a V/V transformer [7]. Despite their effectiveness, these algorithms impose significant computational burdens on differential relays and require extensive datasets for training. Furthermore, they tend to be unpredictable in the presence of frequency noise [6].

Although various methods can be employed to prevent the maloperation of protective relays, transformers remain susceptible to mechanical forces that can reduce their lifespan. It is clear that mitigating or eliminating inrush currents can substantially extend transformer lifetime compared to scenarios where no strategies are used to deal with inrush currents. The literature offers several solutions, including increasing transformer stiffness against inrush currents by temporarily inserting passive resistors or power electronics-based current limiters, and employing three-phase circuit breakers with independently operating poles. Additionally, pre-fluxing and de-fluxing (or demagnetization) methods have been proposed for single-phase and three-phase transformers. For hybrid transformers (HBs), which integrate a conventional low-frequency transformer with a power electronic converter connected to a DC source, various methods have been suggested [8].

While effective, these methods are not universally applicable, particularly for transformers without converters, and they involve additional upfront and maintenance costs. Among these methods, the most widely used in industrial applications is the controlled switching or point-on-wave (POW) energization method. This method mitigates inrush currents by controlling the circuit breaker's closing operation during transformer energization [9]. For example, Switchsync® PWC600, the latest generation of point-on-wave controllers developed by Hitachi Energy, employs this method. In this method, high-power, high-voltage three-phase transformers are energized sequentially, requiring a circuit breaker capable of independently controlling each pole. Additionally, the method

relies on information about the transformer's state following de-magnetization to ensure proper energization. However, this information is not always readily available, which can make the energization process more challenging.

Railway conditioners are widely used in various applications but have not yet been applied to mitigate inrush currents or facilitate smoother energization of traction transformers. Similar to harmonic filters, these conditioners have the potential to address inrush current challenges. Since TPSSs are already equipped with such devices—or, where they are not, small-scale power electronic devices can be used in their place—repurposing them for this purpose incurs no or small additional costs. This makes it a cost-effective and practical solution for managing inrush currents. When properly controlled, power conditioners can be effectively adapted to fulfill this new role. This PhD research focuses on employing existing power conditioners in TPSSs, or employing small-scale power electronics (such as chip-based solutions), to mitigate inrush currents during the energization of traction transformers, especially when different types of circuit breakers are used.

1.2 Literature Review

1.2.1 Traction Transformers

Since electric trains are inherently single-phase heavy loads, they cannot be directly connected to conventional three-phase systems. Thus, an interface is necessary to integrate these single-phase loads into three-phase power systems. Transformers are commonly used for this purpose. The remainder of this section will discuss the various types of transformers employed for this integration.

Phase-Shift Configuration (Single-Phase Transformers)

The simplest configuration involves single-phase transformers, as illustrated in Fig. 1.1. At each substation, single-phase transformers are connected to different phases. For example, in section 1, the transformer is supplied by phases A and B, while in other sections transformers are connected through phases A and C (section 2) and phases C and B (section 3), respectively. In this configuration, different sections must be isolated by neutral sections (NSs) to prevent short circuits [10]. This structure can reduce negative sequence currents, however, it does not completely eliminate them, as

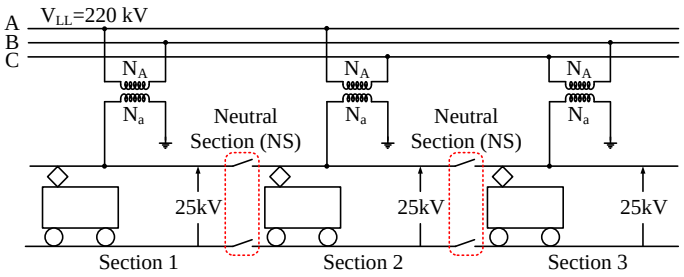

Figure 1.1: Phase-shift configuration.

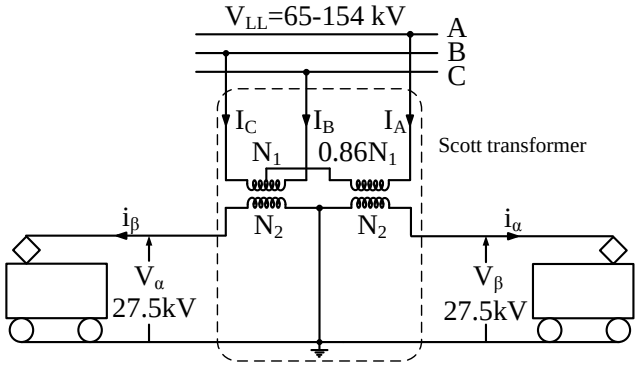

Figure 1.2: Scott-transformer.

the power demand in different sections is not equal at any given time. Only when similar loads are supplied by subsections can zero negative sequence currents be achieved.

Scott-Transformer

One of the most important traction transformers is Scott transformer, which is widely used in different countries, which is shown in Fig. 1.2. This transformer consists of two single-phase transformers. The primary difference between these transformers lies in the number of primary windings. One transformer has two primary windings, each with $\frac{N_1}{2}$ turns, and one secondary winding with N_2 turns. The second transformer, on the other hand, has two simple windings with a turns ratio of $\sqrt{3}N_1 = 2N_2$. It is important to note that in traction substations utilizing Scott transformers, negative sequence currents are significantly reduced compared to phase-shift configurations. Similar to the phase-shift configuration, Scott transformers eliminate negative sequence currents when both sides are equally loaded. However, this transformer cannot eliminate these currents when the

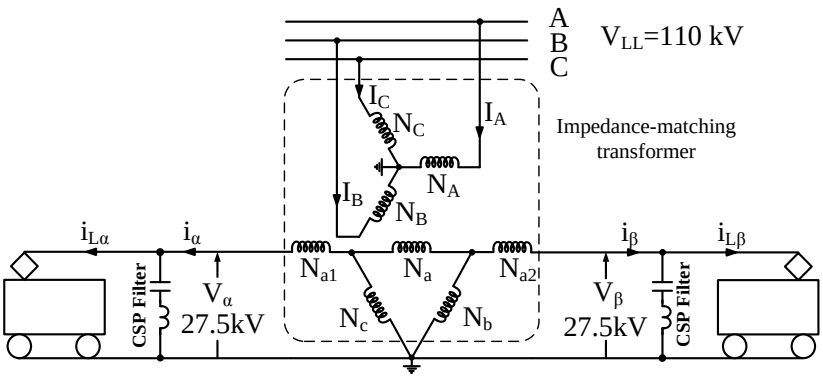

Figure 1.3: IM transformer.

two windings on the secondary side have unequal loads.

Impedance Matching Transformer (IM)

An IM transformer is demonstrated in Fig. 1.3. In this figure, a 110 kV, 50 Hz three-phase system is converted into two 27.5 kV single-phase systems using the IM transformer [11, 12]. This transformer comprises a single-phase multi-winding transformer with one primary winding and three secondary windings, along with two single-phase transformers with double windings [11, 13]. On the primary side, the three single-phase transformers are identical, meaning each primary winding has the same number of turns for each phase ($N_A = N_B = N_C = N_1$). The secondary winding turns are different, given by $N_a = N_b = N_c = N_2$ and $N_{a1} = N_{a2} = K_W \times N_2$, where K_W is a constant. The impedances of the primary windings are equal ($Z_A = Z_B = Z_C = Z_1$), while on the secondary side, the impedance of phase A's winding is K_Z times higher than those of phases B and C ($Z_b = Z_c = Z_2$ and $Z_a = K_Z \times Z_2$) [11, 12]. Using the superposition theorem, the three-phase currents can be expressed as a function of the secondary side currents as shown in equation (1.1) [14].

$$\begin{bmatrix} I_A \\ I_B \\ I_C \end{bmatrix} = \frac{1}{K_1} \begin{bmatrix} -(\frac{1}{K_Z+2} + K_W) & (\frac{1}{K_Z+2} + K_W) \\ -\frac{1}{K_Z+2} & -\frac{K_Z+1}{K_Z+2} \\ \frac{K_Z+1}{K_Z+2} & \frac{1}{K_Z+2} \end{bmatrix} \begin{bmatrix} i_\alpha \\ i_\beta \end{bmatrix} \tag{1.1}$$

IM transformers are categorized as balanced traction transformers, meaning that when supplying balanced loads through their secondary windings, the negative sequence

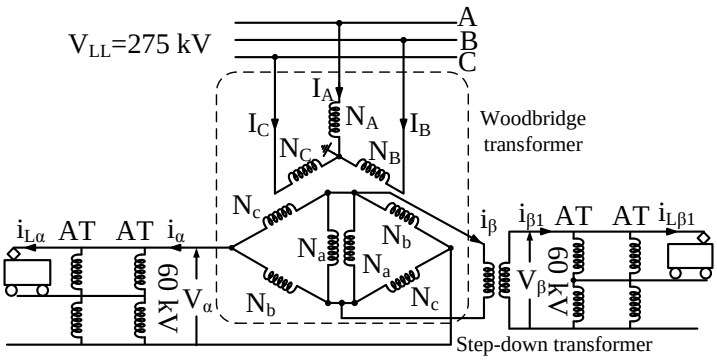

Figure 1.4: Woodbridge transformer.

currents on the primary side are eliminated. Balanced loads are those that draw currents with identical magnitudes and a phase angle difference of 90° (with the α-side current leading the β-side current). To ensure this balance, the values of K_Z and K_W must be set to $\sqrt{3}+1$ and $0.5\times(\sqrt{3}-1)$, respectively [14, 15].

Woodbridge Transformer

As mentioned earlier, Scott transformers are installed to convert three-phase systems to single-phase ones. However, these transformers are used in substations supplied by 66-154 kV networks. For higher network voltages, i.e., 187-275 kV, another type of transformer known as modified Woodbridge transformer is employed for the conversion from three- to single-phase systems. This transformer is shown in Fig. 1.4. According to this figure, two isolated single-phase systems are available for two sides of the substation where this transformer is used. It is noteworthy pointing out that since the voltage of β-side is lower than α-side voltage, a single-phase step-up transformer is connected to increase the output voltage of the β-side [16]. Due to the advantages of the balanced modified Woodbridge transformer, since 1972, it was installed at Sanyo Shinkansen substation [17]. However, compared to other types of traction transformers, this one is really complicated leading to an increase in the initial cost.

V/V Transformer

Among all traction transformers, V/V transformers are widely used to convert three-phase to single-phase systems due to their simple structures, lower costs, and higher

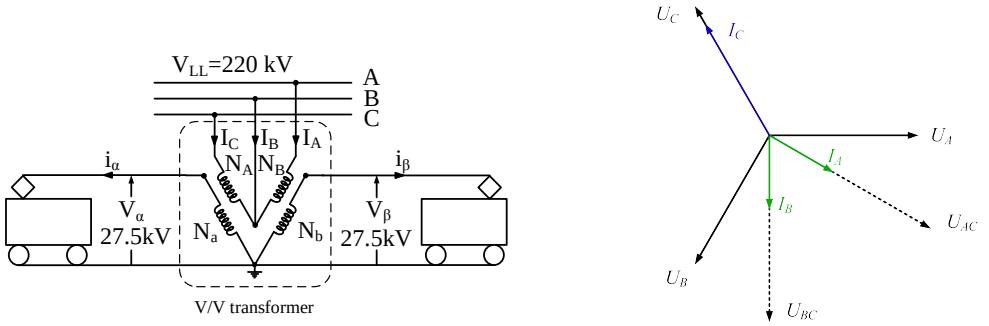

(a) (b)

Figure 1.5: (a) V/V transformer, (b) voltage and current diagrams of the V/V transformer.

capacity utilization ratios [18]. This type of transformer is shown in Fig. 1.5(a). Unlike other transformers, the V/V transformer is unbalanced, meaning that even with equal loads on both secondary sides, the three-phase currents remain unbalanced. The voltage and current phasor diagrams, shown in Fig. 1.5(b), demonstrate that even when the secondary sides are equally loaded, the three-phase currents are not balanced, resulting in negative sequence currents passing through the three-phase system.

1.2.2 Traction Power Quality Compensators

Despite the effectiveness of transformers in addressing negative sequence current issues, they are not capable of resolving harmonic current problems. Additionally, compensating for the reactive power drawn by trains is essential for enhancing the power system's performance. Without effective reactive power compensation, voltage drops increase, leading to a reduction in the length of the overhead system. This voltage drop also limits the number of trains that can be fed simultaneously and restricts the amount of power that the system can provide. To address these challenges, the installation of power compensators that can both compensate reactive power and mitigate harmonic currents is necessary. This section will discuss the performance and configuration of compensators specifically designed for traction transformers.

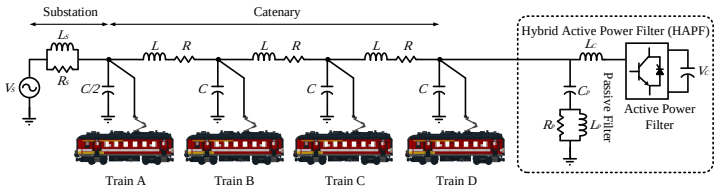

Figure 1.6: HAPF installed at a railway feeding system.

Hybrid Active Power Filter (HAPF)

Active Power Filters (APFs) are electric devices installed in power systems to compensate for reactive power and harmonic contents. To enhance the performance and increase the compensation capacity of an APF, a series or parallel-connected passive filter is used, creating what is known as a Hybrid Active Power Filter (HAPF) [19]. The application of HAPFs in single-phase railway feeding systems is explored in [20], as shown in Fig. 1.6. In this study, the HAPF is installed at the end of the feeding system. While the APF compensates for reactive power and low-order voltage harmonics, the passive filter mitigates harmonic overvoltages caused by the excitation of resonant frequencies with thyristor-based trains. Although the HAPF effectively addresses these issues, it is connected only to one end of the single-phase feeding system and, therefore, cannot eliminate negative sequence currents.

Static Synchronous Compensators (STATCOM)

Another compensator, known as STATCOM, can be installed on the high-voltage side of a traction transformer to address the inherent issues of traction systems. Fig. 1.7 shows the installation of a two-level STATCOM. When there exist electric trains at both sides of a railway substation, negative sequence currents may flow into the three-phase system. However, if these currents are supplied by the STATCOM, the power system only supplies positive sequence currents. This also applies to reactive power and harmonic currents. Consequently, as long as the STATCOM is controlled appropriately, the three-phase power system supplies only active power. Despite these benefits, installing STATCOMs is costly because they are connected to the three-phase side, increasing the cost of electrical insulation and other associated expenses [21].

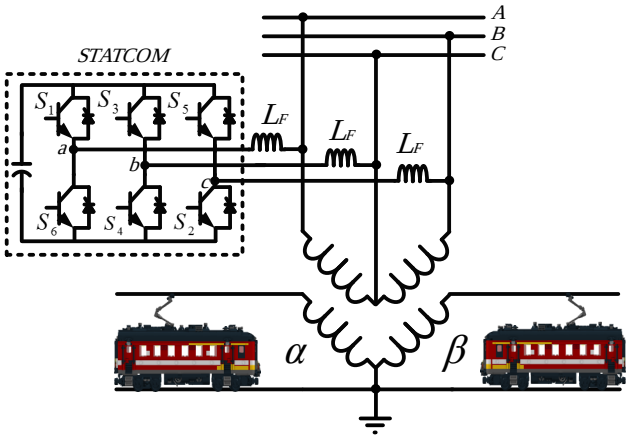

Figure 1.7: STATCOM connected to a V/V transformer.

Active Power Quality Compensator (APQC)

As mentioned above, while STATCOMs are efficient at addressing power quality issues in traction systems, their high initial and maintenance costs limit their widespread use. Consequently, compensators designed for secondary side applications are often preferred. One such compensator is the Active Power Quality Compensator (APQC), which can be installed on the low-voltage side of an impedance matching (IM) traction transformer, however, it is also suitable for other types of traction transformers [11]. Similar to a STATCOM, an APQC consists of a two-level three-phase voltage source converter (VSC). Since the APQC is inherently a three-phase device, an interface is required to connect it to the secondary side of an IM transformer. This interface converts two single-phase systems into a three-phase system using a Scott transformer. The schematic of the APQC is shown in Fig. 1.8. This configuration offers several advantages, which are detailed below:

1. Isolate the APQC from the IM transformer.

2. Reduce the voltage applied to the converter.

Since the APQC uses a capacitor as its energy storage, it can effectively compensate for reactive power. Additionally, its function as an APF allows it to eliminate or mitigate harmonic currents on both sides. One of the most significant capabilities of the APQC is

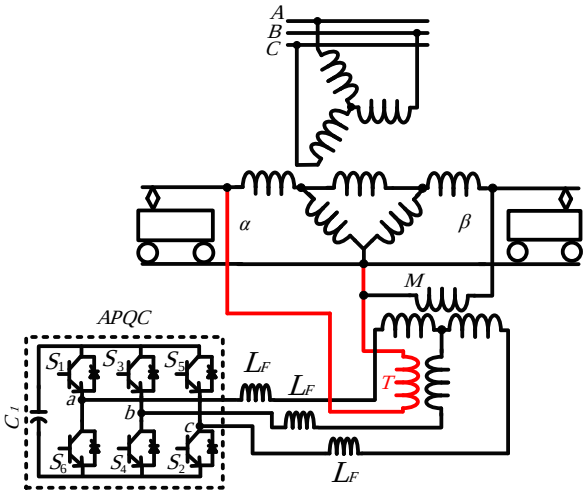

Figure 1.8: APQC connected to an IM transformer.

its ability to shift active power from one secondary side to the other. This ensures that both sides of the IM transformer are equally loaded, even if the loads differ. Technically, an APQC functions as a STATCOM but is installed on the low-voltage side.

Railway Power Conditioner (RPC) and Half-Bridge Railway Power Conditioner (HBRPC)

There exist other power compensators that have been specifically proposed for secondary side connection. To compensate for reactive power and mitigate harmonic currents, a single-phase APF can be used. For comprehensive coverage, two APFs are required, one for each side. To enable active power transfer between the two sides, the APFs must be connected back-to-back [18]. This configuration is known as a Railway Power Conditioner (RPC), which is shown in Fig.1.9(a). An RPC can perform all three main functions of an APQC. Additionally, compared to an APQC, the RPC offers two further advantages:

1. simpler structure due to using two step-down transformers instead of a Scott transformer.

2. higher reliability because the system can act as an APF when one side is damaged.

An RPC is composed of two full-bridge single-phase converters, sharing the same DC

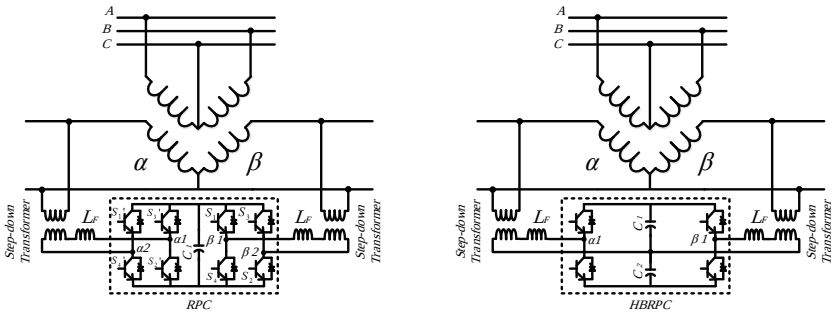

(a) (b)

Figure 1.9: (a) RPC connected to a V/V traction transformer, (b) HBRPC connected to a V/V traction transformer.

link. If two half-bridge converters are used instead of full-bridge ones, the system is known as an HBRPC [12]. This compensator is shown in Fig. 1.9(b). Similar to the RPC and APQC, an HBRPC achieves all three primary objectives when installed. However, it requires two DC capacitors to stabilize its DC link. Since the DC voltage must be equally divided between the two capacitors, an additional control loop is necessary compared to an RPC. Furthermore, an HBRPC operates at a lower switching frequency than an RPC due to higher voltage drops across each IGBT, which consequently leads to increased current harmonic distortion.

Regarding the connection of RPC and HBRPC to traction transformers, two different configurations can be considered. Both RPC and HBRPC can be connected to traction transformers as shown in Figs. 1.9(a) and 1.9(b). Also, there is another configuration known as the co-phase system [22], shown in Fig. 1.10. In co-phase systems, reactive power compensation and harmonic current mitigation are achieved through one side of the compensator, while both sides are involved in active power shifting. For regular systems, active power can be shifted between the α and β sides. In contrast, in co-phase systems, the direction of this shift is always from the three-phase system to the trains.

Modular Multi-Level Converter (MMC) based Conditioners

Typically, the nominal power of trains is on a megawatt scale, making the previously mentioned conditioners inadequate for system requirements. The stress level on all switching devices exceeds acceptable limits. To address this issue, several solutions have

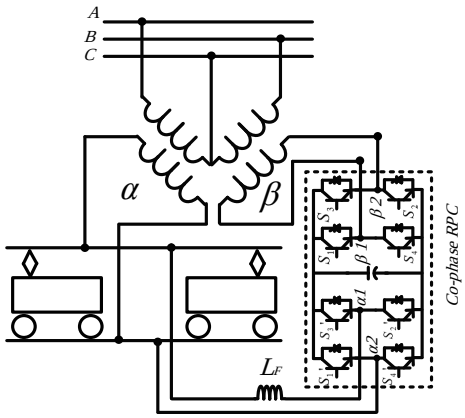

Figure 1.10: Co-phase system.

been proposed using modular multi-level converter (MMC) technology. This technology has been employed to develop new power conditioners based on RPC, APQC, and HBRPC, where two-level VSCs are replaced with MMCs. In [23, 24], a full-bridge indirect modular multi-level converter-based RPC (HB-MMC4 RPC) is introduced. This conditioner, shown in Fig. 1.11, replaces a single switching device in an RPC with a string of cascaded half-bridge submodules.

The HB-MMC4 RPC offers an innovative solution by significantly reducing the output voltage harmonic content. For this conditioner, the effective switching frequency is the product of the individual switching frequency of each submodule (which is the same for all submodules) and the number of submodules in each arm (with a leg containing two arms). Due to the division of stress among all submodules, high-power switching devices, as required in two-level RPCs, are unnecessary. For an N_{th} HB-MMC4 RPC, N-1 submodules are needed. The DC link voltage is the sum of the voltages from all submodules, and the capacitors in each submodule collectively act as a large capacitor, eliminating the need for a separate capacitor to control the DC link voltage. Despite these benefits, the HB-MMC4 RPC has some disadvantages, such as circulating currents and a complex control scheme. Additionally, this configuration requires isolation transformers with a 1:1 turns ratio to prevent short circuits between the two arms. Comprehensive control strategies for this setup are detailed in [25].

Another topology based on MMC technology is the half-bridge three-wire indirect modular multilevel converter RPC (HB-MMC3 RPC), as illustrated in Fig. 1.12. This

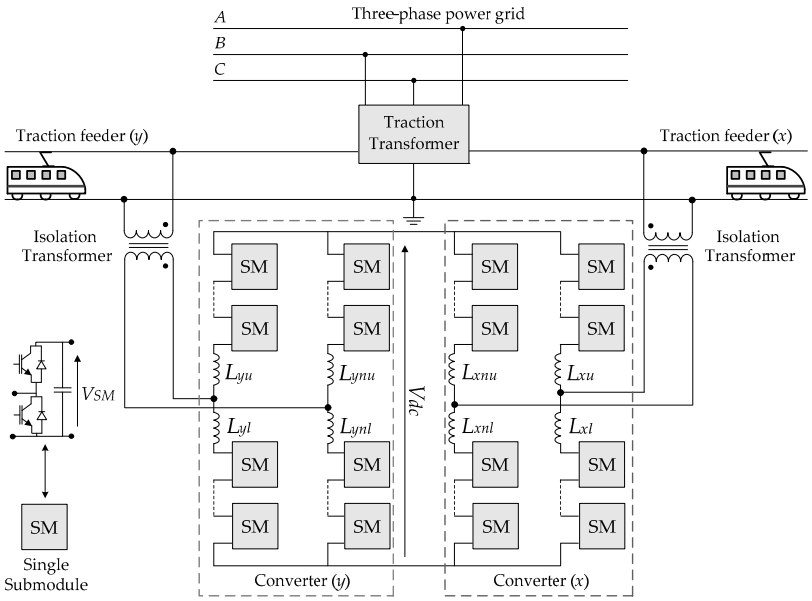

Figure 1.11: HB-MMC4 RPC [25].

topology is derived from the conventional APQC and, like the HB-MMC4 RPC, utilizes a string of cascaded submodules [23, 24]. Despite the similarities between the HB-MMC4 RPC and the HB-MMC3 RPC, each brings its own advantages and faces specific disadvantages. Both topologies require N−1 submodules per arm to generate an N_{th} level output voltage, and inductors are essential for filtering the circulating current between arms. However, there are key technical differences. The HB-MMC3 RPC does not require isolating transformers, whereas the HB-MMC4 RPC relies on them. Also, the HB-MMC3 RPC reduces the required hardware by 25 % compared to the HB-MMC4 RPC. While the HB-MMC3 RPC requires a large capacitor to maintain the DC link voltage, the capacity of each submodule capacitor is reduced [25].

The conditioner based on MMC technology similar to HBRPC is termed the half-bridge indirect modular multilevel converter RPC (HB-MMC2 RPC) [26], as shown in Fig. 1.13. Compared to the other two conditioners, the HB-MMC2 RPC features a simpler hardware structure; however, it requires two bulk capacitors to maintain the DC link voltage at an acceptable level. Due to its leg connections, this configuration does not require isolating transformers. Unlike the HB-MMC3 RPC and HB-MMC4 RPC, the stress on the switching devices in the HB-MMC2 RPC is doubled, which can lead to

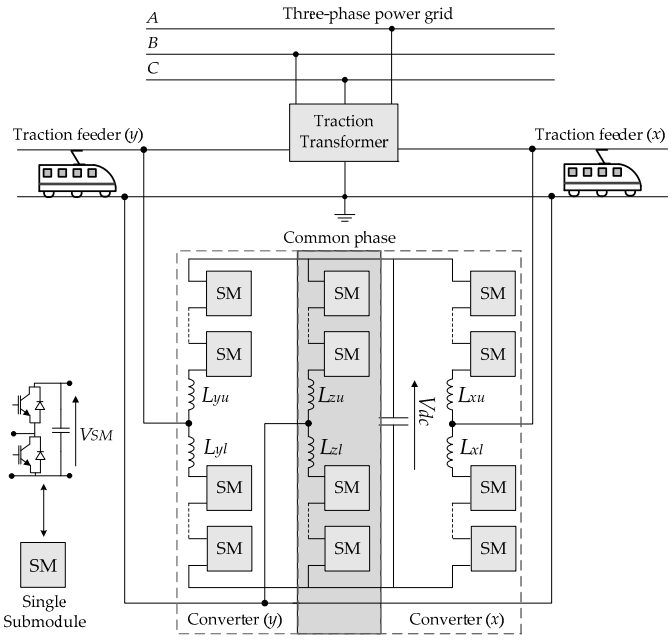

Figure 1.12: HB-MMC3 RPC [25].

a reduced switching frequency. Consequently, the size of the output inductors must be increased to accommodate the higher ripple in the circulating current [25].

1.2.3 Inrush Current and the Reasons Why This Current Flows

As discussed in the previous section, transformers are the core components of all types of TPSSs, facilitating the conversion from three-phase to single-phase systems. While these electrical devices help address various issues associated with TPSSs, they experience high-magnitude excitation currents, known as inrush currents, during energization. Under normal conditions, when a transformer is not loaded, the excitation current flowing into the winding is a small fraction of the transformer's nominal current and contains harmonic components. However, during energization, several factors cause the magnitude of the excitation current to increase significantly.

To explain this effect, let B and H denote the flux density of a ferromagnetic core and the magnetic field strength, respectively. The relationship between B and H is nonlinear and defined by a hysteresis loop (also referred to as the B-H curve). The instantaneous value of B depends not only on the present value of H but also on in what direction H has changed in the past. Let B_r denote the residual flux density of the core, which is

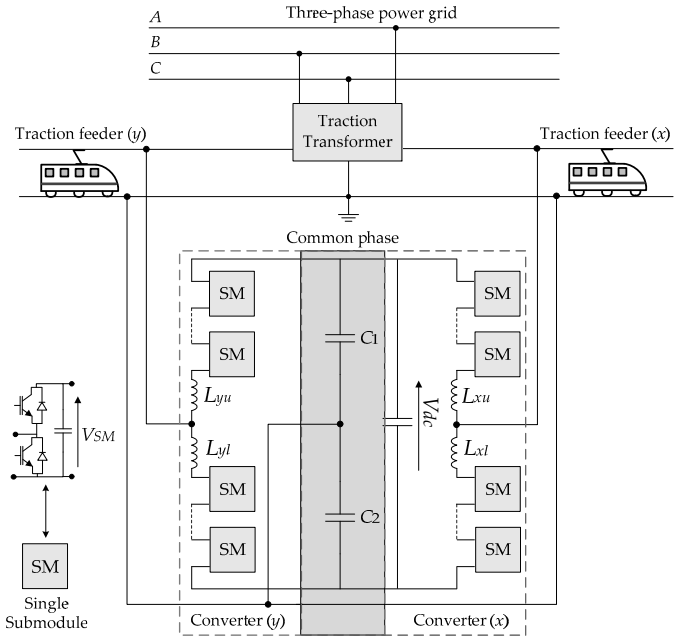

Figure 1.13: HB-MMC RPC [25].

the magnetic field that remains in the core of a transformer after the de-energization of the transformer [27]. To reduce the residual flux density to zero, a coercive magnetizing force, H_c must be applied with a polarity opposite to that of the magnetic field that initially magnetized the core. In other words, to eliminate positive residual flux density, H_c must be negative, and vice versa. The term "steady-state flux density" is used to denote the flux density of the core a long time after a nominal voltage is applied to the transformer winding. Denoted by B_p, the prospective flux is defined as the instantaneous value of the steady-state flux density, at the instant of transformer energization [28, 29]. The reason for the flow of inrush current upon transformer energization is a difference between B_r and B_p.

To detail how a difference between B_r and B_p results in inrush current, a single-phase transformer is considered and energized at $t = t_0$. To this end, let us assume that the nominal voltage $v(t) = V_m \cos(\omega t + \phi_0)$ is applied to the primary winding of the transformer, while its secondary winding is open-circuited. Using Faraday's law, one

can derive the flux density of the core as a function of time as below [30]

$$\begin{aligned} B(t) &= \frac{1}{NA}\int_{t_0}^{t} V_m \cos(\omega t + \phi_0)\mathrm{d}t + B_r \\ &= \underbrace{B^{max}\sin(\omega t + \phi_0)}_{Steady-state\ component} \underbrace{\overbrace{-B^{max}\sin(\omega t_0 + \phi_0)}^{B_p} + B_r}_{DC\ component} \end{aligned} \tag{1.2}$$

where N and A are the number of winding turns and the core's cross-section area, respectively. It can be confirmed that $B^{max} = V_m/NA\omega$ will be the maximum flux density in normal operation, i.e., the RMS peak value of the steady-state flux density of the core. In (1.2), the steady-state component is sinusoidal while B_r and B_p are constant terms causing a DC shift in the core's flux density. The DC component would not exist provided that $B_r = B_p$.

To study how the presence of a DC component in the flux density impacts the energization of a single-phase transformer, two different scenarios are defined and explored. In Scenario 1, the residual flux density is assumed to be zero, i.e., $B_r = 0$, and the transformer is energized at a voltage peak. In Scenario 2, $-B_r$ is slightly greater than $-B_r^{max}$ (which is the negative maximum possible residual flux density). In this scenario, the transformer is energized at the rising zero-crossing of the voltage waveform. Fig. 1.14 (a) demonstrates that the nominal voltage $v(t) = V_m \cos(\omega t + \phi_0)$ is applied to the primary winding at $t = 0$ while the secondary winding is open-circuited. The waveforms corresponding to Scenarios 1 and 2 are shown in blue and red, respectively. As can be seen, ϕ_0 is equal to -90° in Scenario 1, and equal to 0° in Scenario 2. It can be understood from (1.2) that B_p is a function of the time-integral of voltage applied to the winding. It follows from (1.2) that the core flux contains only a sinusoidal oscillating term in Scenario 1 as $B_r = B_p = 0$. In Scenario 2, however, equation (1.2) consists of constant and sinusoidal oscillating components since $B_r \neq B_p$.

Fig. 1.14 (b) shows the core's flux density under Scenarios 1 and 2. The B-H curve and excitation current corresponding to Scenarios 1 and 2 are also shown in Fig. 1.14 (c). The flux density in Scenario 1 is a sinusoidal waveform (shown in blue) that starts from $B_r = 0$ with no DC shift and varies within the range $[-B^{max}, B^{max}]$. These two values refer to the knee points on the B-H curve and mark the bounds of the normal operating region of the core [30]. When the transformer is energized as per Scenario 2, the core's flux density begins to increase from an initial value of $-B_r$. In this scenario, the difference between residual and prospective flux densities leads to a DC shift B_r

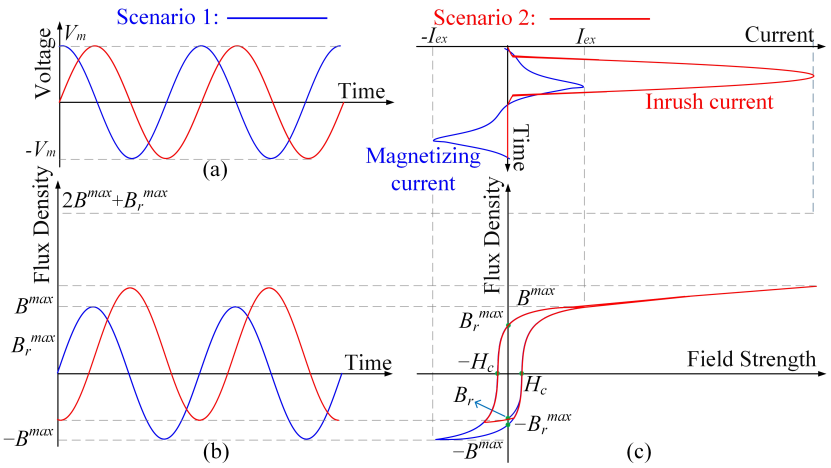

Figure 1.14: Transformer's (a) winding voltage, (b) core's flux density, (c) B-H curve and excitation current following Scenarios 1 and 2.

in the generated flux density in the core. Contrary to the blue curve of Scenario 1 where B varies between $-B^{max}$ to B^{max}, the red curve of Scenario 2 varies between $[-B_r, |B^{max} - B_r| + B^{max}]$ due to the DC shift. As a result, the transformer is driven into the deep saturation region leading to high H.

Indeed, Scenario 1 is the best energization scenario as it only draws the nominal excitation current. In Scenario 2, the current drawn is far greater than the excitation current due to the core saturation. The fact that $B_r = B_p = 0$ in Scenario 1 ensures that the flux density in the core does not exceed $\pm B^{max}$, thus a normal excitation current. A non-zero B_r results in a DC shift in the core's flux density thus deriving part of the magnetization into the saturation region. This is a region where the relationship between B and H is nonlinear and H increases significantly with a small change in B. Therefore, a high-magnitude asymmetric inrush current will flow, which damps out only after several power-frequency cycles (thanks to the series resistances of the systems) [4, 31].

1.2.4 Inrush Current Effects

In power systems, voltages and currents from generators and loads are typically sinusoidal and free from DC offset. However, inrush currents are characterized by substantial harmonic components and asymmetry due to their inherent DC offset. Furthermore, the magnitude of these currents is significantly higher than the normal operating val-

ues of transformers. These characteristics pose substantial challenges to power system components. This section will address the key impacts of inrush currents.

Sympathetic Inrush Current

In substations, transformers are often connected in parallel, and the energization of a new transformer commonly occurs while other transformers are already connected and fully loaded. As previously discussed, inrush currents flow through the transformer windings during energization. When a transformer is energized in the presence of other loaded transformers, these inrush currents can adversely affect the performance of the other transformers. Inrush currents cause voltage drops across the system impedance, which is directly proportional to the magnitude of the currents and the impedance of the system. Due to the DC offset and significant harmonic content of inrush currents, the three-phase voltages at the transformers' terminals become non-sinusoidal. This non-sinusoidal voltage causes the fluxes in the loaded transformers to saturate, leading to the generation of harmonically rich currents. This phenomenon, known as the sympathetic inrush effect, results in what are termed sympathetic inrush currents.

Compared to the energization of a single transformer, the inrush current experienced by a transformer in a substation initially matches the magnitude of the inrush current in the first cycle. However, the inrush current in a substation decays more slowly due to a lower time constant, leading to a prolonged duration of high inrush current. Consequently, at a given time after energization, the inrush current in a substation is significantly higher than that of a single transformer. Notably, the magnitude of sympathetic inrush currents increases exponentially until reaching a peak, after which it gradually declines.

Winding Axial and Radial Forces

During transformers' energization, the transient currents can differ significantly from the steady-state currents. These transient conditions generate unusual forces that can induce mechanical stresses and potentially cause damage to the transformer. Two types of forces, radial and axial, are particularly significant in this context. Radial forces are generated by inrush currents flowing through the windings of the energized side of the transformer. These forces can create mechanical stress, leading to potential issues such as winding buckling and deformation. Radial forces exert pressure from the energized

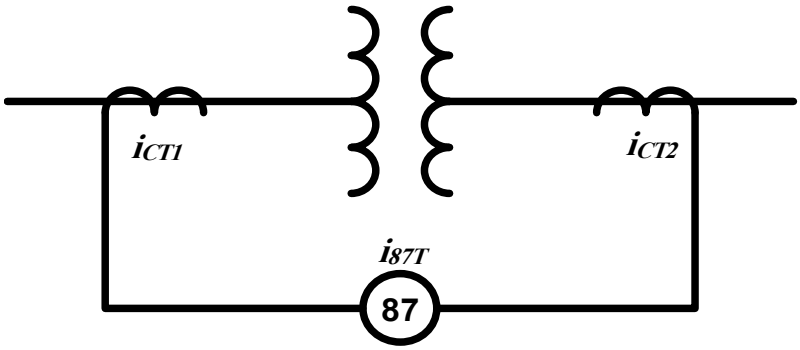

Figure 1.15: Principle of differential protection.

winding towards the exterior of the transformer.

In addition to radial forces, axial forces are also generated by inrush currents. These forces result in axial compression within the windings, increasing the risk of turn-to-turn short-circuits. Both radial and axial forces can compromise the structural integrity of transformers, making it essential to accurately calculate these forces. Two methods are commonly used to determine these forces. The first method involves calculations based on the dimensions of the transformers, which, while simple, may not always offer precise accuracy. The second method utilizes the finite element method (FEM), which provides a detailed and accurate modeling of the transformer's magnetic and electric circuits. Although FEM yields precise results, it is more complex to implement [32, 33].

Protective Relay Mal-Operation

The most significant impact of inrush currents is on the efficacy of transformer protective schemes. Differential protection is commonly employed to protect transformers from a wide range of faults. The principle of differential protection is illustrated in Fig. 1.15. This method involves measuring the currents on both the high- and low-voltage sides of the transformer. Current transformers (CTs) are used for this measurement, and it is important to note that the windings on the two sides of the transformer typically have different numbers of turns. Additionally, CTs may have either identical or differing turns ratios, and three-phase transformers can have various winding configurations, such as star or delta connections.

To design an effective protective scheme, these factors must be carefully considered.

Under normal operating conditions, with no faults, the currents measured on the secondary sides of the CTs should be identical. Consequently, as shown in Fig. 1.15, the current passing through the relay (i_{87T}), indicated as 87T (representing transformer differential protection according to ANSI/IEEE C37.2 Standard), should be zero in an ideal scenario and close to zero in practical conditions. When a fault occurs outside the protection zone (i.e., not between the CTs), both CT currents will increase, but i_{87T} will remain approximately zero, preventing false activation of the protective relay. However, if a fault occurs within the protection zone, the current in one CT may exceed that in the other, leading to an increase in i_{87T}. In such cases, the transformer differential protection will be activated to address the fault.

During transformer energization, as previously discussed, inrush currents flow through the windings connected to the grid, while the secondary winding's current is zero. This situation is analogous to an internal fault, resulting in a discrepancy between the currents measured by two CTs, which in turn causes an increase in i_{87T}. This discrepancy leads to incorrect operation of the relay. This issue is critical to address as it can create significant problems not only for the single transformer being energized but also for other transformers connected in parallel within a substation. Under these conditions, other loaded transformers may experience sympathetic inrush currents, as discussed earlier. In the worst-case scenario, an unplanned transformer energization could induce sympathetic inrush currents across all connected transformers. If protective relays misoperate in response, such incidents could escalate to widespread power outages [34].

Another critical point to highlight is that, similar to fault currents, inrush currents can cause CTs to become saturated. When saturation occurs, the output currents from the CTs become distorted. For instance, Fig. 1.16 shows an example of such distortion when fault occurs at $t = 0.5$ s, with the solid red trace representing the distorted current and the blue solid trace showing a scaled-down version.Both are expressed in per-unit values, normalized using the peak current magnitude before the fault occurred. It is evident that inrush currents can induce significant distortion during the initial cycles. Therefore, addressing this phenomenon is essential when developing new methods for detecting inrush currents [35].

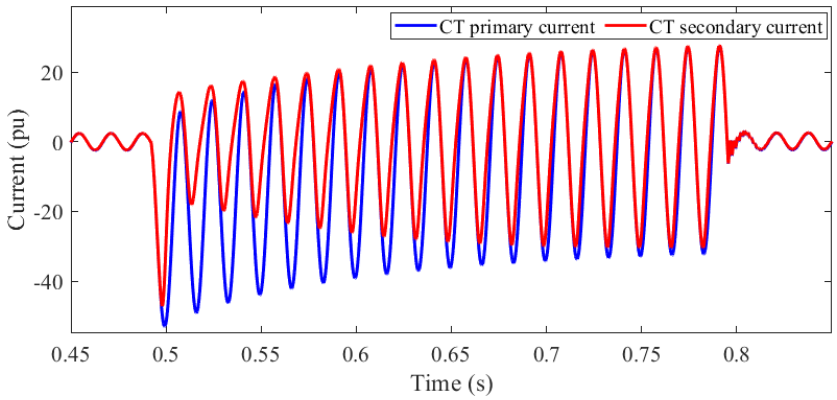

Figure 1.16: Typical CT secondary saturated current (solid red trace) compared with the scaled primary current (solid blue trace).

1.2.5 Solutions of Inrush Current Problems

To address the issues caused by inrush currents, various solutions have been proposed for different applications. In some scenarios, distinguishing between inrush currents and fault currents can resolve the problems, such as in transformer differential protection. Conversely, in other cases, it is preferable to either reduce or eliminate inrush currents. The following subsections will discuss each group of solutions separately.

Discrimination of Inrush Currents from Internal Fault Currents

Since transformer protection relays encounter challenges during energization, it is crucial to develop solutions that help relays differentiate inrush currents from internal fault currents. The second-order harmonic criterion is commonly employed for this purpose. Various second-order harmonic restraint methods have been proposed to detect inrush currents effectively [36], including:

1. Pre-phase method: This is the simplest harmonic restraint method, where the second-order harmonic of each phase is compared to its corresponding fundamental harmonic component. If the condition for each phase is met (i.e., the ratio exceeds a specific threshold, such as 20%), the differential protection for that phase is blocked.

2. Cross-blocking method: Similar to the pre-phase method, this method involves generating a restraint signal for one phase and subsequently blocking the differen-

tial protection for all phases. However, this method has a significant drawback: if there is a fault in one winding, it may go undetected.

3. Percent average blocking method: This method computes the average ratio of second-order harmonics across all phases and compares it to a predetermined setpoint. If the average exceeds the setpoint, the protection for all phases is blocked. While this method enhances security compared to the previous two methods, it still has a potential drawback: a fault in a single phase might go undetected.

4. Harmonic sharing method: In this approach, the second-order harmonic components of all three phases are summed to obtain I_{2ndSUM}. This combined value is then compared to the fundamental component of each individual phase. Protection for a phase is inhibited if the ratio of I_{2ndSUM} to the corresponding fundamental frequency exceeds a specified threshold.

The protection relays sometimes encounter challenges due to low second-order harmonic levels, rendering the second-order criterion ineffective in correctly blocking differential protection. In such cases, additional factors must be considered. With the introduction of high-voltage (500 kV) underground lines, the second-order harmonic in fault currents increases significantly, complicating discrimination between currents. To address this issue, a method is proposed in [37]. Besides the second-order criterion, this method calculates the sum of active power flowing into the transformer terminals. During inrush current events, this power is nearly zero, whereas fault currents consume significant active power.

The intervals within inrush currents can serve as the second factor for consideration. During these intervals, the current remains small and flat for at least one-sixth of the power system cycle. It has been demonstrated that for higher residual fluxes, detecting inrush current intervals is more effective than using second-order harmonic detection [38]. A method based on identifying these inrush current intervals, known as the gap detection technique, has been proposed [38]. This technique utilizes the instantaneous values of three-phase currents and their derivatives to detect inrush currents. For three-phase three-leg transformers, these intervals occur simultaneously. Thus, when all instantaneous currents and their corresponding derivatives are small, it indicates that the transformer is being energized, necessitating the blocking of differential protection.

One issue to highlight is the reduced effectiveness of the gap detection method due to

CT saturation. To mitigate this, the second-order harmonic and gap detection criteria are often used together for inrush current detection. However, even with this combined approach, certain scenarios with high-magnitude inrush currents and CT saturation can still prevent timely detection, resulting in the differential protection not being blocked [6]. Extensive research has been conducted to address this challenge. A notable method for detecting inrush currents in YNd three-phase transformers is proposed in [6]. This method leverages the asymmetry of the inrush current peaks in YNd transformers. Based on this asymmetry, a factor called the normalized difference function (NDF) is defined. When the NDF exceeds a predefined threshold, it indicates that the differential protection should be inhibited.

In some research, wavelet transforms (WTs) have been utilized to distinguish inrush currents from fault currents. WT is a robust technique that decomposes a signal into its various harmonic components. Unlike the discrete Fourier transform (DFT), which analyzes signals in the frequency domain, WT is capable of decomposing signals with non-stationary or transient characteristics. A method based on WT for discriminating inrush currents has been proposed in [39]. This approach introduces a frequency level referred to as $D5$. After a change in current magnitude, the values of the first two peaks in the $D5$ level are measured—designated as X and Y, respectively. For inrush currents, it is observed that $X < Y$, whereas for fault currents, $X > Y$.

A method combining WTs and median absolute deviation (MAD) is introduced in [40]. In this method, the MAD of the 3^{rd} and 4^{th} wavelet components is first computed, and their ratio, denoted as MAD_4/MAD_3, is determined. This ratio is then plotted against the sample number. The resulting curve for inrush currents exhibits greater magnitude oscillations compared to the curve for fault currents. By evaluating these plotted curves and monitoring when differential currents surpass preset thresholds, this method effectively distinguishes between inrush and fault currents.

Another approach for distinguishing inrush currents using WT is described in [41]. In this method, WT is employed to calculate correlation coefficients (CF), represented as $CF = [\rho_{1,2}, \rho_{2,3}, \ldots, \rho_{j-1,j}]$, where j denotes the number of samples in each window. The number of signal dips is then determined from these coefficients. If this count exceeds one, the currents are identified as inrush; otherwise, the signal is attributed to fault currents, prompting the protective relays to activate.

Artificial Neural Networks (ANNs) are computational models designed to simulate

the behavior of the human brain in processing data. These systems can be trained on various datasets to recognize patterns and relationships, which makes them useful for detecting inrush currents during transformer energization. One approach involves using a feed-forward neural network (FFNN) to identify inrush current signatures [42]. This method employs the back-propagation algorithm to train the network with datasets comprising both inrush and fault currents.

Additionally, [43] proposes a technique for reconstructing the output currents of saturated CTs. Since CTs often fail to accurately measure currents immediately following a fault due to core saturation, this study trains an ANN to reconstruct current data and enhance transformer differential protection. To further improve ANN performance, combined approaches have been explored. For instance, [44] integrates WTs with ANNs, using WT to extract various frequency components and ANNs for inrush current detection. Additionally, [45] introduces a method that employs S-transform to extract harmonic components and utilizes ANNs to distinguish inrush currents from other transients.

A method utilizing fuzzy logic to improve the second-order harmonic criterion for inrush current detection is proposed in [46]. This approach involves collecting various data types, including internal and external fault current samples as well as energization current samples, to establish criterion signals, their combinations, and corresponding threshold values. These signals are then mapped into suitable fuzzy sets. To identify inrush currents, differential currents must first surpass a predefined threshold. Subsequently, all fuzzy sets are evaluated. If the fuzzy sets indicate the presence of inrush currents, the differential protection system will be inhibited.

Although methods utilizing ANNs, fuzzy logic, and wavelet analysis are effective in distinguishing inrush currents from fault currents, they require extensive data for training and impose considerable computational demands. To address these challenges, a simpler method based on the normalized grille curve has been proposed [47]. This method plots and analyzes a grille curve. If the curve remains constant over time, it indicates the presence of an internal fault, prompting the protective relay to activate. Conversely, if the curve shows significant variation, it suggests that no internal fault is present (or that inrush currents are occurring), leading to the blocking of differential protection.

A method utilizing a non-linear state-space model of a transformer, which accounts

for hysteresis effects, along with an extended Kalman filter (EKF), has been proposed in [48]. This method defines a residual signal (RS) as the difference between the measured three-phase currents and their estimated values. During energization, the RS is nearly zero, whereas, in the presence of an internal fault, the residual signal deviates from zero.

A method that combines normalized differential current with a fitted sine wave is presented in [49]. A sine wave is fitted to the data using the least-squares technique, and the RSs are calculated as the difference between the normalized differential currents and the fitted sine wave. The extent of oscillations in the RS is used to detect inrush currents. Numerical results indicate that for inrush currents, the amplitude of these oscillations is significantly greater compared to that observed for fault currents.

Inrush Current Elimination Techniques

While the aforementioned methods can effectively differentiate inrush currents from internal fault currents, they do not mitigate the adverse effects of inrush currents. Consequently, several approaches have been developed to either reduce or eliminate these currents. These methods can be categorized as follows:

1. transformer configuration improvements.

2. employing additional compnents.

The first modification to transformer structures involves adding windings to the transformer cores. It has been shown that an air gap in a core produces demagnetizing effects, reducing the impact of residual flux and its associated inrush currents. This concept is utilized in a technique known as the *virtual air gap* [50]. This technique involves embedding a winding within the core and passing a DC current through it. The demagnetizing effect, or the thickness of the virtual air gap, depends on the current flowing through the winding. When the current flows, the winding section becomes saturated, and its permeability approaches that of air (μ_0), thereby reducing the magnitude of the inrush current.

A novel approach for designing transformers to reduce inrush currents is detailed in [51]. This method employs asymmetrical winding configurations, specifically $S-P-S$ and $S-P-S-P$, where P and S denote primary and secondary windings, respectively. By altering the transformer cross-section area, this method achieves high inrush current

inductance while maintaining appropriate leakage inductance. Thus, this significantly reduces inrush currents.

Regarding the use of additional facilities and control circuits, the simplest method is to insert resistors in series with the transformer [52]. While this approach partially mitigates the issue, it does not completely eliminate inrush currents and incurs extra costs. A DC reactor type inrush current limiter for single- and three-phase transformers is proposed in [53]. This limiter comprises a full-bridge uncontrolled rectifier and a DC reactor. Before transformer energization, the reactor's stored energy is zero. Upon connection to the grid, two diodes become forward biased, charging the reactor until the current peaks. Subsequently, all diodes conduct as the reactor discharges, and the reactor current surpasses the transformer current. The reduction of reactor current continues until it matches the transformer's nominal current peak. When the reactor size is optimized, this limiter effectively reduces inrush currents without needing additional control circuits, and with negligible energy loss. However, it distorts voltage and current waveforms in steady-state conditions.

To address waveform distortion, a DC source created by a transformer and full-bridge uncontrolled rectifier is connected in series with the reactor [54]. This approach eliminates waveform distortion but incurs additional costs. An improved limiter for three-phase transformers with a grounded star point, proposed in [55], reduces inrush current magnitude and the number of diodes and reactors by approximately 50% and 33%, respectively, lowering initial and maintenance costs while reducing voltage distortions and losses. Although these limiters reduce inrush current magnitude, they require additional facilities and do not completely solve the issue.

Fault current limiters (FCLs) are also explored for integrating transformers into power systems. A hybrid superconducting fault current limiter (SFCL) is proposed for transformers connecting generators to the grid [56]. This hybrid SFCL includes two SFCLs: one for fault current limitation and another for inrush current mitigation. A control scheme is necessary to differentiate between inrush and fault currents and to determine the SFCLs' impedance. The effect of SFCLs on inrush and sympathetic inrush currents in transformers connected in parallel in a substation is examined in [57]. Results indicate that SFCLs effectively reduce inrush and sympathetic inrush currents, ensuring protective relays operate correctly and can discriminate between inrush and fault currents. Notably, resistive SFCLs (RSFCLs) perform better than impedance SFCLs

(ZSFCLs). Additionally, a method using series-connected PWM converters acting as dynamic resistors for three-phase transformers is addressed, which does not require information about switch-on angles and residual fluxes [58]. This method reduces inrush current magnitude; however, the proportion of harmonic currents remains significant.

Another method involving resistor insertion is the sequential phase energization technique [59, 60]. Unlike the pre-insertion resistor method, this method utilizes a single grounding resistor connected to the neutral point of the star-connected three-phase windings. When all three phases are energized simultaneously, theoretically, no current flows through the grounding resistor, rendering it ineffective against inrush currents. To address this issue, each phase must be energized sequentially with a specific interval between phases (ranging from 5 to 60 cycles). For the first phase, the magnitude of the inrush current decreases monotonically as the grounding resistor's value increases, similar to the pre-insertion resistor technique. For the second phase, the inrush current initially decreases but starts to increase after reaching a specific resistor value. For the third phase, the inrush current magnitude increases monotonically with the resistor value.

In addition to the methods discussed, other strategies known as controlled switching methods have been proposed. As noted in section 1.2.3, inrush currents can be eliminated when prospective fluxes equal residual fluxes. Based on this concept, various switching strategies have been developed [28, 61–63]:

1. Rapid Closing Strategy: This strategy involves obtaining the prospective flux and the residual flux for each phase. The transformer is connected by first engaging the phase with the lowest residual flux. During this time, the fluxes of the other two phases begin to adjust. Each subsequent phase is connected when its residual flux equals its prospective flux, using the corresponding CBs. For phases with zero residual flux or cases that the value of B_r is unknown, phase A is connected first, followed by the other phases when their prospective flux matches their residual flux. Notably, a few milliseconds after energizing the first phase, the prospective fluxes of the remaining two phases will approximately match with their residual fluxes.

2. Delayed Closing Strategy: To implement this strategy, a phase is first energized when its prospective flux matches its residual flux. Subsequently, the residual fluxes of the other phases adjust. For three-phase three-limb transformers, after

a few cycles, the flux of the energized limb is evenly distributed among the other phases. When the flux of the energized limb reaches its positive maximum value, the dynamic fluxes of the other phases become negative and equal to their prospective fluxes. Energizing the remaining two phases at this point effectively eliminates inrush currents.

3. Simultaneous Closing Strategy: Unlike the previous strategies that use independent-pole-operated CBs, this strategy is designed for non-independent-pole CBs (also known as gang-operated CBs), requiring all poles to operate simultaneously. To reduce inrush current magnitudes, optimal points are selected so that the residual flux pattern follows a positive (or negative)/zero (or near zero)/negative (or positive) sequence. For example, if a three-phase three-limb transformer has residual flux densities of 0.5 T/0.15 T/−0.65 T, and the maximum prospective flux is 1 T, the optimal point is where the prospective flux of the second limb is at its zero point on the rising edge. This selection significantly reduces the flux differences, thereby decreasing the magnitude of the three-phase inrush currents.

Theoretically, these strategies can eliminate inrush currents. However, in real applications, some factors are affecting the performance of these strategies which are:

1. CB closing time delays.
2. CB prestrike (also known as the pre-arcing phenomenon).
3. errors in residual flux measurement.

In real conditions, CBs cannot operate instantaneously; their closing time delay ranges from 0.5 to 2 milliseconds. Prestrike is a phenomenon that occurs when the dielectric between the poles of a CB breaks down before metal-to-metal contact is made. This happens when the dielectric strength is lower than the voltage across the CB contacts, causing the insulating capability to be lost and allowing current to flow before physical contact is made. The study in [29] examines the impact of these factors on controlled switching strategies. It concludes that, compared to uncontrolled switching, these strategies effectively reduce the magnitude of inrush currents. The most significant reductions are achieved when transformer limbs are deeply saturated. Similar results are observed when the transformer residual fluxes are zero, although the reduction is less pronounced than in the former case.

Residual fluxes are typically not directly measurable; instead, they are determined by integrating the corresponding phase voltage during de-energization. Several factors can influence this measurement process, making it necessary to account for potential errors in residual flux measurements. The stray or shunt capacitances can discharge through a transformer and reduce the residual flux, which is known as ringdown transient [4]. This phenomenon is a natural resonant response of the circuit formed by the transformer's main inductance and capacitances after transformer de-energization complicating the estimation of residual flux. The impact of these errors on the efficancy of controlled switching strategies is examined in [64]. The study finds that controlled switching strategies remain effective in eliminating inrush currents even with measurement errors of ± 0.22 per unit (pu).

A controlled-switching technique designed for star-connected ungrounded transformers is introduced in [65]. This method involves precise control over both de-energization and energization processes. Initially, to de-energize the transformer, the CB for phase B is opened when its current crosses zero. After a few cycles, the CBs for the remaining phases are opened at their respective zero-crossing points. Using records from the de-energization process, the voltage angle at which two phases are de-energized is determined. For energization, this angle is applied to switch on phases A and C, while phase B is energized when its voltage reaches its positive maximum value. A limitation of this approach is that it may not adequately handle scenarios such as fault occurrences, which can affect de-energization control. To address this issue, [66] proposes an alternative method. This study performs a theoretical analysis based on the transformer's equivalent circuit to determine optimal switching (energizing) angles. According to the study, energizing phases A and C at a voltage angle of $\frac{2\pi}{3}$ radians relative to phase A, and phase B at $\frac{\pi}{2}$ radians relative to phase B, effectively eliminates inrush currents. Although these angles do not account for residual flux effects, they can reduce the magnitude of inrush currents by up to 60.4%.

The *pre-fluxing method* is another method, as outlined in [67, 68], is designed for single-phase transformers and does not require knowledge of residual flux. This method involves injecting energy from a capacitor into a single-phase transformer through one of its windings. By energizing the transformer via the capacitor, the residual flux transitions from its initial value to a maximum positive or negative flux, depending on the polarity of the capacitor voltage. The maximum flux value is determined by the intersec-

tion of the core's B-H curve with the H axis. During energization, the switch-on angle is chosen to minimize the difference between the residual and prospective fluxes. This method is also applicable to three-phase three-limb Yd transformers, as described in [69]. In this configuration, a capacitor is connected to two of the delta-connected windings on the low-voltage side, with induced voltages on these windings being opposite. Consequently, the voltage drop across the third winding is zero, leading to a modification of the residual fluxes in a positive (or negative)/zero/negative (or positive) pattern. With an appropriate voltage angle, significant reduction in inrush currents is achieved.

Additionally, two soft energization methods for hybrid transformers (HTs) equipped with converters are proposed in [8]. In the first method, the transformer is de-energized using energy from a battery, ensuring that the residual fluxes become zero. The battery then gradually increases the fluxes to match the prospective values by either incrementally increasing the converter voltages or applying specific three-phase voltages through the converter. Once the residual fluxes reach the desired levels, the transformer is energized, thereby eliminating inrush currents due to the absence of a difference between residual and prospective fluxes.

A method, known as de-fluxing or demagnetization is introduced in [70]. This ethod employs an ultra-low frequency power source with a gradually decreasing voltage magnitude connected the transformer. As the voltage decreases, the flux in the transformer is shifted from its initial value towards zero, thereby diminishing the magnitude of inrush currents. This method is not ideal for energizing a single power transformer [71], but it can reduce the collective inrush current of parallel transformers by 60% when they are energized simultaneously as reported in [70].

1.3 Motivations and Objectives

As discussed in Section 1.2.5, existing inrush current mitigation methods have primarily been developed for conventional single- and three-phase transformers. While these methods are effective for conventional transformers, they may not be suitable for traction transformers and often require additional facilities or components, which can be cost-prohibitive. Therefore, the primary motivation of this research is to explore and identify methods appropriate for traction transformers that utilize existing facilities in TPSSs, such as power conditioners, to mitigate inrush currents and facilitate smoother transformer energization. The key objectives to achieve this motivation are:

1. **Exploration of New Methods**: Investigate and propose new methods specifically designed for mitigating inrush currents during the energization of traction transformers. These methods should be distinct from those designed for conventional transformers, ensuring compatibility and effectiveness for traction transformers.

2. **Employing Existing Infrastructure or Low-Cost Solutions:** The goal is to develop methods that reduce reliance on additional infrastructure, unlike many traditional inrush current mitigation techniques. These methods seek to maximize the use of existing facilities, such as power conditioners and voltage and current transducers, to their fullest potential. In cases where this is not feasible, the focus shifts to utilizing small-scale devices that do not incur significant additional costs.

3. **Minimal Design Information Requirement:** Ensure that the proposed methods do not require extensive design and parameter information of the transformers, which is often unavailable (is not provided from transformers' manufacturers) or unreliable due to factors such as aging or internal faults. The methods should be capable of safely and reliably acquiring all necessary information during operation.

4. **Robustness Against Measurement Inaccuracies:** Ensure that the proposed methods are resilient to potential threats to their performance, such as inaccuracies and DC offsets in the outputs of measurement devices like voltage and current sensors. The methods should be capable of compensating for these inaccuracies to maintain high levels of performance.

5. **Matching Prospective and Residual Flux:** As discussed in 1.2.3, inrush current can theoretically be eliminated if the prospective and residual fluxes are matched. Most conventional methods do not aim for this exact match but instead focus on having fluxes with the same polarity. The primary goal of the proposed methods should adjust the residual flux to precisely match the prospective flux, even in worst-case scenarios with maximum uncertainties in flux adjustment and CB closing operation. This aim will ensure that the difference between these fluxes is minimal, thereby effectively mitigating inrush current.

6. **Consideration of Operational Uncertainties:** Account for all uncertainties related to the operation of employed components, such as CBs, to minimize their

impact on the performance of the proposed methods. In certain inrush current mitigation methods, such as the pre-fluxing method, uncertainties in the CB closing operation can render the method counterproductive, potentially increasing the magnitude of inrush current instead of reducing it. Therefore, the proposed methods should account for all involved uncertainties and adapt their performance to minimize the impact of these uncertainties.

1.4 Publications and Thesis Structure

1.4.1 Publications

The research and findings presented in this thesis are supported by the following publications:

1. A. Aghazadeh, K. Li, V. Terzija, and S. Azizi, "Modified Pre-Fluxing Method for Energization of Single-Phase Transformers," in 2023 IEEE International Conference on Energy Technologies for Future Grids (ETFG), Wollongong, Australia, 2023, pp. 1-6.

2. A. Aghazadeh, E. Hajipour, K. Li, and S. Azizi, "Mitigating the Inrush Current of V/V Transformers using Railway Conditioners,"*IEEE Access*, vol. 12, pp. 50885-50897, 2024.

3. A. Aghazadeh, E. Hajipour, V. Terzija, and S. Azizi, "A Flux Matching Method for Mitigating the Inrush Current of Single-Phase Transformers," published in *IEEE Transaction on Power Delivery*.

4. A. Aghazadeh, K. Li, M. Popov, V. Terzija, and S. Azizi, "A Modified Pre-Fluxing Method for the Energization of Single-Phase Transformers," submitted to *IEEE Transaction on Industrial Applications*.

5. A. Aghazadeh, E. Hajipour, K. Li, V. Terzija, and S. Azizi, "V/V Traction Transformers' Inrush Current Mitigation using Gang-Operated Circuit Breakers ," will be submitted to *IEEE Transactions on Transportation Electrification*.

1.4.2 Thesis Structure

The rest of this thesis is structured as below:

Chapter 2 details the modeling of traction transformers using the terminal duality model (TDM) in PSCAD/EMTDC. Additionally, it introduces the inverse Jiles-Atherton method for modeling the nonlinearity of transformer cores. This chapter uses a single-phase traction transformer as an example to demonstrate the combined application of the TDM and the inverse JA method for transformer modeling.

Chapter 3 introduces an effective and rapid flux matching energization method for mitigating inrush current in single-phase power transformers, which can be used in phase-shift configuration as detailed in section 1.2.1. This method provides exceptional flexibility in adjusting the transformer's residual flux density to any desired value within a *B-H* curve of the transformer's core (known as feasible range). The only required information is the magnitude of the transformer's excitation current, with all other essential data acquired during the flux adjustment process. By not requiring transformer parameters and design information, this method eliminates significant source of complexities and uncertainties. A key concept introduced is the "compatibility flux density range," within which the reference residual flux density is determined, reducing the impact of CB closing operation limitations. The method adjusts the residual flux density to the reference value by injecting controlled current into the transformer's winding. Finally, it identifies an optimal instant for transformer energization, ensuring the instantaneous value of the steady-state flux density matches the adjusted residual flux density.

Chapter 4 presents a method to effectively mitigate inrush current in single-phase transformers. This method, referred to as the modified pre-fluxing method, overcomes the limitations of the traditional pre-fluxing method. One key advantage of this method is that it does not require detailed information about transformer design, relying solely on measurements for flux adjustment. The proposed method is extremely fast, regardless of transformer size, and can adjust residual flux to any desired value within the feasible range. It accounts for uncertainties in CB closing operations by modifying the core's residual flux to an appropriate reference value, thereby minimizing adverse impacts. Flux adjustment is achieved through power electronic circuitry that applies a suitable voltage across the transformer's low-voltage winding. Rigorous flux estimation and adjustment are enabled by compensating for the DC offset typically present in voltage and current measurements from commercial transducers. The energization process is then initiated at an optimal instant, ensuring that the core's steady-state flux matches the adjusted

residual flux.

Chapter 5 proposes a flux matching method for mitigating inrush current in V/V transformers, commonly used in traction systems. This method requires only nominal voltage and excitation current, eliminating the need for detailed transformer parameters or design information. Unlike existing methods, it can adjust the transformer's residual flux density to any value within the feasible range. Inrush current mitigation is achieved by adjusting the core's residual flux to an appropriate reference value and then identifying the optimal energization instant to energize the transformer by independent-pole circuit breakers. The reference residual flux is chosen to ensure that it can be adjusted to this value and also considere the CB's operating characteristics. The railway power conditioner, typically located on the low-voltage side of the V/V transformer, serves as a current source to inject sinusoidal current into the transformer windings prior to energization. The energization instant is then determined to ensure that the adjusted flux density matches with the steady-state flux corresponding to the applied voltage.

Chapter 6 introduces a flux matching method designed to mitigate inrush current in V/V transformers energized by gang-operated CBs. This method eliminates the need for detailed transformer information and parameters, instead calculating the peak value of the transformer's excitation current through a step-by-step current injection process. Unlike existing methods, it allows adjustment of the transformer's residual flux density to any value within the feasible range. Inrush current mitigation is achieved by adjusting the core's residual flux to an appropriate reference value and identifying the optimal energization instant. The reference residual flux is selected between two optimal points to ensure it can be adjusted to this value, regardless of the transformer's core material, while minimizing the impact of uncertainties involved in the CB closing operation. A technique is proposed to compensate for the DC offset typically exist in voltage measurements from transducers, enabling accurate flux estimation and adjustment. For flux adjustment, sinusoidal current is injected into the the transformer windings through the railway power conditioner installed at the secondary side of the transformer. The energization instant is then determined to ensure the adjusted flux density matches the steady-state flux corresponding to the applied voltage.

Chapter 7 offers a critical discussion and conclusion, along with suggestions for future research directions related to the author's work.

Chapter 2

Traction Transformer Modelling for Inrush Current Mitigation Studies

2.1 Overview

To study various inrush current mitigation methods, it is essential to implement these methods in computer software or real hardware. Conducting experiments on a wide range of actual transformers may be infeasible due to technical challenges and budget constraints. Therefore, having an accurate computer-based model is crucial for conducting different studies. This chapter introduces an effective approach for simulating a traction transformer in PSCAD/EMTDC. For this purpose, the terminal duality model (TDM) is employed, which integrates terminal models with those derived from the principle of duality between electric and magnetic equivalent circuits. TDM can be used with various Electromagnetic Transient Programs, as it relies on a set of mutually coupled inductors available in any circuit simulation software. To account for the non-linearity of the transformer's core, the inverse Jiles-Atherton (JA) method is used to represent magnetizing inductance. The chapter begins with a comprehensive explanation of the TDM and inverse Jiles-Atherton method, followed by the modeling of traction transformers using these methods.

2.2 Terminal-Duality Model

In this section, the TDM proposed by [72] is explained. This novel method for modeling transformers with windings in any configuration is derived through the duality principle between electric and magnetic equivalent circuits, supported by terminal-leakage and short-circuit admittance measurements. To illustrate the TDM methodology, one window of a three-leg three-phase transformer, as shown in Fig. 2.1(a), is employed. The flux path is estimated based on the geometric arrangement of the core and windings relative to each other. Using the estimated flux paths and core dimensions, the transformer's equivalent reluctance circuit is determined, as shown in Fig. 2.1. By applying the duality principle and converting the leakage and core reluctances to linear and nonlinear inductors, respectively, the transformer's dual circuit is obtained (see Fig. 2.1(b)).

Assume that the number of windings visible in the window of the three-phase transformer is five, i.e., $n = 5$. Accordingly, the leakage electric circuit (the portion of the circuit in Fig. 2.1(b) consisting only of leakage inductors) can be derived by considering the mutual inductances between different inductors (e.g., $M_{1,2}$, $M_{1,3}$, etc.), as shown in

Fig. 2.2. In this circuit, U_1 to U_5 represent the nodal voltages, I_1 to I_5 denote the nodal currents, and U_{L_1} to U_{L_5} indicate the voltage drops across the leakage inductors. This circuit enables an accurate determination of the transformer's branch inductance matrix $\boldsymbol{L}$, which can be written as:

$$\boldsymbol{L} = \begin{bmatrix} L_1 & M_{1,2} & M_{1,3} & M_{1,4} \\ M_{1,2} & L_2 & M_{2,3} & M_{2,4} \\ M_{1,3} & M_{2,3} & L_3 & M_{3,4} \\ M_{1,4} & M_{2,4} & M_{3,4} & L_4 \end{bmatrix} \tag{2.1}$$

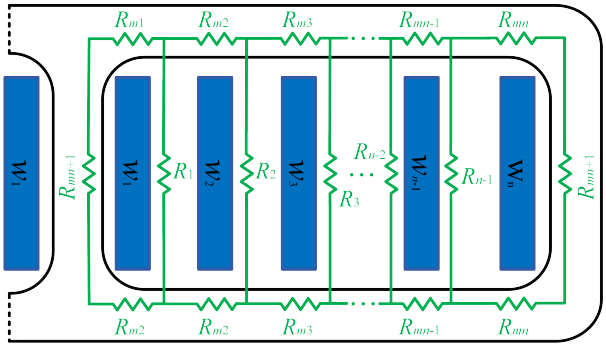

(a)

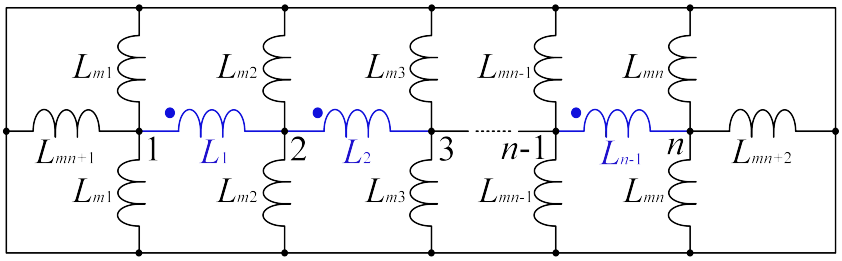

(b)

Figure 2.1: (a) A window of three-leg three-phase transformer and corresponding reluctance circuit, and (b) inductance circuit with the magnetizing (black) and leakage (blue) inductors.

To calculate the matrix $\boldsymbol{L}$, the incidence matrix $\boldsymbol{A}$ must first be derived. In this matrix, the number of rows corresponds to the number of inductors (four in Fig. 2.2), while the number of columns corresponds to the number of nodes, which in this case is five. Each row of $\boldsymbol{A}$ is associated with a specific inductor. For the first inductor, L_1, it

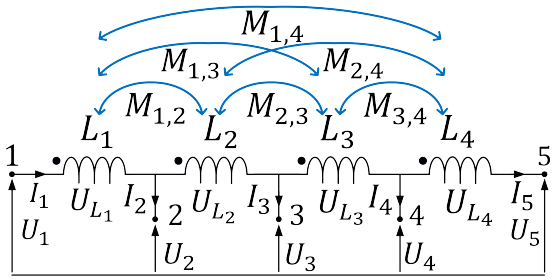

Figure 2.2: Leakage electric circuit of the TDM for five concentric windings.

is connected between nodes 1 and 2, with its positive terminal (indicated by the black circle) connected to node 1. Thus, the first row of $\boldsymbol{A}$ will have a value of 1 in the first column (representing node 1), -1 in the second column (representing node 2), and zeros in all other columns. Similarly, for the second inductor, L_2, connected between nodes 2 and 3, the first column of the second row is zero, the second column is 1 (representing node 2), the third column is -1 (representing node 3), and the remaining columns are zero. Following this pattern for the remaining inductors, the complete incidence matrix $\boldsymbol{A}$ can be expressed as:

$$\boldsymbol{A} = \begin{bmatrix} 1 & -1 & 0 & 0 & 0 \\ 0 & 1 & -1 & 0 & 0 \\ 0 & 0 & 1 & -1 & 0 \\ 0 & 0 & 0 & 1 & -1 \end{bmatrix} \tag{2.2}$$

The matrix $\boldsymbol{A}$ facilitates the transformation of the branch current vector $\boldsymbol{I_b}$ (containing the currents passing through the leakage inductors L_1 to L_4) and the branch voltage vector $\boldsymbol{V_b}$ (representing the voltage drops across the leakage inductors, i.e., U_{L_1} to U_{L_4}) into the nodal current vector (composed of I_1 to I_5) flowing through the windings and the nodal voltage vector $\boldsymbol{V_n}$ at the terminals (composed of U_1 to U_5), as expressed below:

$$\boldsymbol{V_b} = \boldsymbol{A}\boldsymbol{V_n} \tag{2.3a}$$
$$\boldsymbol{I_n} = \boldsymbol{A}^{\boldsymbol{T}}\boldsymbol{I_b} \tag{2.3b}$$

On the other hand, in this model, it is also necessary to determine the nodal admittance matrix $\boldsymbol{Y_n}$ and the transformer's leakage inductance matrix $\boldsymbol{L_S}$. These matrices can be derived through direct measurements, established formulas, or finite element simulations. The nodal admittance matrix $\boldsymbol{Y_n}$ defines the relationship between the voltage

and current phasors at the transformer's terminals in the steady state, as shown in equation (2.4):

$$\boldsymbol{Y_n V_n = I_n} \tag{2.4}$$

To analyze the dynamic behavior of a transformer during energization, it is essential to determine the transformer's branch inductance matrix $\boldsymbol{L}$. This matrix accurately represents the dynamic behavior of the transformer's windings. To derive $\boldsymbol{L}$, we consider the relationship between the voltage and current of each branch, expressed as follows:

$$\boldsymbol{Z_b^{-1} V_b = I_b \Rightarrow V_b = Z_b I_b} \tag{2.5}$$

In this equation, $\boldsymbol{Z_b}$ denotes the branch impedance matrix. By substituting equations (2.3) into this relationship, we obtain:

$$\boldsymbol{I_n = A^T Z_b^{-1} A V_n} \tag{2.6}$$

Assuming the resistive component of the branch impedance is negligible, such that $\boldsymbol{Z_b} = j\omega\boldsymbol{L}$, one can obtain nodal admittance matrix from:

$$\boldsymbol{Y_n = A^T (j\omega L)^{-1} A} \tag{2.7}$$

Consequently, the transformer's branch inductance matrix $\boldsymbol{L}$ can be computed using the nodal admittance matrix $\boldsymbol{Y_n}$ and matrix $\boldsymbol{A}$ as specified by equation (2.7). However, this method has a limitation: matrix $\boldsymbol{A}$ is not necessarily a square, invertible matrix, and the resulting products in the relationship may not always be invertible. Therefore, an objective function must be defined, as outlined in equation (2.8). Numerical techniques are then employed to minimize this objective function, facilitating the determination of matrix $\boldsymbol{L}$.

$$\boldsymbol{F = A^T (j\omega L)^{-1} A - Y_n} \tag{2.8}$$

To resolve this nonlinear equation, the least squares method in MATLAB can be employed. The initial estimate for this solution is derived from the transformer's leakage inductance matrix $\boldsymbol{L_S}$. The solution is refined iteratively until the value of the objective function falls below a specified small error threshold.

The standard impedance voltage test and the nonstandard short-circuit admittance test can be used to obtain the elements of the matrices $\boldsymbol{L_S}$ and $\boldsymbol{Y_n}$, respectively. The standard impedance voltage test [73] is performed between pairs of windings. Assuming there are n windings, to calculate the leakage inductance between the i-th and j-th windings, the i-th winding is energized while the j-th winding is short-circuited and the other windings remain open-circuited. This test determines the leakage impedance between these windings as follows:

$$\begin{aligned} Zs_{ij} &= \frac{U_i}{I_i}\Big|_{U_j=0, I_q=0} \\ &= j\omega Ls_{ij}; i \neq j; q \neq i, j; i, j, q = 1, \ldots, n. \end{aligned} \tag{2.9}$$

The voltage applied to the i-th winding is U_i, and the current flowing through it is I_i. The current flowing through the other windings is denoted as I_q, and ω represents the angular frequency. Using 2.9, one can obtain the matrix $\boldsymbol{L_S}$ as:

$$\boldsymbol{L_S} = \begin{bmatrix} Ls_{12} & 0 & 0 & 0 \\ 0 & Ls_{23} & 0 & 0 \\ 0 & 0 & Ls_{34} & 0 \\ 0 & 0 & 0 & Ls_{45} \end{bmatrix} \tag{2.10}$$

where the leakage inductance between nodes 1 and 2 is Ls_{12}, which equals L_1 in Fig. 2.2. Similary, $Ls_{23} = L_2$, $Ls_{34} = L_3$, and $Ls_{45} = L_4$.

To determine the nodal admittance matrix, non-standard tests should be employed. In these tests, to determine the elements of a row (for example, i) the i-th winding should be connected to a variable voltage source while the other windings are short-circuited. In this case, the voltage of the i-th winding is gradually increased from zero volts until the nominal current flows through the i-th winding. Under these conditions, we have:

$$Y_{ij} = \frac{I_j}{V_i}\Big|_{U_k=0} \quad k \neq i; i, j, k = 1, 2, \ldots, n. \tag{2.11}$$

The voltage applied to the i-th winding is denoted as V_i, the current flowing through the j-th winding is denoted as I_j, and n represents the number of coils per phase. Using 2.11, one can obtain the matrix $\boldsymbol{Y_n}$ as:

$$\boldsymbol{Y_n} = \begin{bmatrix} -Y_{11} & Y_{12} & Y_{13} & Y_{14} & Y_{15} \\ Y_{21} & -Y_{22} & Y_{23} & Y_{24} & Y_{25} \\ Y_{31} & Y_{32} & -Y_{33} & Y_{34} & Y_{35} \\ Y_{41} & Y_{42} & Y_{43} & -Y_{44} & Y_{45} \\ Y_{51} & Y_{52} & Y_{53} & Y_{54} & -Y_{55} \end{bmatrix} \tag{2.12}$$

where $Y_{11} = (Y_{12} + Y_{13} + Y_{14} + Y_{15})$, $Y_{22} = (Y_{21} + Y_{23} + Y_{24} + Y_{25})$, $Y_{33} = (Y_{31} + Y_{32} + Y_{34} + Y_{35})$, $Y_{44} = (Y_{41} + Y_{42} + Y_{43} + Y_{45})$, and $Y_{55} = (Y_{51} + Y_{52} + Y_{53} + Y_{54})$.

Using the matrices $\boldsymbol{Y_n}$, $\boldsymbol{A}$, and $\boldsymbol{L_S}$ along with a numerical solution approach, matrix $\boldsymbol{L}$ can be determined. Subsequently, with the duality-based transformer model established, the nonlinear inductors (modeled with the inverse Jiles-Atherton Model as explained in section 2.3) must be accurately connected to their specific locations at the transformer's terminals to obtain the equivalent electrical circuit of the transformer. This model is thus based on the configuration of the core and windings, with the transformer model representing this equivalent electrical circuit. Detailed explanations of these relationships and the procedure for computing matrix $\boldsymbol{L}$ will be provided in section 2.4, complete with diagrams and examples.

2.3 Inverse Jiles-Atherton (JA) Method

As mentioned in section 1.2.3, the nonlinear relationship between B and H is depicted by hysteresis loops, as shown in Fig. 2.3. This nonlinear behavior of ferromagnetic materials affects the reluctance of transformer cores, causing it to vary when transformers are connected to power networks. To account for the hysteresis effect in simulations, the Jiles-Atherton method is commonly employed, which determines the value of B for a given input of H [74]. The Simulink implementation of this method is detailed in Appendix A. However, the JA method is not ideal for transformer modeling, as it requires the magnetic field strength H, whereas in transformer simulations, the flux density B can be easily derived from the integral of the applied voltage. Consequently, the inverse Jiles-Atherton method is preferred, as it computes H based on a given value of B [75–77]. When modeling a power transformer, it is beneficial to express H as a function of B, since the flux density value can be readily calculated from the transformer winding voltages in time-domain simulations. The inverse JA method decomposes the

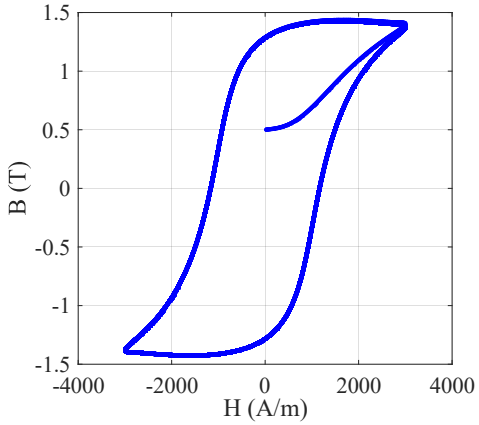

Figure 2.3: B-H curve with 0.5 T residual flux density.

magnetization into reversible (M_{rev}) and irreversible (M_{irr}) components as follows:

$$M = M_{rev} + M_{irr} \tag{2.13}$$

These two components of magnetization are related to e anhysteretic magnetisation (M_{an}) as follows:

$$M_{rev} = c(M_{an} - M_{irr}) \tag{2.14}$$

The anhysteretic magnetization M_{an} is characterized by the Langevin function, which illustrates the saturation behavior of the magnetic core

$$M_{an} = M_s \left[\coth\left(\frac{H_e}{a}\right) - \left(\frac{a}{H_e}\right) \right] \tag{2.15}$$

where $H_e = H + \alpha M$, referred to as the effective magnetic field. By considering B as the input variable, the inverse JA method is simplified as follows:

$$\frac{\mathrm{d}M}{\mathrm{d}B} = \frac{(1-c)\left(\frac{\mathrm{d}M_{irr}}{\mathrm{d}B_e}\right) + \left(\frac{c}{\mu_0}\right)\left(\frac{\mathrm{d}M_{an}}{\mathrm{d}H_e}\right)}{1 + \mu_0(1-c)(1-\alpha)\left(\frac{\mathrm{d}M_{irr}}{\mathrm{d}B_e}\right) + c(1-\alpha)\left(\frac{\mathrm{d}M_{an}}{\mathrm{d}H_e}\right)} \tag{2.16}$$

where

$$\frac{\mathrm{d}M_{irr}}{\mathrm{d}B_e} = \frac{M_{an} - M_{irr}}{\mu_0 k \delta} \tag{2.17}$$

In equation (2.16), the effective magnetic induction is $B_e = \mu_0 H_e$. The directional parameter δ, which indicates whether the magnetic fields are increasing or decreasing, is determined by:

$$\delta = \begin{cases} 1, \ if \ \frac{\mathrm{d}H}{\mathrm{d}t} > 0 \ (increasing field) \\ -1, \ if \ \frac{\mathrm{d}H}{\mathrm{d}t} < 0 \ (decreasing field) \end{cases} \tag{2.18}$$

The derivative of anhysteretic magnetisation can be calculated by using (2.15) as:

$$\frac{dM_{an}}{dH_e} = \frac{M_s}{a}\left[1 - \coth^2\left(\frac{H_e}{a}\right) + \left(\frac{a}{H_e}\right)^2\right] \tag{2.19}$$

where c, α, δ, M_s, and k are various coefficients of the inverse JA method.

By selecting suitable values for these coefficients, the B-H curves of transformers can be accurately modeled. The input for the inverse JA method is the flux density, which can be derived from the integral of the voltage across the transformer winding, as shown in equation (1.2). The excitation current of the transformer is directly related to the magnetic field strength H, and can be obtained from:

$$i(t) = \frac{l_m}{N} H(t) \tag{2.20}$$

In this context, l_m represents the length of the magnetic path. Fig. 2.4 shows the numerical procedure for calculating the excitation current as a function of flux density [75]. In this figure, $v_s(t)$ denotes the voltage applied to the transformer's winding, R_s is the winding resistance, and L_s represents the transformer leakage inductance. The Simulink implementation of inverse JA method is detailed in Appendix A.

2.4 Model of a Single-Phase Traction Transformer

In this section, a 25-MVA, 220 kV/27.5 kV core-type single-phase traction transformer is modeled using the TDM for implementation in PSCAD/EMTDC software. Fig. 2.5 shows this single-phase traction transformer. The low-voltage windings, connected in series, are first wound on both limbs of the transformer. After applying a layer of insulation, the high-voltage windings are then wound over them. In Fig. 2.6, the core and winding dimensions are reported in meters. To demonstrate the application of TDM in modeling this traction transformer, two different cases are considered: one where the transformer is in a healthy condition, and another where a turn-to-turn fault occurs in one of the high-voltage windings (which is explained in Appendix B).

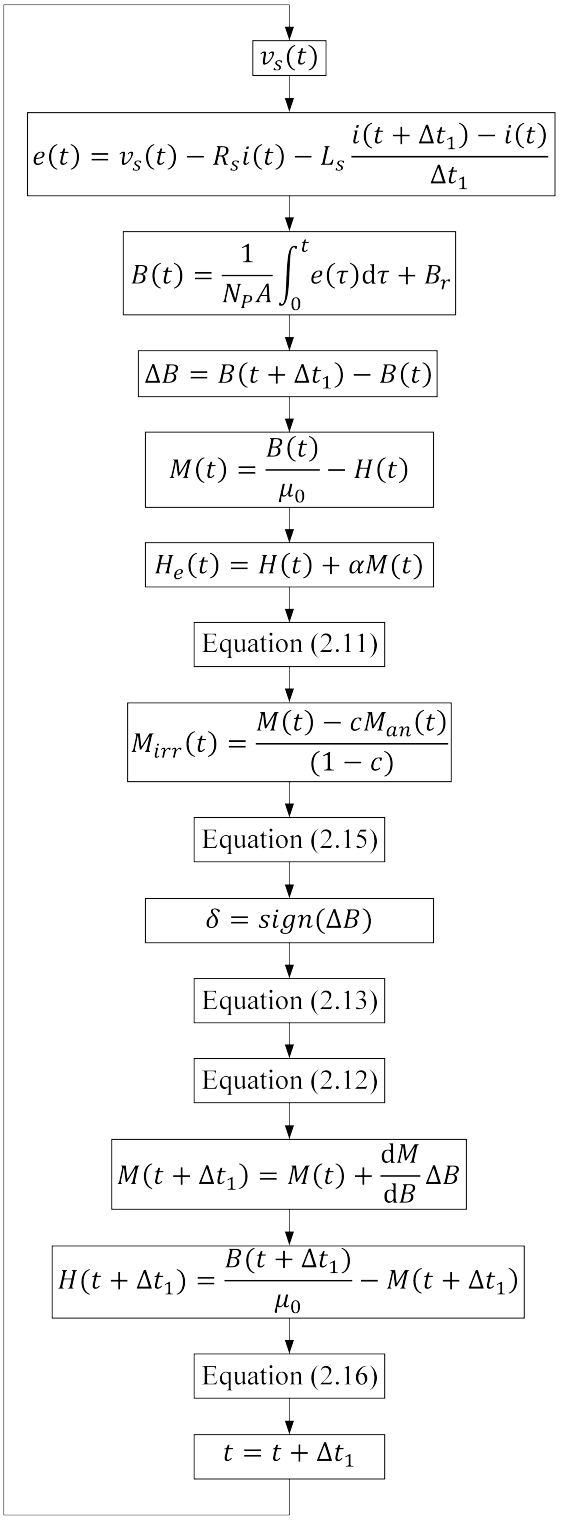

Figure 2.4: Flowchart of numerical procedure to implement the inverse JA.

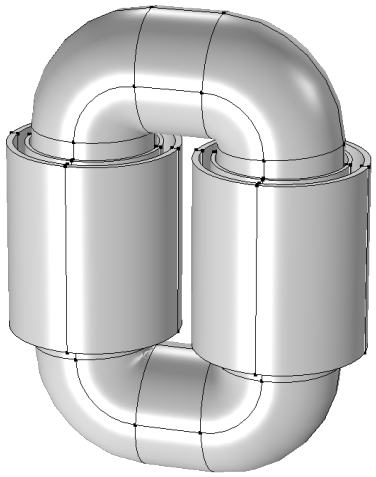

Figure 2.5: A 25-MVA, 220 kV/27.5 kV core-type single-phase traction transformer.

2.4.1 Healthy Transformer

Fig. 2.7 illustrates the winding arrangement and core of the single-phase traction transformer in a healthy operating condition. This figure also shows the voltages across each winding and the associated terminals, labeled as V_H and V_L. Here, $2V_H$ represents the voltage applied to the high-voltage winding (since the high-voltage windings are connected in series), while $2V_L$ represents the voltage induced on the low-voltage winding under normal operation. Additionally, the dual equivalent circuit is depicted. In this figure, the nonlinear inductors L_m correspond to the reluctances of the transformer's limbs and yokes. For simplicity, the reluctance of the upper yoke sections is not shown, but their effect is accounted for by doubling the reluctance values of the lower yokes due to symmetry. These nonlinear reluctances are determined based on the core dimensions along the estimated flux path and the nonlinear permeability coefficient of the core, effectively modeling the core, which will be further elaborated upon later.

The linear inductors L_s between the windings are calculated based on the fluxes and leakage inductances between each pair of windings. The winding model involves determining these linear inductors. On each leg, there are only two windings, resulting in one leakage inductance between the windings, with no mutual inductance. If there were additional windings, mutual inductance would also exist between the leakage inductors, in addition to the leakage inductance.

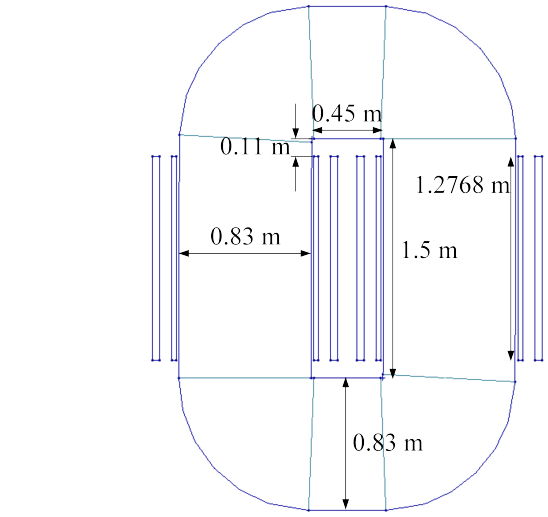

(a)

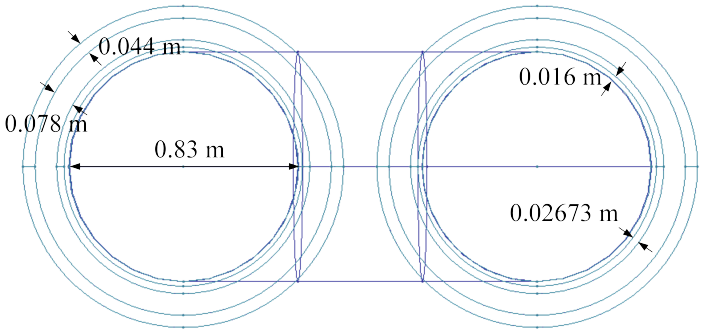

(b)

Figure 2.6: Transformer (a) front view, and (b) cross-sectional view.

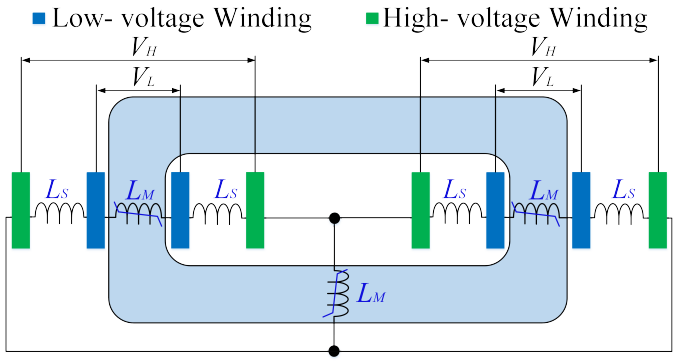

Figure 2.7: The core and winding arrangement of the single-phase traction transformer, along with its corresponding inductance circuit in a healthy operating condition.

The value of the leakage inductance, i.e., $\boldsymbol{L_S}$, should be determined through conducting the standard impedance voltage test. In this thesis, finite element simulation is used to measure the leakage inductances $\boldsymbol{L_S}$. For this purpose, the Maxwell ANSYS software, a powerful tool for finite element simulation, is utilized. The mesh used in the simulation must be fine enough that further refinement does not alter the results. To ensure the simulation conditions match standard test procedures, windings that need to be open-circuited are connected to a zero-current source in the finite element simulation. Windings that need to be short-circuited are connected to a zero-voltage source with a very small resistance. Instead of using a variable voltage source that causes the rated current to flow through the winding, the winding is directly connected to a current source with a current equal to the rated current.

For example, to measure the leakage inductance between two windings using Maxwell ANSYS software, the second winding should be connected to a zero-voltage source, simulating a short circuit. The first winding is connected to a current source with a current equal to the rated current. All other windings should be completely open-circuited, meaning they are connected to a zero-current source. In this scenario, using equation (2.9), the ratio of the voltage of the first winding to the current passing through it will equal the leakage inductance. All these measurements must be reported relative to a reference number of turns of winding (N_b). This means during the finite element simulation to model the test transformer, the number of turns for all windings is the same. In this thesis, the reference number of turns is considered to be $N_b = 100$. However, the actual turn ratios will be incorporated into the final model.

In the Maxwell software, when 5-A current passes through the high-voltage winding while the low-voltage winding is short-circuited, the voltage across the high-voltage winding is 4.62 V. Using equation (2.9), the value of the leakage inductance is determined as follows:

$$L_s = \frac{4.62}{5 \times 2\pi \times 50} = 2.94 \text{ mH} \tag{2.21}$$

Since the leakage inductance between two windings is modeled with two inductors, the inductance of each inductor is set to 1.47 mH. For a healthy transformer, there are only two windings with a single leakage inductance between them, making it impossible to compute mutual inductances between different inductors. To demonstrate how the

TDM can be applied to model a transformer, the single-phase transformer with a turn-to-turn fault is considered and modeled, as detailed in Appendix B.

The inverse JA method is employed to model the nonlinear inductors L_M, shown in Fig. 2.7, accounting for the nonlinearity of the transformer's core. The maximum flux density is set to 1.5 T. Three different core types are examined: *Type* 1, with a maximum feasible residual flux density of 0.6 B^{max}, *Type* 2, with B_r^{max} of 0.75 B^{max}, and *Type* 3, with B_r^{max} of 0.853 B^{max}. Table 2.1 lists the parameters used in the inverse JA method for these core types, and the corresponding B-H curves are shown in Fig. 2.8. The peak amplitude of the excitation currents for *Type* 1, *Type* 2, and *Type* 3 transformers are 0.4 A, 0.3 A, and 0.32 A respectively.

Table 2.1: The B-H curve parameters

	M_s	α	a	k	c
Type 1	1.41×10^6	2.5×10^{-5}	13.55	10	0.08
Type 2	1.41×10^6	2.5×10^{-5}	11.55	10	0.08
Type 3	1.41×10^6	2.5×10^{-5}	10	20	0.08

Fig. 2.9 presents the final model of the single-phase traction transformer. In addition to the inductance circuit depicted in Fig. 2.6, the model incorporates four ideal transformers without losses and magnetizing branches (denoted as $HV01$, $HV02$, $LV01$, and $LV02$), and series-connected resistors, i.e., R_{CU} and R_{CL}. The ideal transformers are used to account for the nominal turn ratio of the single-phase traction transformer. As mentioned earlier, the number of turns considered during measurements in Maxwell ANSYS software is $N_b = 100$, which differs from the actual number of turns in the winding. To accurately represent the turn ratio of the single-phase transformer, which is N_H/N_L, these ideal transformers are employed with a turn ratio of N_H/N_b for the $HV01$ and $HV02$ transformers and N_L/N_b for the $LV01$ and $LV02$ transformers. The series connected resistors are used to model the copper losses of the transformer. In this model, $R_{CU} = 1.71\Omega$ and $R_{CL} = 0.033\Omega$, leading to 97.4 kW copper losses.

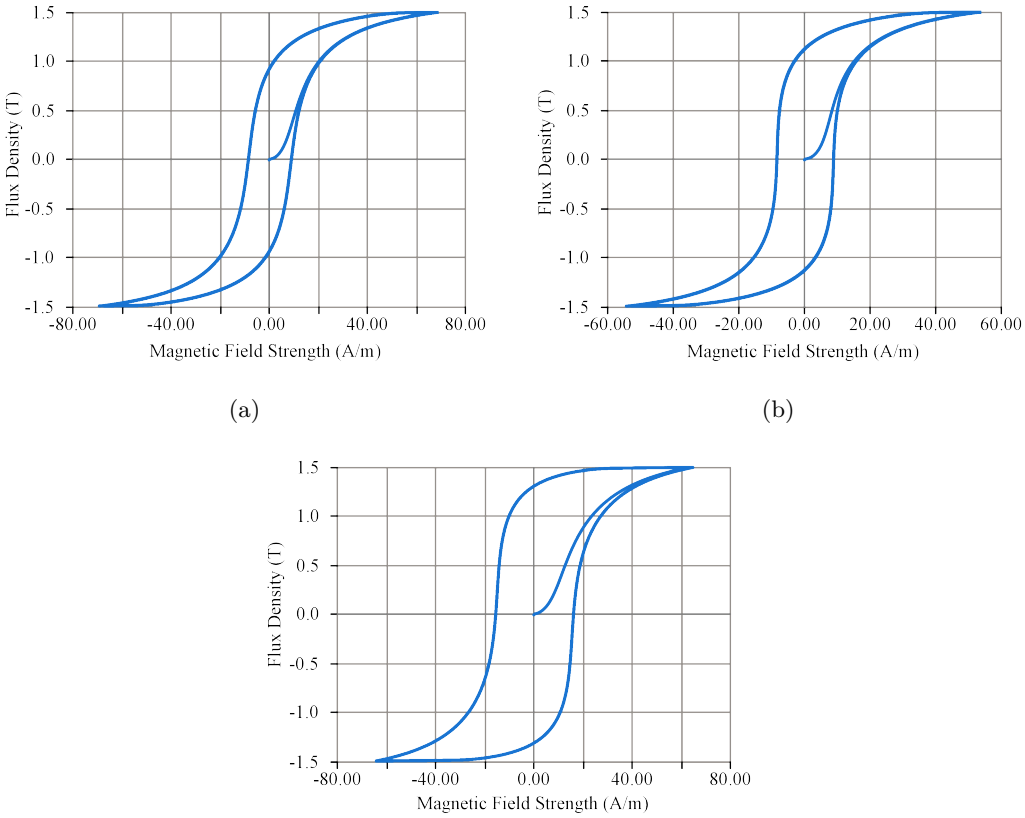

Figure 2.8: *B-H* curve of (a) *Type* 1, (b) *Type* 2, and (c) *Type* 3 transformers.

2.5 Summary

This chapter detailed the application of TDM to simulate a single-phase traction transformer in PSCAD/EMTDC software. Beyond TDM, the chapter also explored the inverse JA method to model the nonlinearity of transformer cores. By combining TDM with the inverse JA method, the chapter demonstrates how high-power transformers can be accurately modeled and implemented in PSCAD/EMTDC software. To illustrate the use of TDM and the inverse JA method, a single-phase traction transformer was used as an example, modeling both its healthy condition and its state with a turn-to-turn fault.

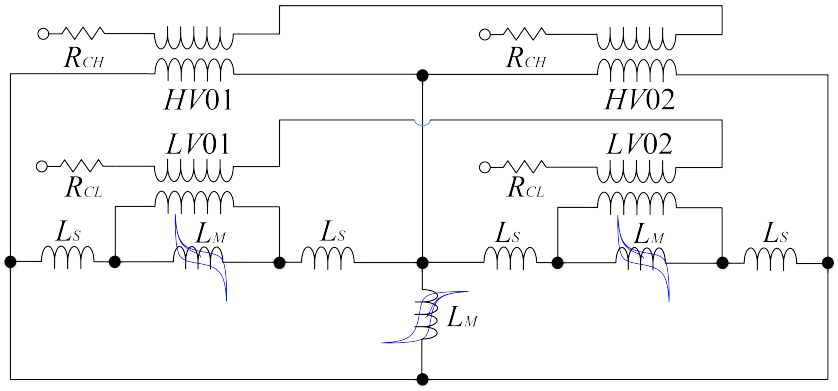

Figure 2.9: Electric Circuit of the TDM for the single-phase traction transformer in healthy operating condition.

Chapter 3

Flux Matching Method for Single-Phase Traction Transformers

3.1 Overview

This chapter introduces an effective and rapid flux matching energization method for mitigating inrush current in single-phase power transformers, which are widely used in TPSSs. The proposed method provides exceptional speed and flexibility in adjusting the transformer's residual flux density to any appropriate value within the feasible range, regardless of the transformer's capacity. This adjustment minimizes the impact of uncertainties associated with CB closing operations on transformer energization. The chapter details how these uncertainties and limitations can affect transformer energization and introduces the concept of a "compatibility flux density range." Values within this range possess two important characteristics: they fall within the feasible range for the transformer's residual flux density, and the corresponding making voltage (which leads to the same prospective flux) can be achieved by the CB even under extreme uncertainties.

The method adjusts the residual flux density to the reference value by injecting controlled current into the transformer's winding. A novel technique is introduced to estimate flux density during current injection, which operates independently of transformer design parameters and requires only compensated voltage transducers with no DC offset. This current injection is carefully regulated to prevent damage to the transformer. The peak value of the injected current is limited to the peak value of the excitation current, ensuring the transformer is not driven into saturation. Additionally, the rate of change of current during injection is controlled to ensure that the voltage induced on the open-circuit winding does not exceed the transformer's nominal voltage, thereby avoiding damage. After adjusting the flux, an optimal energization instant is determined, considering all uncertainties, to minimize the difference between the instantaneous value of the steady-state flux density and the adjusted flux density.

3.2 Flux Matching: Fundamental Principles and Potential Obstacles

Flux matching methods are designed to minimize discrepancies between the residual and prospective flux densities, significantly reducing or even entirely eliminating inrush currents—particularly in an ideal scenario free from uncertainties. The process begins with accurately estimating the core's residual flux density or adjusting it to a predetermined value. Then, the transformer is energized at the optimal instant to ensure smooth

operation.

Adjusting the flux density to a specific value is generally preferred over simply estimating the residual flux density for two main reasons. First, accurately monitoring transformer flux density just before disconnection is challenging, as disconnection is often preceded by disturbances and sudden waveform distortions that can make measurements unreliable [78]. Second, the residual flux density is not stable after the transformer is switched off; it diminishes gradually due to the formation of a resonant circuit between the transformer's inductance and stray or shunt capacitances. This phenomenon, known as ringdown transient, is a natural resonant response of the circuit after de-energization, complicating the estimation of residual flux [4].

The pre-fluxing method [67, 69] is an effective method for adjusting flux prior to the controlled switching of CBs. For this method, let B_r^{ad} represent the adjusted residual flux density of the core, where the superscript "ad" distinguishes it from the core's initial flux density, B_r. During the flux adjustment phase, B_r is modified to $\pm B_r^{max}$ by discharging a capacitor into the transformer's winding. Following this, a controlled switching stage is employed to minimize the difference between B_r^{ad} and B_p. To successfully match the prospective fluxes corresponding to $\pm B_r^{max}$, the transformer must be energized at specific instants, which may or may not be feasible given the constraints and operating characteristics of the CB. In fact, the limitations of CBs prevent a range of making instants—and therefore a range of prospective fluxes—from being achievable. As a result, using pre-fluxing method may result in a significant discrepancy between B_r^{ad} and B_p, as will be demonstrated in the simulation section.

Due to the B-H curve of the transformers' cores, in principle, the adjusted residual flux can only be adjusted to values within the feasible range $[-B_r^{max}, B_r^{max}]$. To effectively mitigate inrush currents, it is necessary to avoid prospective fluxes that fall within the ranges $(B_r^{max}, B^{max}]$ and $[-B^{max}, -B_r^{max})$. It is also important to recognize that the inherent uncertainty in the closing operation of CBs makes it impossible to detect the exact instant the transformer will be energized. Therefore, an effective flux matching method aimed at reducing inrush current in transformers must:

1. enable precise adjustment of residual flux density.
2. consider the CB's dynamics and uncertainties.
3. minimize dependence on transformer specific design information.

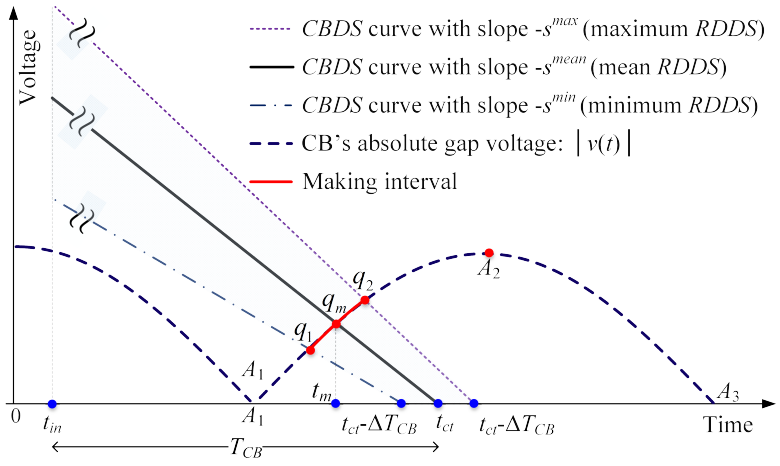

Figure 3.1: Effect of mechanical and *RDDS* uncertainties on the making instant.

3.3 Safe and Compatibility Flux Density Ranges Associated with CB Closing Operation

To understand how the closing operation of a CB impacts the energization of transformers, it is essential to analyze the details of this operation and the associated uncertainties. Fig. 3.1 shows the closing operation of a CB while the nominal voltage $v(t) = V_m \cos(\omega t)$ is applied to the transformer. This process begins at t_{in} and extends until the contact touch instant, t_{ct}, which marks the instant when the fixed and moving contacts of the CB make metal-to-metal contact. The duration from t_{in} to t_{ct} is referred to as the closing time, T_{CB}. This interval is influenced by the velocity of the CB's moving contact as it approaches the fixed contact following the closing signal. During this interval, the dielectric strength of the CB (*CBDS*) progressively reduces as the gap between the fixed and moving contacts decreases. The rate at which this dielectric strength decreases is referred to as the rate of decrease of dielectric strength (*RDDS*). After receiving the closing signal, the *CBDS* is represented by a descending line, where the slope of the line is the negative of the *RDDS* [79].

As the CB approaches the end of its closing operation, current begins to flow through it due to the establishment of an electric arc, which creates an electrical connection. This conduction process starts at a specific instant known as the making instant (t_m), which occurs when the *CBDS* curve of the CB first intersects the absolute gap voltage—the

voltage across the CB poles. For a given contact touch instant (t_{ct}), the making instant is defined as the earliest time t that satisfies the following equation:

$$|v(t)|+s(t-t_{ct})=0 \tag{3.1}$$

where $|v(t)|$ represents the instantaneous gap voltage of the circuit breaker, and s is *RDDS*. To determine the solution to this equation, iterative numerical methods such as the *fzero* function in MATLAB can be employed. The MATLAB code used for solving this equation is provided in Appendix D.

In practice, *RDDS* is not fixed but is instead expected to vary within a known range, $[s^{min}, s^{max}]$, with an anticipated mean value s_{mean}. This uncertainty in *RDDS* is often referred to as *RDDS* scatter. Similarly, the closing time of a CB is not precise and is generally assumed to fall within a range of length ΔT_{CB}, with an average of T_{CB}, which is termed mechanical scatter. Due to these uncertainties, both *RDDS* and closing time exhibit probabilistic characteristics across different closing attempts. While the CB initiates its closing operation at a specified instant, mechanical scatter means that the actual contact touch occurs within a time window spanning $[t_{ct}-\Delta T_{CB}, t_{ct}+\Delta T_{CB}]$.

Due to the mechanical and *RDDS* scatter, the actual making point of the CB may not match precisely with the target making point but instead occur within a range surrounding it on the absolute gap voltage. In Fig. 3.1, the target making point is indicated by q_m, and the feasible making range is highlighted in red, spaning from q_1 to q_2. Consequently, the actual making instant could deviate slightly from the ideal target making instant t_m. The true *CBDS* curve for any given closing attempt appears as an oblique line within the shaded area depicted in Fig. 3.1. The maximum deviations from the target making instant are represented by s_{min} and $t_{ct}-\Delta T_{CB}$ for negative deviations, and s_{min} and $t_{ct}+\Delta T_{CB}$ for positive deviations, as shown in Fig. 3.1. This study assumes that *RDDS* and T_{CB} follow normal distributions around their mean values. The standard deviations of these variables are calculated based on their respective variation ranges and the 3-σ criterion [79].

The deviation from the ideal target making instant is minimized when the transformer is energized within the range from A_1 to A_2, rather than from A_2 to A_3. Therefore, it is recommended to energize the transformer during the rising half of an absolute gap voltage hump [80]. Following this approach reduces the impact of *RDDS* and mechanical scatter, thereby narrowing the making interval. Moreover, initiating the energiz-

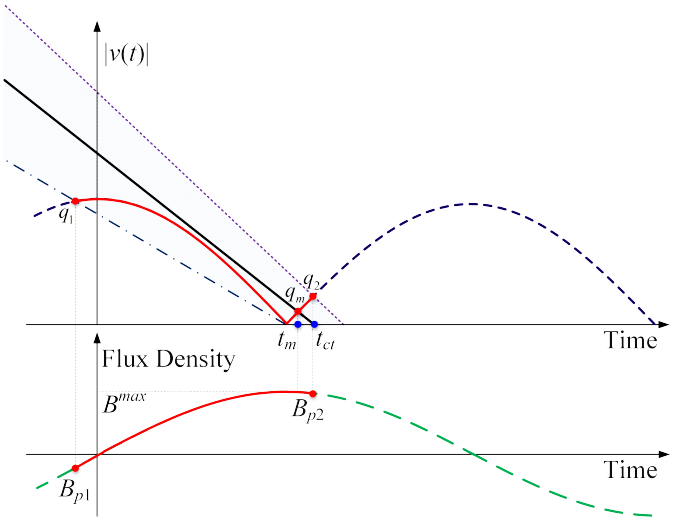

Figure 3.2: Extreme expansion of the quadrilateral region to the previous hump.

ation process closer to the lower end of the A_1 to A_2 range is advisable, as points nearer to A_1 exhibit even less sensitivity to scatter [80].

Makings that occur too close to A_1 can cause the shaded quadrilateral region in Fig. 3.1 to cover the previous hump, as shown in Fig. 3.2. In such cases, the lower boundary of this region may intersect with the previous voltage hump, leading to a broader feasible making range and a considerable difference between B_r^{ad} and B_p. For example, if the residual flux density is adjusted based on the prospective flux density corresponding to the point q_m near B^{max}, but the actual prospective flux density is negative and falls below zero (e.g., near B_{p1} in Fig. 3.2), this mismatch can occur. To prevent this, the closing operation must begin after a specific instant referred to as the "critical initiation instant." This instant is the earliest point at which the risk of making on the previous hump is eliminated, even under extreme conditions.

To determine the critical initiation instant, the quadrilateral region in Fig. 3.1 must be shifted to the left until its lower side becomes tangent to the previous hump at q_{tan}, as illustrated in Fig. 3.3. In Fig. 3.3, time instants are denoted by the Greek letter τ to differentiate them from those in Fig. 3.1. The lower side of the quadrilateral region in Fig. 3.3 corresponds to $\tau_{ct} - \Delta T_{CB}$ and s^{min}. Therefore, the derivative of the absolute gap voltage at τ_{tan} equals $-s^{min}$, as shown below:

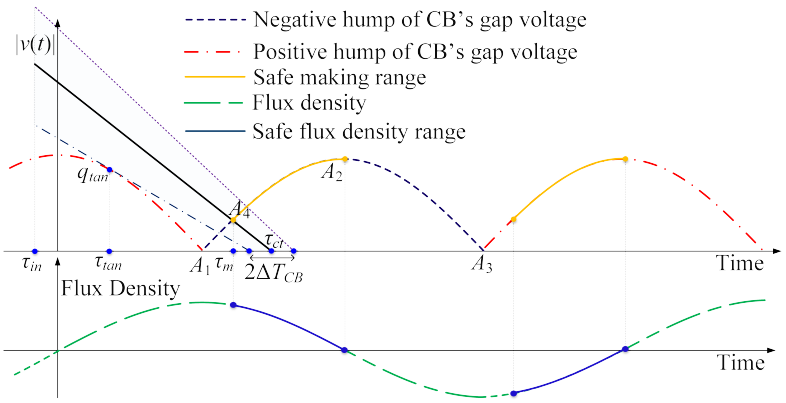

Figure 3.3: Safe making range on the absolute gap voltage and safe flux density range with reference to the CB operating characteristics.

$$-\omega V_m \sin(\omega\tau_{tan}) = -s^{min} \tag{3.2}$$

As a result, τ_{tan} is given by $\tau_{tan} = \sin^{-1}\left(\frac{s^{min}}{\omega V_m}\right)/\omega$, and the critical contact touch instant τ_{ct} satisfies the following condition:

$$|V_m \cos(\omega\tau_{tan})| = s^{min}((\tau_{ct} - \Delta T_{CB}) - \tau_{tan}) \tag{3.3}$$

Solving (3.3) for τ_{ct} gives

$$\tau_{ct} = \tau_{tan} + \Delta T_{CB} + \frac{|V_m \cos(\omega\tau_{tan})|}{s^{min}} \tag{3.4}$$

To ensure that making does not occur on the previous hump, the closing operation should be initiated after $\tau_{in} = \tau_{ct} - T_{CB}$. The process of determining the safe flux density range begins by calculating the making instant (τ_m) associated with τ_{ct} and s^{mean}. This instant, corresponding to the making point at A_4, is found by substituting τ_{ct} and s^{mean} into equation (3.1). The critical prospective flux density is then defined as the minimum value between the prospective flux density at the argument $\omega\tau_m + \phi_0$ and the maximum feasible residual flux density, as shown below:

$$B_{crit} = min[B^{max} \sin(\omega\tau_m + \phi_0), B_r^{max}] \tag{3.5}$$

Indeed, B_{crit} defines the upper boundary of the compatibility flux density range. When the rising half of the positive gap voltage is chosen, the lower boundary of this range is set at $-B_{crit}$. Combining these two limits, the compatibility flux density range is identified as a subset of the entire feasible flux density range, specifically $[-B_{crit}, B_{crit}] \subset [-B_r^{max}, B_r^{max}]$. As mentioned, any point within the compatibility flux density range has two important characteristics: it can be achieved by the residual flux density, and with proper switching, the transformer can be energized at a voltage corresponding to this prospective flux.

3.4 Residual Flux Adjustment

This section presents the proposed method for adjusting the residual flux of single-phase transformers. Consider the single-phase transformer depicted in Fig. 1.1 that supplies Section 2. In this scenario, the transformer is disconnected from the upstream three-phase power network and is about to be energized, with its residual flux density potentially lying anywhere within the feasible range $[-B_r^{max}, B_r^{max}]$. Section 2 is isolated from the other two sections, and no load is being supplied in this section, as the transformer's secondary winding is open-circuited. Once energized, this transformer will supply electric trains operating in Section 2 as they move to or from adjacent sections. Consequently, the transformer is energized to ensure the availability of power for these trains. Depending on the number of trains present in Section 2, the transformer may intermittently supply power or remain idle. However, its primary side will remain energized following the energization process.

This scenario is typical in practice, representing a situation where the section is not connected to auxiliary power circuits but is about to be reconnected to the transformer after being disconnected from the upstream power network (e.g., for maintenance or due to a fault). Once re-energized, the transformer will supply power to electric trains operating in this section. In this case, the circuit can be simplified to the one shown in Fig. 3.4. It is assumed that a current source is available to inject current into the transformer's secondary winding, as shown in Fig. 3.4. This compact, low-power source can be integrated into existing transformer testing equipment and is used to adjust the residual flux density to a reference value within the feasible range of $[-B_r^{max}, B_r^{max}]$.

Accurate flux adjustment requires real-time estimation of flux density during current injection. This is achieved using a novel technique developed in this research, which es-

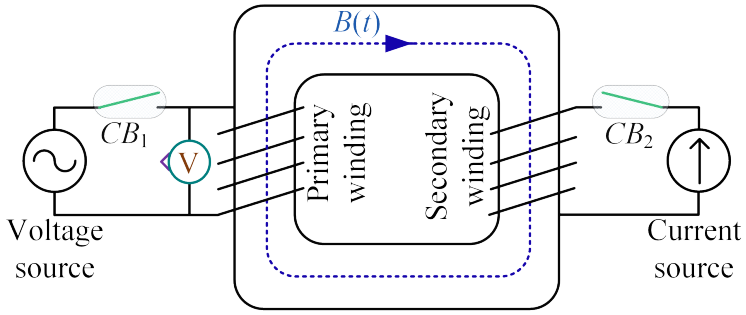

Figure 3.4: Single-phase transformer with a current source on its secondary side, and a voltage transducer on its primary winding.

timates flux density based on the voltage induced on the open-circuited primary winding. This voltage is measured by a transducer installed across the primary winding, as shown in Fig. 3.4. Once the flux adjustment is complete, the current source is disconnected by opening CB_2. The transformer is then energized by closing CB_1 at a precise instant, ensuring the difference between B_r^{ad} and B_p is minimized, ideally to zero.

The flexibility and ease of use in transformer operations can be significantly enhanced by the ability to adjust flux density without relying on the initial residual flux or specific transformer design details. This subsection introduces an innovative method for adjusting residual flux density through controlled current injection, which eliminates the need for prior knowledge of the initial value of B_r. This achievement is particularly noteworthy, as it has been made possible by emphasizing the per-unit value of the flux density.

Let us begin by assuming $B_r = 0$. Fig. 3.5 shows the B-H curve generated by injecting a biphasic half-hexagonal current with a peak amplitude equal to the peak value of the transformer's excitation current (I_{ex}). When this current, depicted in Fig. 3.5(a), is injected into the secondary winding of the single-phase transformer, it adjusts the residual flux density to B_r^{max}. In this scenario, the magnetic field strength within the core decreases from zero to $-H_{ex}$ as the current drops from zero to $-I_{ex}$, causing the flux density to shift from zero to $-B^{max}$, as shown in Fig. 3.5(b).

The transition from the initial residual flux density to $-B^{max}$ is the only phase of flux adjustment that is affected by the initial residual flux density. Once $-B^{max}$ is reached at $\frac{2T}{9}$, the subsequent magnetization path becomes independent of the initial residual

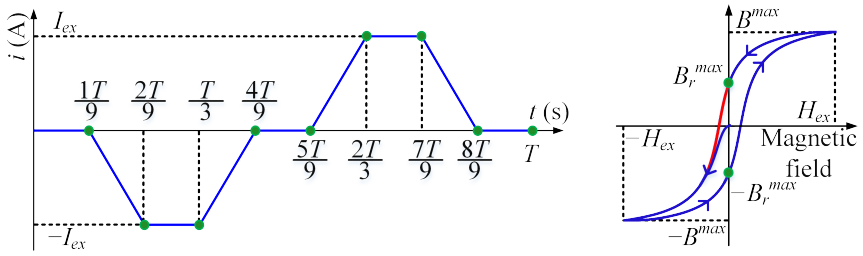

(a) (b)

Figure 3.5: Transformer (a) current waveform, and (b) B-H curve during current injection.

flux density. The flux density remains stable at $-B^{max}$ until $t = \frac{T}{3}$. Afterward, the current begins to rise towards zero and then continues to I_{ex} before eventually dropping back to zero. These current transitions correspond to flux densities of $-B_r^{max}$ at $t = \frac{5T}{9}$, B^{max} at $t = \frac{7T}{9}$, and B_r^{max} at T. Injecting the biphasic half-hexagonal current into the transformer as outlined adjusts the residual flux density to B_r^{max}. The red path on the B-H curve in Fig. 3.5(b) would not be followed by the flux density unless the initial residual flux density was B_r^{max}. Reversing the polarity of the current shown in blue in Fig. 3.5(a) results in an adjusted residual flux density of $-B_r^{max}$.

In this research, per-unit flux density, denoted by $\hat{B}(t)$, is utilized as a method for enabling flux adjustment with minimal input data. To implement this approach, B^{max} is determined and used as the reference (or base) flux density. Calculating $\hat{B}(t)$ requires measuring the voltage induced on the open-circuited primary winding during current injection, represented by $v_p(t)$. This voltage is captured using the voltage transducer depicted in Fig. 3.4, with the assumption that any DC offset in its output is compensated before initiating the flux adjustment. The flux density at any given time t can then be calculated using the following expression:

$$B(t) = \frac{1}{NA}\int_0^t v_p(t)\mathrm{d}t + B_r \tag{3.6}$$

As previously noted, the flux density attains the values of $-B^{max}$ and B^{max} at $\frac{T}{3}$ and $\frac{7T}{9}$, respectively. To determine B_r and B^{max}, equation (3.6) can be employed as

follows:

$$\begin{cases} B_r = \frac{-1}{2NA}[\int_0^{\frac{7T}{9}} v_p(t)\mathrm{d}t + \int_0^{\frac{T}{3}} v_p(t)\mathrm{d}t] \\ B^{max} = \frac{1}{2NA}[\int_0^{\frac{7T}{9}} v_p(t)\mathrm{d}t - \int_0^{\frac{T}{3}} v_p(t)\mathrm{d}t] \end{cases} \tag{3.7}$$

Using equations (3.6) and (3.7), $\hat{B}(t)$ can be determined from:

$$\hat{B}(t) = \frac{B(t)}{B^{max}} = \frac{2\int_0^t v_p(t)\mathrm{d}t - \int_0^{\frac{7T}{9}} v_p(t)\mathrm{d}t - \int_0^{\frac{T}{3}} v_p(t)\mathrm{d}t}{\int_0^{\frac{7T}{9}} v_p(t)\mathrm{d}t - \int_0^{\frac{T}{3}} v_p(t)\mathrm{d}t} \tag{3.8}$$

Starting at $t = T$, the per-unit flux density can be obtained using Equation (9). Injecting current for the duration T adjusts the flux density to its maximum feasible residual value, i.e., $\hat{B}(T) = \hat{B}_r^{max}$. If $\hat{B}(T) = \hat{B}_{crit}$, the current injected by $t = T$ ensures that the residual flux density can be matched through proper switching, with no risk of making on the previous hump. If not, the controlled current injection must continue until the adjusted residual flux density falls within the compatibility flux density range.

For adjusting the flux density to values below B_r^{max}, this research proposes the injection of a negative triangular current, as shown in Fig. 3.6(a). In this figure, corresponding points on current and flux density curves are marked by symbols of matching shapes and colors. The rate of change of injected current is reversed when $\hat{B}(t)$ reaches a value sufficiently below $\hat{B}_{crit}$. In other words, once $\hat{B}(t) = \alpha\hat{B}_{crit}$ where α is a real number such that $0 < \alpha < 1$. The reversal of the rate of change of injected current would make the magnetic field strength ascend from a negative value to zero again. By doing so, first, the adjusted residual flux density moves from its starting point towards $\alpha\hat{B}_{crit}$. Then, as demonstrated in Fig. 3.6(b), the adjusted residual flux density takes a value slightly higher than $\alpha\hat{B}_{crit}$. If needed, this process can be repeated until the residual flux density falls within the compatibility range, i.e., $\hat{B}_r^{ad} < \hat{B}_{crit}$.

Fig. 3.7 illustrates the flux adjustment procedure through two iterations, with red arrows indicating the direction of flux density changes. In the first iteration, the flux density rises to B_1, which is greater than B_{crit}; however, in the second iteration, the residual flux is adjusted to a value below B_{crit}, denoted as B_2. In all simulations and experiments presented in this research, the desired flux density was achieved in a single iteration with $\alpha = 0.9$. For α values below 0.9, the adjusted residual flux density would be lower, shifting the ideal target point on the absolute voltage curve closer to the

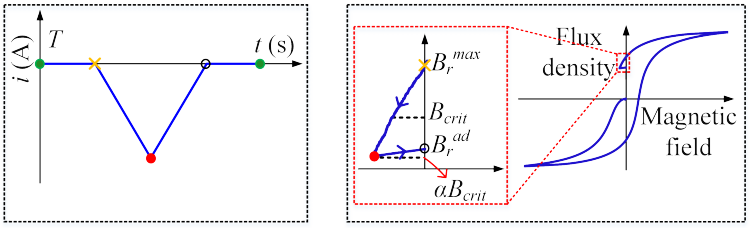

(a) (b)

Figure 3.6: Transformer (a) current waveform, and (b) *B*-*H* curve during current injection.

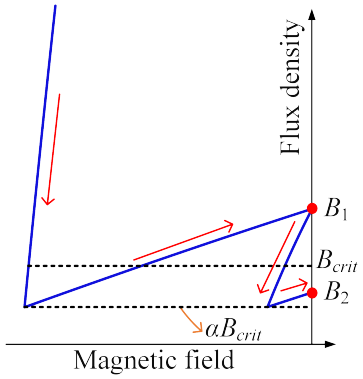

Figure 3.7: *B*-*H* curve during current injection to adjust the residual flux density below $0.9B_{crit}$ with two repetitions.

waveform's peak. This increases the negative impact of *RDDS* and mechanical scatter on the making instant [80].

3.5 Minimum Time Period for Flux Adjustment

The biphasic half-hexagonal current shown in Fig. 3.6 is defined by its peak value I_{ex}, time period T, and slope m. Let Δt represent the time interval during which the injected current increases from 0 to I_{ex}. This interval is given by $\Delta t = \dfrac{T}{9}$. Therefore,

$$T = 9\overbrace{\left(\frac{I_{ex}}{m}\right)}^{\Delta t} = \frac{9I_{ex}}{m} \tag{3.9}$$

The voltage across the open-circuited primary winding when the current $i(t)$ is in-

jected into the secondary winding can be expressed as [81, 82]:

$$v_p(t) = \frac{N_p N_s A}{l} \frac{\mathrm{d}B}{\mathrm{d}H} \frac{\mathrm{d}i}{\mathrm{d}t} \tag{3.10}$$

In this equation, N_p and N_s are the number of turns in primary and secondary windings, and the length of the magnetic path is denoted by l. Assuming a linear transformer model, the derivative of flux density with respect to field strength is considered constant and equal to the permeability (μ) of the core's material. As a result, the mutual magnetizing inductance between the primary and secondary windings is given by:

$$L_m = \frac{N_p N_s A}{l} \frac{\mathrm{d}B}{\mathrm{d}H} \tag{3.11}$$

By neglecting transformer losses and leakage flux, one can arrive at $I_{ex} = \dfrac{V_m}{\omega L_m}$, where V_m is the transformer's nominal peak voltage of the primary side [83]. In reality, $\dfrac{\mathrm{d}B}{\mathrm{d}H}$ varies along the hysteresis loop and its maximum occurs at the points where the magnetic field H is changing rapidly around the coercive field values, i.e., the slope of the B-H curve is normally steepest at the coercive points where the magnetization is switching direction [84]. Transformer cores are typically made from materials with high magnetic permeability and low coercivity (i.e., Silicon Steel, Amorphous Steel, and Ferrites), as these characteristics minimize energy losses and improve efficiency. The maximum $\dfrac{\mathrm{d}B}{\mathrm{d}H}$ can be several times higher than what the transformer's linear inductance model assumes. This can be represented as $\left(\dfrac{\mathrm{d}B}{\mathrm{d}H}\right)_{max}$, with the scaling factor K generally much lower than 30 for most core materials [84–87].

To determine an upper bound for the rate of change of the injected current, it is assumed that the current source is sufficiently robust, with no limitations on its rate of change of current. Injecting current at a slower rate through any source that injects the biphasic half-hexagonal current to the transformer's winding will not compromise the insulation of the transformer. The injected current into the secondary winding can be modeled as $i(t) = mt + b$, which will induce a voltage on the primary winding. Over the course of flux adjustment, the maximum voltage induced on the primary winding can be obtained from

$$(v_p(t))_{max} = KmL_m = \frac{KmV_m}{\omega I_{ex}} \tag{3.12}$$

To prevent damage to the transformer's insulation during flux adjustment, it is essential to ensure that the induced voltage does not exceed the transformer's nominal peak voltage. Consequently, the maximum allowable slope of the injected current can be determined using the formula $m_{max} = \frac{\omega I_{ex}}{K}$ as given in (3.12). Ensuring that the biphasic half-hexagonal current injection remains within this limit will protect the transformer from damage. By substituting m_{max} with m in (3.9), the minimum time period can be calculated as follows:

$$T_{min} = \frac{9I_{ex}}{m_{max}} = \frac{9K}{\omega} \tag{3.13}$$

Adjusting the flux by injecting a biphasic half-hexagonal current with a period exceeding T_{min} ensures that the transformer insulation remains protected from damage caused by overvoltage.

3.6 Single-Phase Transformer Controlled Switching

The transformer energization is the next stage after the flux density is adjusted to an appropriate value. At this stage, the current source shown in Fig. 3.4 is disconnected from the transformer via CB_2, and the transformer is then energized using CB_1 at the appropriate instant. To find this instant, let $v(t) = V_m \cos(\omega t + \phi_0)$ represent the voltage applied to the primary winding to energize an unloaded single-phase transformer. Without loss of generality, the time reference can be chosen such that $\phi_0 = 0$. To match the residual flux density with the prospective flux density, the phase angle of the rising half of the gap voltage that ensures this is obtained from

$$\phi = \pi - \sin^{-1}(\hat{B}_r^{ad}) \tag{3.14}$$

This phase angle corresponds to making at $t_m = \frac{\phi}{2\pi f}$, where f is the power system frequency. The corresponding contact touch and closing operation instants can then be obtained from

$$t_{ct} = t_m + \frac{|V_m \cos(\omega t_m)|}{s^{mean}} \tag{3.15}$$

$$t_{in} = t_{ct} - T_{CB} \tag{3.16}$$

Fig. 3.8 presents the flowchart of the flux matching method proposed. The flowchart shows two main stages: Flux adjustment and controlled switching stages. The

flux adjustment is accomplished by controlled current injection using a current source connected to the secondary side of the transformer when the primary side is left open-circuited. The safe flux density range is obtained with reference to the CB operating characteristics. The compatibility flux density range is determined, and the flux density is adjusted within this range using the flux adjustment procedure described. This is followed by disconnecting the current source and administering the controlled switching stage. To this end, the secondary side of the transformer is open-circuited and the closing command is issued at t_{in}. Minimizing the difference between the residual and prospective flux densities can ideally eliminate inrush current completely, or significantly reduce it considering uncertainties introduced by the CB operating characteristics.

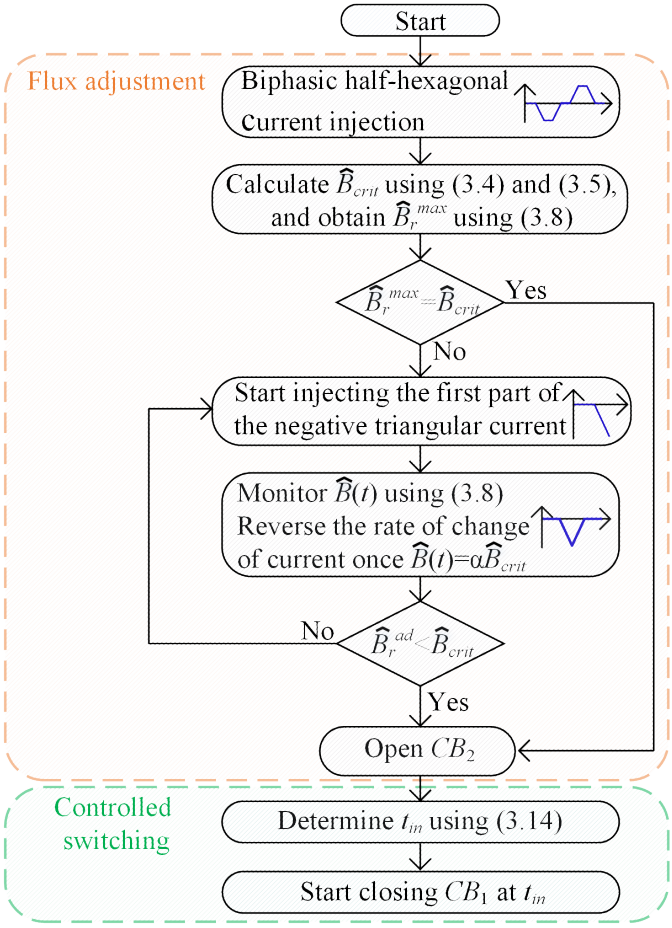

Figure 3.8: Flowchart of the proposed flux matching method.

3.7 Performance Evaluation

To demonstrate the effectiveness of the proposed method, a 25-MVA, 220 kV/27.5 kV core-type single-phase transformer is simulated in PSCAD/EMTDC based on the terminal duality method (TDM) [72]. The inverse Jiles-Atherton model is used to account for the nonlinearity of the core [75–77]. The *Type* 1 and *Type* 2 different cores, which are explained in section 2.3, are studied. To model mechanical and *RDDS* scatter, *RDDS* and closing operation time are modeled as random variables with normal distributions. The standard deviation of each random variable is set based on the associated scatter and the 3-σ criterion [79]. A full-bridge single-phase inverter is used as a current source for flux adjustment. The DC-link voltage of the inverter is 1.5 kV, and hysteresis current control is employed to regulate the inverter's output. Finally, a test rig containing a 400-VA, 260 V/120 V shell-type single-phase transformer is used to experimentally evaluate the performance of the proposed method.

In what follows, first, inrush current drawn by randomly energizing the transformers is scrutinized. Next, a general performance evaluation is conducted considering the uncertainties of the CB operation. Section 3.7.2 focuses on the flux adjustment procedure for a single-phase transformer. In Section 3.7.3, a comparison study is conducted between the proposed, pre-fluxing [67], de-fluxing [68], and random energization methods. Finally, the experimental validation results are presented and discussed.

3.7.1 Problems of Random Energization

Random energization, also known as casual energization, refers to energizing the transformer without specific measures to mitigate inrush current. To simulate random energization, the closing command is assumed to be received with a random uniform distribution over an interval of 20 ms. For this evaluation, $RDDS = 50$ kV/ms with $\pm 30\%$ scatter, and $T_{CB} = 40$ ms with ± 1.5 ms mechanical scatter. In evaluating the severity and distribution of inrush current following random energization, the worst-case energization scenario is taken as the reference to compare the results. To this end, the transformer is energized at the rising zero-crossing of the voltage (the prospective flux density is equal to $(-B^{max})$, when $B_r = B_r^{max}$. This results in the maximum difference between the two. Fig. 3.9 shows the resulting inrush currents for *Type* 1 and *Type* 2 single-phase transformers. In the worst-case scenario, the inrush current drawn by the

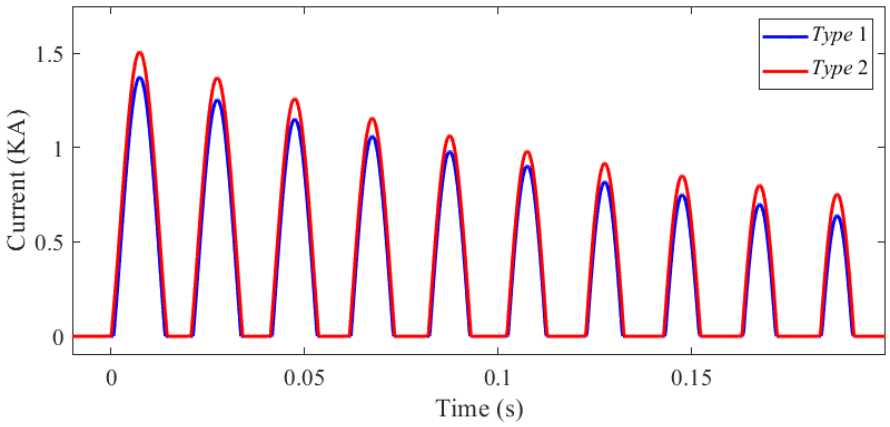

Figure 3.9: Inrush currents during the worst-case energization.

transformers reaches 1.37 kA and 1.5 kA in terms of magnitude, respectively.

In random energization, the residual flux density may take any random value within the feasible range $[-B_r^{max}, B_r^{max}]$. To account for the randomness of variables, the simulations are repeated 1000 times. For the *Type* 1 transformer, the highest current magnitude lies within the range $[0.463, 1370]$ Amps with mean 739 A. For the *Type* 2 transformer, this lies between 0.32 A to 1500 A with mean 788 A. As expected, inrush current could become several times larger than the peak amplitude of the nominal current (which is 160 A). In addition to troubling protective relays, the recurrence of high-magnitude inrush current would reduce the transformer's lifespan.

3.7.2 General Evaluation of the Proposed Method

In this subsection, first, the impact of CB's *RDDS* on the critical prospective flux density is demonstrated. To this end, it is assumed that $\Delta T_{CB} = 1.5$ ms and *RDDS* scatter is $\pm 30\%$. Figs. 3.10(a) and 3.10(b) demonstrate critical prospective flux density as a function of *RDDS* and the maximum feasible residual flux density for both transformers. In these figures, the maximum feasible residual flux density is shown as a straight line in red. The CB cannot ensure a per-unit prospective flux density greater than $\sin(\omega t_m + \phi_0)$, which is marked in blue. The minimum of these two curves is actually the critical prospective flux density, as per equation (3.5). As shown in Fig. 3.10(a), the *Type* 1 transformer cannot be energized with $B_p = B_r^{max}$ if the CB's $RDDS \leq 32$ kV/ms because, under this condition, B_{crit} is less than 0.6. If the CB's $RDDS > 32$ kV/ms, the

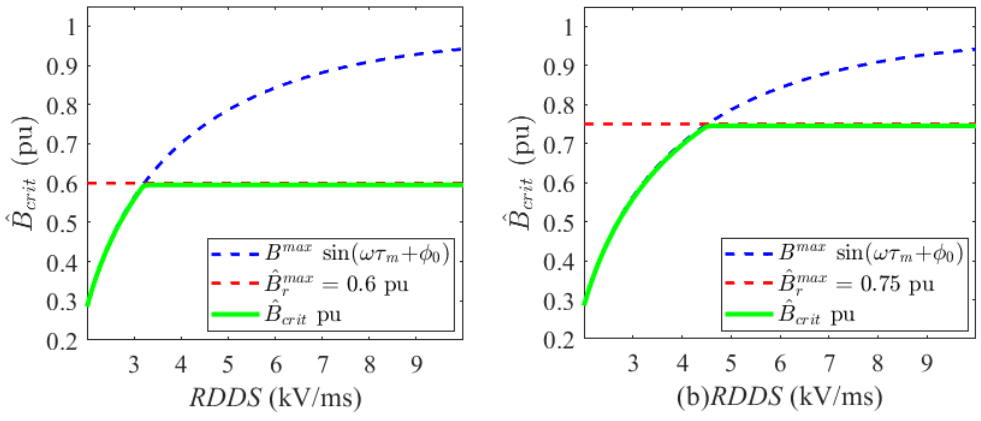

Figure 3.10: Critical prospective flux density for (a) *Type* 1, and (b) *Type* 2.

transformer can be safely fluxed such that $B_p = B_r^{max}$, with no risk of making on the previous hump. For the *Type* 2 transformer, the same arguments can be respectively established for CB's *RDDS* of smaller and greater than 45 kV/ms.

For general performance evaluation, a CB with $RDDS = 50$ kV/ms and $T_{CB} = 40$ ms is used. To account for the uncertainties involved in the CB closing operation, $\Delta T_{CB} = 1.5$ ms and $0.7s^{mean} < RDDS < 1.3s^{mean}$ are considered. The upper limit of the compatibility flux density range equals B_r^{max} for the two transformers. This implies that the CB can safely energize both types of transformers when the residual flux density is adjusted to B_r^{max}, with no risk of making occurrence on the previous hump.

To stochastically assess the influence of scatter on the proposed method, a sensitivity analysis is conducted by running 10,000 simulations on each transformer. Table 3.1 summarizes the impact of scatter on the transformer energization. Making instants for the *Type* 1 and *Type* 2 transformers fall within the ranges [6.76 ms, 9.67 ms] and [6.3 ms, 8.59 ms], respectively. These correspond to the prospective flux densities within the ranges [0.1pu, 0.85pu] and [0.43 pu, 0.91 pu].

Fig. 3.11 shows the distributions of making instants for both transformers. The ideal target making instants at 7.9 ms and 7.3 ms (denoted by the dashed and solid red lines) show the highest probability of occurrence, as expected. In most cases, a small difference exists between the real and ideal target making instants. The probability of making occurrence decreases as farther we go from the ideal target making instant.

Table 3.1: Scatter's Effect on the Proposed Method's Performance

RDDS		s^{min}	s^{mean}	s^{max}
Closing Time		$T_{CB} - \Delta T_{CB}$	T_{CB}	$T_{CB} + \Delta T_{CB}$
Type 1	t_{ct} (ms)	11.43	12.93	14.43
	t_m (ms)	6.76	7.9	9.67
	$\hat{B}_p$ (pu)	0.85	0.6	0.1
Type 2	t_{ct} (ms)	9.91	11.41	12.91
	t_m (ms)	6.3	7.3	8.59
	$\hat{B}_p$ (pu)	0.91	0.75	0.43

This probability becomes eventually zero at the lower and upper bounds of the making interval, which are indicated by the dashed and solid black and purple lines. Fig. 3.11 also demonstrates the impact of larger B_r^{max} (as is the case for the *Type* 2 transformer). Higher values of B_r^{max} are associated with narrower making intervals, thereby better matching between the residual and prospective flux densities.

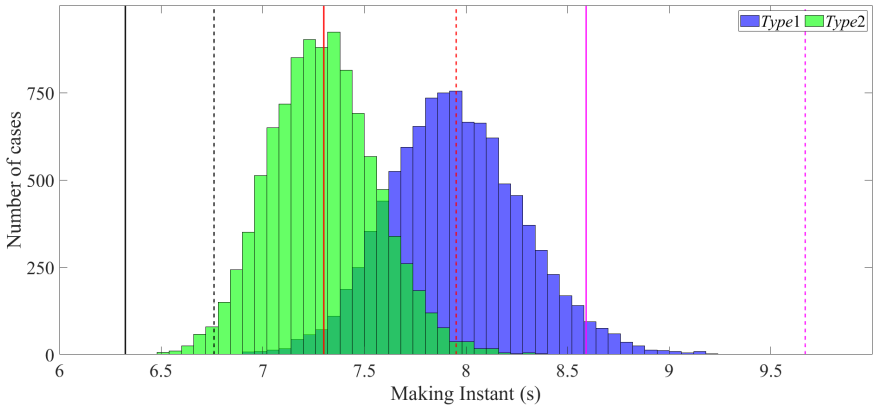

Figure 3.11: Making instant distributions for *Type* 1 and *Type* 2 transformers.

3.7.3 Flux Adjustment by the Proposed Method

To determine the minimum time period required for flux adjustment, we suppose there is no accurate knowledge of the transformer core materials or the parameter K. Therefore, K is conservatively assumed to be 30, leading to a maximum allowable rate of change

Table 3.2: Estimation of Maximum Feasible Residual Flux Density

Type	$B_r(T)$	-0.9	-0.6	-0.3	0	0.3	0.6	0.9
1	$\hat{B}(T)$	0.61	0.6	0.6	0.59	0.61	0.6	0.6
2	$\hat{B}(T)$	0.75	0.74	0.75	0.76	0.76	0.75	0.74

of current m_{max} of 33.5 A/s for the *Type* 1 transformer, and 25.13 A/s for the *Type* 2 transformer. According to equation (3.13), this results in a minimum time T_{min} of 0.87 seconds for both transformers.

Flux adjustment for *Type* 1 and *Type* 2 transformers is achieved by connecting a single-phase inverter to the secondary winding, where I_{ex} would be equal to 3.2 A and 2.4 A, respectively. The period of the injected current waveform is $T = 4.5$ s, which is greater than the minimum time needed for flux adjustment. Fig. 3.12 shows the flux adjustment procedure for the *Type* 1 transformer with three different initial residual flux densities. Fig. 3.12(a) shows the reference and real currents, which demonstrate the injected current is independent of the initial residual flux density and follows the reference current. In Fig. 3.12(b), it is shown that the residual flux density is adjusted to B_r^{max} after 4.5 s regardless of the initial value of B_r. Using equation (3.7), the maximum feasible residual flux density is estimated at $t = 4.5$ s. Table 3.2 presents results obtained on both transformers with different residual flux densities. As can be seen, the proposed method's ability to estimate B_r^{max} is not affected by the transformer type or initial residual flux density.

Fig. 3.13 shows how the proposed method can adjust the residual flux density to a value below B_r^{max}, using the *Type* 1 transformer with $B_r = 0$ and $\hat{B}_{crit} = 0.51$ pu. As per Fig. 3.13(a), the injected current into the secondary winding is a biphasic half-hexagonal with an amplitude of 3.2 A and time period of $T = 4.5$ s. The injection of the biphasic half-hexagonal current enables the adjustment of the flux density at B_r^{max} and also enables the estimation of the core's flux density in pu starting from $t = 4.5$ s, as shown in Fig. 3.13(b). Since $\hat{B}_{crit} < \hat{B}_r^{max}$, a negative triangular current injection will be needed after $t = 4.5$ s to reduce the residual flux density. The positive and negative slopes of the negative triangular injection are respectively set first to -1.3 mA/s and then to 1.3 mA/s (i.e., 20% of the maximum slope of the biphasic half-hexagonal current in

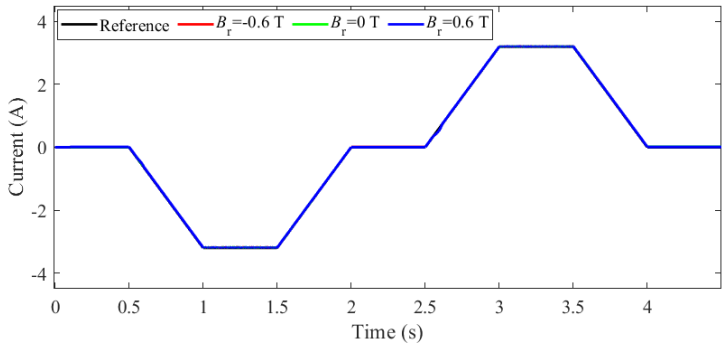

(a)

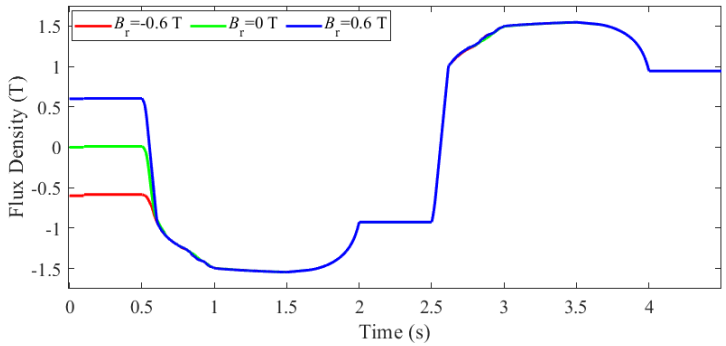

(b)

Figure 3.12: (a) Secondary winding current, and (b) true flux density.

terms of size). The current reduction after $t = 5$ s makes the flux density reduce from the starting point of 0.6 pu. Once the current reaches -0.22 A at $t = 5.186$ s, the flux density becomes 0.46 pu corresponding to $0.9\hat{B}_{crit}$. The current then starts returning to 0 A at $t = 5.186$ s, and again reaches 0 A at $t = 5.395$ s. The flux density, responding to the current increase after $t = 5.186$ s, rises from 0.46 pu. The flux density reaches 0.47 pu with current becoming 0 A, which is within the compatibility flux density range.

3.7.4 Comparison with Other Methods

This subsection demonstrates the superiority of the proposed method over the pre-fluxing [67], de-fluxing [68], and random energization methods. A total of 2,000 simulations are conducted for each method, with 1,000 simulations on the *Type* 1 transformer and 1,000 simulations on the *Type* 2 transformer. The CB remains the same as the one used in Section 3.7.2. A uniformly distributed random error with upper and lower bounds of

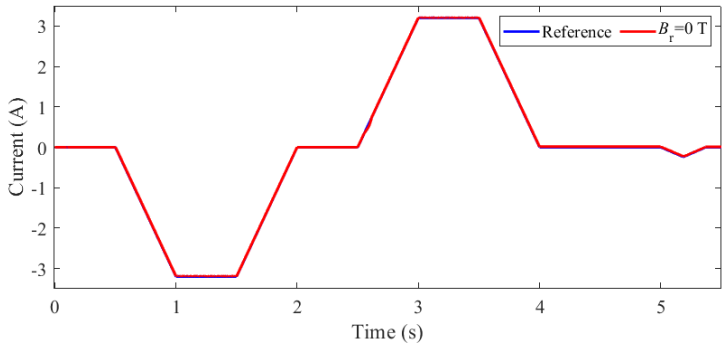

(a)

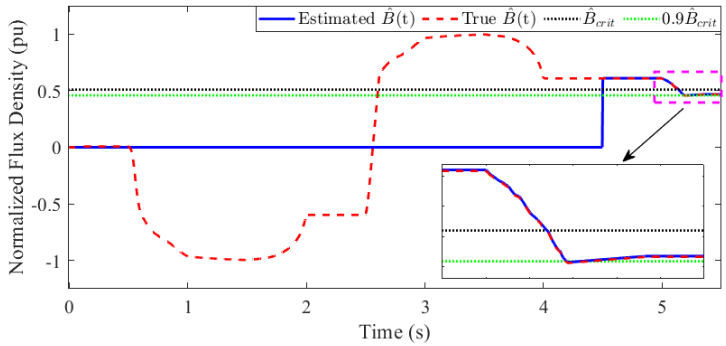

(b)

Figure 3.13: (a) Secondary winding current, and (b) true and estimated flux density.

$\pm 5\%$ is introduced to account for potential fluctuations in flux adjustment using both the proposed method and the de-fluxing method. The pre-fluxing method can energize the transformer on both the rising and falling halves of the absolute gap voltage. Between the two, the energization on the rising half, which is studied in this article, outperforms the energization on the falling half. The corresponding prospective flux density is set at $0.87B^{max}$ for the pre-fluxing method.

Figs. 3.14(a) and 3.14(b) show the inrush current distribution for *Type* 1 and *Type* 2 transformers using different energization methods. The random energization results are not presented, as they exhibit a nearly even distribution spanning from zero to the highest possible inrush current. The proposed method demonstrates the best performance in reducing the magnitude of inrush current. In an ideal scenario without any uncertainties in the operation of the CB, this method would eliminate inrush current. Even with the CB uncertainties, the proposed method successfully maintains the current

amplitude around the transformer's excitation current in over 50% of cases. In extreme cases, the method can still limit the amplitude of current drawn to 75% (120 A) and 50% (80 A) of the peak amplitude of the nominal current for *Type* 1 and *Type* 2 transformers. The larger the current, the less the likelihood of occurrence, with seldom instances where the current amplitude reaches 120 A and 80 A.

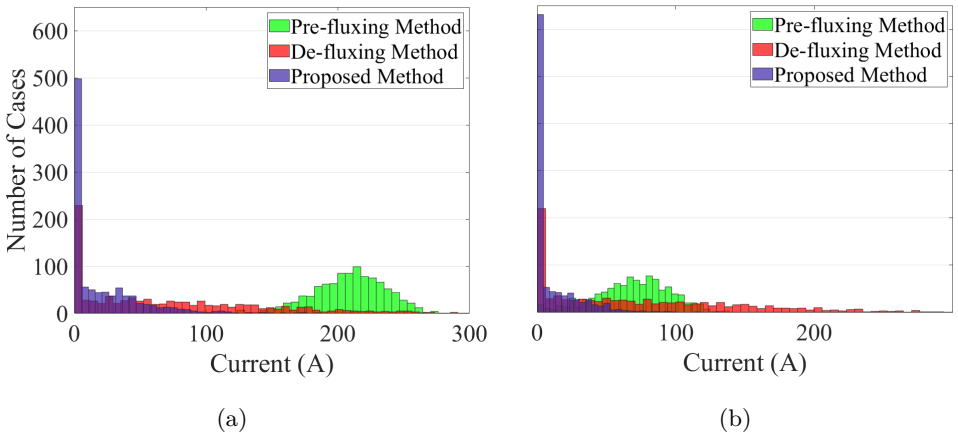

Figure 3.14: Inrush current distributions for (a) *Type* 1, and (b) *Type* 2 transformers.

The de-fluxing method operates independently of the transformer types. This method can be ranked as the second-best method, as it constrains the inrush current magnitude to below 187%(300 A) of the peak amplitude of the nominal current. This method can potentially eliminate inrush current, but less frequently compared to the energization by the proposed method. The performance of the pre-fluxing method improves on cores with higher B_r^{max}. As B_r^{max} increases, the maximum possible size of inrush current decreases (reducing from 250 A to 160 A between the two cores tested). However, even with a high B_r^{max}, this method does not remove inrush current completely. On average, the use of this method reduces the current amplitude to 200 A and 80 A for *Type* 1 and *Type* 2 transformers, respectively.

3.7.5 Experimental Validation

A test rig containing a 400-VA, 260 V/120 V shell-type single-phase transformer is used to experimentally evaluate the performance of the proposed method as shown in Fig. 3.15. The peak amplitudes of excitation current at the primary and secondary sides are 0.22 A and 0.5 A, respectively. The maximum feasible residual flux density is

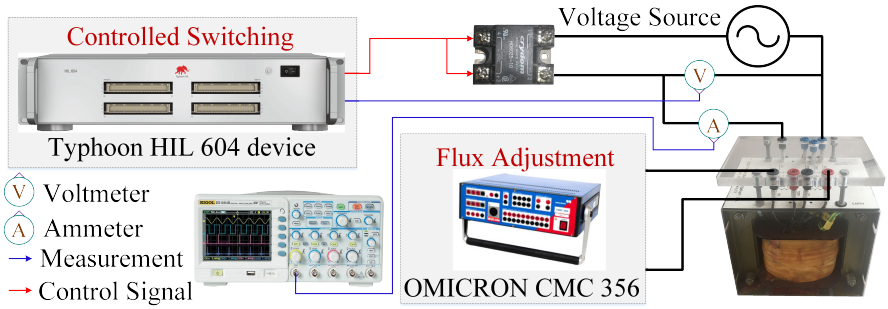

Figure 3.15: Experimental setup.

78% of B^{max}. Current at the primary side might be as high as 50 A in the worst-case energization. The flux density is adjusted via an Omicron CMC 356 relay tester employed as a current source. After flux adjustment, the relay tester is disconnected, and the secondary winding is left open-circuited. The modeling of the CB, with corresponding mechanical and *RDDS* scatter is accomplished using an HD6025-10 solid-state relay, controlled by a Typhoon HIL 604 device.

For the tested transformer, K is conservatively assumed to be 30, resulting in a minimum time T_{min} of 0.87 seconds. Fig. 3.16 shows the proposed method's performance in regulating the residual flux density from -0.078 pu to a value below $\hat{B}_{crit} = 0.7$ pu. As shown in Fig. 3.16(a), the current contains one complete cycle with an amplitude of 0.5 A and time period $T = 4.5$ s. Fig. 3.16(b) demonstrates how the current injection induces voltage on on the primary winding, the amplitude of which is lower than 15 V. In Figs. 3.16(c) and 3.16(d), the red dotted curve shows that the current injection up to $t = 4.5$ s adjusts the residual flux density from -0.078 pu to 0.78 pu, matching the B_r^{max} value. The comparison between the true and estimated flux densities (red dotted and blue solid curves) demonstrates that the flux density can be estimated accurately after $t = 4.5$ s. The current gradually descends below zero at $t = 5$ s with a slope equivalent to 20% of the maximum slope observed before $t = T$, leading to a consequent reduction in the flux density. By $t = 5.51$ s, the flux density reaches 0.637 pu, which is equivalent to $0.9\hat{B}_{crit}$. Then, the current is reduced back to zero, ultimately reaching zero at $t = 6.02$ s. As a result, the flux density experiences an increase from 0.637 pu, and becomes 0.665 pu when the current reaches zero at $t = 6.02$ s.

To confirm the result of the flux adjustment procedure, the transformer is energized such that $\hat{B}_p = \hat{B}_r^{ad} = 0.665$ pu. The current drawn by the transformer is shown in Fig.

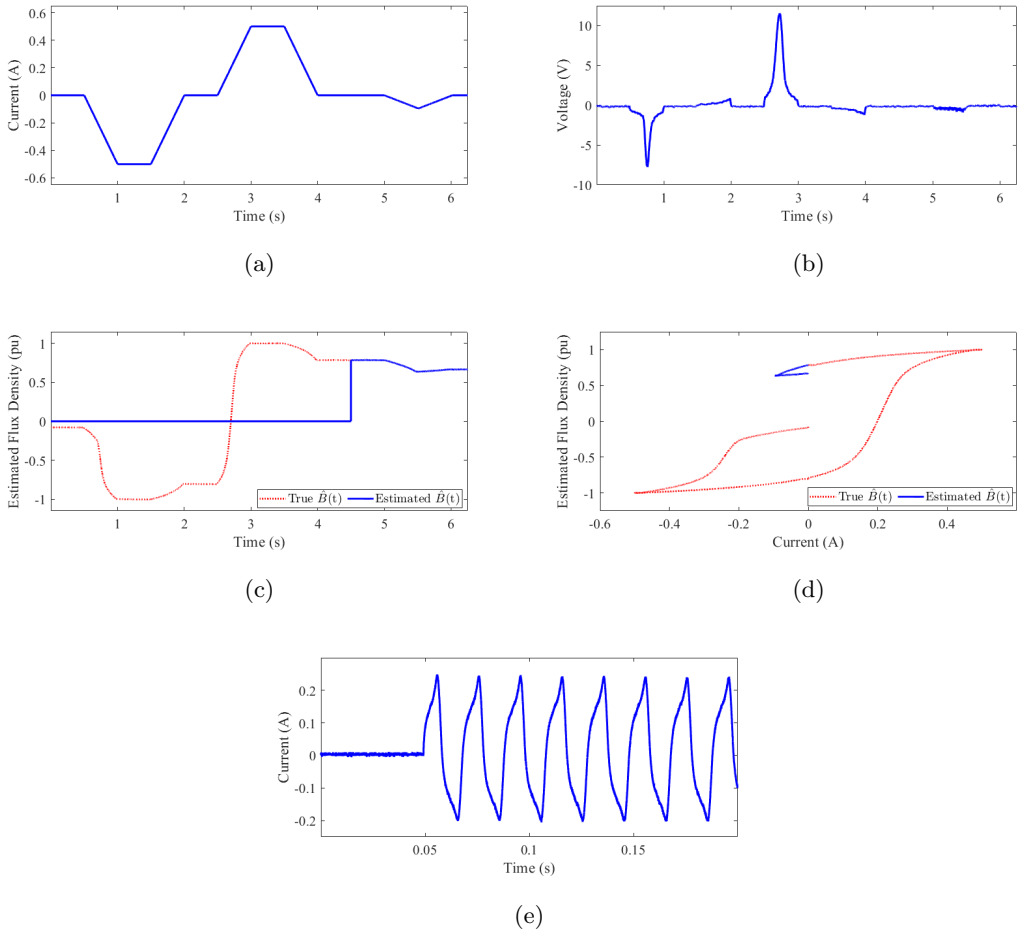

Figure 3.16: (a) Injected current, (b) voltage induced on the primary winding, (c) true and estimated flux densities, (d) *B-H* curve during current injection, and (d) transformer primary side current.

3.16(e). As can be seen, the current matches the transformer's excitation current. This shows the effectiveness of the proposed method in adjusting the residual flux density. When energized with an ideal CB, the peak amplitude of the current drawn by the transformer is 0.22 A using both the proposed method and the de-fluxing method. The current reaches 0.7 A when using the pre-fluxing method. Considering the uncertainties involved in the operation of the CB, the peak current amplitude can vary.

Figs. 3.17(a) and 3.17(b) show the current magnitude at different instants within the making interval and corresponding making instant distributions. It is assumed that

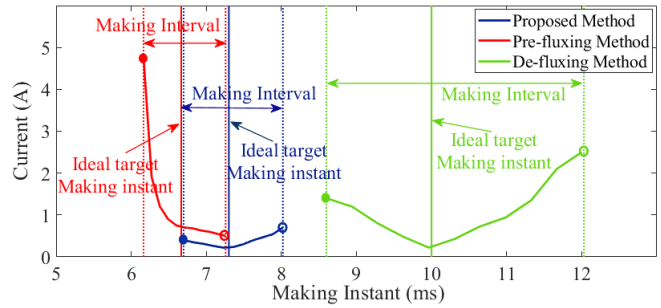

(a)

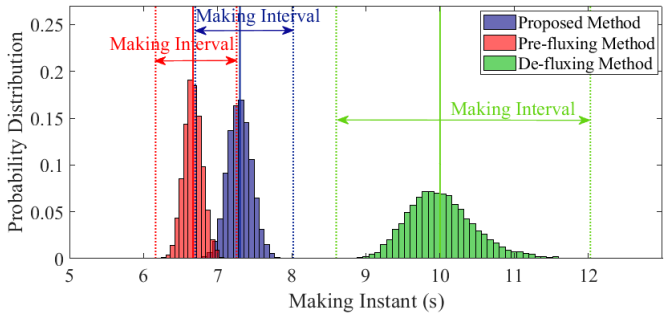

(b)

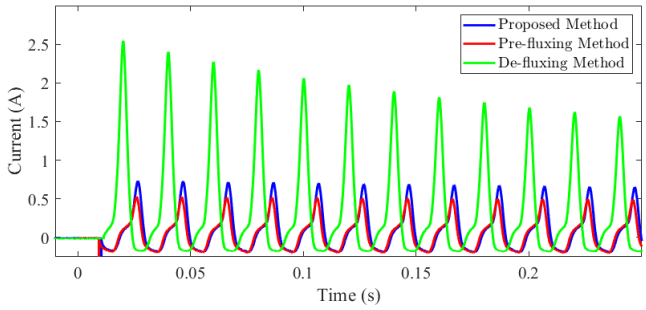

(c)

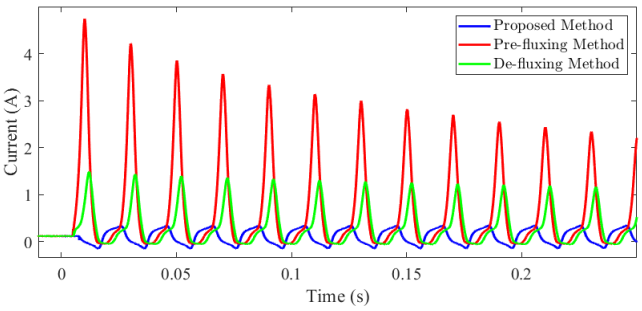

(d)

Figure 3.17: (a) Peak current magnitude for energization at different points within the making interval, (b) probability distributions of making instant, (c) current drawn by the transformer for making at upper, and (d) lower bounds of making interval.

Table 3.3: Comparing Different Methods with Respect to the Worst-Case Scenario

Methods	Lower bound (%)	No sccater (%)	Upper bound (%)
Proposed Method	99.2	99.56	98.6
Pre-fluxing Method	90.4	98.6	99
De-fluxing Method	97.2	99.56	95

ΔT_{CB} is 3.5% of T_{CB} with $0.7s^{mean} < s < 1.3s^{mean}$. As can be seen from Fig. 3.17(a), the peak amplitude of the current drawn by the transformer is confined to 0.4 A and 0.7 A for energization at the lower and upper bounds. In contrast, these by the pre-fluxing method are 0.5 A and 4.8 A. The de-fluxing method results in 2.5 A and 1.4 A, respectively.

Figs. 3.17(c) and 3.17(d) show the inrush current drawn following the energization at the upper and lower bounds of the making interval, respectively, corresponding to the open and filled circles in Fig. 3.17(a). As shown in Fig. 3.17(b), however, the chances of making occurring at the lower and upper bounds of the making interval are practically zero for all methods. The probability of making increases as the making instant approaches the ideal target making instant. Using the proposed method, the current magnitude lies within the range [0.22 A, 0.6 A] with expected value 0.22 A. For the pre-fluxing and de-fluxing methods, these ranges are [0.6 A, 1 A] with expected value 0.7 A, and [0.22 A, 2.15 A] with expected value 0.22 A, respectively. The proposed method exhibits the least sensitivity to CB uncertainties compared to the other two methods.

Table 3.3 presents the results of various methods and the corresponding reduction in current magnitude compared to the worst-case energization scenario, which produces a peak current of 50 A. As illustrated, the best performance under ideal conditions is achieved by the proposed method and the de-fluxing method, both yielding the highest reduction in current magnitude. These are followed by the performance of the pre-fluxing method under ideal conditions. However, the proposed method demonstrates lower sensitivity to scatter, as its performance is less affected by the lower and upper bounds of the making interval. Notably, the proposed method achieves an improvement range of 98.6% to 99.56%, which is significantly better than the corresponding ranges of

90.4% to 99% for the pre-fluxing method and 95% to 99.56% for the de-fluxing method.

In this chapter, the Typhoon HIL604 device and the Omicron CMC 356 relay tester are used to validate the proposed method for controlled switching and flux adjustment. These devices are chosen because they are already available in the laboratory, meaning their use does not incur additional costs for the project. The HIL604 device provides a high-fidelity simulation environment, enabling rigorous testing and validation of control strategies without requiring physical hardware. The Omicron CMC 356 relay tester also facilitates the creation of an open-loop system for injecting current during flux adjustment, simplifying the process.

However, for real-world implementation, the HIL604 and the Omicron CMC 356 relay tester should be replaced with a digital signal processor, such as the TMS320F2812 DSP, and a real single-phase inverter, such as the PEB4050 IGBT power module, as these alternatives are more practical and cost-effective. The TMS320F2812 DSP is specifically designed for real-time control applications, with built-in peripherals such as PWM modules and analog-to-digital converters (ADCs), making it highly suitable for current regulation in inverters. Additionally, the PEB4050 IGBT power module can be used to implement a current source and is significantly cheaper, costing approximately 1,000 £, compared to the Omicron CMC 356 relay tester, which costs around 30,000 £.

As shown in [88, 89], the TMS320F2812 DSP is capable of implementing controllers for systems that are even more complex than the proposed method in this chapter. This confirms the feasibility of using the TMS320F2812 DSP for implementing the proposed method. The DSP, with its 150 MHz fixed-point processor, executes the primary control algorithms (e.g., flux-matching and current regulation) within a cycle time of 5 μs, utilizing approximately 40% of the processor's capacity. The memory requirements for the implementation include 10 KB of RAM for intermediate calculations and 50 KB of Flash memory for program storage, both of which are well within the hardware's available 18 KB of RAM and 128 KB of flash [90]. These metrics demonstrate that the proposed methods can be efficiently implemented within the computational limits of the TMS320F2812 DSP.

In terms of cost, the TMS320F2812 DSP offers a significant advantage. The DSP itself is available for approximately 15 $ to 25 $ depending on the supplier, while development kits such as the Texas Instruments F2812 eZdsp Starter Kit are available for around 300 $ to 500 $. These costs are substantially lower than the Typhoon HIL604

device, which typically requires an investment exceeding 15,000 $. Additionally, the TMS320F2812 can be directly embedded into the inverter hardware, avoiding the need for external simulation tools during deployment and further reducing overall expenses. While the HIL604 is indispensable for validating the methods in a simulated environment, the TMS320F2812 DSP is recommended for practical implementation. It offers a cost-efficient, computationally capable, and easily implementable solution for the methods proposed in this work, making it a more suitable choice for real-world applications.

3.8 Summary

This chapter proposed a flux matching energization method to mitigate inrush currents in single-phase transformers, which are crucial components in many TPSSs. To address the challenges posed by CB operation during transformer energization, the concept of a "compatibility flux density range" is introduced. This range not only falls within the feasible range of the transformer core but also minimizes the impact of CB operation and related uncertainties on transformer energization.

A novel method for adjusting residual flux density is proposed, where controlled current is injected into the transformer winding, rather than applying voltage. Specifically, a biphasic half-hexagonal current with a peak amplitude equal to the transformer's excitation current is used to adjsut the residual flux density within the feasible range. To facilitate this adjustment, a technique for estimating flux density during current injection is introduced, which does not require transformer design information. Accurate flux estimation relies on voltage transducers with compensated DC offset (i.e., no DC offset). Together, the current injection and flux density estimation effectively minimize the difference between prospective and residual flux densities, even in the presence of significant uncertainties.

The effectiveness of the proposed method has been validated through analytical, simulation, and experimental studies, all of which demonstrate its superiority over traditional pre-fluxing, de-fluxing, and random energization methods for single-phase transformer energization. The method shows remarkable resilience to uncertainties related to CB operating characteristics, such as *RDDS* and mechanical scatter. Despite these uncertainties, the inrush current remains close to the transformer's excitation current and rarely approaches its nominal current.

Chapter 4

A Modified Pre-Fluxing Method for the Energization of Single-Phase Transformers

4.1 Overview

As discussed in section 1.2.5, the pre-fluxing method is one of the techniques available for energizing single- and three-phase transformers. However, this method has several limitations that make it ineffective for many transformer energization scenarios. One significant drawback is that it does not account for the closing operation of CBs, which can sometimes render the method counterproductive rather than beneficial. Additionally, the pre-fluxing method is limited in its ability to adjust the residual flux density, offering only a few predetermined values, which reduces its flexibility in matching the residual and prospective fluxes. Furthermore, the method's efficiency decreases with larger transformer capacities, requiring time on the scale of minutes for power transformers. These limitations highlight the need for a modified pre-fluxing method, particularly for high-power single-phase traction transformers in TPSSs.

This chapter introduces modified pre-fluxing methods for the energization of single-phase transformers. These modifications are implemented progressively, starting with the integration of the CB closing operation, resulting in the first modification, followed by enhancements that increase the speed of the final pre-fluxing method. As a result, the final method offers exceptional speed and flexibility in adjusting the transformer's residual flux density to any suitable reference value within the feasible range, ensuring compatibility with the prospective flux as determined by the CB, regardless of the transformer's capacity.

The method adjusts the residual flux density to the reference value by applying a controlled voltage to the transformer winding. A novel technique is presented for estimating flux density during this adjustment, which operates independently of transformer design parameters and relies solely on voltage transducers. This approach also includes the capability to calculate and compensate the DC offset in the voltage transducer output, enabling accurate flux density estimation throughout the adjustment process. Unlike the method discussed in the previous chapter, these modified pre-fluxing methods do not require knowledge of the transformer's peak excitation current, which may not always be readily available. Additionally, the method only utilizes DC voltage that is a fraction of the transformer's nominal voltage, ensuring that the transformer's insulation remains protected from damaging high-voltage surges.

4.2 Conventional Pre-Fluxing Method

The conventional pre-fluxing method (CPFM) [67, 69] is designed to reduce, but not completely eliminate, the difference between residual and prospective flux densities, which is crucial for mitigating inrush currents [28, 29]. To achieve this reduction, a pre-fluxing device, illustrated in Fig. 4.1, is employed. This device works by charging a capacitor, which is then connected to the transformer's secondary winding, thereby adjusting the residual flux density from its initial, unknown value. A diode is included to bypass the capacitor once its voltage reaches zero. Depending on the polarity of the capacitor, the residual flux density is adjusted to either $\pm B_r^{max}$, as shown in Fig. 4.2.

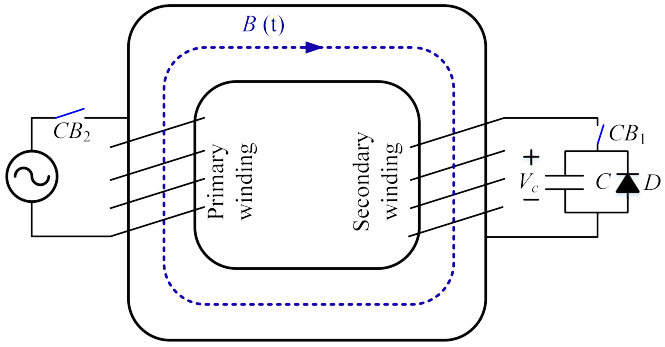

Figure 4.1: Pre-fluxing device used by the CPFM.

Assuming an initial residual flux density $B_r \neq 0$ (point 1 in Fig. 4.2), the transformer undergoes flux adjustment via the pre-fluxing device. If the capacitor's voltage is negative, connecting it to the transformer shifts B_r from point 1 to point 2. As the capacitor discharges, the current flowing into the transformer decreases exponentially, causing a further transition from point 2 to point 3, ultimately resulting in a residual flux density of $-B_r^{max}$ at point 3. Conversely, a positively charged capacitor would shift B_r to B_r^{max}, changing the flux density from point 1 to point 4, and finally from point 4 to point 5. Once the residual flux density is adjusted to $\pm B_r^{max}$, the pre-fluxing device is disconnected by CB_1, and the transformer is energized by CB_2 at one of two specific angles based on the polarity of B_r^{ad}. Considering the rising zero-crossing of the voltage waveform as time reference, the single-phase transformer is energized at 210°(corresponding to $B_p = 0.87B^{max}$) for B_r^{max} and at 330°(corresponding to $B_p = -0.87B^{max}$) for $-B_r^{max}$ [67].

To guarantee a successful pre-fluxing, the capacitor should be sized carefully. By

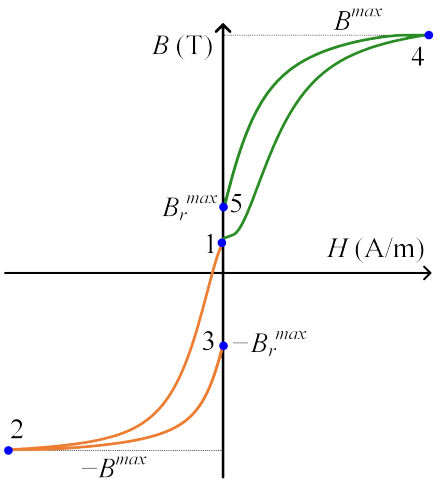

Figure 4.2: B-H curve during flux density adjustment using the CPFM.

using the volt-second method, one can calculate the size of C as [67]:

$$C = \frac{1}{L_m}\left(\frac{\sqrt{2}}{2\pi}\frac{U}{fV_c}\right)^2 \tag{4.1}$$

where f, L_m, U, and V_c are the rated frequency of the transformer, magnetizing inductance of the transformer, transformer nominal voltage, and capacitor voltage, respectively. One can approximate L_m from

$$L_m = \frac{U^2}{2\pi fkS} \tag{4.2}$$

where S and k are the transformer's nominal power and the transformer's per-unit magnetizing current.

Theoretically, this method has the potential to mitigate inrush currents effectively. However, in practice, it falls short in sufficiently reducing the difference between B_r^{ad} and B_p, resulting in only partial mitigation of inrush currents. One key reason for this limitation is the use of fixed angles— 210°(corresponding to $B_p = 0.87B^{max}$) and at 330°(corresponding to $B_p = -0.87B^{max}$)— for transformer energization [67], regardless of the transformer's core type and the corresponding B-H curve. With this method, B_r^{ad} is set to B_r^{max} or $-B_r^{max}$, which, depending on the core material, ranges from

approximately $50-90\%$ of B^{max} for grain-oriented electrical steel, and even lower for transformers made of amorphous metal [36]. As a result, the difference between B_r^{ad} and B_p is not always significantly reduced by using this method.

Moreover, the CB closing operation can negatively impact the performance of the CPFM. As discussed in Section 3.3, the making instant should be considered the precise energization instant. To ensure proper timing, the closing command must be issued so that the making occurs at either 210° or 330°. However, it may be difficult to energize the transforer such that $B_p - B_r^{ad}$ is minimized due to the the operating characteristics/limitations of CBs. In practice, these limitations often make it challenging, if not impossible, to energize the transformer at the required instant. Therefore, the pre-fluxing method proposed in [67] struggles to achieve its full potential in realistic conditions. Fig. 4.3(a) illustrates how the operational constraints of CBs can render the CPFM counterproductive. As shown, the quadrilateral region associated with making at 210° covers the previous voltage hump, potentially resulting in making on the previous hump, and leading to a significant discrepancy between the residual and prospective flux densities. This happens since the CPFM does not consider the CB closing operation.

It is important to note that 330° falls on the descending slope of the absolute voltage curve, which requires a CB with a large *RDDS* to energize the transformer at this angle. As illustrated in Fig. 4.3(b), targeting 330° demands a CB with a higher *RDDS* (i.e., $RDDS_1 < RDDS_2$) to avoid making on the previous hump or precisely hitting 330° which is more challenging compared to 210°. This necessity increases the cost of the CB, both in terms of initial investment and maintenance. Therefore, energization at 210° should be prioritized as the preferred method for transformer energization.

Another major challenge the conventional pre-fluxing method faces is the method's speed especially when the transformer's capacity increases. Let us consider a scenario where C has just been bypassed by D, and the current of D is at its peak value. In this condition, the transformer can be represented by an equivalent inductor (L_{eq}) and a resistor (R_{eq}), forming an RL circuit without a voltage source. The time constant of the zero response of this first-order circuit is $\tau = \frac{L_{eq}}{R_{eq}}$ [91]. Practically speaking, it takes 5τ for the current to descends to zero. Since $L_{eq} \gg R_{eq}$ for high-power transformers, a substantial amount of time is required for the current to decay. This means with an increase in the power rating of the transformer, the time needed for flux adjustment by the pre-fluxing method significantly increases. It follows that the pre-fluxing method is

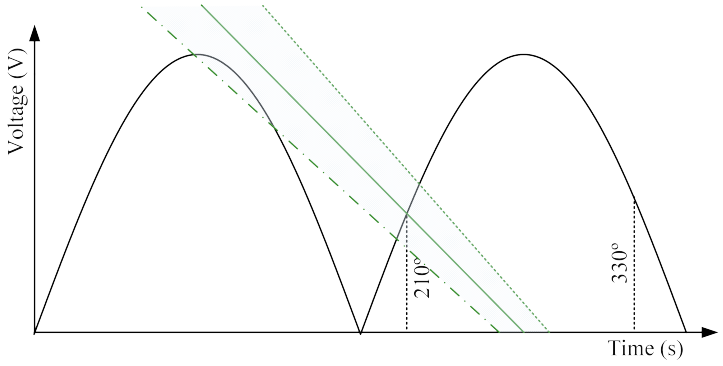

(a)

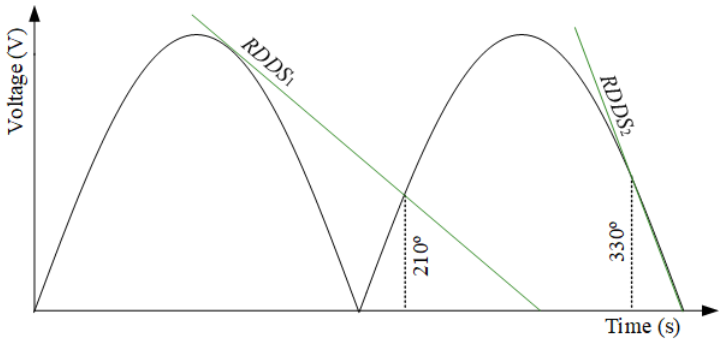

(b)

Figure 4.3: (a) The quadrilateral region of making at 210°, and (b) the minimum *RDDS* for targeting 210° and 330°.

quite slow for high-power transformers.

As discussed, the CPFM is not well-suited for energizing single-phase traction transformers due to its potential counterproductive effects and slow performance, particularly for high-power transformers. To address these limitations, two modifications are proposed in this research, leading to the development of two modified pre-fluxing methods: MPFM 1 and MPFM 2. The first modification, resulting in MPFM 1, eliminates the reliance on fixed angles for transformer energization by enabling the calculation of B_r^{max} relative to B^{max}. In contrast, MPFM 2 focuses on providing a faster energization method that is effective regardless of transformer capacity and less sensitive to CB closing operations and related uncertainties.

4.3 Modified Pre-Fluxing Method 1 (MPFM 1)

In this section, we introduce MPFM 1, a method designed to determine the optimal energization instant based on the transformer's core material. Unlike CPFM, MPFM 1 does not rely on fixed angles for energizing a single-phase transformer, which helps to minimize the impact of CB closing operations on the performance of MPFM 1. The method begins by fluxing the transformer and measuring the voltage induced on the open-circuited winding. This voltage is measured using a transducer that compensates for any DC offset, ensuring the output is free from DC offset. MPFM 1 then calculates the ideal time to issue the CB closing command, taking into account the measured voltage, CB closing time, and *RDDS*. The following subsections provide a detailed explanation of these stages.

4.3.1 Fluxing and Measurement

Fig. 4.4 illustrates the pre-fluxing device connected to the secondary winding, as utilized in MPFM 1. Unlike CPFM, the proposed method employs two charged capacitors with opposite voltage polarities to flux the transformer. Similar to CPFM, the capacity of these capacitors is determined using equation (4.1). The pre-fluxing process is detailed in Fig. 4.5. Initially, C_1 is connected to the transformer, which starts with an initial flux density, B_r, at point 1. As C_1 discharges its stored energy into the transformer, the flux density shifts from point 1 to point 2 due to the polarity of C_1's voltage. At point 2, the current from C_1 to the transformer reaches its peak before decreasing to zero at point 3, adjusting the flux density to $-B_r^{max}$. Once C_1 is fully discharged, it is disconnected, and C_2 is connected. Given that C_2 has a voltage polarity opposite to that of C_1, the flux density moves from $-B_r^{max}$ to B^{max} at point 4. As with C_1, the current from C_2 begins to decrease, reaching zero at point 5. At this stage, B_r^{ad} is adjusted to B^{max}, and C_2 is disconnected from the transformer. As demonstrated in the simulation section, the initial value of B_r does not influence this process, allowing B_r^{ad} to be consistently adjusted to B_r^{max}, regardless of the starting value of B_r. Additionally, since the adjusted flux density B_r^{ad} is positive, the corresponding making occurs on the rising edge of the absolute voltage (similar to the 210° used in CPFM), eliminating the need for a CB with a high *RDDS*.

Over the course of fluxing, the induced voltage across the primary winding is meas-

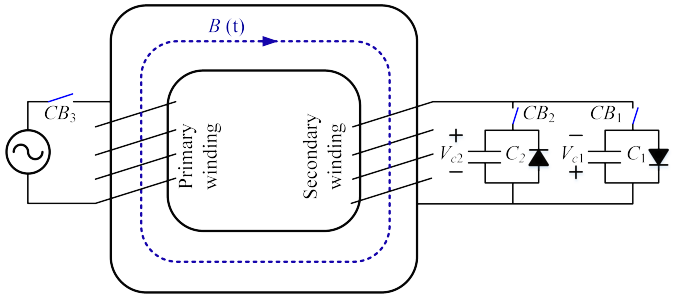

Figure 4.4: Pre-fluxing device used by the MPFM 1.

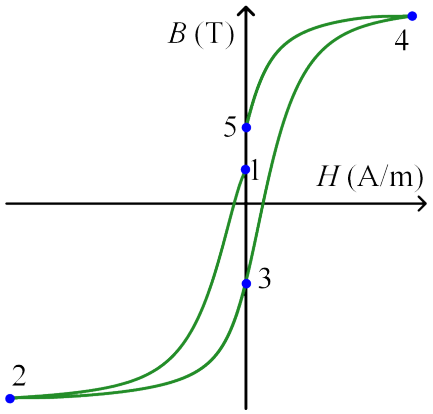

Figure 4.5: *B-H* curve during flux density adjustment using the MPFM 1 method.

ured. The integration of this voltage is known as relative flux density (B_{re}) and is used to estimate the ratio between B_r^{max} and B^{max}. Fig. 4.6 shows B_{re} for a single-phase transformer with different values of B_r. According to this figure, positive or negative B_r leads to a downward or upward shift in B_{re}. However, this shift does not affect the difference between the maximum and minimum values on these curves, which will be shown in the simulation section. In other words, $A_0 = A_P = A_N$, and $B_0 = B_P = B_N$. As a result, irrespective of the value of B_r, one obtains the ratio between B_r^{max} and B^{max} by

$$\frac{B_r^{max}}{B^{max}} = \frac{|B_{re}^{f1} - B_{re}^{f2}|}{|B_{re}^{m1} - B_{re}^{m2}|} \tag{4.3}$$

where B_{re}^{m1}, and B_{re}^{m2} the minimum and maximum values of B_{re}. In addition, B_{re}^{f1}, and B_{re}^{f2} are the value of B_{re} when the current of the pre-fluxing device becomes zero before and after the connection of C_2.

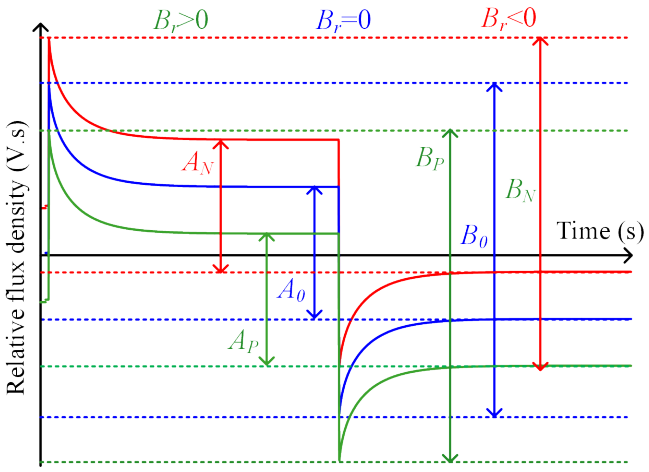

Figure 4.6: Relative flux density for $B_r = 0$, $B_r < 0$, and $B_r > 0$.

4.3.2 Closing Operation Instant Determination

As mentioned earlier, B_r^{ad} should match B_p to eliminate inrush current. After adjusting the residual flux, the CB is controlled such that $B_r^{ad} = B_p$. To achieve this, the closing operation initiation instant, i.e., t_{in}, which is shown in Fig. 3.1 can be obtained from

$$t_{in} = \frac{2k\pi + \phi}{2\pi f} + \frac{U\sin(\phi)}{RDDS} - T_{CB} \tag{4.4}$$

To determine the value of k, the CB's closing time, T_{CB}, is considered. For instance, if the CB operates within $T_{CB} = 50$ ms and the frequency is $f = 50$ Hz, the closing operation will span 2.5 cycles. To ensure equation (4.4) does not produce a negative value, this 2.5 is rounded up to the nearest integer, which is 3. Additionally, ϕ represents the angle at which the making occurs and can be calculated from

$$\phi = \frac{\pi}{2} + \sin^{-1}\left(\frac{B_r^{max}}{B^{max}}\right) \tag{4.5}$$

By using t_{in}, the contact touch istant can be optained by:

$$t_{ct} = t_{in} + T_{CB} \tag{4.6}$$

Now, the making instant can be calculated by equation (3.1).

4.3.3 Performance Evaluation

To evaluate the performance of the MPFM 1, a 120 V/120 V single-phase transformer is used. A high-power transformer is not used since it needs more time for flux adjustment. The 120 V/120 single-phase transformer is modeled by the π equivalent circuit [92] in PSCAD/EMTDC, as shown in Fig. 4.7. Two identical non-linear inductors are modeled by the inverse JA method to take the non-linearity of the core into account [74]. By employing this method, different B-H curves can be considered to evaluate the performance of the proposed method under different conditions.

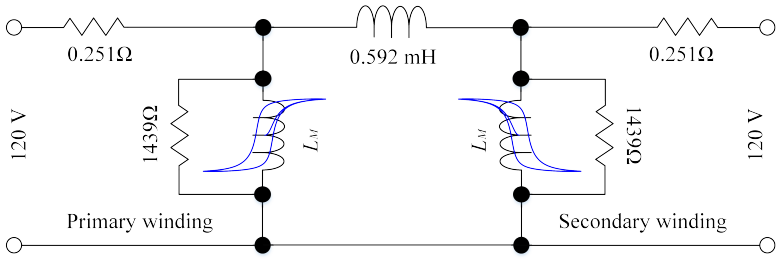

Figure 4.7: Single-phase transformer modeled based on π equivalent circuit.

Fig. 4.8 shows the inrush current that flows into the single-phase transformer (as the worst-case scenario) following the transformer's energization by the CPFM and MPFM 1. For this transformer, $B_r^{max} = 0.5B^{max}$. In the worst-case scenario, the transformer is energized at $t = 0.18$ s (at voltage zero-point rising edge) while $B_r^{ad} = B_r^{max}$, which leads to an inrush current that reaches 185 A at the first peak (the highest value). Compared to the transformer excitation current, which is 10 A, the worst-case scenario increases the current significantly. For both the CPFM and MPFM 1, a CB with $RDDS = 70$ kV/ms and $T_{CB} = 50$ ms is selected. For CPFM, it is assumed that the rising zero-point voltage is detected at $t = 0.1$ s, the closing command is generated at $t = 0.11833$ s, and the making occurs at $t = 0.16833$ s. The effectiveness of the CPFM is shown in Fig. 4.8. According to this figure, the CPFM reduces the inrush current to 95 A, which shows 48.64% reduction in inrush current compared to the worst-case scenario.

Over the course of flux adjustment, MPFM 1 measures B_r^{max}. Based on this measurement, the closing command is generated at 0.1166 s, and making happens at 0.1666 s after a voltage zero-point rising edge is detected at 0.1 s. It can be seen from Fig. 4.8 that the inrush current is limited to 30 A when MPFM 1 is used. In comparison with the worst-case scenario and the CPFM, MPFM 1 reduces the magnitude of inrush

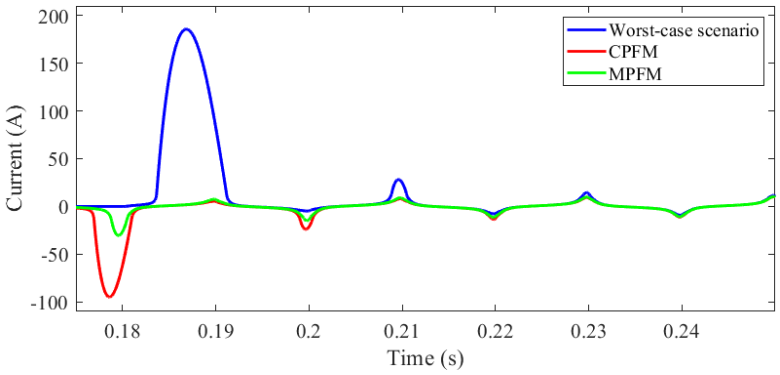

Figure 4.8: Inrush current in the worst-case scenario, energization with the CPFM, and energization with the MPFM 1.

current 83.7% and 68.4%, respectively.

Fig. 4.9 demonstrates the highest magnitude of inrush current when the CPFM and MPFM 1 are implemented. For the CPFM, the highest magnitude of the current is reduced with an increase in B_r^{max}/B^{max}. The reason for this reduction is that the difference between B_r^{max} and B_p is reduced due to the change in the B-H curve. As can be seen, the lowest magnitude is achieved when $B_r^{max}/B^{max} = 0.8$. On the other hand, MPFM 1 shows a consistent performance because a change in B_r^{max}/B^{max} does not change the current magnitude significantly. By implementing MPFM 1, the current varies around 30 A. Contrary to the CPFM, the accuracy of the MPFM 1 is dependent on the measurement during flux adjustment.

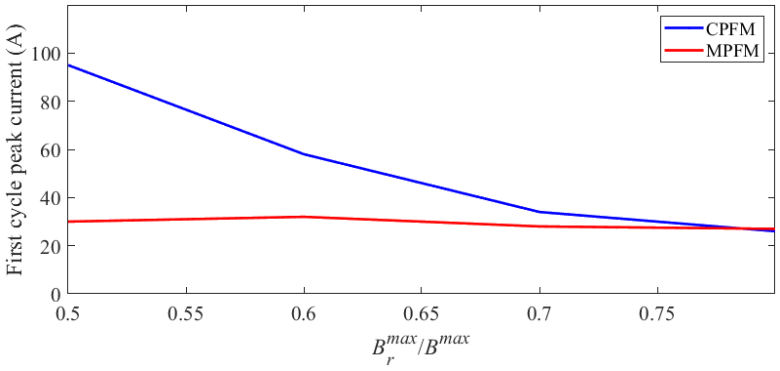

Figure 4.9: Inrush current versus B_r^{max}/B^{max} for CPFM and MPFM 1.

To obtain satisfactory results, the MPFM 1 should be able to flux a single-phase

transformer properly and measure the ratio between B_r^{max} and B^{max}. Different conditions of $B_r = -0.5$ T, $B_r = 0$ T, and $B_r = 0.5$ T are taken into account to evaluate the performance of the MPFM 1. For this, the pre-fluxing device shown in Fig. 4.4 is employed, which is made using two 1-mF capacitors. The capacitor's initial voltage is 46 V. The results of transformer fluxing are shown in Fig. 4.10. As can be seen, B_r does not affect the performance of the MPFM 1 since B_r^{ad} is successfully adjusted to B_r^{max}, which is 0.65 T. The important point that should be mentioned here is that the only impact of B_r is on H. According to Fig. 11, when $B_r < 0$, H increases more than in other cases. Based on Fig. 4.10(a), H reaches -5000 A/m while this number for the case with $B_r = 0$ and $B_r > 0$ is -2900 A/m and -2000 A/m, respectively. This phenomenon happens because the polarity of the voltage of C_1 is the same as B_r in Fig. 4.10(a) and opposite to B_r in Fig. 4.10(c).

For the B-H curve shown in Fig. 4.9, $B_r^{max} = 0.65$ T, and $B^{max} = 1.55$ T in normal operation. It means that $B_r^{max}/B^{max} = 0.42$. To determine the closing operation initiation instant at which the inrush current is minimized, B_r^{max}/B^{max} should be calculated through equations (4.3)-(4.6) during flux adjustment. Fig. 4.11 shows the relative flux density for cases with $B_r = -0.5$ T, $B_r = 0$, and $B_r = 0.5$ T. For $B_r = -0.5$ T (blue trace), B_{re}^{m1}, B_{re}^{m2}, B_{re}^{f1}, and B_{re}^{f2} are -382×10^{-3}, 670×10^{-3}, -50.7×10^{-3}, and 369.8×10^{3}, respectively. By employing (4.3), $B_r^{max}/B^{max} = 0.4$ which shows acceptable accuracy compared to 0.42. In addition, for cases with $B_r = 0$, and $B_r = 0.5$ T, B_r^{max}/B^{max} is equal to 0.402 and 0.406, respectively.

In Fig. 4.12, the current that flows from the pre-fluxing device to the single-phase transformer is shown. According to this figure, for $B_r = 0$ T, the current reaches -10 A when C_1 is connected. This current is the same as the excitation current of the transformer. For other cases, the current magnitude varies when C_1 is connected. While current decreases for $B_r = 0.5$ T (-7.28 A), a negative B_r results in a higher current that is -16.92 A. This result is compatible with the B-H curves in Fig. 4.9 where a negative B_r leads to higher magnetic field strength compared to zero or positive B_r. Unlike the time when C_1 is connected, the currents are similar when C_1 is disconnected and C_2 is connected to the transformer. In this situation, the currents reach 5 A. Again, this result is compatible with Fig. 4.9. When C_2 is connected, magnetic field strength is similar for all cases. It turns out that B_r only affects current and magnetic field strength when C_1 is connected and does have no impacts after the connection of C_2.

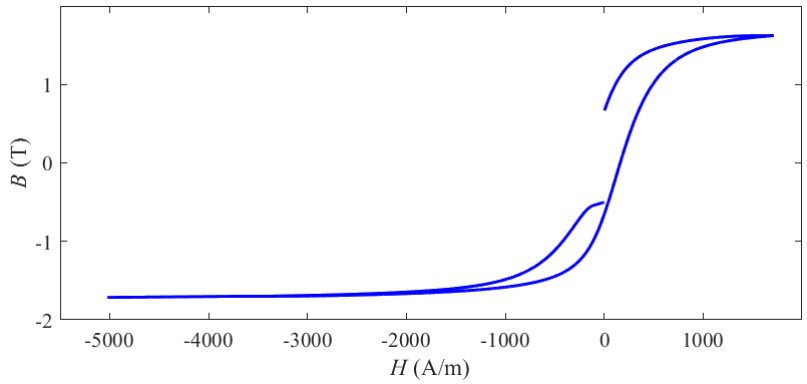

(a)

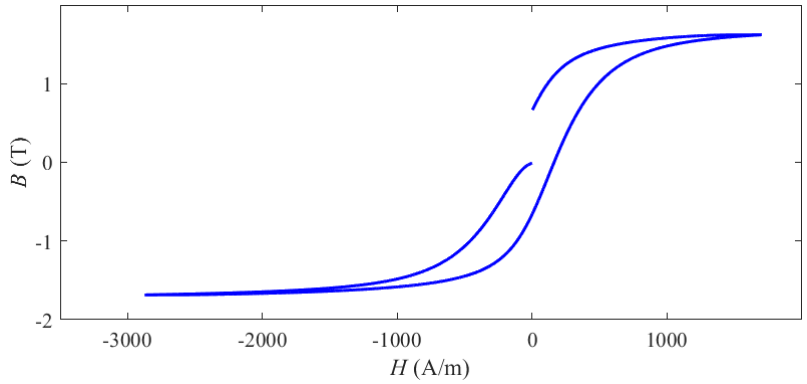

(b)

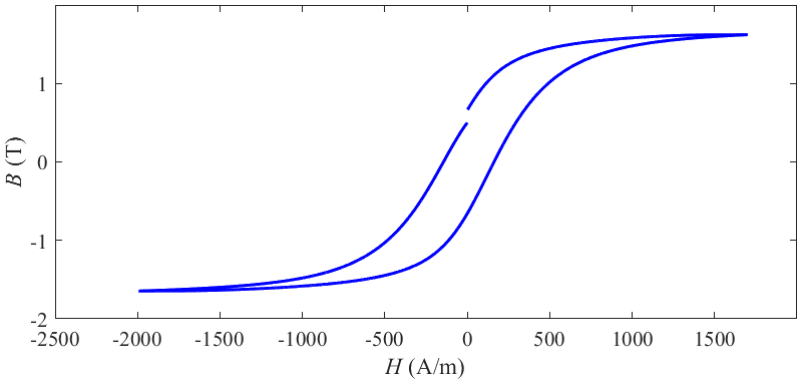

(c)

Figure 4.10: Flux adjustment with (a) $B_r = -0.5$ T, (b) $B_r = 0$, and (c) $B_r = 0.5$ T.

Table 4.1 shows the performance of the MPFM 1 in estimating B_r^{max}/B^{max} with cores of different B-H characteristics. As can be seen, for a vast range of B_rs and B-H

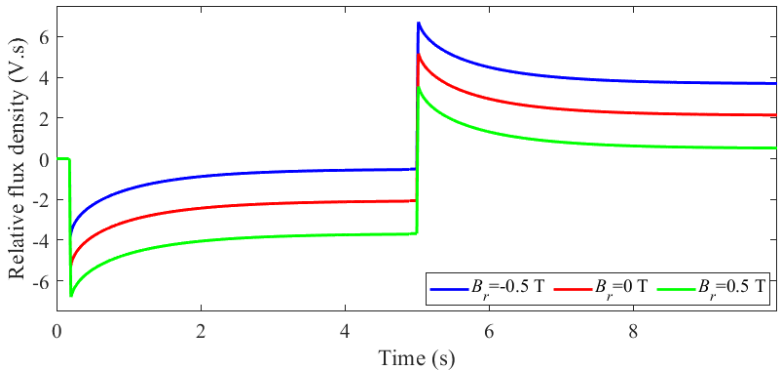

Figure 4.11: The integration of the voltage induced on primary winding.

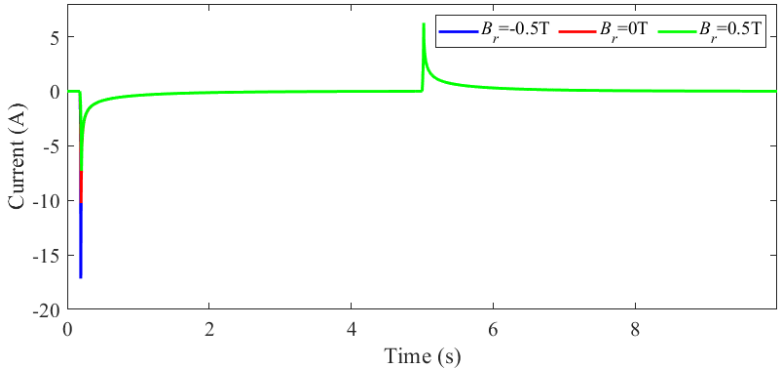

Figure 4.12: Current flow from the pre-fluxing device to the transformer.

curves, the proposed method can obtain B_r^{max}/B^{max} with high accuracy. This means that the value of B_r and the transformer core materials do not affect the ability of the proposed method in estimating B_r^{max}/B^{max}. This feature helps to determine an accurate switching instant, thereby mitigating inrush current.

4.4 Modified Pre-Fluxing Method 2 (MPFM 2)

Although MPFM 1 improves upon CPFM by calculating the ratio of B_r^{max} to B^{max} and determining the optimal instant for transformer energization, leading to a reduction in inrush current, it still suffers from several limitations. The method is slow when adjusting flux in high-power transformers. Additionally, achieving a DC offset-free output from the voltage transducer is not always feasible, making flux estimation impossible. These challenges justify further modifications to the pre-fluxing method to enhance its speed,

Table 4.1: MPFM 1's Estimation for Different B-H Curves

B_r	-0.5 T			0.0			0.5 T		
B_r^{max}/B^{max}	0.5	0.6	0.7	0.5	0.6	0.7	0.5	0.6	0.7
B_{re}^{m1} (mV.s)	-391	-402	-723	-514	-528	-467	-710	-715	-409
B_{re}^{m2} (mV.s)	697	683	-103	553	558	564	367	366	209
B_{re}^{f1} (mV.s)	-110	-177	-651	-250	-299	-341	-432	-495	-334
B_{re}^{f2} (mV.s)	428	474	-217	291	359	492	103	157	95.6
Eq. (4.3)	0.497	0.600	0.702	0.507	0.605	0.702	0.496	0.603	0.696

account for CB limitations and uncertainties, and ensure reliable operation even when the voltage measurement contains a DC offset. These considerations have led to the development of the Modified Pre-Fluxing Method 2 (MPFM 2). The MPFM 2 is designed such that it can adjust the residual flux to any value within the feasible range. This adjustment aims to strike a balance between two conflicting factors: Minimizing the impact of CB scatter while ensuring no risk of making on the previous hump. After flux adjustment, the transformer is energized at an instant that minimizes the difference between the residual and prospective flux densities.

4.4.1 Safe Flux Range Associated with CB Closing Operation

As discussed in Section 3.3, to determine the critical making instant, the quadrilateral region in Fig. 3.1 must be shifted left until its lower side becomes tangent to the previous voltage hump at q_{tan}, as illustrated in Fig. 3.3. For convenience, Fig. 3.3 is shown again here as Fig. 4.13. The critical making instant, denoted as τ_m, corresponds to the making occurrence at point A_4. This point marks the lower limit of the safe making range, which extends from A_4 to A_2. On the next hump, this range shifts from A_5 to A_6 on the rising half of the positive gap voltage. The flux linkage associated with to A_4, referred to as λ_{safe}, is derived from

$$\lambda_{safe} = \lambda^{max} \sin(\omega\tau_m) \tag{4.7}$$

Here, λ^{max} represents the maximum flux linkage, defined as $\lambda^{max} = NAB^{max}$. Choosing the rising half of the positive gap voltage sets the lower limit of this range at $-\lambda_{safe}$, which corresponds to A_5 as target making instant. Combining these two pieces yields

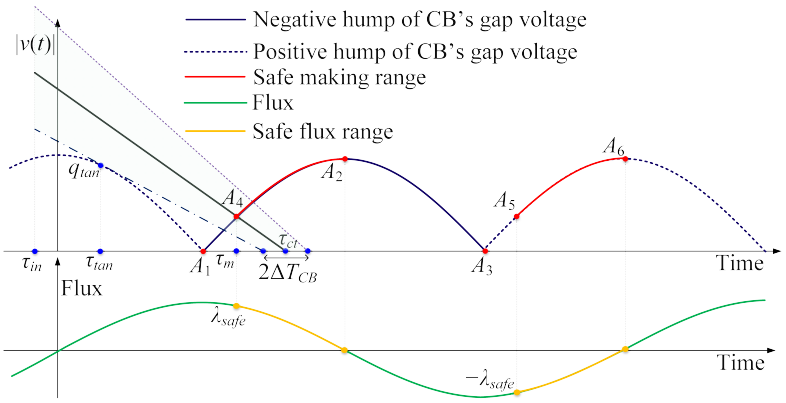

Figure 4.13: Preferred making range and corresponding safe flux range.

the range $[-\lambda_{safe}, \lambda_{safe}]$ which is referred to as the safe flux range. Any value in the safe range is the prospective flux of a target making instant that involves no risk of making on the previous hump. Flux values closer to the lower and upper bounds of the safe range (which respectively corresponds to A_4 and A_5) are preferred since they are associated with less sensitivity to *RDDS* and mechanical scatter. Depending on the core material, λ_r^{max} may or may not fall in the safe range. In the case of the latter, inrush current cannot be dealt with properly using the pre-fluxing method [93]. This is because the transformer might get energized undesirably within the previous hump, thereby rendering high-magnitude inrush current unavoidable.

4.4.2 Pre-Fluxing Device

For flux adjustment, MPFM 2 employs a pre-fluxing device shown in Fig. 4.14. This device is composed of a full-bridge single-phase inverter (with four switches S_1-S_4 and four anti-parallel diodes D_1-D_4), a DC voltage source with voltage denoted as V_{DC}, and a resistor connected in series with the transformer. A voltage transducer and a current transducer are employed to measure the voltage induced on the open-circuited primary winding and the current injected into the transformer by the pre-fluxing device. The theory behind determining the voltage of the DC voltage source is explained in [68]. The resistor ensures that the current of the pre-fluxing device does not exceed the peak value of the transformer's nominal current. The size of the resistor can be readily determined from $R = \frac{V_{DC}}{I_n}$, where I_n is the transformer's nominal peak current.

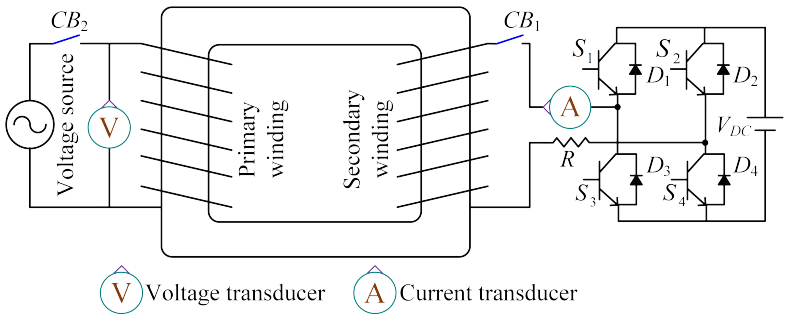

Figure 4.14: Pre-fluxing device used by the MPFM 2.

4.4.3 Residual Flux Adjustment Stage

A method is proposed in this subsection for adjusting the residual flux from an initial unknown value of λ_r to values that can be met by the prospective flux, given the limitations of the CB. This is achieved by applying a square-wave voltage to the transformer via the pre-fluxing device and regulating the current flowing into the transformer. For new transformers employing highly efficient designs, the excitation current ranges from 0.1% to 1% of the nominal transformer current, while this value can increase to as high as 6% for older transformers [94]. This means that when the excitation current reaches $0.1I_n$, it is guaranteed that the transformer has been driven into saturation.

For the sake of illustration, let us assume that the pre-fluxing device is connected to the secondary winding of the transformer with an initial residual flux of $\lambda_r = 0$ (without loss of generality). To start the flux adjustment, switches S_1 and S_4 are turned on at $t = 0$, and positive voltage (V_{DC}) is applied to the transformer, as shown in Fig. 4.15(a). Fig. 4.15(b) demonstrates the waveforms of the actual and measured currents during flux adjustment. Current starts flowing through switches S_1 and S_4, as shown in Fig. 4.16(a). At $t = t_1$, the measured current reaches $0.1I_n$. The actual current is different from the measured current due to the presence of a DC offset. As can be observed from Fig. 4.15(c), by the application of voltage, the transformer is driven into positive saturation, causing the actual flux to surpass λ^{max} and reach λ_{sat}. The positive saturation on B-H curves is shown in Fig. 4.17 as point 1.

At $t = t_1$, switches S_1 and S_4 are turned off while switches S_2 and S_3 are turned on. Due to the inductive nature of the transformer, the current does not change immediately and continues to flow through diodes D_2 and D_3 (see Fig. 4.16(b)) until it descends to

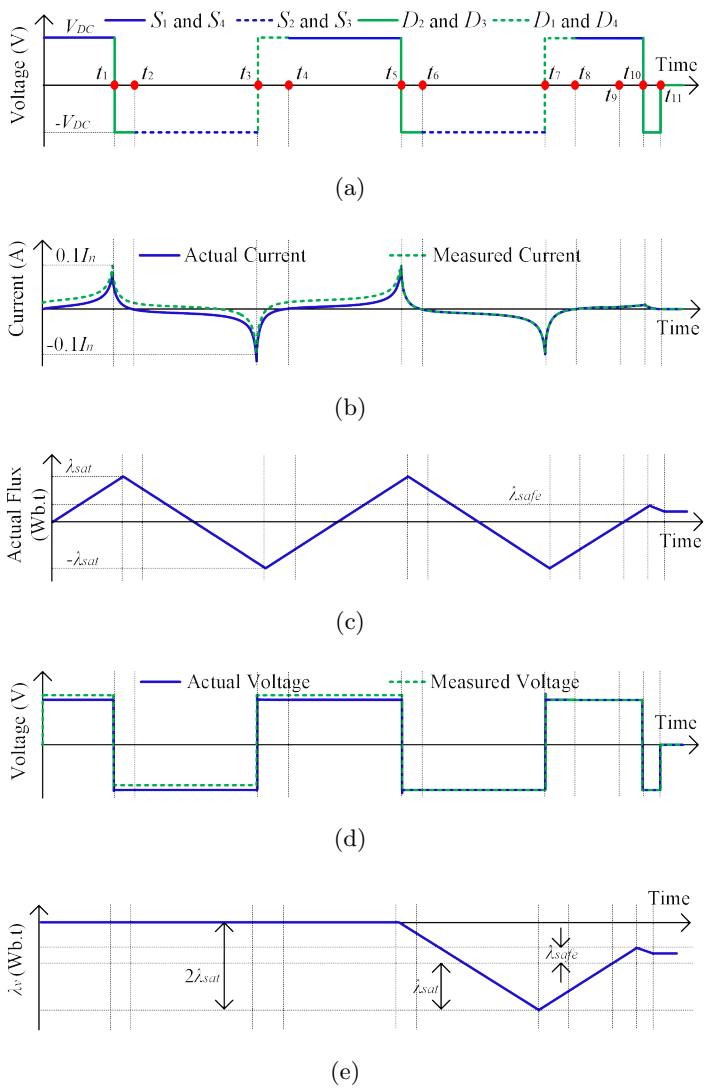

Figure 4.15: (a) Secondary winding voltage, (b) actual and measured currents, (c) actual flux, (d) primary winding actual and measured voltage, and (e) voltage integral.

zero at $t = t_2$. Throughout diode conduction (between $t = t_1$ and $t = t_2$), a negative voltage ($-V_{DC}$) is applied to the transformer, which accelerates the current reduction to zero. After $t = t_2$, the current continues to decrease, with switches S_2 and S_3 creating a path for the current, as shown in Fig. 4.16(c). When switches S_2 and S_3 conduct, again ($-V_{DC}$) is applied to the transformer. The current reduction continues until the measured current reaches $-0.1I_n$ at $t = t_3$, which is equivalent to $-\lambda_{sat}$ (i.e., negative saturation, marked as point 2 in Fig. 4.17). At $t = t_3$, switches S_2 and S_3 are turned

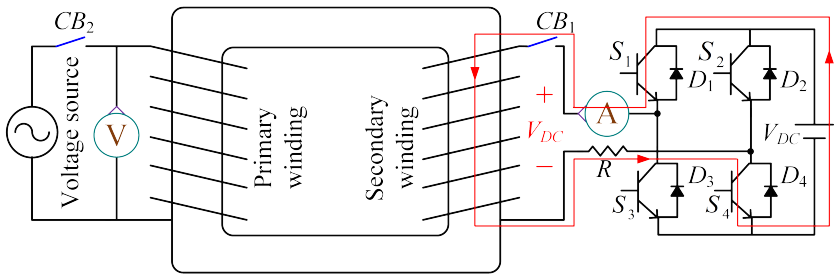

(a)

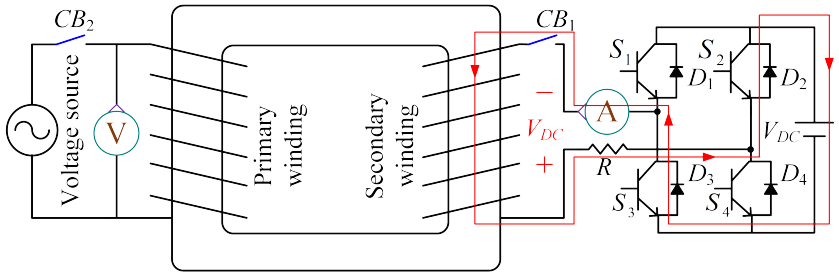

(b)

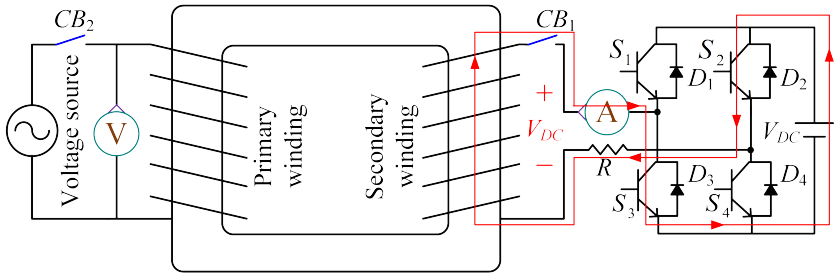

(c)

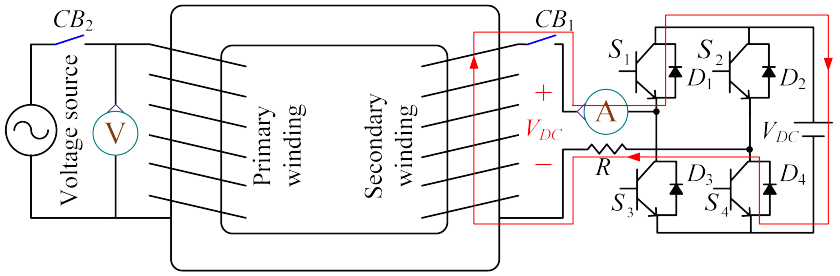

(d)

Figure 4.16: Current passing through (a) S_1 and S_4, (b) D_2 and D_3, (c) S_2 and S_3, and (d) D_1 and D_4.

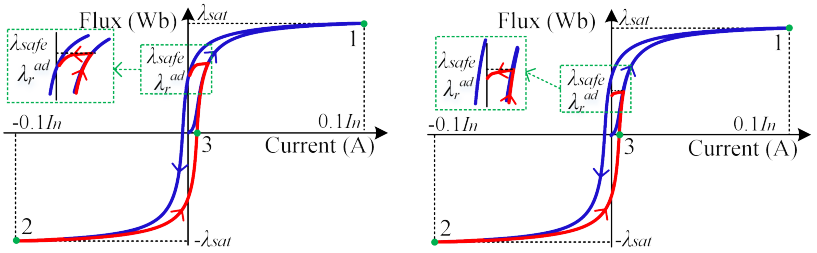

Figure 4.17: Hysteresis curve for (a) $\lambda_{safe} > \lambda_r^{max}$, and (b) $\lambda_{safe} < \lambda_r^{max}$.

off, and once more, switches S_1 and S_4 are turned on. The current flows through diodes D_1 and D_4 (see Fig. 4.16(d)) until it becomes zero at $t = t_4$, and then through switches S_1 and S_4 until it reaches $0.1I_n$ at $t = t_5$.

An important point to consider is that the voltage transducer's output usually contains a DC offset. This offset, if not dealt with properly, can make the flux estimation inaccurate. Let $v_p(t)$ show the voltage induced on the open-circuited primary winding. The voltage transducer adds the DC offset ΔV_{DC} to the signal, and outputs $v_p^m(t) = v_p(t) + \Delta V_{DC}$, where the superscript "m" is used to mark transducer measurements. To estimate the DC offset, $v_p^m(t)$ can be integrated from t_1 to t_5 and averaged as below

$$\Delta V_{DC} = \frac{1}{t_5 - t_1}\left[\int_0^{t_5} v_p^m(t)\mathrm{d}t - \int_0^{t_1} v_p^m(t)\mathrm{d}t\right] \tag{4.8}$$

where the integral of $v_p(t)$ over a full period ($t_5 - t_1 = T$) is zero. Now, let $i_{inj}(t)$ denote the current injected into the secondary winding and $i_{inj}^m(t)$=$i_{inj}(t) + \Delta I_{DC}$ where the variable on the left-hand side denotes the measured current and ΔI_{DC} expresses the DC offset in this measurement, respectively. The DC offset ΔI_{DC} can be determined from:

$$\Delta I_{DC} = \frac{1}{t_5 - t_1}\left[\int_0^{t_5} i_{inj}^m(t)\mathrm{d}t - \int_0^{t_1} i_{inj}^m(t)\mathrm{d}t\right] \tag{4.9}$$

Using equations (4.8) and (4.9), $v_p(t)$ and $i_{inj}(t)$ can be derived from the transducers' outputs. Now let us define the voltage integral $\lambda_v(t)$ as

$$\lambda_v(t) = \int_{t_5}^{t} v_p(t)\mathrm{d}t \tag{4.10}$$

By comparing Figs. 4.15(c) and 4.15(e), it can be seen that after $t = t_5$, $\lambda_v(t)$ represents the actual flux which is shifted downward by $-\lambda_{sat}$, i.e., $\lambda_v(t) = \lambda(t) - \lambda_{sat}$. This allows us to estimate the actual flux by λ_v.

The transformer is subject to a negative voltage at $t = t_5$, leading to negative saturation at $t = t_7$. At this time, $\lambda_v(t_7)$ reaches $-2\lambda_{sat}$, as shown in Fig. 4.15(e). Therefore, one can readily obtain λ_{sat} from:

$$\lambda_{sat} = \frac{1}{2}\left[\lambda_v(t_5) - \lambda_v(t_7)\right] \tag{4.11}$$

After $t = t_7$, switches S_2 and S_3 are turned off, and a positive voltage is applied to the transformer firstly through diodes D_1 and D_4 and then through switches S_1 and S_4. The positive voltage changes the voltage integral λ_v from $-2\lambda_{sat}$ to $-\lambda_{sat}$ at $t = t_9$, corresponding to a rise from $-\lambda_{sat}$ to zero in actual flux (representing core demagnetization, marked as point 3 in Fig. 4.17). The voltage integral further increases to $-\lambda_{sat} + \lambda_{safe}$ at $t = t_{10}$, which corresponds to λ_{safe} in the actual flux, as shown in Fig. 4.15(c). Once $\lambda_v(t_{10})$ reaches $-\lambda_{sat} + \lambda_{safe}$, switches S_1 and S_4 are turned off, and current flows through diodes D_2 and D_3, applying negative voltage to the transformer. This voltage facilitates the process of current reduction to zero. At $t = t_{11}$, current reaches zero and remains unchanged since switches S_2 and S_3 are turned off. This current reduction causes the actual flux to reduce from λ_{safe} and reaches a value lower than λ_{safe} at $t = t_{11}$ due to the hysteresis phenomenon. This settling value of the adjusted residual flux can be obtained from

$$\lambda_r^{ad} = \left[\lambda_{sat} + \lambda_v(t_{11})\right] \tag{4.12}$$

Fig. 4.17 shows the hysteresis loops traversed during flux adjustment for two different scenarios. One scenario is where $\lambda_{safe} > \lambda_r^{max}$ and another is where $\lambda_{safe} < \lambda_r^{max}$. The actual flux's transition from $-\lambda_{sat}$ to λ_r^{ad} is highlighted in red. In the former case, the adjusted residual flux lies on the maximum feasible residual flux, as depicted in Fig. 4.17(a). In the latter scenario, the adjusted residual flux falls within the feasible range $[-\lambda_r^{max}, \lambda_r^{max}]$, as shown in Fig. 4.17(b). Both scenarios prevent making on the previous hump and reduce the impact of scatters on transformer energization.

4.4.4 Controlled Switching Stage

The next stage after flux adjustment is transformer energization. Without loss of generality, let us assume that the nominal voltage $v(t) = V_m \cos(\omega t)$ is applied to the primary winding of the transformer while the secondary winding is open-circuited. The hat sign is used to refer to the per-unit flux with λ^{max} as the base value. The phase angle of the rising half of the gap voltage that results in a match between residual and prospective fluxes is calculated from:

$$\phi = \pi - \sin^{-1}(\hat{\lambda}_r^{ad}) \tag{4.13}$$

The making instant corresponding to ϕ is $t_m = \dfrac{\phi}{2\pi f}$, where f is the power system frequency. The contact touch and closing operation initiation instants can be calculated from

$$t_{ct} = t_m + \frac{|V_m \cos(\omega t_m)|}{s^{mean}} \tag{4.14}$$

$$t_{in} = t_{ct} - T_{CB} \tag{4.15}$$

The initiation of the closing operation of the CB at t_{in} guarantees that the prospective flux ideally matches the adjusted flux by making at t_m. Thanks to the considerations made to account for the impact of scatter in the closing operation of the CB, the difference between the two fluxes would be minimal.

4.4.5 Performance Evaluation

The results of simulation and experimental evaluation studies are presented and discussed in this section. The single-phase transformers introduced in section 2.4.1 are used to verify the performance of the MPFM 2' performance. The CB closing operation is modeled considering mechanical and *RDDS* scatter as random variables with normal distributions [79]. The pre-fluxing device shown in Fig. 4.14 is used for flux adjustment, with a DC-link voltage of 60 V. In addition, an hardware-in-the-loop test system

including a single-phase transformer and a pre-fluxing device is used to experimentally investigate the MPFM 2's performance.

First, the proposed method is rigorously tested under conditions that simulate the uncertainties inherent in CB closing operations. Next, the focus shifts to examining the flux adjustment process in detail. This is followed by a comparative analysis of MPFM 2, MPFM 1, demagnetization [9], and random energization methods (as discussed in Section 3.7.1). Finally, the results from experimental validation are presented and discussed in depth.

General Evaluation of the MPFM 2

To assess the performance of the MPFM 2, the *RDDS* and closing time of the CB is assumed to vary in the ranges [28 kV/ms,52 kV/ms], and [48.5 ms,51.5 ms], respectively. The safe flux range, normalized by λ^{max}, expands from -0.7 pu to 0.7 pu. Following flux adjustment, the adjusted residual flux for *Type* 1 and *Type* 2 transformers, normalized with respect to λ^{max}, are 0.6 pu and 0.69 pu, respectively. A sensitivity analysis is carried out by conducting 10,000 simulations for each transformer, evaluating the impact of scatter values on the MPFM 2's performance. The outcomes of this analysis are presented in Table 4.2. For *Type* 1 and *Type* 2 transformers, the making instants fall within the ranges of [6.8 ms,9.7 ms] and [6.6 ms,9.1 ms] , respectively. Correspondingly, the values of λ_r^{ad} are [0.09 pu,0.84 pu] and [0.28 pu,0.88 pu].

Table 4.2: Different Scatter's Impact on the MPFM 2's Performance

RDDS		s^{min}	s^{mean}	s^{max}
Closing Time		$T_{CB} - \Delta T_{CB}$	T_{CB}	$T_{CB} + \Delta T_{CB}$
Type 1	t_{ct} (ms)	12.7	14.2	15.7
	t_m (ms)	6.8	8	9.7
	$\hat{\lambda}_r^{ad}$	0.84	0.6	0.09
Type 2	t_{ct} (ms)	11.8	13.3	14.8
	t_m (ms)	6.6	7.6	9.1
	$\hat{\lambda}_r^{ad}$	0.88	0.68	0.28

The making instant distributions are demonstrated in Fig. 4.18. The probability of making occurrence is the highest at the ideal target making instants (8 ms and 7.6 ms for

the two transformers) as marked by the dashed black lines. In most cases, there is only a slight difference between the true and ideal target making instants. The probability of making occurrence decreases as we go farther away from the ideal target making instant. This probability soon becomes zero at the upper and lower bounds of the making interval, indicated by the dashed blue and red lines. The impact of larger λ_r^{ad} is also shown in Fig. 4.18. A higher value of λ_r^{ad} results in a narrower making interval (as seen in the energization of the *Type* 2 transformer).

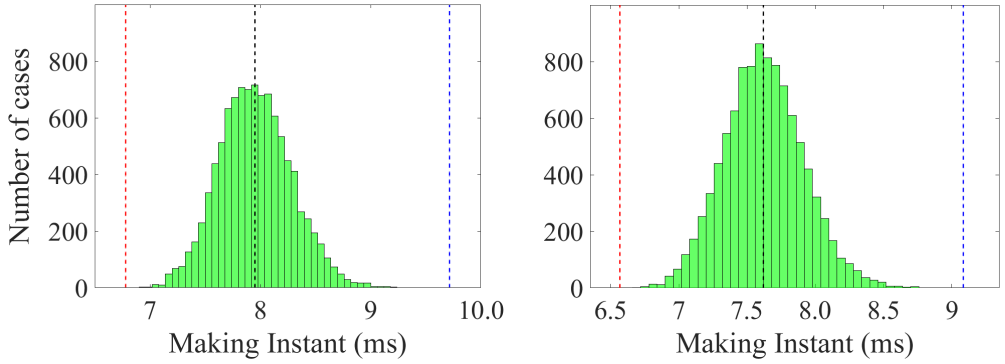

Figure 4.18: (a) *Type* 1, and (b) *Type* 2 transformers' making instant distributions.

Flux Adjustment by the MPFM 2

The flux adjustment procedure for the *Type* 1 transformer is shown in Fig. 4.19. For this evaluation, the initial residual flux is set to zero, $-0.5\lambda^{max}$, and $0.5\lambda^{max}$, respectively. The DC offset on voltage and current transducer outputs is 100 V and 1 A. The safe flux range, normalized by λ^{max}, spans from -0.7 pu to 0.7 pu. The voltage applied to the secondary winding via the pre-fluxing device is shown in Fig. 4.19(a). As can be seen, the initial residual flux impacts the time required for flux adjustment by the MPFM 2. The fastest adjustment occurs when $\lambda_r = 0.5\lambda^{max}$, as the flux reaches λ_{sat} for the first time more quickly. As λ_r decreases, the time needed for flux adjustment increases. Based on λ_r value, the MPFM 2 needs 1.92 to 2.13 seconds for flux adjustment. The MPFM 1, however, requires nearly 10 minutes to flux this transformer.

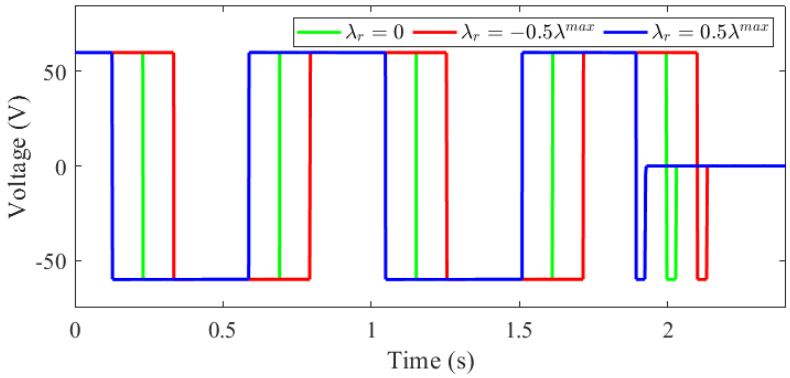

(a)

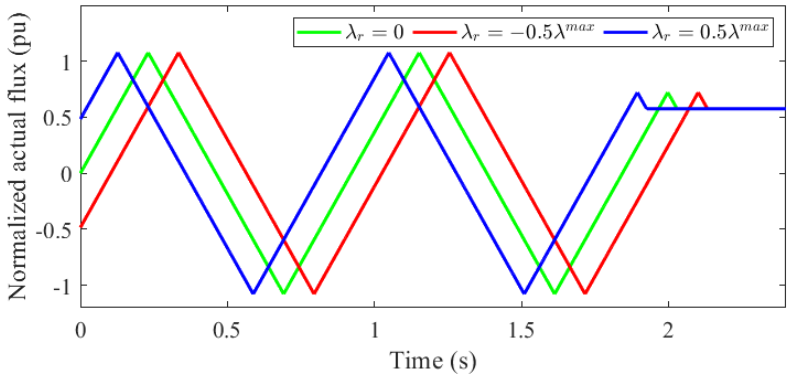

(b)

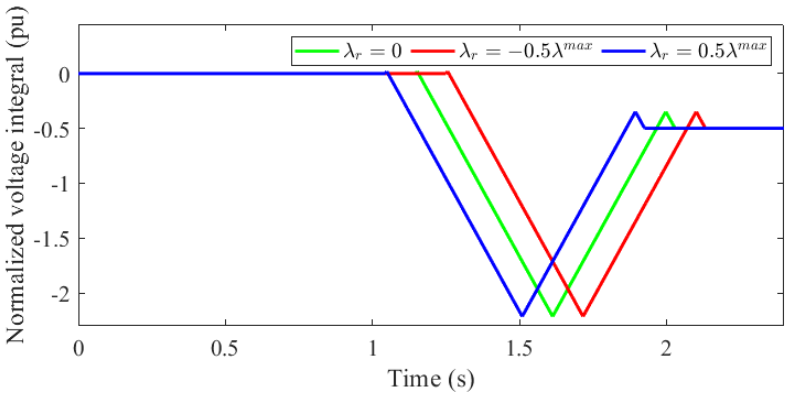

(c)

Figure 4.19: (a) Voltage applied to the secondary winding, (b) normalized actual flux, and (c) normalized voltage integral.

In Fig. 4.19(b), the waveforms of actual flux normalized by λ^{max} are shown. Since the maximum feasible residual flux lies in the safe flux range, the residual flux is adjusted to the maximum feasible residual flux, i.e., $\lambda_r^{ad} = 0.6\lambda^{max}$. This figure also shows that regardless of the initial value of residual flux, the MPFM 2 can easily adjust the residual flux to λ_r^{max}. Fig. 4.19(c) shows the voltage integral λ_v, normalized by λ^{max}. Substituting the voltage integral values at t_5, t_7, and t_{11} into equations (4.11) and (4.12), the per-unit value of adjusted residual flux is found to be 0.61, 0.59, and 0.59 for cases with $\lambda_r = 0$, $\lambda_r = -0.5\lambda^{max}$, and $\lambda_r = 0.5\lambda^{max}$, respectively. Table 4.3 summarizes the details of flux adjustment for both transformers, including the initial residual flux value, the true and estimated values of adjusted residual flux using (4.12), and the time taken for the flux adjustment. As shown, the MPFM 2 adjusts the residual flux to a value within the safe flux range in a few seconds. The MPFM 2 estimates the adjusted residual flux regardless of the initial residual flux value.

Table 4.3: Flux Adjustment Results

Type	λ_r/λ^{max}	-0.75	-0.5	-0.25	0	0.25	0.5	0.75
1	$\lambda_r^{ad}/\lambda^{max}$	N.A	0.6	0.6	0.6	0.6	0.6	N.A
	Eq. (4.12)	N.A	0.59	0.59	0.61	0.6	0.61	N.A
	$t_{11}(s)$	N.A	2.14	2.07	2.05	1.98	1.93	N.A
2	$\lambda_r^{ad}/\lambda^{max}$	0.69	0.69	0.69	0.69	0.69	0.69	0.69
	Eq. (4.12)	0.69	0.68	0.70	0.68	0.69	0.70	0.70
	$t_{11}(s)$	2.18	2.13	2.08	2.03	1.97	1.92	1.87

Comparison with Other Methods

This subsection compares MPFM 2 with MPFM 1, demagnetization [9], and random energization methods. Two types of CBs are considered: A slow CB and a fast CB. For slow CB, *RDDS*=40 kV/ms with ±30% scatter and T_{CB} = 50 ms, with a mechanical scatter of ±1.5 ms. The fast CB has an *RDDS* of 70 kV/ms with ±15% scatter and a closing time of 30 ms, with a mechanical scatter of ±1.0 ms. The safe flux range, normalized by λ^{max}, for slow and fast CBs is [-0.7 pu,0.7 pu] and [-0.96 pu,0.96 pu], respectively. For each method, 4,000 simulations are conducted, using both CBs to energize the *Type* 1 and *Type* 2 transformers. The MPFM 2 and MPFM 1 adjust the

residual flux to λ_r^{max}. However, for the case with the *Type* 2 transformer and slow CB, the MPFM 2 adjusts the residual flux to $0.69\lambda^{max}$.

Fig. 11 shows the distributions of inrush current in numerous different conditions tested. Only results ranging from zero to 400 A are shown, and undesirable cases where making occurs on the previous hump using MPFM 1 and demagnetization method are excluded. The MPFM 2 is the only method that does not result in such undesirable makings. The results of random energization are excluded from Fig. 4.20 as they are uniformly spread out from zero to the highest attainable magnitude. As shown in Figs. 4.20(a), 4.20(c), and 4.20(d), both MPFM 2 and MPFM 1 exhibit a great performance. These two methods perform identically in all scenarios involving the *Type* 1 transformer and when a fast CB is used to energize the *Type* 2 transformer. In these cases, the peak current magnitude does not surpass 160 A, matching the peak amplitude of the nominal current. In the case of the *Type* 2 transformer with the slow CB, the MPFM 1 demonstrates a superior performance in successful cases with MPFM 2 ranking as the second-best method. Both methods limit the current well below the magnitude at the peak amplitude of the nominal current. However, MPFM 1 suffers from making on the previous hump in about 1.0% of cases in which the current range from 600 A to 1100 A. The MPFM 2, however, remains unaffected, always limiting the current to 160 A.

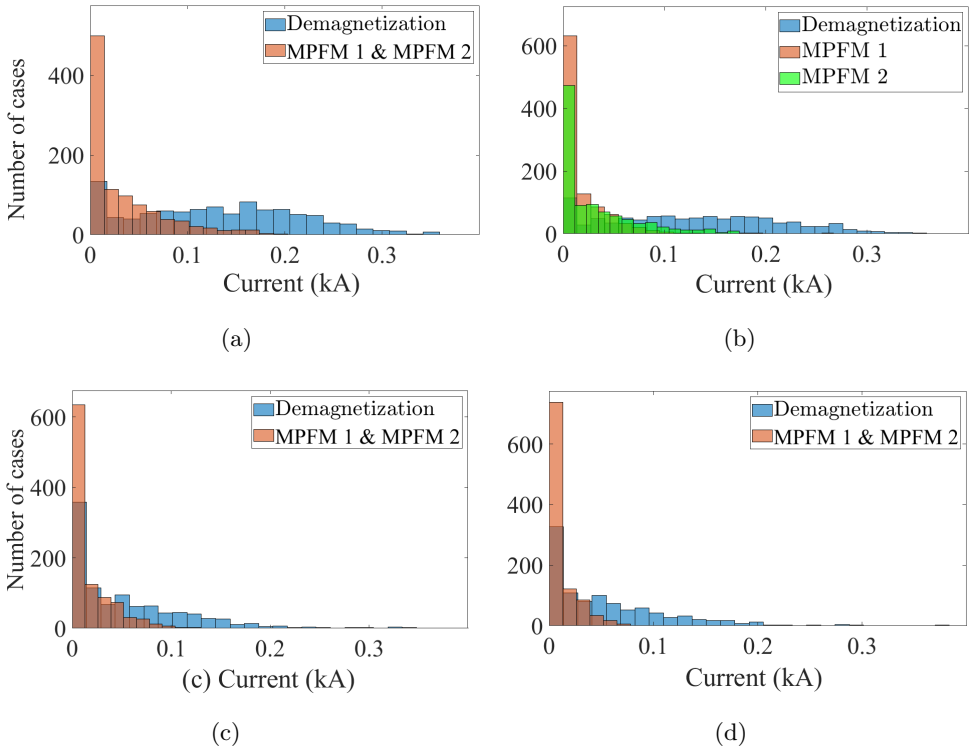

Figure 4.20: (a) *Type* 1, slow CB, (b) *Type* 2, slow CB, (c) *Type* 1, fast CB, and (d) *Type* 2, fast CB.

Experimental Validation

A HIL test system shown in Fig. 4.21 is employed to experimentally examine the MPFM 2's performance. The system is composed of a 400-VA, 260 V/120 V shell-type single-phase transformer, a Typhoon HIL 604 device, a PEB4050 IGBT power module, and an HD6025-10 solid-state relay. The transformer's peak excitation current at the primary side is 0.22 A. This excitation current could reach 50 A in worst-case energization conditions. The HIL device controls the IGBT power module as the pre-fluxing device and the solid-state relay as a CB with associated *RDDS* and mechanical scatter. A 30-V DC voltage supplies the pre-fluxing device, and a 15-Ω resistor is included to cap the device's current at 2 A.

The MPFM 2's ability to adjust the residual flux to a value below $\hat{\lambda}_{safe} = 0.65$ pu is shown in Fig. 4.22. Figs. 4.22(a) and 4.22(b) demonstrate the voltage applied to the secondary winding and the induced voltage on the primary winding, respectively. At

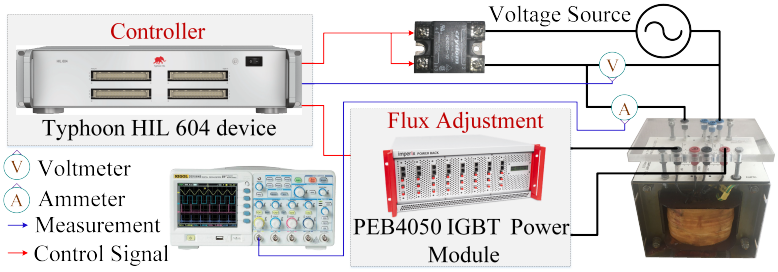

Figure 4.21: Experimental setup.

$t = 0.086$ s, the DC offset of the voltage transducer output is calculated, enabling the measurement of the actual voltage induced on the primary winding. Similarly, the DC offset compensation is implemented to the current transducer output, as seen in Fig. 4.22(c). Using the compensated voltage, the voltage integral $\lambda_v(t)$ is derived, as shown in Fig. 4.22(d). Equation (4.12) yields the value of the adjusted residual flux as 0.62 pu, also represented in Fig. 4.22(e) demonstrating the associated hysteresis loop after DC offset compensation. To validate the efficiency of the flux adjustment, the transformer is energized such that the prospective and residual fluxes are matched. The resulting current flowing into the transformer, energized by an ideal CB, is shown in Fig. 4.22(f). The current magnitude reaches 0.24 A, which closely matches the transformer excitation current. This proves the effectiveness of the MPFM 2 in adjusting and estimating the residual flux.

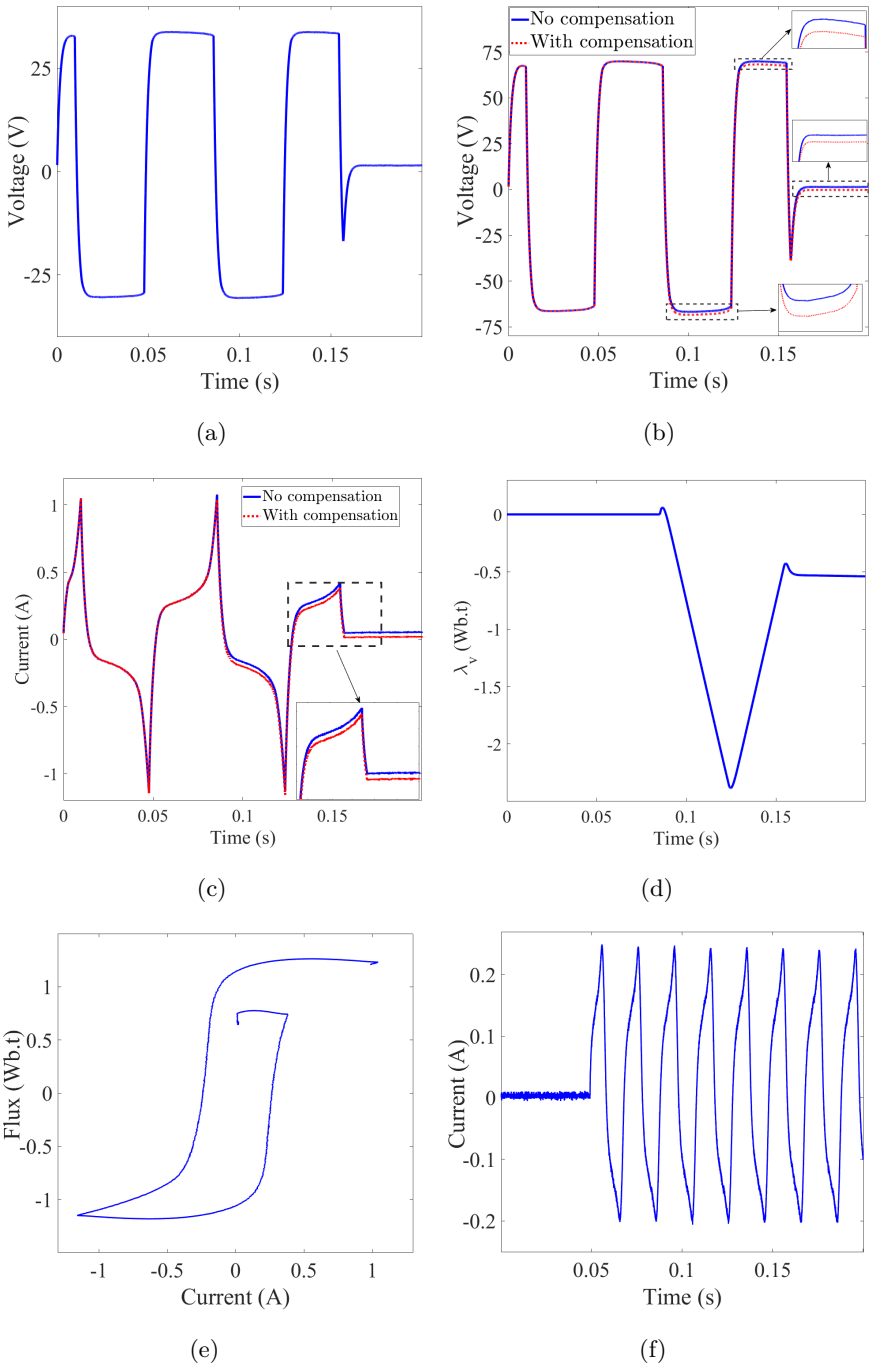

Figure 4.22: (a) Voltage applied to the secondary winding, (b) voltage induced on the primary winding, (c) secondary winding current, (d) voltage integral, (e) hysteresis curve after $t = 0.086$ s normalized by λ^{max}, and (f) primary winding current after transformer energization.

Table 4.4: Comparing Different Methods with Respect to the Worst-Case Scenario

Methods	Lower bound (%)	No sccater (%)	Upper bound (%)
MPFM 1 and MPFM 2	99.38	99.52	98.4
Demagnetization Method	94.8	99.52	97.2

Fig. 4.23 shows the currents flowing into the transformer energized by MPFM 2, MPFM 1, and the demagnetization method, assuming making only occurs at the upper and lower bounds of the making interval. It is assumed that the *RDDS* and mechanical scatter are ±20% and ±3.0%, respectively. For this CB, both the MFPM 2 and MPFM 1 perform identically. By employing these methods, the peak current drawn by the transformer is limited to 0.31 A and 0.8 A for energization at the lower and upper bounds. The results of the demagnetization method are 2.6 A and 1.25 A, respectively. Compared to the demagnetization method, the MPFM 2 and MPFM 1 demonstrate much less sensitivity to CB uncertainties.

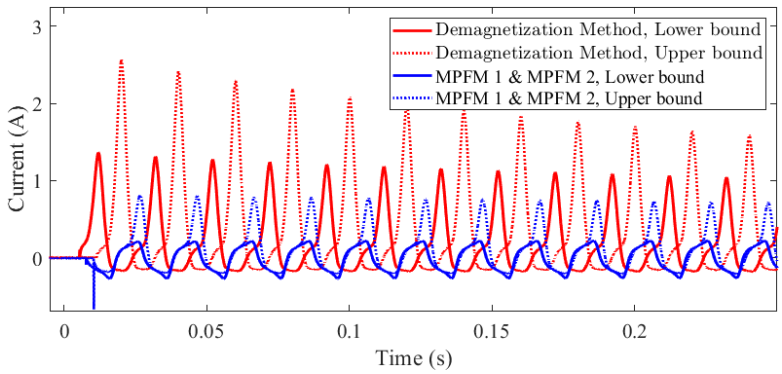

Figure 4.23: Currents flows into the transformer for energization at the upper and lower bounds of making interval.

Table 4.4 presents the results of various methods and the corresponding reduction in current magnitude compared to the worst-case energization scenario, which produces a peak current of 50 A. As illustrated, the best performance under ideal conditions is achieved by the proposed methods, both yielding the highest reduction in current magnitude. These are followed by the performance of the demagnetization method. The proposed methods demonstrate lower sensitivity to scatter, as their performance

is less affected by the lower and upper bounds of the making interval. The proposed methods achieve an improvement range of 98.4% to 99.52%, which is significantly better than the corresponding ranges of 94.8% to 99.52% for the demagnetization method. Similar to the method proposed in Chapter 3, the method proposed in this chapter can be implemented using the TMS320F2812 DSP, which is cost-effective and suitable for real-world applications.

4.5 Summary

This chapter introduces modified pre-fluxing methods designed to mitigate inrush currents in single-phase transformers, which are vital components in many TPSSs. The conventional pre-fluxing method faces significant challenges that render it impractical for traction transformers. The proposed methods, referred to as MPFM 1 and MPFM 2, aim to address these issues and provide a more effective solution for high-power single-phase transformers.

MPFM 1 adjusts the residual flux to the maximum feasible residual flux of the transformer's core and calculates the ratio of this feasible residual flux to the core's maximum flux under normal operation. This adjusted flux estimate is then used to optimize the CB closing operation, minimizing the difference between the residual and prospective flux to eliminate inrush current. Extensive simulations confirm that MPFM 1 effectively mitigates inrush current, with the residual flux estimation achieving an error of less than 1%. MPFM 1's performance is especially superior to the conventional pre-fluxing method when applied to cores made of ferromagnetic materials with a lower ratio between the maximum feasible residual flux and the maximum operational flux.

Although MPFM 1 offers a much better performance with less sensetivitiy to the closing operation of CB for the traction single-phase transformers compared to the conventional pre-fluxing method, MPFM 1 is not fast enough (similar to the conventional pre-fluxing method) for high-power transformers. To find a faster solution, the MPFM 2 is proposed which is able to flux high-power transformers. MPFM 2 effectively mitigates inrush current in single-phase transformers by introducing the concept of a "safe flux range", which is essential for its flux adjustment process. This range includes values that can be set as the core's residual flux and matched with the prospective flux, taking into account the CB's operating characteristics and limitations. A pre-fluxing device is developed to apply voltage to the transformer, adjusting the residual flux to an optimal

value within this safe range. Throughout the adjustment process, MPFM 2 compensates for any DC offset in the transducers, ensuring accurate residual flux estimation and minimizing the difference between prospective and residual fluxes.

Both MPFM 1 and MPFM 2 exhibit similar performance in reducing inrush current, effectively limiting the current magnitude to levels below the transformer's nominal current. MPFM 2 offers a distinct advantage by adjusting the residual flux within seconds, even for high-power transformers, whereas MPFM 1 may take several minutes for the same task. Additionally, MPFM 2 is specifically designed to account for and minimize the uncertainties associated with CB closing operations, addressing a potential drawback of MPFM 1, which might occasionally lead to making on the previous voltage hump. In essence, MPFM 2 retains all the benefits of MPFM 1 while eliminating its shortcomings.

Chapter 5

Mitigating the Inrush Current of V/V Transformers Using Railway Conditioners and Independent-Pole-Operated Circuit Breakers

5.1 Overview

In Chapters 3 and 4, various energization methods for single-phase traction transformers were introduced. However, V/V traction transformers, known for their simple structure and efficiency in powering electric trains, are also widely used in TPSSs. This chapter introduces a novel flux matching method to mitigate inrush currents during the energization of V/V traction transformers. Unlike existing methods for three-phase transformers, the proposed method adjusts the transformer's residual flux density to any value within the feasible range by injecting the appropriate current into the V/V transformer using a railway power conditioner. The only parameter required is the transformer's nominal excitation current; all other necessary data is gathered during the flux adjustment process. This method removes the need for detailed transformer design information, thereby reducing significant sources of difficulty and uncertainty. The selected reference value for residual flux density is chosen from the feasible range to minimize the impact of CB closing operations and any associated uncertainties on the energization process. For flux adjustment, the railway power conditioner injects sinusoidal current into the transformer prior to its energization, ensuring that the residual flux density is accurately matched with the reference value. Following flux adjustment, different phases of the V/V transformer are energized sequentially at optimal instants using an independent-pole-operated CB.

5.2 Traction Power Supply System Based on V/V Transformer

A V/V transformer contains two single-phase transformers known as the α-side and β-side transformers. Fig. 5.1 shows a typical traction power supply system with a V/V transformer, which is equipped with a railway power conditioner, which can be the power conditioners explained in section 1.2.2. The α-side and β-side transformers are identical but magnetically decoupled, which means their cores are not connected. Hence, the residual flux of each of the two single-phase transformers can be adjusted independently. To flux the α-side and β-side transformers from the secondary side, each leg of the railway power conditioner can be controlled separately. The α- and R-legs can be used to flux the α-side transformer, and the β-side transformer is fluxed via the β-leg and R-leg. The R-leg is common between α-side and β-side transformers, and hence, its

current is the opposite of the sum of α- and β-legs' currents. The CB used to energize the V/V transformer is an independent-pole-operated CB, meaning that its poles can be controlled separately.

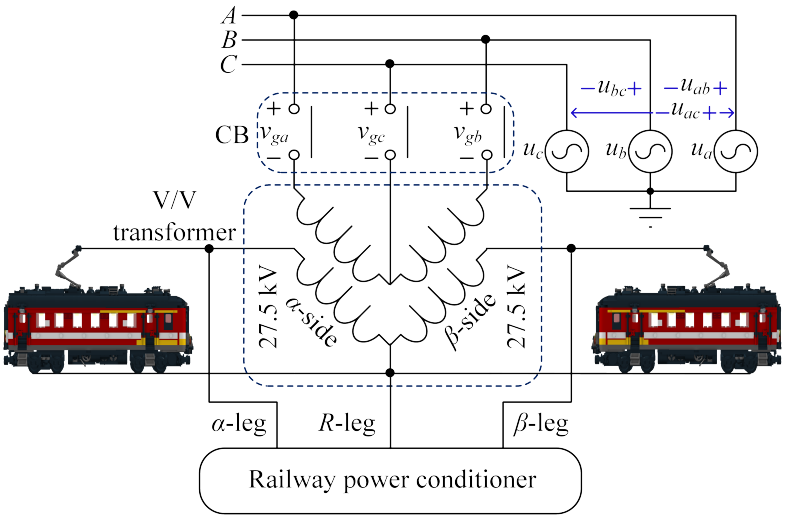

Figure 5.1: V/V traction transformer equipped with a railway power conditioner.

5.3 Inrush Current Mitigation Method for V/V Transformer

This section proposes an effective method for adjusting the residual flux density of the α-side and β-side transformers to any given $B_r^{ad} \in [-0.5B^{max}, 0.5B^{max}]$, which is called the guaranteed range as will be explained in section 5.3.1. The energization instant for each of the two transformers is then obtained so as to minimize the difference between B_r^{ad} and B_p. The operating characteristics and limitations of CBs are taken into account to establish a sound flux matching procedure capable of stopping inrush current from occurring.

5.3.1 Controlled Switching on the V/V Transformer

The first step in controlled switching is to obtain the voltage between the moving and fixed contacts of each CB pole when the CB is open. When all CB poles are open in Fig. 5.1, the gap voltages v_{ga}, v_{gb} and v_{gc}, are equal to the phase voltages u_a, u_b, and u_c,

respectively. It can be easily confirmed that the gap voltages are not independent and change when any of the three poles is closed. For example, if pole C of the CB is closed, $v_{ga} = u_{ac}$, $v_{gb} = u_{bc}$, and $v_{gc} = 0$. Let us suppose that pole C is closed after poles A and B have been closed. This makes the voltages across the α-side and β-side windings jump immediately from u_{ab} and $-u_{ab}$ to u_{ac} and u_{bc}, respectively. The transformer's core may get saturated due to this sudden voltage change, which is not desirable. Hence, it is recommended that pole C (the pole in the middle in Fig. 5.1) must get closed before the other two poles. This is to avoid any core saturation due to a sudden change in the windings' voltage.

With pole C closed and poles A and B open, v_{ga} and v_{gb} become equal to u_{ac} and u_{bc}, respectively. In this way, the gap voltages of the two transformers, i.e., v_{ac} and v_{bc}, will be identical but with 60° phase-angle displacement. Let us denote the fundamental frequency of the CB's gap voltage by f. The period of this voltage will be the reciprocal of the frequency as $T = \frac{1}{f}$. The absolute value of the CB's gap voltage is also a periodic function with period $\frac{1}{2f}$. Without loss of generality, the same making voltage can be aimed for energizing each of the α-side and β-side transformers. For this to happen, the time difference for energizing the two transformers should be $\frac{T}{6}$.

The maximum residual flux density of the core can take a value from 50% to 90% of B^{max}, depending on the core's material [36]. This means adjusting the absolute value of B_r to quantities greater than $0.5B^{max}$ may or may not be feasible. Conversely, a residual flux equal to or below $0.5B^{max}$ is almost always possible. To remove the need for any detailed information about the B-H characteristics of the core, this research suggests taking $[-0.5B^{max}, 0.5B^{max}]$ as the guaranteed range for adjusting the residual flux within.

Fig. 5.2 shows part of the CB's absolute gap voltage, which is a sinusoidal hump that repeats at time intervals of $\frac{T}{2}$ (equivalent to an argument of π rad). A rising zero-crossing of the gap voltage is taken as the reference, i.e., $t = 0$. Here, our analysis is focused on the first and second humps. To energize during any other hump, it is sufficient to shift the timing of the actions by an appropriate multiple of the time constant T when following the steps outlined for the first or second hump. With reference to Q_1 and Q_2, the first hump can be divided into three regions; one from the origin to Q_1, another region from Q_1 to Q_2, and the third region from Q_2 to the end of that hump. Similarly, the points Q_3 and Q_4 on the second hump also divide that hump into three different

regions.

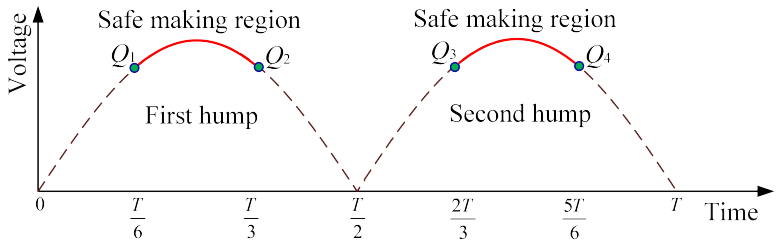

Figure 5.2: Safe making regions whose corresponding prospective flux can be equated by the residual flux density regardless of the core's material.

Making at the boundary points Q_1 or Q_2 results in $B_p = -0.5B^{max}$ or $B_p = 0.5B^{max}$, respectively. It can also be confirmed that making between Q_1 and Q_2 ensures that $-0.5B^{max} \leq B_p \leq 0.5B^{max}$. The region between Q_1 and Q_2 on the first hump of the absolute gap voltage, which is marked in red in Fig. 5.2, is of special importance to us and is called a safe making region. The safe region on the second hump lies between Q_3 and Q_4. The prospective flux density associated with a making anywhere in these safe regions can be equated by an identical residual flux density regardless of the transformer's core material. The same does not necessarily apply to making points, for example, on the first hump but outside the feasible region corresponding to $|B_p| > |0.5B^{max}|$. Similarly, whether the prospective flux of a making on the second hump (outside the safe marking region) can be equated by an identical residual flux density is uncertain and depends on the core material.

As mentioned earlier, making cannot be guaranteed to happen at a certain target time but a range around it, owing to *RDDS* and mechanical scatter. As discussed in [80], targeting points on the rising half of the absolute gap voltage results in a smaller making range around the target point. Thus, Q_1 can be considered an optimal target point for making in the safe region of the first hump. This will ideally result in energization at $t = \frac{T}{6}$ and a prospective flux of $B_p = -0.5B^{max}$. Aiming for Q_3 the second hump will ideally result in energization at $t = \frac{2T}{3}$ with prospective flux $B_p = 0.5B^{max}$.

Now, let us obtain the closing initiation and mechanical contact touch instants that correspond to making at Q_1 on the first hump. As per the time reference chosen in Fig. 5.2, $|V_m \sin(\omega t)|$ denotes the absolute gap voltage. First, mechanical and *RDDS* scatter is disregarded, and the prime sign is used to mark the corresponding instant of contact

touch as t'_{ct}. With making voltage $\frac{\sqrt{3}V_m}{2}$ and $-s^{mean}$ as the slope of the *CBDS* curve, t'_{ct} can be obtained from

$$t'_{ct} = \frac{T}{6} + \frac{\sqrt{3}V_m}{2s^{mean}} \tag{5.1}$$

Equation 5.1 gives t'_{ct} with the assumption that there is no mechanical or *RDDS* scatter. In practice, however, the *RDDS* and closing time may vary slightly in different closing attempts, thereby resulting in a range instead of a certain making instant.

This range might be even so wide that includes part of the previous sinusoidal hump. Making on a previous hump with an opposite voltage polarity could result in a considerable difference between the true and target prospective fluxes. Let us assume that t_{crit} (which is identical as τ_{in} explained in 5.3.1) demonstrates the earliest closing initiation instant that prohibits making on the previous hump even with extreme values for closing time and *RDDS*, i.e. s^{min} and $T_{CB} - \Delta T_{CB}$. To guarantee making happens on the first hump, the closing initiation instant must be obtained from

$$t_{in} = \max(t'_{ct} - T_{CB}, t_{crit}) \tag{5.2}$$

It can be easily confirmed that when $t'_{ct} - T_{CB} < t_{crit}$, the resulting t_m would be slightly greater than $\frac{T}{6}$. This conservative t_{in} ensures that making does not happen on the previous hump, while the target making remains the same or as close as possible to Q_1. In this case, t_m can be calculated by setting $s = s^{mean}$ and $t_{ct} = t_{in} + T_{CB}$ in 3.1. With the time reference of Fig. 5.2, energizing the transformer at t_m will result in

$$B_p = -B^{max}\cos(\omega t_m) \tag{5.3}$$

The next step is to adjust the core's residual flux to the value given by (5.3) and then energize the transformer at $t = t_m$. With pole C of the high voltage CB closed, the absolute gap voltages $|v_{ga}|$ and $|v_{gb}|$ will have $\frac{\pi}{3}$ rad phase displacement. If the β-side transformer is energized with a time delay of $\frac{T}{6}$ after the α-side transformer is energized, the prospective fluxes of the two transformers will have the same magnitude and sign. To take advantage of this, the residual flux density of the α-side and β-side transformers can be adjusted to the same value using the technique that will be explained in the next section. Then the two transformers are energized with T/6 time delay.

5.3.2 Residual Flux Adjustment

The purpose of flux adjustment is to take advantage of the B-H characteristic to modify the core's residual flux density from an unknown initial value of B_r to a desired value of B_r^{ad}. It will be quite advantageous and sometimes even necessary if the flux adjustment process does not require the knowledge of the initial residual flux or the core's B-H characteristics. The subsection argues that current injection is the preferred method for adjusting residual flux density, as opposed to applying voltage to the winding. It is also shown that the amplitude of the excitation current is the only information needed to accomplish this. Then, a simple yet effective technique is presented for the estimation of the core's flux density over the course of the flux adjustment process.

Voltage or Current Control

By varying either the flux density or the magnetic field (B or H) in a controlled way, a given hysteresis loop can be traversed. Nevertheless, neither of these variables is directly accessible and they can only be indirectly controlled by changing voltage across and current injected into the transformer windings. This part explains how injecting appropriate sinusoidal current into the winding can adjust the residual flux to a credible reference value. It also discusses why applying sinusoidal voltage across the winding should be avoided, by highlighting complications this may introduce into the flux adjustment process.

Without loss of generality, let us consider a single-phase transformer with a unity turns-ratio. The nominal voltage and amplitude of nominal excitation current (i.e., V_m and I_{ex}, respectively) are assumed to be known. No information about the nominal and inner hysteresis loops of the core (B-H characteristics) is assumed to be available. To begin our discussion, let us consider an easy case where the initial residual flux density of the core is zero ($B_r = 0$ T). The nominal voltage $v(t) = V_m \cos(\omega t)$ shown in blue in Fig. 5.3(a) can be applied to the secondary winding while the primary winding is left open-circuited. This results in a sinusoidal flux density that varies in the range $[-B^{max}, B^{max}]$. Examining Fig. 5.3 in an anticlockwise direction and beginning with Fig. 5.3(a), one can observe how applying the nominal sinusoidal voltage to the secondary winding leads to the flow of a non-sinusoidal excitation current with amplitude I_{ex}. In the general case of non-zero initial flux density, however, applying nominal voltage to the transformer is not as convenient. This can saturate the core as explaine in section 1.2.3 and cause

inrush current, which defeats the purpose of flux adjustment.

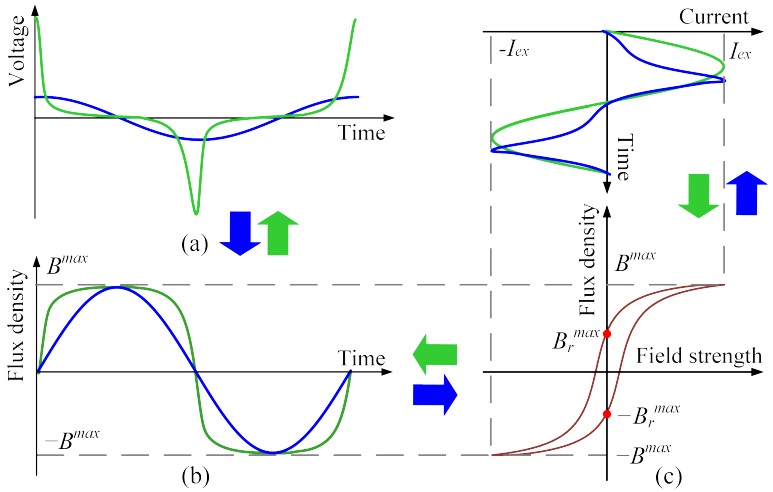

Figure 5.3: Transformer's (a) winding voltage, (b) core's flux density, (c) current and B-H curve following Scenarios 1 and 2.

Now let us assume a sinusoidal current with amplitude I_{ex} is injected into the secondary winding. As a result, a non-sinusoidal voltage will be induced across the open-circuited primary winding, as indicated by examining Fig. 5.3 clockwise and starting at Fig. 5.3(c). The resulting flux density is not sinusoidal yet varies in the linear range $[-B^{max}, B^{max}]$. The flux density reaches $+B_r^{max}$ and $-B_r^{max}$ at falling and rising zero-crossings of the current waveform, respectively.

The magnetic field strength is assumed to be linearly proportional to the excitation current, while the flux density is a more complicated function of the voltage applied to the winding, as per (1.2). The coefficient and constant of this integral depend on the core parameters and original flux density, respectively. Without knowledge of this information, controlling the applied voltage to trace a given hysteresis loop would be difficult and time consuming. The initial flux density of the core could potentially cause an offset in the flux density. Such an asymmetry can easily saturate the core and push the magnetization of the core out of the nominal hysteresis loop.

The transition from the residual flux to the knee point for the first time is the only part of the magnetization that is influenced by the initial residual flux density, over the course of current injection. Once the knee point is reached, the subsequent trace of flux density becomes independent of the initial residual flux value. Thereafter, the trace is

solely determined by the B-H characteristics of the transformer. At a zero-excitation current (while traversing the nominal hysteresis loop), the flux density is offset from the origin by the residual flux density $\pm B_r^{max}$. To be able to achieve smaller residual flux densities, inner hysteresis loops must be traversed. This can be achieved by injecting smaller sinusoidal current into the winding, as will be detailed in following sections.

Flux Density Estimation

The transformer's flux density right at the de-energization instant may be estimated using two different approaches. One approach is to utilize (1.2), provided that N, A, B_r and the voltage applied are all known. An alternative approach is monitoring primary and secondary currents and voltages to track the core's magnetization along a hysteresis loop, if known. These two approaches require knowledge of the transformer's design information or the core's B-H characteristics. On the other hand, current and voltage measurements prior to the transformer disconnection may not be sufficiently accurate due to the transient responses of instrument transformers [78]. This is the case, for example, when the transformer disconnection has been caused by abnormal conditions such as a short-circuit fault. Once de-energized, the transformer's residual flux density begins to decline gradually through the CB grading capacitors and the stray capacitors of transformer bushings [95].

A simple technique is presented here to estimate the core's flux density relative to B^{max}, which will also be shown to be enough to enable the mitigation of inrush current. The sinusoidal alteration of H along the nominal hysteresis loop induces a voltage across the primary winding, which is not sinusoidal but periodic with the same period as that of the injected sinusoidal current. This is caused by the cyclic traversal of the closed hysteresis loop while the relationship between B and H is nonlinear. Let us assume i_{inj}(t) is injected into the secondary winding at $t = 0$ and the induced voltage across the open-circuited primary winding of the transformer is measured , i.e., $v_p(t)$. Let $T_r = \frac{1}{f_r}$ denote the period of the injected sinusoidal current. The core flux density is a function of time and is shown by $B(t)$. It can be seen from Fig. 5.3 that $B(t)$ reaches its maximum, i.e., B^{max}, when $i_{inj}(\frac{T_r}{4}) = I_{ex}$. In its travel along the nominal hysteresis loop, $B(t)$ reaches $+B_r^{max}$, $-B^{max}$ and $-B_r^{max}$ when the injected current respectively reduces to zero and $-I_{ex}$ and then ascends to zero. These happen at $\frac{1}{2}T_r$, $\frac{3}{4}T_r$, and T_r, respectively.

Throughout the flux adjustment process, (1.2) in a more general form can be used

to estimate the core's flux density at time t as below

$$B(t) = \frac{1}{NA}\int_0^t v_p(t)\mathrm{d}t + B_r \tag{5.4}$$

In (5.4), the multiplier before the integral and B_r are unknown. The flux density at $\frac{T_r}{4}$ and $\frac{3T_r}{4}$ are respectively equal to B^{max} and $-B^{max}$, which can be examined using (5.4). The maximum and the initial residual flux densities (B^{max} and B_r) are unknown. Nevertheless, the integral term of (5.4) can be calculated using the terminal voltage, and can thus be considered known. In this way, a system of two equations in two unknowns can be formed and solved for the unknowns to arrive at

$$\begin{cases} B^{max} = \frac{1}{2NA}\left[\int_0^{\frac{T_r}{4}} v_p(t)\mathrm{d}t - \int_0^{\frac{3T_r}{4}} v_p(t)\mathrm{d}t\right] \\ B_r = \frac{-1}{2NA}\left[\int_0^{\frac{T_r}{4}} v_p(t)\mathrm{d}t + \int_0^{\frac{3T_r}{4}} v_p(t)\mathrm{d}t\right] \end{cases} \tag{5.5}$$

Let us use the hat sign to refer to the per-unit value of flux density. The per-unit value of $B(t)$, i.e., $\hat{B}(t)$, can be calculated based on (5.4) and (5.5) as

$$\hat{B}(t) = \frac{B(t)}{B^{max}} = \frac{2\int_0^t v_p(t)\mathrm{d}t - \int_0^{\frac{T_r}{4}} v_p(t)\mathrm{d}t - \int_0^{\frac{3T_r}{4}} v_p(t)\mathrm{d}t}{\int_0^{\frac{T_r}{4}} v_p(t)\mathrm{d}t - \int_0^{\frac{3T_r}{4}} v_p(t)\mathrm{d}t} \tag{5.6}$$

Current Injection

For a successful flux adjustment, the frequency and amplitude of the injected current are both to be appropriately controlled. This current, denoted as $i_{inj}(t) = I_p \sin(2\pi f_r t)$, must be controlled to prevent core saturation, ensuring that I_p does not exceed I_{ex}. The amplitude of the injected current plays a key role in adjusting the residual flux density to any value within the feasible range $[-B_r^{max}, B_r^{max}]$ rather than to its lower and upper bounds only.

The voltage induced across the primary winding by injecting current into the secondary winding is a function of the B-H curve and is also directly proportional to the rate of change of current based on Faraday's law [27]. Current of higher frequency may force the primary voltage to exceed the transformer's normal voltage. This means that a sinusoidal current with a larger f_r induces voltage with larger amplitude on the primary winding. This is in addition to the fact that at the same frequency, a current with a higher amplitude induces a higher voltage on the primary winding.

The amplitude of the injected current, i.e. I_p, is first set to I_{ex} to steer magnetization along the nominal hysteresis loop. An initial frequency of 1 Hz is adopted and then is increased in steps of 1 Hz at the end of each cycle. This is to increase the speed of the flux adjustment process by seeking a maximal yet safe frequency. To account for a safety margin, the frequency increment is continued until the amplitude of the induced voltage reaches 60% of the nominal voltage.

After fixing f_r, a current with amplitude $I_p = I_{ex}$ is injected for a full period. Removal of this current at $t = T_r$ adjusts the residual flux to $B_r^{ad} = -B_r^{max}$. If the same current is continued to be injected for an extra half-cycle, $B_r^{ad} = B_r^{max}$. Nevertheless, the (desired) reference residual flux might be lower than $\pm B_r^{max}$. The main idea here is to constantly alter the current amplitude to travel between inner hysteresis loops, as shown in Fig. 5.4. The current amplitude can gradually be decreased in order to move inward through inner hysteresis loops. This allows for reaching lower residual flux densities depending on the hysteresis loop being traversed. The red arrows in the figure show the direction of current reduction and the dotted red arrows signify the direction of residual flux reduction. A threshold can be set around the reference residual flux density to stop the current injection when the estimated residual flux density is within tolerance. In case the residual flux density exceeds the reference value by more than a certain percentage, the direction of change in current amplitude could be reversed at a lower rate to achieve the desired precision.

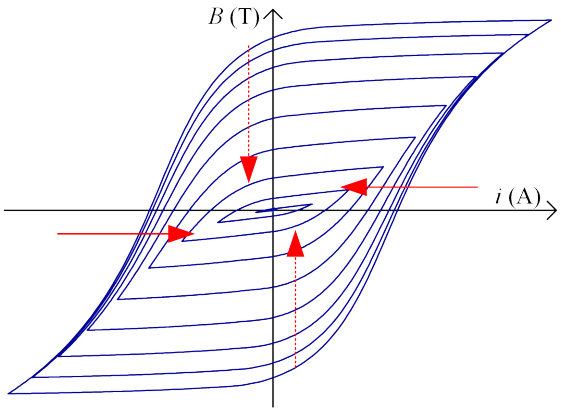

Figure 5.4: Moving inward through hysteresis loops by reducing the excitation current.

5.3.3 Simulation-Based Performance Evaluation

To evaluate the performance of the proposed method, the traction power supply system (connected to a 220-kV, 50-Hz power system) shown in Fig. 5.1 is simulated in PSCAD/EMTDC. This V/V transformer contains two 25-MVA, 220 kV/27.5 kV core-type single-phase transformers that are simulated based on the TDM, as explained in section 2.4. The peak value of the primary side nominal current of the transformer is 160 A. The *Type* 1 and *Type* 2 transformers introduced in section 2.4 are used to evaluate the proposed method. A nine-level modular multilevel railway power conditioner (HB-MMC3 RPC [23]) with a DC link voltage of 41 kV is used as a current source for flux adjustment. The controls used on this HB-MMC3 RPC are as detailed in [96].

In the following sections, we first define and examine three typical energization scenarios—random, simultaneous, and Pole-C first—focusing on their associated inrush currents. Subsequently, we analyze the proposed method's ability to target Q_1 on the first peak of the gap voltage. A comparative evaluation of the proposed method, the pre-fluxing method [67], and the random energization method is then presented. Finally, we provide a detailed overview of the flux adjustment process for the V/V transformer.

Transformer Casual Energization

A casual energization scenario refers to switching sequences that are not aimed at removing inrush current. It goes without saying that the inrush current drawn following a casual energization scenario could become very large. First, let us consider an extreme case for core *Type* 1 where $B_r = B_r^{max} = 0.9$T and the α-side and β-side transformers are energized at 0 s and 3.3 ms, which mark the rising zero-crossing of their corresponding gap voltages, respectively. Fig. 5.5 shows the inrush current drawn by the *Type* 1 V/V transformer following this energization scenario. The currents of phases A, B, and C reach 1.329 kA, 1.33 kA, and -1.96 kA, respectively. The current of phase A reduces to normal faster than the currents of phases B and C. The main reason for this is that v_{bc} is not sinusoidal at the energization instant due to the presence of the inrush current of the α-side transformer and its impact on v_c.

Table 5.1 summarizes the result of three casual energization scenarios, namely random, simultaneous, and phase-C-closed scenarios. The highest values among the three phases are reported. In a random energization scenario, the three CB poles are all closed over an interval of 20 ms with a random uniform distribution. The second scenario is

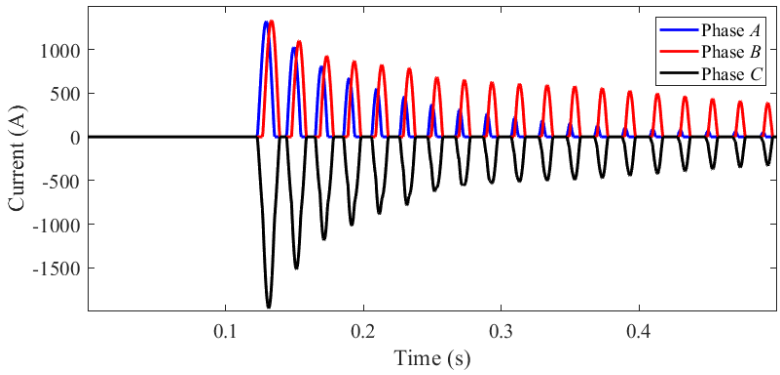

Figure 5.5: Inrush current drawn following the worst-case energization scenario.

simultaneous energization where the closing operations of the CB poles are initiated simultaneously. The third scenario ensures that pole C is already closed for a long time before the other two poles are randomly closed within a 20-ms period. It should be noted that in all scenarios, $RDDS$ = 50 kV/ms with ±10% scatter, and T_{CB} =40 ms with ±1 ms mechanical scatter. To account for the probabilistic nature of the parameters, each casual energization scenario is repeated 1000 times. As expected, the three-phase currents are several times larger than the transformer's nominal current (which is 160 A). In addition to troubling protective relays, such undesirable high-magnitude current would reduce the transformer's lifetime.

Table 5.1: Inrush Current Following Casual Transformer Energizations

Casual Energization Scenario	Current (A)					
	Type 1			*Type* 2		
	Min	Mean	Max	Min	Mean	Max
Random	7.39	761	1950.6	46.3	780	2283
Simultaneous	3.32	658.1	1922.6	0.61	688	2250
Pole-C First	0.518	721.6	1907.6	0.454	838.7	2277

General Performance Evaluation: Proposed Method

The method's performance is first evaluated assuming the CBs are ideal (without $RDDS$ and mechanical scatter). This means T_{CB} = 40 ms, and $RDDS$ = 50 kV/ms. The α-side and β-side transformers are energized at Q_1 on the first odd hump. As per (5.1),

the closing initiation instants are obtained to be -31.3 ms and -28 ms. These correspond to contact touch instants 8.7 ms and 12 ms, respectively. Making ideally takes place at 3.3 ms and 6.6 ms and results in a prospective flux density of $\hat{B}_p = -0.5$ pu for both transformers. This means with $B_r^{ad} = -0.5$ pu, inrush current can be fully mitigated, and hence, the V/V transformer's energization merely results in the flow of excitation current.

As mentioned earlier, unintentional making on a previous hump can result in a large discrepancy between the true and target prospective fluxes. This is not a concern with a primary voltage of 220-kV and an *RDDS* of $s^{mean} \geq 25$ kV/ms with a maximum of 30% scatter. It can be shown that even with mechanical scatter of up to $\Delta T_{CB} = 1$ ms, targeting Q_1 does not lead to making on the previous hump. Table 5.2 summarizes the impact of scatter on the energization of the α-side transformer with Q_1 as the target making point. Considering the non-idealities, making on the α-side transformer does not happen at 3.3 ms, rather it happens within the range [2.3 ms, 4.5 ms]. The same range for the β-side transformer in milliseconds is [5.6, 7.8] which includes the ideal instant of $t = 6.6$ ms.

Table 5.2: Performance of the Proposed Method with and without Scatter

RDDS	s^{min}	s^{mean}	s^{max}
Closing Time	$T_{CB} - \Delta T_{CB}$	T_{CB}	$T_{CB} + \Delta T_{CB}$
$t_{ct}(ms)$	7.7	8.7	9.7
$t_m(ms)$	2.4	3.3	4.5
$\hat{B}_p(pu)$	-0.7291	-0.5	-0.131

To statistically evaluate the effect of scatter on t_m, a sensitivity analysis is carried out by conducting 10,000 simulations. To account for the scatter, it is assumed that $\Delta T_{CB} = 1$ ms and $0.8s^{mean} < s < 1.2s^{mean}$. Fig. 5.6 shows the normal distribution of making instant for the α-side and β-side transformers. The target making instants, i.e., 3.3 ms and 6.6 ms, lie inside the area with the highest probability of occurrence. In most cases, a small difference exists between the true and target making instants.

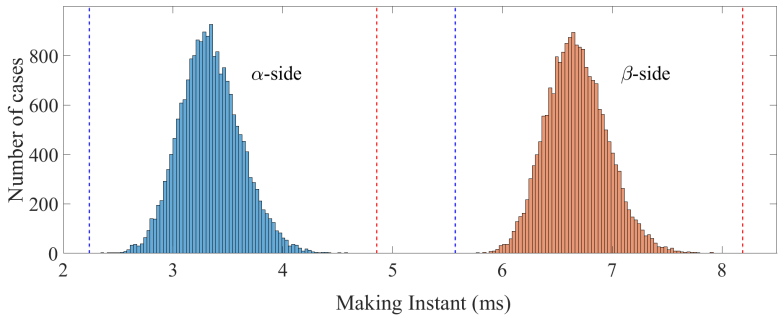

Figure 5.6: Distribution of the making instant for the α-side and β-side transformers.

Comparison with Other Methods

The adjusted residual flux by the pre-fluxing method is either of the upper or the lower bound of the feasible range $[-B_r^{max}, B_r^{max}]$. The adjusted residual flux by the random energization method can take any value within this range. In this subsection, the proposed method is compared with the pre-fluxing method and the random energization scenario described in subsection entitled "*Transformer Casual Energization*". A total of 2,000 simulations are conducted to evaluate the performance of each method. The pre-fluxing method energizes the transformer at either the rising or falling halves of the absolute gap voltage. These target makings correspond to the prospective flux densities $0.87B^{max}$ and $-0.87B^{max}$, respectively. The adjusted residual flux densities by the proposed methods are assumed to be $B_r^{ad} = \pm 0.5B^{max}$. A uniformly distributed random error with upper and lower bounds of $\pm 5\%$ is considered for flux adjustment.

Figs. 5.7(a) and 5.7(b) demonstrate the distributions of inrush current of the V/V transformer by the proposed method and the pre-fluxing method targeting the rising and falling halves of the gap voltage. The outcome of random energization is not shown for it is almost evenly distributed from zero to the highest possible inrush current. The type of transformer core does not impact the performance of the proposed method. As shown, the method effectively limits the inrush current magnitude to 66% of the nominal current. The discrepancy between $0.87B^{max}$ and B_r^{max} is larger on the *Type* 1 core than on the *Type* 2 core. Thus, the energization of *Type* 1 by the pre-fluxing method results in a higher inrush current compared to that of *Type* 2.

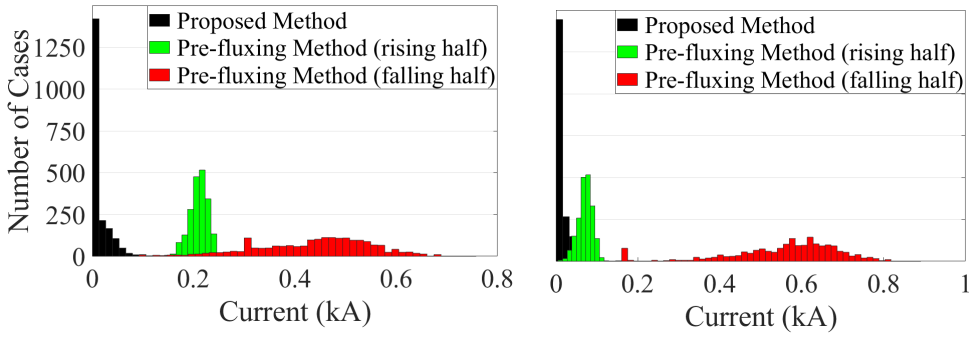

Figure 5.7: Distribution of inrush current amplitude upon V/V transformer energization of (a) *Type* 1 and (b) *Type* 2 transformers by different methods.

Flux Adjustment

This subsection details the proposed residual flux adjustment procedure on the *Type* 1 core, as an example. The residual flux densities of the α-side and β-side transformers are assumed to be 0.6 T and -0.3 T, respectively. Taking B^{max} as the base flux density, the initial residual flux densities of the α-side and β-side transformers, and the maximum residual flux density of the core are 0.4, -0.2, and 0.6 pu, respectively. The injection of a sinusoidal current to the secondary winding with amplitude $I_{ex} = 3.2$ A is initiated at $t = 0$. The frequency of the injected current is maintained at 1 Hz for a full cycle and is then continuously increased at the end of each cycle in 1-Hz steps. The voltage induced on the primary winding happens to exceed 60% of the nominal voltage when the frequency reaches 5 Hz. Therefore at $t = 2.18$ s, f_r is fixed at 5 Hz to avoid any potential damage due to overvoltage.

Before targeting Q_1 on the first hump, it should be ensured that the residual flux is adjusted to -0.5 pu. Since this value is larger than B_r^{max} (-0.6 pu), the current amplitude is reduced at a rate of 1 A/s. The process will be stopped once the residual flux density lies within $\pm 5\%$ of the reference value -0.5 pu. Fig. 5.8(a) shows the injected current, and Fig. 5.8(b) shows the true and estimated flux densities of the α-side transformer's core in per unit. As can be seen from Fig. 5.8(a), the current injection is stopped at $t = 4.68$ s when the residual flux density is adjusted to -0.48 pu, as depicted in Fig. 5.8(b).

The proposed flux adjustment method is faster than that presented in [67]. To show

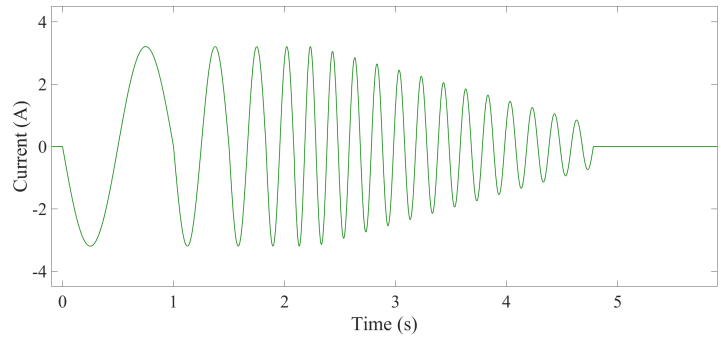

(a)

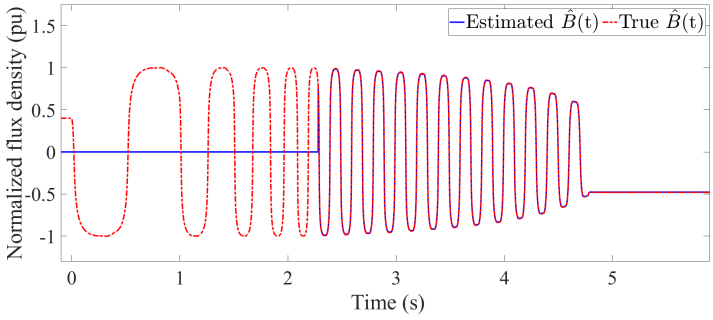

(b)

Figure 5.8: (a) Current injected into the secondary winding, and (b) true and estimated flux densities of the α-side transformer.

this, *Type* 1 and *Type* 2 cores are considered. The proposed method is tested with reference values ranging from -0.66 pu to 0.66 pu. The initial residual flux of the core is assumed to have the maximum possible distance from the reference value. Results show that the proposed method does not take more than 10 s for flux adjustment. Achieving the same using the pre-fluxing method needs a few minutes [67]. Speedy flux adjustment is in addition to the proposed method's ability to adjust the flux at any value within the feasible range. These have been achieved with no need for knowing any information about the *B*-*H* curve, which can be considered a great advantage.

5.3.4 Experimental Validation and Performance Analysis

To demonstrate the effectiveness of the proposed method, a laboratory-scale V/V transformer is extensively tested on the test rig shown in Fig. 5.9. This V/V transformer

is composed of two 400-VA, 220 V/120 V core-type single-phase transformers with $B_r^{max} = 0.78B^{max}$. The peak amplitude of the transformer's excitation current is 0.22 A. In the worst-case energization scenario, the current might increase as high as 50 A. An omicron CMC 356 relay tester is utilized as a current source for flux adjustment. The CB is modeled with an instantaneous turn-on solid-state relay controlled with a Typhoon HIL 604 device. All experimental results verify the obtained simulation results in the previous subsections.

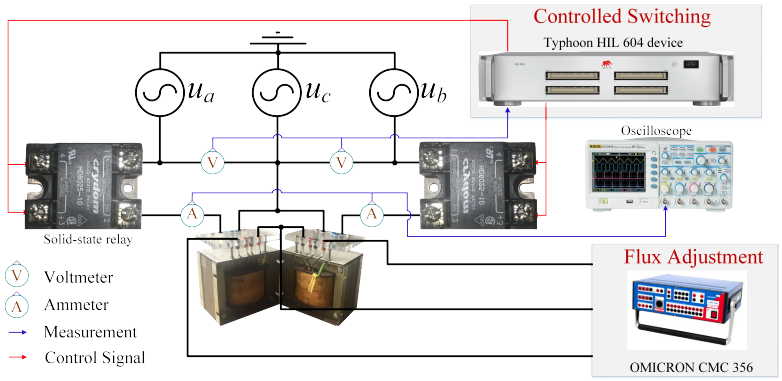

Figure 5.9: Test rig used to study different inrush current mitigating methods.

An example of the flux adjustment process is shown in Fig. 5.10. At $t = 0$, a sinusoidal current with an amplitude of 0.5 A is injected into the secondary winding as shown in Fig. 5.10(a). At $t = 1.5$ s, the frequency of the current waveform is fixed at 2 Hz to avoid overvoltage in windings. As depicted in Fig. 5.10(b), the voltage is limited to 60 V, which is a safe voltage for the transformer. The current amplitude is then gradually reduced at a rate of 0.1 A/s to traverse inner B-H loops, as shown in Fig. 5.10(c). The injection process is set to stop when the residual flux density lies within ±5% of the reference value of -0.5 pu. According to Figs. 5.10(a) and 5.10(d), the injection process is stopped at $t = 5.26$ s when the residual flux reaches -0.46 pu.

Fig. 5.10(d) distinguishes two periods; the red part of the graph corresponds to the period before the frequency of the injected current is fixed when the flux density is not estimated. The blue part of the graph corresponds to the period after the frequency of the injected current is fixed when the flux density begins to be estimated. Finally, Fig. **??** demonstrates the current drawn by the transformer following its energization by the proposed and pre-fluxing methods. Using the proposed method, the current is

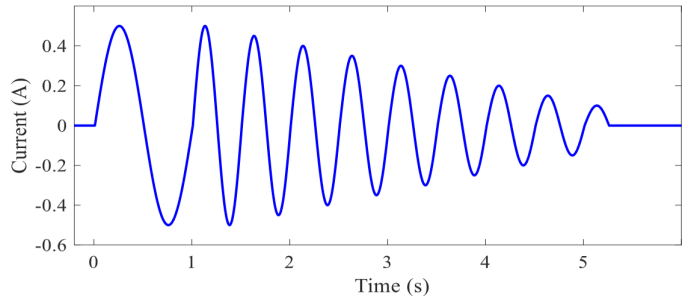

(a)

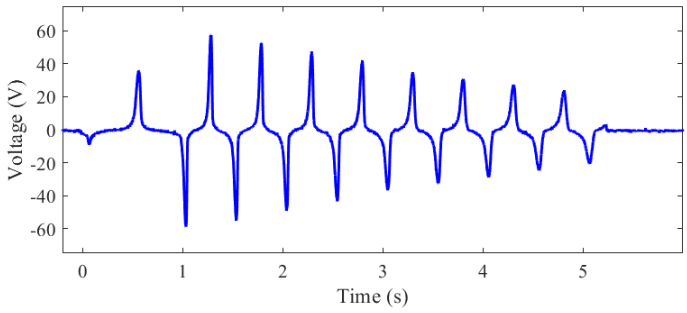

(b)

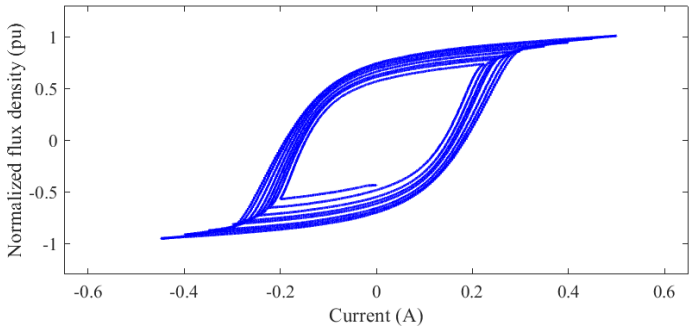

(c)

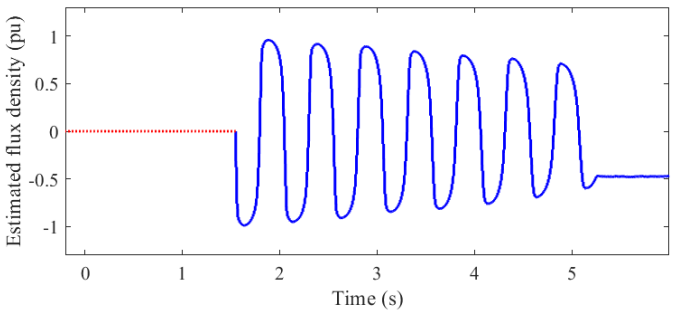

(d)

Figure 5.10: (a) Current injected into the secondary winding, (b) voltage induced on the primary winding of the α-side transformer, (c) B-H curve during current injection, and (d) estimated flux density of the α-side transformer.

limited to 250 mA, which is nearly equal to the transformer's excitation current. On the other hand, the inrush current reaches 800 mA by the pre-fluxing method. This 68% reduction in inrush current demonstrates that the proposed method outperforms the pre-fluxing method, even for transformers with high B_r^{max} values. When compared to the worst-case energization scenario, where the single-phase transformers of the V/V transformer can draw a peak current of 50 A, the proposed method achieves a reduction of 99.5%. In comparison, the pre-fluxing method achieves a reduction of 98.4%, further underscoring the enhanced effectiveness of the proposed approach.

5.4 Summary

This chapter proposes a flux matching method to mitigate the inrush current of V/V traction transformers upon energization energized with an independent-pole-operated CB. The guaranteed range for adjusting residual flux is derived and an effective technique is proposed for achieving any desirable values in this range, as per the energization requirements. This is in contrast with previous methods that can only adjust the residual flux at a few certain values such that the difference between residual and prospective fluxes is minimized. The proposed method determines a suitable making instant for energization considering the CB operating characteristics and scatter. The closing initiation instant is chosen in a way that ensures the difference between the prospective and adjusted flux density is minimal. This successfully mitigates the flow of inrush current without resorting to impractical tools and/or unrealistic assumptions.

The results of extensive simulations and experiments conducted confirm that the proposed method functions properly regardless of the transformer's core material and its initial flux density. It is also shown that the method is robust against a wide range of uncertainties emanating from *RDDS* and mechanical scatter. Remarkably, it is capable of maintaining the inrush current well below the nominal current, representing a significant advancement despite the inherent uncertainties. This is while with the pre-fluxing method used to energize V/V transformers, inrush current may exceed several times the nominal current, depending on the circumstances.

Chapter 6

Mitigating the Inrush Current of V/V Transformers Using Railway Conditioners and Gang-Operated Circuit Breakers

6.1 Overview

In Chapter 5, a method was introduced to energize V/V traction transformers using independent-pole-operated CBs. While this method effectively eliminates inrush currents with independent-pole-operated CBs, it is important to note that for voltages of 220 kV or lower, gang-operated CBs are typically used instead [4, 95, 97]. Moreover, the method from the previous chapter depends on the availability of the transformer's peak excitation current value, which is not always accessible. Even when conducting open- and short-circuit tests, only the true root mean square (TRMS) value of the excitation current is obtained. However, this TRMS value cannot be directly used to calculate the peak excitation current simply by multiplying it by $\sqrt{2}$. Moreover, the method presented in Chapter 5 also assumes that measurements obtained from voltage transducers are free of DC offset. This poses a vulnerability, as the method's accuracy may be compromised if the transducer's output cannot be corrected to eliminate the DC offset.

Based on the available literature, the most widely used transformer energization method involving gang-operated circuit breakers is the Simultaneous Closing Strategy, briefly introduced in Chapter 1. This approach requires estimating the residual flux density and then determining the optimal energization instant. As mentioned earlier, methods that rely on the residual flux density are susceptible to errors caused by changes in the residual flux after transformer de-energization due to ringdown transients [4]. Moreover, these methods are often applicable only to transformers with specific winding configurations. For instance, the method proposed in [61, 62] is designed exclusively for transformers with star-connected windings, while the method in [88] is limited to transformers with delta-connected primary windings. Clearly, these methods are unsuitable for the energization of V/V transformers.

To address these challenges, this chapter presents a flux matching energization method designed for V/V transformers that are energized using gang-operated CBs and for which no information about the excitation current is available. Similar to the method introduced in Chapter 5, this method adjusts the transformer's residual flux density to any reference value within the feasible range by injecting an appropriate current into the V/V transformer via a railway power conditioner. The only necessary parameter is the transformer's nominal voltage, which is used to determine the peak excitation current during the current injection. The reference value for the residual flux density is carefully selected from the feasible range to minimize the impact of the CB closing operations and

related uncertainties on the energization process.

A novel technique is introduced for estimating flux density during the adjustment process, which operates independently of the transformer's design parameters and relies solely on voltage transducers. This method also incorporates a mechanism to calculate and compensate for any DC offset in the transducer's output, ensuring accurate flux density estimation throughout the procedure. Following the flux adjustment, the V/V transformer is energized at optimal instants using a gang-operated CB.

6.2 Traction Power Supply System with Gang-Operated CB

Fig. 6.1 shows a typical traction power supply system, which is composed of a V/V transformer, a gang-operated CB for transformer energization via the 220-kV power network, and a three-wire railway power conditioner connected to the transformer's secondary side. To flux the α-side and β-side transformers from the secondary side, each leg of the railway power conditioner can be controlled separately. To achieve the same residual flux density with the same polarity in both single-phase transformers, the α- and R-legs are used to flux the α-side transformer, while the β- and R-legs flux the β-side transformer. To generate residual flux densities with opposite signs in both single-phase transformers, the α- and β-legs can be used to inject current into both transformers.

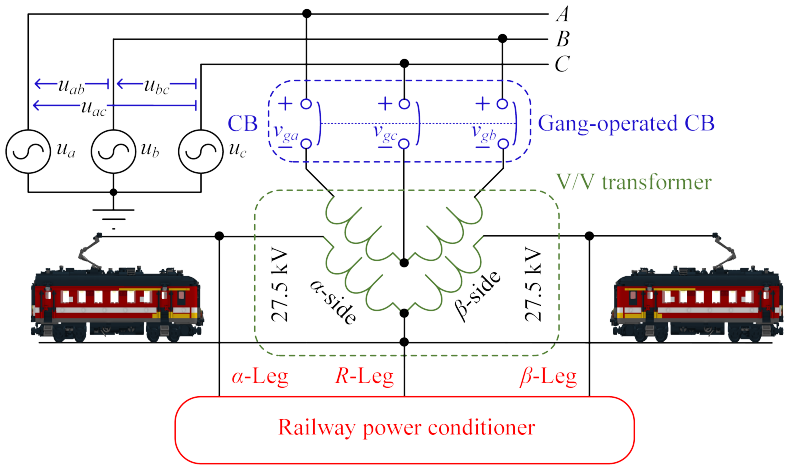

Figure 6.1: Typical traction power supply system with a railway power conditioner.

When the gang-operated CB is open, the gap voltage equals the phase voltage, i.e., $v_{ga} = u_a$, $v_{gb} = u_b$, and $v_{gc} = u_c$. The fundamental frequency of gap voltages is represented by f, with a period of $T = \frac{1}{f}$. To analyze the energization of the V/V transformer using a gang-operated CB, let us assume that the phase A voltage is $u_a = V_m \sin(\omega t)$, where the rising zero-crossing of phase A voltage is taken as the time reference, i.e., $t = 0$. Assume the CB closes at $t = \frac{5T}{12}$ s, coinciding with the negative peak of phase C voltage. Fig. 6.2 illustrates the use of a gang-operated CB to prioritize closing at this negative peak. When the CB is closed, the gap voltage drops to zero (blue waveform), indicating that pole C is closed. Applying Kirchhoff's Voltage Law at this point, the new gap voltages for phases A and B are given by $v_{ga} = u_a - u_c = u_{ac}$ and $v_{gb} = u_b - u_c = u_{bc}$. Thus, immediately after closing pole C, the gap voltages of poles A and B change to the line voltages, causing an intersection between the *CBDS* curves and the gap voltages. In Fig. 6.2, the dotted red waveform demonstrates the voltage when an independent-pole-operated CB is used, while the blue waveform shows the voltage when a gang-operated CB is employed. As shown, closing the pole C leads to an immediate closure of all poles.

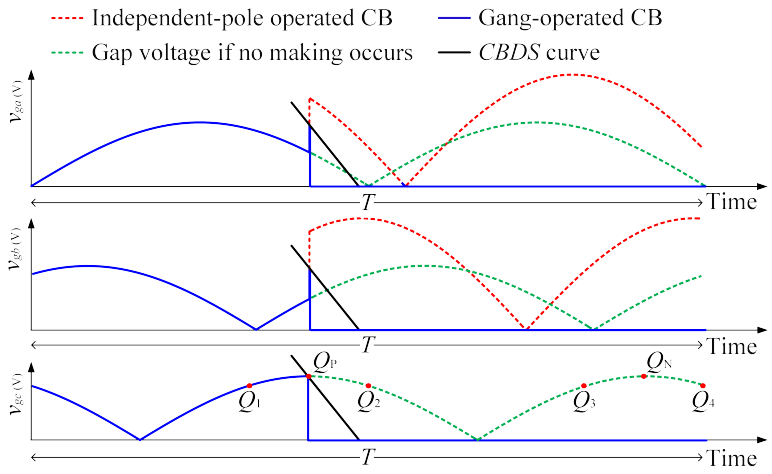

Figure 6.2: Gap voltages during making occurrence with a gang-operated CB.

Simultaneous making of all three poles occurs when making happens at any arbitrary point within the ranges between Q_1 and Q_2, and between Q_3 and Q_4, where the absolute value of pole C gap voltage exceeds the absolute value of the other two gap voltages. Similarly, simultaneous making for all three poles happens from making first on the gap voltages of phases A and B at specific time intervals. It means that in one complete

cycle, the phase with the highest absolute gap voltage at any given time is of primary importance. Thus, the effective voltage determining the energization instant of the V/V transformer using the gang-operated CB is a DC voltage, as shown in Fig. 6.3, which is named peak-value DC voltage. When making occurs, this applies u_{ac} and u_{bc} to the primary windings of the α-side and β-side transformers.

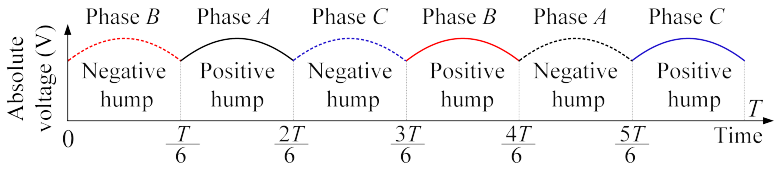

Figure 6.3: Peak-value DC voltage.

6.3 V/V Traction Transformer Inrush Current Mitigation Using Gang-Operated CB

As discussed in Section 1.2.3, effective elimination of inrush currents during transformer energization requires matching both the prospective and residual flux densities. While the residual flux density is constrained by the B-H curve of the transformer core, the prospective flux density limitation comes from the CB closing operation. In the following sections, we will explore strategies for mitigating inrush currents in V/V traction transformers under various conditions, including different CB types and transformer core designs, to identify the most effective approach.

6.3.1 Ideal Gang-Operated CB and $B_r^{max} = B^{max}$ (Ideal Case)

Let $u_a = V_m \sin(\omega t)$ denote phase A voltage. As illustrated in Fig. 1.5(b), if we consider the rising zero-crossing of the phase A voltage as the time reference, i.e., $t = 0$, the voltages applied to the primary windings of the α- and β-side transformers are u_{ac} and u_{bc}, respectively, lagging the phase A voltage by $-\frac{\pi}{6}$ radians and $-\frac{\pi}{2}$ radians. Assume the use of an ideal gang-operated CB (which conducts immediately upon receiving the closing signal) capable of ensuring simultaneous closure of all three phases of a V/V transformer at any desired making instant, i.e., t_m. As per (1.2), complete elimination of inrush current at any desired making instant t_m can be achieved by adjusting the

initial residual flux densities in the two single-phase transformers (i.e., B_r^{α} and B_r^{β}), considering that the flux density lags the voltage by 90°, as follows:

$$B_r^{\alpha} = B^{max} \sin\left(\omega t_m - \frac{2\pi}{3}\right) \tag{6.1a}$$

$$B_r^{\beta} = B^{max} \sin(\omega t_m - \pi) \tag{6.1b}$$

Therefore, assuming an ideal CB, the CB can be closed at any instant in time without observing any inrush current, provided that the residual flux densities in the two single-phase transformers is adjusted according to the above equations.

6.3.2 Non-Ideal Gang-Operated CB and $B_r^{max} = B^{max}$ (Quasi-Ideal Case)

Now, let us assume that the CB is not ideal and may have a timing error of ΔT (which is the maximum deviation as a result of both *RDDS* and mechanical scatter) during closing operation. In this case, while the initial residual flux densities in the single-phase transformers are adjusted according 6.1, making happens at time $t_m + \Delta T$. By formulating the flux equations for the single-phase transformers, the resulting DC flux, which is the DC component in (1.2), at making instant can be expressed as follows:

$$B_{\alpha}^{DC} = -B^{max} \sin\left(\omega(t_m + \Delta T) - \frac{2\pi}{3}\right) + B_r^{\alpha} \tag{6.2a}$$

$$B_{\beta}^{DC} = -B^{max} \sin(\omega(t_m + \Delta T) - \pi) + B_r^{\beta} \tag{6.2b}$$

Now, the question is: What is the optimal making instant to minimize the maximum possible values of B_{α}^{DC} and B_{β}^{DC}, even in the presence of a timing error ΔT. Since the primary objective is to prevent inrush current in both single-phase transformers, the optimization problem focuses on determining the optimal making instant such that:

$$\min_{t_m \in [0,T]} \max\left\{\left|B_{\alpha}^{DC}\right|, \left|B_{\beta}^{DC}\right|\right\} \tag{6.3}$$

In other words, this is a min-max optimization problem, where the objective is to determine making instant t_m within in the range $[0, T]$ such that the maximum DC flux in the two single-phase transformers is minimized, accounting for the CB's timing error ΔT. By solving this mathematical problem, the optimal switching time and the corresponding maximum flux after switching are found to be:

$$t_m^{op} = -\frac{\Delta T}{2} + \frac{4\pi}{3\omega} \tag{6.4}$$

$$\left|B_\alpha^{DC,max}\right| = \left|B_\beta^{DC,max}\right| = B^{max}\sin\left(\frac{\omega\Delta T}{2}\right) \tag{6.5}$$

Assuming the CB has an unbiased timing error, meaning ΔT could be either positive or negative with equal probability, the optimal switching time t_m^{op} is most likely to fall within the range $[-\frac{\Delta T}{2} + \frac{4\pi}{3\omega}, \frac{\Delta T}{2} + \frac{4\pi}{3\omega}]$. Therefore, the ideal switching time is $t_m^{op} = \frac{4\pi}{3\omega}$. Given this assumption, the optimal residual flux adjustment for the single-phase transformers in the V/V transformer, accounting for random CB timing errors (with no bias), would be:

$$\begin{aligned} B_r^{\alpha,op} &= B^{max}\sin\left(\omega\left(\frac{4\pi}{3\omega}\right) - \frac{2\pi}{3}\right) \\ &= \frac{\sqrt{3}}{2}B^{max} \end{aligned} \tag{6.6a}$$

$$\begin{aligned} B_r^{\beta,op} &= B^{max}\sin\left(\omega\left(\frac{4\pi}{3\omega}\right) - \pi\right) \\ &= \frac{\sqrt{3}}{2}B^{max} \end{aligned} \tag{6.6b}$$

6.3.3 Non-Ideal Gang-Operated CB and Limited B_r^{max} (Non-Ideal Case)

In the previous section, it was assumed that the residual flux could be adjusted to any desired value within the range $[-B^{max}, B^{max}]$. Under this condition, it was demonstrated that the optimal residual flux adjustment for the V/V transformer, considering circuit breaker timing error, would be $\frac{\sqrt{3}}{2}B^{max}$. However, in practical magnetic materials, due to hysteresis loop behavior, the residual flux in the magnetic core cannot be set to any arbitrary value. For example, in conventional magnetic materials, the maximum feasible residual flux density is typically 80% of the maximum flux density of the material, and this maximum residual flux may be lower for other materials. Assuming an ideal CB, in order to completely eliminate inrush current, it is necessary to select the making instant t_m within specific time intervals where the following conditions are met:

$$B_r^{max} \geq B^{max}\sin\left(\omega t_m - \frac{2\pi}{3}\right) \tag{6.7a}$$

$$B_r^{max} \geq B^{max}\sin(\omega t_m - \pi) \tag{6.7b}$$

Under these conditions, complete elimination of inrush current is feasible only within specific limited time intervals of t_m. Let us assume that $\kappa = \frac{B_r^{max}}{B^{max}}$. Fig. 6.4 shows the value of equation (6.7) for different making instants and various values of κ under the assumption of ideal switching (i.e., $\Delta T = 0$). As shown in the figure, as long as $\kappa \geq \frac{\sqrt{3}}{2}$, inrush current can be completely eliminated by appropriately adjusting the residual flux and switching at $\omega t_m = \frac{4\pi}{3}$. However, as κ decreases, inrush current can only be mitigated within time intervals around $\omega t_m = \frac{11\pi}{6}$. If $\kappa < 0.5$ (a situation that is unlikely in real ferromagnetic materials [36]), it will not be possible to eliminate inrush current entirely at any moment during switching in the V/V transformer.

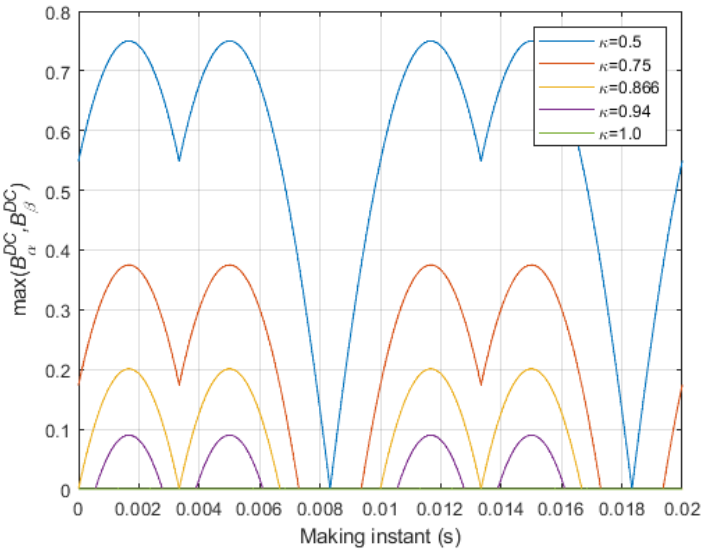

Figure 6.4: The value of $\max\left\{\left|B_\alpha^{DC}\right|, \left|B_\beta^{DC}\right|\right\}$.

If, as indicated in section 6.3.2, we assume that the CB has a timing error ΔT and conduct a similar analysis (assuming a normal random distribution), it is found that, given the constraint on the maximum residual flux, there are two candidate optimal switching times: $t_m = \frac{4\pi}{3\omega}$ and $t_m = \frac{11\pi}{6\omega}$. For each of these making instants, the optimal residual flux adjustment is as follows (assuming $\frac{1}{2} < \kappa \leq \frac{\sqrt{3}}{2}$):

$$\begin{aligned} B_r^{\alpha,op} &= B_r^{\beta,op} = B_r^{max} & \forall t_m^{op} &= \frac{4\pi}{3\omega} \\ B_r^{\alpha,op} &= -B_r^{\beta,op} = -\frac{1}{2}B_r^{max} & \forall t_m^{op} &= \frac{11\pi}{6\omega} \end{aligned} \tag{6.8}$$

In this case, by formulating the equations and assuming a CB with timing error of ΔT, equation (6.3) can be written:

$$\max\left\{\left|B_{\alpha}^{DC}\right|,\left|B_{\beta}^{DC}\right|\right\}_{t_m=\frac{4\pi}{3\omega}}=\begin{cases}B^{max}\sin(\omega\Delta T+\frac{\pi}{3})-B_r^{max} & \Delta T\leq\frac{1}{\omega}\cos^{-1}(\frac{2\kappa}{\sqrt{3}})\\ B_r^{max}-B^{max}\sin\left(\omega\Delta T+\frac{2\pi}{3}\right) & \text{Otherwise}\end{cases} \tag{6.9}$$

$$\max\left\{\left|B_{\alpha}^{DC}\right|,\left|B_{\beta}^{DC}\right|\right\}_{t_m=\frac{11\pi}{6\omega}}=\frac{B^{max}}{2}-B^{max}\sin\left(\omega\Delta T+\frac{5\pi}{6}\right) \tag{6.10}$$

Now, to determine the optimal making instant, we have:

$$t_m^{op}=\begin{cases}\frac{4\pi}{3\omega} & \frac{1}{\omega}\left[\cos^{-1}\left(\frac{0.5+\kappa}{\sqrt{2}}\right)-\frac{\pi}{12}\right]<\Delta T<\frac{1}{\omega}\left[\frac{3\pi}{4}-\sin^{-1}\left(\frac{\kappa-0.5}{2\sin(\frac{\pi}{12})}\right)\right]\\ \frac{11\pi}{6\omega} & \text{Otherwise}\end{cases} \tag{6.11}$$

As observed, the optimal making instant and consequently the optimal residual flux adjustment in the V/V transformer depend on both the adjustable residual flux and the circuit breaker timing error ΔT.

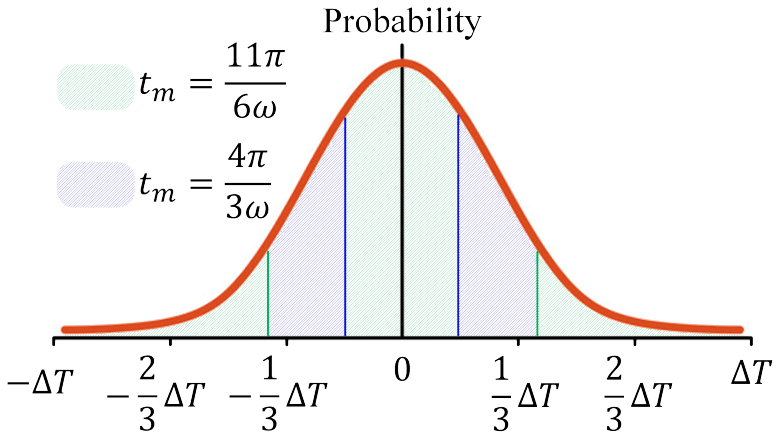

Figure 6.5: Corresponding ranges to each making instant on a normal distribution curve.

Now, let us assume that the probability distribution ΔT follows a normal distribution as shown in Fig. 6.5. The equation (6.11) represents a range within this probability distribution where it is preferable to close the CB at $t_m=\frac{4\pi}{3\omega}$. The remaining area indicates the advantage of switching at $t_m=\frac{11\pi}{6\omega}$. By calculating the area of each range, we can determine the probability of the advantage of switching at $t_m=\frac{4\pi}{3\omega}$ versus

$t_m = \frac{11\pi}{6\omega}$. Fig. 6.6 illustrates how, if the value of κ varies between 0.5 and 1, the probability of favoring each candidate switching time changes according to the CB's performance (σ is the standard deviation of the probability distribution).

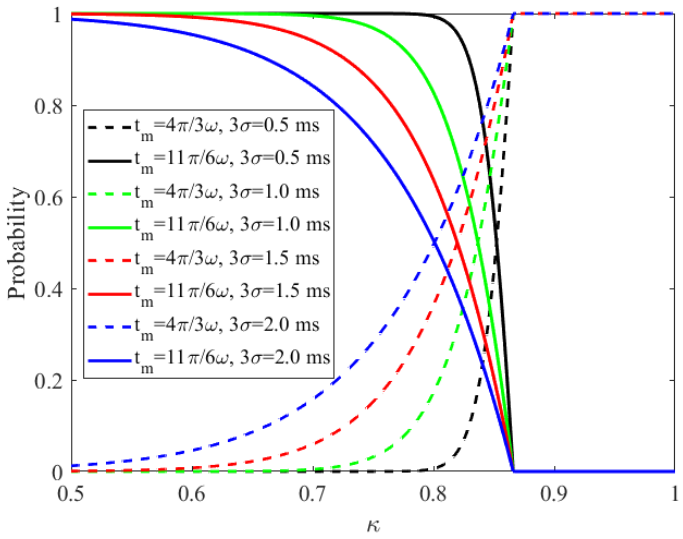

Figure 6.6: Probability of each making instant versus κ.

According to Fig. 6.6, the following conclusions can be drawn:

1. If $\kappa \geq \frac{\sqrt{3}}{2}$, making at $t_m = \frac{4\pi}{3\omega}$ clearly offers an advantage.
2. As σ decreases and $\kappa \leq \frac{\sqrt{3}}{2}$, the preference shifts towards making at $t_m = \frac{11\pi}{6\omega}$.
3. As σ increases, the point where the probabilities of favoring either making instant $t_m = \frac{4\pi}{3\omega}$ or $t_m = \frac{11\pi}{6\omega}$ are equal (with a probability of 0.5 for each) shifts towards values of κ smaller than $\frac{\sqrt{3}}{2}$.
4. For practical ranges of κ in modern CB, the point of equal probability for the two making instants falls within this range $0.8 < \kappa \leq \frac{\sqrt{3}}{2}$.

Based on these observations, a heuristic rule has been proposed for studies, suggesting that the optimal switching time can be approximated as the midpoint of the range under consideration.

$$t_m^{op} = \begin{cases} \frac{4\pi}{3\omega} & \kappa \geq 0.833 \\ \frac{11\pi}{6\omega} & \text{Otherwise} \end{cases} \tag{6.12}$$

6.4 Proposed Method

In this section, a flux matching method is proposed for V/V traction transformers that are energized using gang-operated CBs. This method determines the transformer's peak excitation current, measures the value of κ, and adjusts residual flux densities to the desired values all by injecting current into the transformer. The goal of flux adjustment is to modify the core's residual flux density from an unknown value B_r, to $-0.5B^{max}$ and $0.5B^{max}$ for the α-side and β-side transformers, or to $0.866B^{max}$ for both transformers. This section first introduces a simple yet effective method for estimating flux density during current injection and calculate the value of κ, followed by a discussion on how to control the amplitude of the injected current for proper flux adjustment. Finally, the optimal closing initiation instant, t_{in}, is determined based on the adjusted residual flux densities to minimize the difference between the residual and prospective flux densities.

6.4.1 Estimation of Transformer Flux Density

For accurate flux adjustment, it is essential to estimate the flux density in the core throughout current injection. The transformer's flux density may be obtained using equation (1.2), should the applied voltage, B_r, N, and A are all known. Through current injection into the secondary winding, the voltage induced on the primary winding is used to estimate the flux density, however, other variables still remain unknown. Hence, flux linkage is utilized to estimate flux density, as it solely requires the voltage induced on the primary winding and does not necessitate information about other variables. The process of flux density estimation using the flux linkage is explained only using the α-side transformer since the process is the same for both transformers.

Let us consider a scenario where a sinusoidal current, represented as $i_{inj}(t) = I_m \sin(2\pi f_r t)$, is injected into the secondary winding while the primary winding is left open-circuited. The periodic function $v_p(t)$, with a time period $T_r = \frac{1}{f_r}$, represents the real voltage induced on the primary winding of the α-side transformer. This voltage is measured using the voltage transducer installed on the primary winding, which introduces a DC offset to its output, resulting in $v_p(t) + c$. To accurately calculate the flux

linkage, this DC offset must be compensated. To achieve this, let us define functions $g(t)$ and $h(t)$ at time t as follows:

$$g(t) = \int_0^t [v_p(t)t + c]\mathrm{d}t + \int_{\frac{T_r}{2}}^t [v_p(t)t + c]\mathrm{d}t \tag{6.13}$$

$$h(t) = \int_0^t [v_p(t)t + c]\mathrm{d}t + \int_{T_r}^t [v_p(t)t + c]\mathrm{d}t \tag{6.14}$$

Solving (6.13) and (6.14) gives

$$g(t) = \int_0^t v_p(t)\mathrm{d}t + ct - \int_{\frac{T_r}{2}}^t v_p(t)\mathrm{d}t - ct + \frac{cT_r}{2} \tag{6.15}$$

$$h(t) = \int_0^t v_p(t)\mathrm{d}t + ct - \int_{T_r}^t v_p(t)\mathrm{d}t - ct + cT_r \tag{6.16}$$

For the periodic function v_p, we have the relationships $\int_0^t v_p(t)\mathrm{d}t = -\int_{\frac{T_r}{2}}^t v_p(t)\mathrm{d}t$ and $\int_0^t v_p(t)\mathrm{d}t = \int_{T_r}^t v_p(t)\mathrm{d}t$. As a result, equations (6.15) and (6.16) simplify to:

$$g(t) = 2\int_0^t v_p(t)\mathrm{d}t + \frac{cT_r}{2} \tag{6.17}$$

$$h(t) = cT_r \tag{6.18}$$

Now, one can obtain the flux linkage from

$$\lambda(t) = \frac{1}{2}\left[g(t) - \frac{1}{2}h(t)\right] \tag{6.19}$$

Equation (6.19) can be used after $t = T_r$, representing that one cycle of current injection needed for this calculation.

6.4.2 Residual Flux Measurement and Adjustment

For flux adjustment, the railway power conditioner is employed to inject current into the V/V transformer. The process begins by injecting current from the β-leg to the α-leg, causing current to flow through both the α-side and β-side transformers. The accuracy of flux adjustment depends on precise control of current amplitude and frequency, necessitating knowledge of the peak magnitude of the excitation current. However, this

information is typically absent from transformer nameplates and cannot be obtained from open- and short-circuit tests, which only provide the true root mean square (RMS) value of the excitation current. Hence, the proposed method initially needs to determine the value of the transformer excitation current, followed by adjusting the residual flux density.

Determining Excitation Current Magnitude

For newer transformers employing highly efficient designs, the excitation current may range from 0.1% to 1% of the nominal transformer current, whereas for older transformers, this value can increase to as high as 6% [27]. Without loss of generality, let us assume the β-side transformer with an initial residual flux density of $B_r = 0$. Fig. 6.7 shows how the proposed method determines the value of transformer excitation current of the β-side transformer by injecting sinusoidal current $i_{inj}(t) = I_m \sin(2\pi f_r t)$. Initially, the proposed method employs a low initial frequency (e.g., f_r is 1 Hz or 2 Hz) and starts injecting sinusoidal current with a magnitude equivalent to 0.1% of the transformer's nominal current, as shown in Fig. 6.7(a). During this injection, the voltage induced in the primary winding is measured to calculate flux linkage using equation (6.19). This current injection lasts for two cycles: the first cycle is necessary to measure the flux linkage using equation (6.19), shown by the dashed red waveform in Fig. 6.7(b), while after $t = T_r$, the second cycle is utilized to determine whether the peak value of the flux linkage can reach $\lambda^{max} = \frac{V_m}{\omega}$.

In cases where the flux linkage does not reach λ^{max}, the magnitude of the current increases in steps of 0.1% of the nominal current, lasting for two cycles at each step. This iterative procedure continues until the maximum measured value of the flux linkage surpasses λ^{max} and $-\lambda^{max}$, as shown in Fig. 6.7(b) at $t = \frac{29}{4}T_r$ and $t = \frac{31}{4}T_r$. This demonstrates that the injected current is close to the excitation current of the transformer. After $t = \frac{31}{4}T_r$, the flux linkage value can be used to estimate κ. At $t = 8T_r$, the injected current returns to zero, indicating that the flux crosses the B-axis on the B-H curve. Using this value at $t = 8T_r$, κ can be determined from the following equation:

$$\kappa = \frac{|\lambda(8T_r)|}{\lambda^{max}} \tag{6.20}$$

The value of κ determines which legs of the railway power conditioner should be

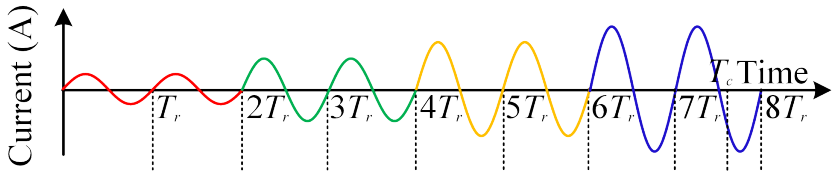

(a)

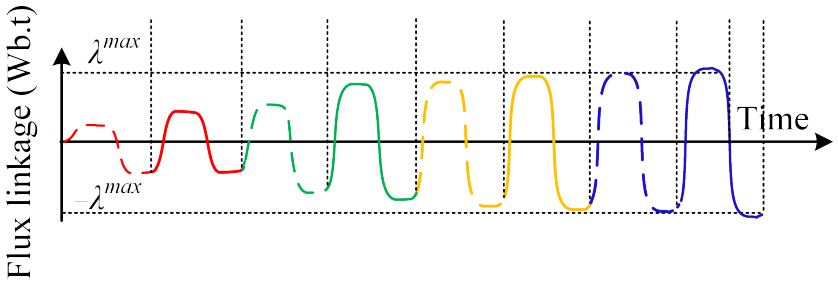

(b)

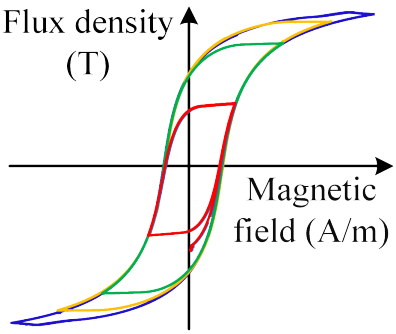

(c)

Figure 6.7: (a) Injected current, (b) flux density of the β-side transformer, and (c) B-H curve.

utilized for flux adjustment. According to equation (6.12), if κ is less than 0.833, current injection through the β-leg and α-leg continues to adjust the residual flux densities to $-0.5B^{max}$ and $0.5B^{max}$ for the α-side and β-side transformers. However, if κ exceeds 0.833, the α-side transformer is fluxed using the α-leg and R-leg, while the β-side transformer is fluxed using current injection from the β-leg to R-leg in order to adjust the residual flux densities to $0.866B^{max}$.

Fig. 6.7(c) shows the corresponding B-H curves for the current injection procedure.

The path from the initial residual flux to the smallest inner loop (depicted in red) represents the only part where the initial residual flux density affects magnetization. Afterward, the trajectory is only dictated by the B-H characteristics of the transformer. An increase in current magnitude leads to traversal of outer loops until, upon reaching the transformer excitation current value, the major B-H curve is traversed, as depicted by blue curve in Fig. 6.7(c).

At each step of current injection, the voltage induced on the primary winding is monitored to prevent transformer damage caused by induced voltage exceeding the transformer's nominal voltage. As explained in [98], control of the injected current frequency should be implemented to mitigate the risk of high-magnitude voltage. The current frequency remains constant, provided that the peak value of the induced voltage remains below the peak value of the transformer's nominal voltage. Otherwise, the frequency is reduced to prevent transformer damage during current injection.

The importance of obtaining the peak value of the excitation current is illustrated in Fig. 6.8. If residual flux exists in the transformer core before flux adjustment, the resulting B-H curve after current injection will resemble the one shown in Fig. 6.8(a). In this figure, the smallest hysteresis loop is asymmetrical with respect to the current axis. However, as the injected current magnitude increases, the larger hysteresis loops become symmetrical around the axis. When the current reaches the transformer's excitation current, the physical limitations of the core enforce symmetry in the loops. Fig. 6.8(b) shows the estimated B-H curve calculated using equation (6.19). Unlike Fig. 6.8(a), all the hysteresis loops in this figure are symmetrical with respect to the current axis, which is inaccurate. To prevent calculation errors when using equation (6.19) for flux estimation, it is crucial that the current first reaches the peak excitation value before adjusting its magnitude for flux control. This ensures that the flux follows a symmetrical loop during the injection, consistent with the core's physical constraints.

Adjusting Residual Flux Density

After determining the value of the excitation current and κ, the residual flux density is adjusted by controlling the current amplitude. This section focuses on the flux adjustment to $0.5B^{max}$, although the same procedure applies to other values. To achieve this, the current amplitude should be reduced after $t = 8T_r$. This step requires extra care because reducing the current can lead to traversing minor loops that are not symmetrical

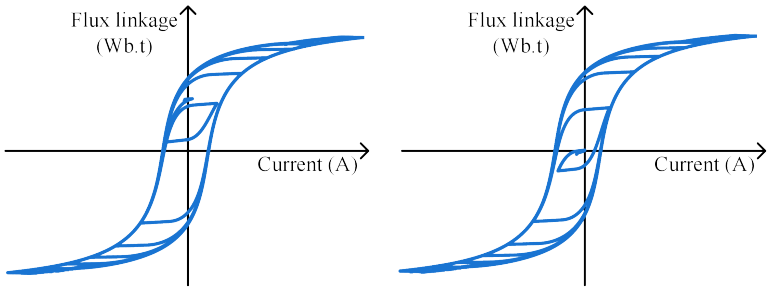

(a) (b)

Figure 6.8: (a) Real B-H curve, and (b) estimated B-H curve using equation (6.19).

with respect to the origin of the B-H curve. To establish the limit for current reduction, a sensitivity analysis is performed using the inverse JA model, considering different cores for cases in which the current decreases from the transformer's excitation current after $t = 8T_r$. As shown in Fig. 6.9, current reduction can result in three different scenarios:

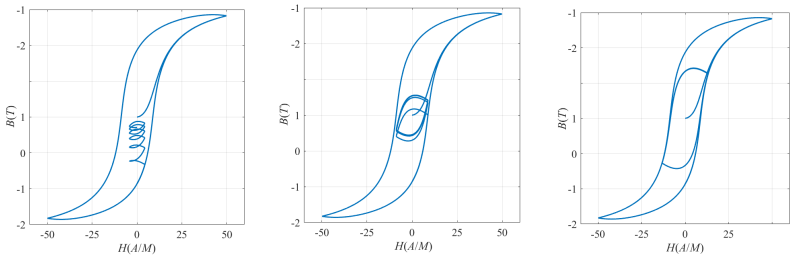

(a) (b) (c)

Figure 6.9: B-H curve when current is reduced (a) below I_c, (b) to I_c, and (c) to $1.5I_c$ or higher.

1. The flux density will traverse asymmetrical minor loops, as shown in Fig. 6.9(a), if the magnetic field strength reduces below H_c. This scenario requires more than two cycles of current injection after $t = 8T_r$ to reach a symmetrical minor loop.

2. If the magnetic field strength reduces to H_c, the flux density will traverse only one asymmetrical minor loop, and after one cycle of current injection, the flux density will reach symmetrical minor loops, as shown in Fig. 6.9(b).

3. As shown in Fig. 6.9(c), if the magnetic field strength is reduced to $1.5H_c$ or higher, the flux density will traverse only symmetrical minor loops.

Based on the results of this analysis, it is recommended to avoid reducing the magnetic field strength below H_c and to always maintain the magnitude at or above H_c. This ensures that when flux linkage is estimated using equation (6.19)—which occurs after the first cycle following a change in current amplitude—the flux density will traverse a symmetrical minor loop, regardless of changes in current amplitude. Let I_c denote the current corresponding to H_c, calculated by $I_c = |i_{inj}(T_c)|$. As shown in Fig. 6.7(b), T_c is the instant when the flux linkage first reaches zero after exceeding λ^{max}. To avoid traversing asymmetrical minor loops during flux adjustment, the current amplitude should not reduce below I_c.

Fig. 6.10 explains the flux adjustment procedure of the proposed method to adjust the residual flux density to $\pm 0.5B^{max}$. The injected current waveform is shown in Fig. 6.10(a). After $t = 8T_r$, the current amplitude is reduced by 50%. This reduction should not cause the current amplitude to fall below I_c; otherwise, the current magnitude is considered equal to I_c. The current injection continues for two cycles. The first cycle, represented by the dashed red waveform in Fig. 6.10(b), is necessary to apply equation (6.19), while the second cycle, shown by the solid red waveform, measures the flux density. If the measured flux linkage at $t = 9.5T_r$ falls within the range $[0.45\lambda^{max}, 0.55\lambda^{max}]$, the current injection is stopped.

However, as shown in Fig. 6.10(b), $\lambda(9.5T_r)$ exceeds $0.55\lambda^{max}$, necessitating a further reduction in current amplitude. The reduction amount is halved from the previous adjustment. For instance, if the previous reduction was 1 A, the current now decreases by 0.5 A. It is important to note that the current must remain above I_c; if it drops below I_c, it should be adjusted accordingly. At $t = 11.5T_r$, the flux linkage falls within the desired range of $[0.45\lambda^{max}, 0.55\lambda^{max}]$, allowing the current injection to stop. If the flux linkage had fallen below $0.45\lambda^{max}$ at $t = 11.5T_r$, the current would have been increased by half the previous reduction—adding 0.25 A to the current. Conversely, if the flux linkage had exceeded $0.55\lambda^{max}$, the current would have been reduced by 0.25 A, with the injection continuing for additional cycles. This iterative process repeats until the flux linkage consistently remains within the range of $[0.45\lambda^{max}, 0.55\lambda^{max}]$.

The procedure for adjusting residual flux density to values greater than $0.833B^{max}$ is simpler than adjusting it to $\pm 0.5B^{max}$. When residual flux needs to exceed $0.833B^{max}$, the current injection continues at full magnitude for an additional half-cycle after $t = 8T_r$. The reason is that injecting current equal to the transformer's peak excitation current

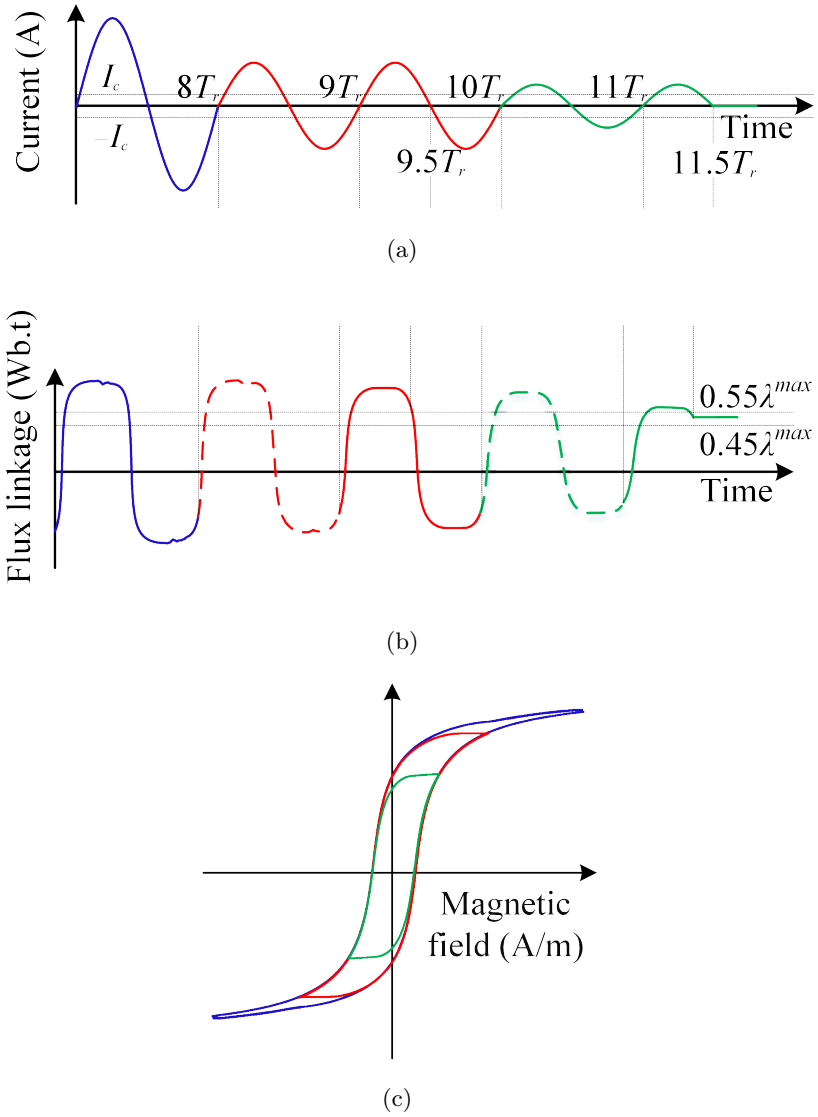

Figure 6.10: (a) Injected current, (b) flux density of β-side transformer, and (c) B-H curve.

adjusts the residual flux density to B_r^{max}. As mentioned earlier, the ratio of B_r^{max} to B^{max} does not exceed 0.9 [36], thus continuing current injection for half a cycle brings the residual flux density within the acceptable range of $[0.833B^{max}, 0.9B^{max}]$. This range is suitable for targeting a prospective flux density of $0.866B^{max}$. An important point to mention is that, compared to adjusting the residual flux density to $\pm 0.5B^{max}$, the current direction in the β-side transformer remains unchanged, while it is reversed for

the α-side transformer. This is accomplished by utilizing the α- and R-legs to flux the α-side transformer, and the β- and R-legs to flux the β-side transformer.

6.4.3 Transformer Controlled Energization

The next step after adjusting the flux density to the appropriate value is to energize the transformer. Let us assume that the rising zero-crossing of phase A voltage denoted by $v_a(t) = V_m \sin(2\pi f t)$ is considered as the time reference. As discussed in the previous sections, there are two potential instants for switching: $t_m = \frac{4\pi}{3\omega}$ and $t_m = \frac{11\pi}{6\omega}$, corresponding to gap voltages of V_m and $0.866V_m$. To determine the closing initiation instant, t_{in}, it is first necessary to calculate the contact touch instant , i.e., t_{ct}. At $t = t_{ct}$, the gap voltage is zero. By formulating the line equation and using s^{mean} as the slope of this equation, the contact touch instant can be calculated as follows:

$$t_{ct} = t_m + \frac{V_0}{s^{mean}} \tag{6.21}$$

where V_0 is either V_m or $0.866V_m$, depending on the value of t_m. Once t_{ct} is calculated, the closing initiation instant can be determined as $t_{in} = t_{ct} - T_{CB}$.

6.5 Simulation-Based Performance Evaluation

To assess the effectiveness of the proposed method, the traction power supply system connected to a 220-kV, 50-Hz power network (depicted in Fig. 6.1) is simulated using PSCAD/EMTDC. The V/V transformer and the railway power conditioner connected to the transformer are identical to those used in Chapter 5 for evaluating the energization of V/V traction transformers. However, in this case, a *Type* 3 transformer is used alongside a *Type* 1 transformer, instead of a *Type* 2. In the following sections, the flux adjustment procedure described in section 6.4.2 is first implemented in PSCAD to adjust the residual flux of the V/V transformer. This is followed by an analysis of the proposed method's effectiveness in achieving precise making at $t_m = \frac{4\pi}{3\omega}$ and $t_m = \frac{11\pi}{6\omega}$. A comparative evaluation is then conducted between the proposed method and the one introduced in Chapter 5 for V/V traction transformers energized using an independent-pole-operated CB.

6.5.1 Flux Adjustment

In this section, the performance of the proposed method for determining the transformer's peak excitation current and adjusting its residual flux density is evaluated. Two transformers are considered for this evaluation: the *Type* 1 and *Type* 3 transformers, as described in section 2.4.1. To clarify the process, the two stages—obtaining the peak excitation current and adjusting the residual flux density— are presented separately. For these stages, the positive direction for current injection is from the β-side transformer to the α-side transformer. Only the flux linkage of the β-side transformer is presented here, as the α-side transformer follows the same pattern, either with identical or reversed polarity.

The procedure for finding the *Type* 1 transformer's peak excitation current is illustrated in Fig. 6.11. The current injection starts at 0.909 A (0.1% of transformer's nominal current), increasing by 0.909 A in each step. After four steps, the current reaches 3.616 A. At this value, during the second cycle, i.e., from $t = 7$ s to $t = 8$ s, the positive and negative peaks of the flux linkage exceed λ^{max} and $-\lambda^{max}$, respectively. This indicates that the peak excitation current is approximately 3.616 A. In reality, the peak excitation current of the *Type* 1 transformer's secondary winding is 3.2 A, demonstrating that the proposed method estimates the transformer's peak excitation current with acceptable accuracy.

Using the calculated flux linkage, the value of κ, which represents the ratio of B_r^{max} to B^{max}, can be determined. At $t = 8$ s, the flux linkage is -587 Wb.t, while λ^{max} is 990.348 Wb.t. Applying equation (6.20), κ is calculated to be 0.5929, which closely approximates the actual value of κ, which is 0.6. This demonstrates that the proposed method can estimate κ with acceptable accuracy. Additionally, the calculated value of I_c by using the flux linkage is 0.36 A. Fig. 6.11(c) shows the actual flux density during current injection. The figure presents three different cases with $B_r = -0.7$ T, $B_r = 0$, and $B_r = 0.7$ T. As illustrated, the initial value of B_r does not affect the method's performance, and after the first cycle of current injection, the flux path becomes independent of the initial B_r value.

After determining the peak value of the transformer's excitation current, the residual flux can now be adjusted. Since $\kappa < 0.833$, the residual flux densities are set to $-0.5B^{max}$ and $0.5B^{max}$ for the α-side and β-side transformers, respectively. To achieve this, the current injection from the β-side to the α-side transformer is maintained. Fig. 6.12

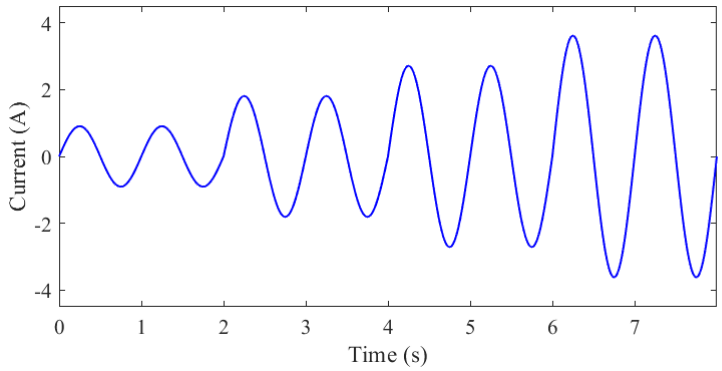

(a)

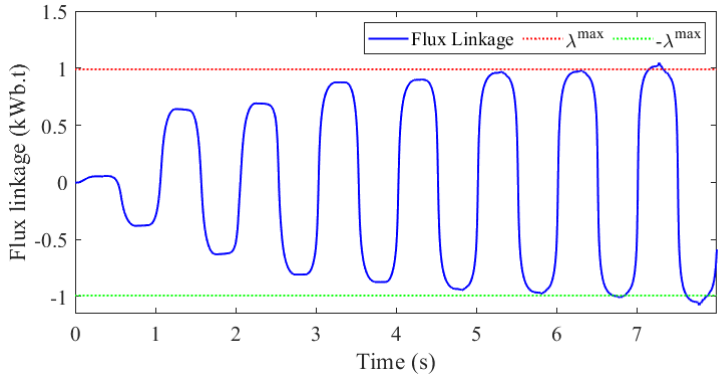

(b)

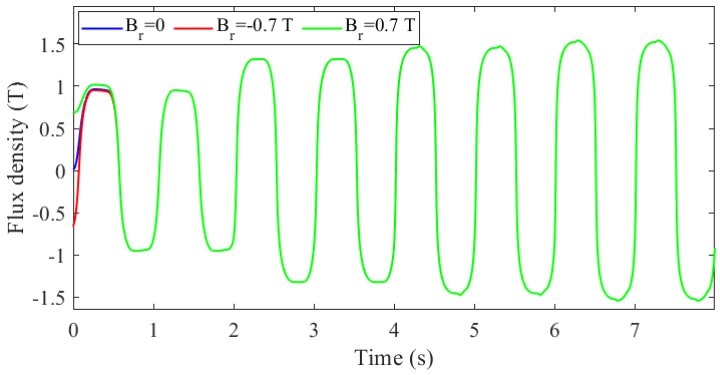

(c)

Figure 6.11: (a) Injected current, (b) flux linkage of the β-side transformer calculated by equation (6.19), and (c) flux density of the β-side transformer.

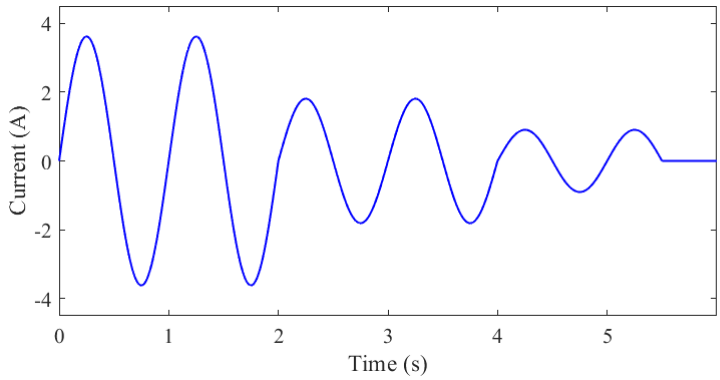

(a)

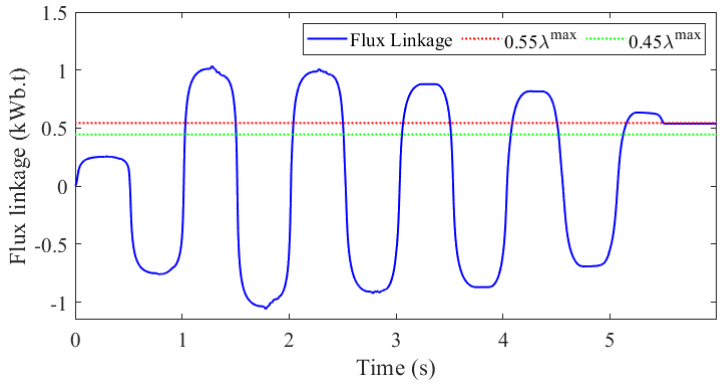

(b)

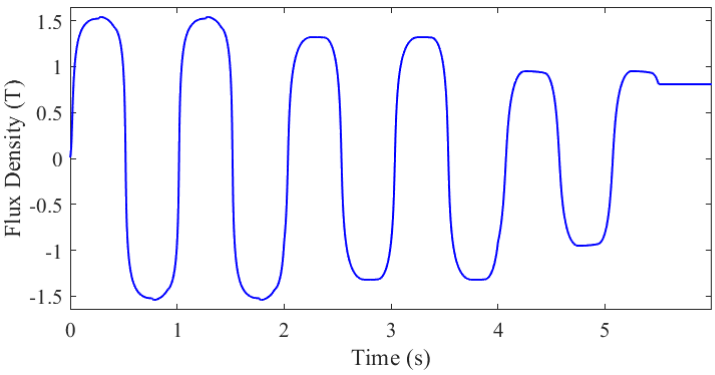

(c)

Figure 6.12: (a) Injected current, (b) flux linkage of the β-side transformer calculated by equation (6.19), and (c) actual flux density.

illustrates the flux adjustment process. In this figure, the current injection sequence from $t = 0$ to $t = 2$ s depicts the final step of the previous stage, where the peak excitation current was determined. At $t = 2$ s, as shown in Fig. 6.12(a), the current magnitude is reduced by 50%, lowering it's magnitude to 1.808 A. The current injection continues for two more cycles. At $t = 3.5$ s, as depicted in Fig. 6.12(b), the flux linkage is checked and found to be above the upper bound of the range $[0.45B^{max}, 0.55B^{max}]$. As a result, the current magnitude is reduced again by 0.909 A (50% of the previous reduction). Current injection continues with magnitude of 0.909 A after $t = 4$ s. At $t = 5.5$ s, when the current reaches zero, the flux adjustment falls within the range $[0.45\lambda^{max}, 0.55\lambda^{max}]$, thus the current injection is stopped. Fig. 6.12(c) shows the actual flux density of the β-side transformer, confirming that the flux has been successfully adjusted to 0.8 T (53.33% of B^{max}), demonstrating the accuracy of the flux adjustment process.

The performance of the proposed method for determining the peak excitation current and adjusting the residual flux density for making at $t_m = \frac{4\pi}{3\omega}$ using the *Type* 3 transformer is illustrated in Figs. 6.13 and 6.14. Similar to the procedure used for the *Type* 1 transformer, the current injection begins with a magnitude of 0.909 A, as shown in Fig. 6.13(a). After three increments in current, when it reaches 2.712 A, the positive and negative peaks of the flux linkage surpass λ^{max} and $-\lambda^{max}$, respectively, as illustrated by the flux linkage of the β-side transformer in Fig. 6.13(b). This indicates that the peak excitation current has been approximately determined. The actual peak excitation current of this transformer, when energized from its secondary winding, is 2.536 A, confirming the accuracy of the proposed method in estimating the peak excitation current. Based on the calculated flux linkage, the value of κ is 0.84, which closely matches the actual value of 0.853. Additionally, the value of I_c is found to be 0.77 A. Fig. 6.13(c) presents the actual flux density for the β-side transformer, showing a flux density of 1.5 T, which confirms that the transformer is approaching normal operating conditions when current reaches 2.712 A.

The flux adjustment procedure for the *Type* 3 transformer is illustrated in Fig. 6.14. Since $\kappa > 0.833$, after determining the peak excitation current, the current injection at a magnitude of 2.712 A continues for an additional half-cycle, as shown in Fig. 6.14(a). This results in a flux linkage of 831.89 Wb.t after the adjustment. Fig. 6.14(c) presents the actual flux density, demonstrating that the flux has been successfully adjusted to a value of 1.2822 T, which is close to 1.299 T (approximately 86.66% of B^{max}).

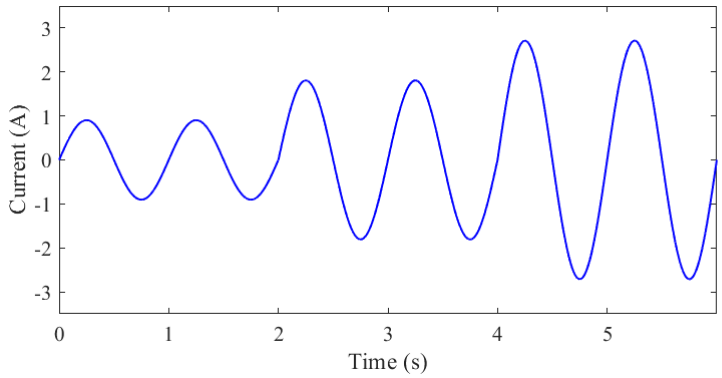

(a)

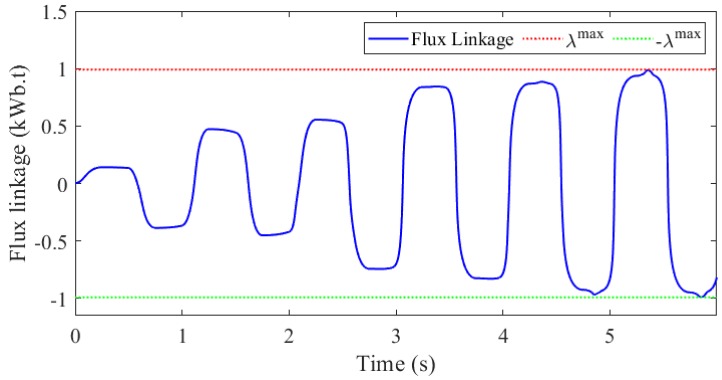

(b)

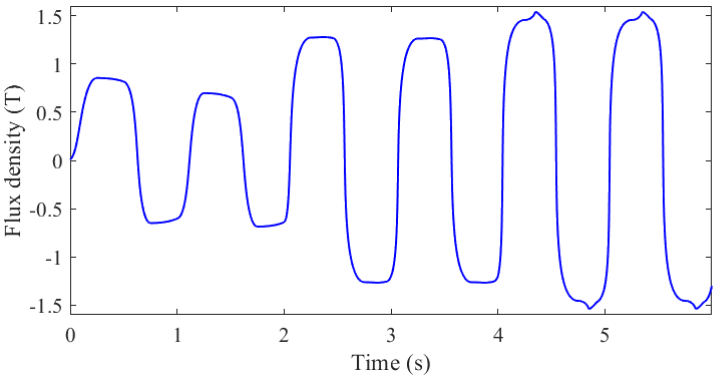

(c)

Figure 6.13: (a) Injected current, (b) flux linkage of the β-side transformer calculated by equation (6.19), and (c) flux density.

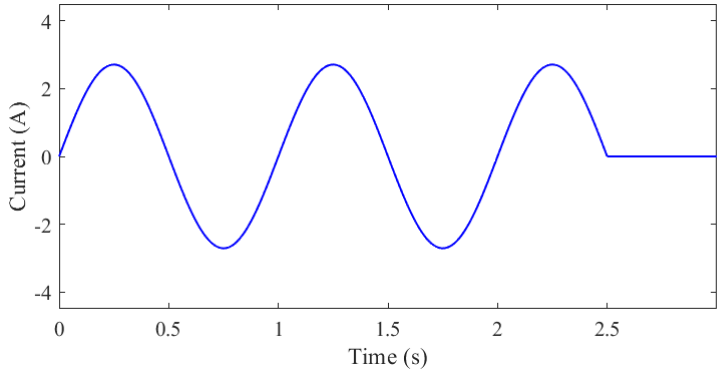

(a)

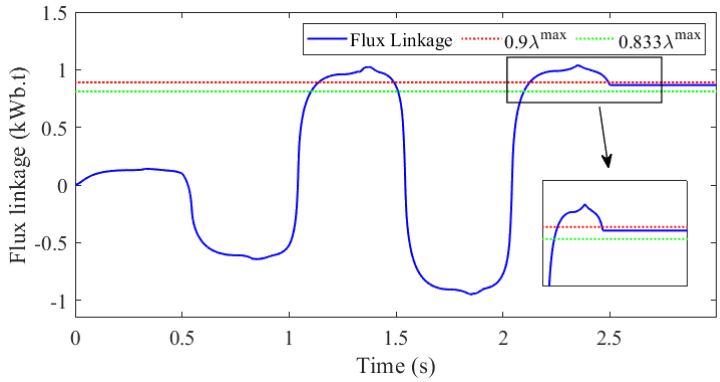

(b)

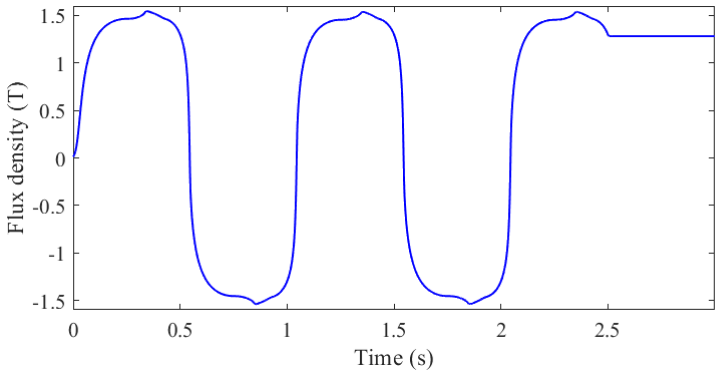

(c)

Figure 6.14: (a) Injected current, (b) flux linkage of the β-side transformer calculated by equation (6.19), and (c) flux density.

6.5.2 Proposed Method General Evaluation

In this section, the overall performance of the proposed method is assessed. A gang-operated CB with an *RDDS* of 50 kV/ms and a closing time of 40 ms is used. The *RDDS* scatter and mechanical scatter of the CB are 10% and ±1 ms, respectively. Fig. 6.15 illustrates the distribution of making instants for $t_m = \frac{4\pi}{3\omega}$ and $t_m = \frac{11\pi}{6\omega}$. Similar to the making instant distributions for single-phase and V/V transformers discussed in previous chapters, the probability of making at the upper and lower bounds (i.e., yellow and purple lines) of the making interval is zero. As the making instant approaches the target value (indicated by red lines), the probability of occurrence increases.

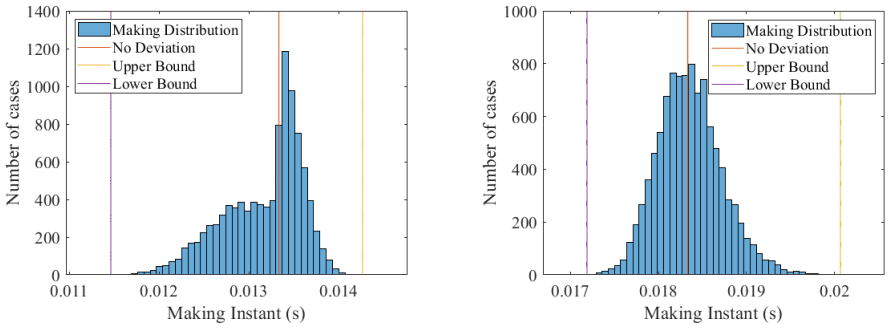

Figure 6.15: Making instant distribution for (a) $t_m = \frac{4\pi}{3\omega}$, and (b) $t_m = \frac{11\pi}{6\omega}$.

An important observation in Figs. 6.15(a) and 6.15(b) is that the time difference between the lower and upper bounds of the making interval is smaller for $t_m = \frac{4\pi}{3\omega}$ (2.8 ms) compared to 2.875 ms for $t_m = \frac{11\pi}{6\omega}$. This was previously demonstrated through the mathematical evaluation in section 6.3. Therefore, if the B-H curve of the transformer allows the residual flux to be adjusted to $0.833B^{max}$ or above, targeting $t_m = \frac{4\pi}{3\omega}$ results in less deviation from the desired making instant.

Fig. 6.15 highlights another key difference between the making instant distributions of $t_m = \frac{4\pi}{3\omega}$ and $t_m = \frac{11\pi}{6\omega}$. Unlike the distribution for $t_m = \frac{11\pi}{6\omega}$, which resembles a normal distribution curve (as seen in Fig. 6.15(b)), the distribution for $t_m = \frac{4\pi}{3\omega}$ does not follow this pattern, as shown in Fig. 6.15(a). The primary reason for this discrepancy is illustrated in Fig. 6.3. For $t_m = \frac{11\pi}{6\omega}$, the making occurs exclusively on the phase C voltage curve, whereas for $t_m = \frac{4\pi}{3\omega}$, it can occur on both phase A and B curves. Since the rising half of phase A and the falling half of phase B are involved, the scatter impacts

them differently, leading to asymmetry in the distribution.

6.5.3 Comparing Proposed Method's Performance with the Method Presented in Chapter 5

In this section, the performance of the proposed method is evaluated by comparing it to the method introduced for the V/V transformer in Chapter 5. For this comparison, both a gang-operated CB and an independent-pole-operated CB are evaluated, with their closing time, *RDDS*, and *RDDS* and mechanical scatter identical to those described in section 6.5.2. To assess energization at $t_m = \frac{4\pi}{3\omega}$, the *Type* 3 transformer is used, as its ratio of B_r^{max}/B_r^{max} equals 0.853. Additionally, the *Type* 1 transformer is employed for evaluating energization at $t_m = \frac{11\pi}{6\omega}$.

Figs. 6.16 and 6.17 show the three-phase currents drawn by the *Type* 1 and *Type* 3 V/V transformers when energized with both a gang-operated CB and an independent-pole-operated CB. As shown, both methods successfully limit the current magnitude to a value below or equal to the transformer's nominal current. While the method utilizing the independent-pole-operated CB shows better performance, it is important to note that the proposed method employs a gang-operated CB, which has fewer degrees of control. Given this limitation, the proposed method's performance is still acceptable, closely approaching the results of the method in Chapter 5 and effectively keeping the current within the transformer's nominal range.

6.6 Experimental Validation and Performance Analysis

To validate the effectiveness of the proposed method, comprehensive testing is conducted on a laboratory-scale V/V transformer using the test rig illustrated in Fig. 5.9, which was also utilized in the previous chapter. The key difference in this setup is the control of the instantaneous turn-on solid-state relays, designed to replicate the behavior of a gang-operated circuit breaker to connect the laboratory-scale V/V transformer to a 220-V, 50-Hz power system. This section begins by discussing how the proposed method determines the peak value of the transformer's excitation current, followed by a detailed explanation of the flux adjustment process. Finally, the transformer's energization after flux adjustment is examined.

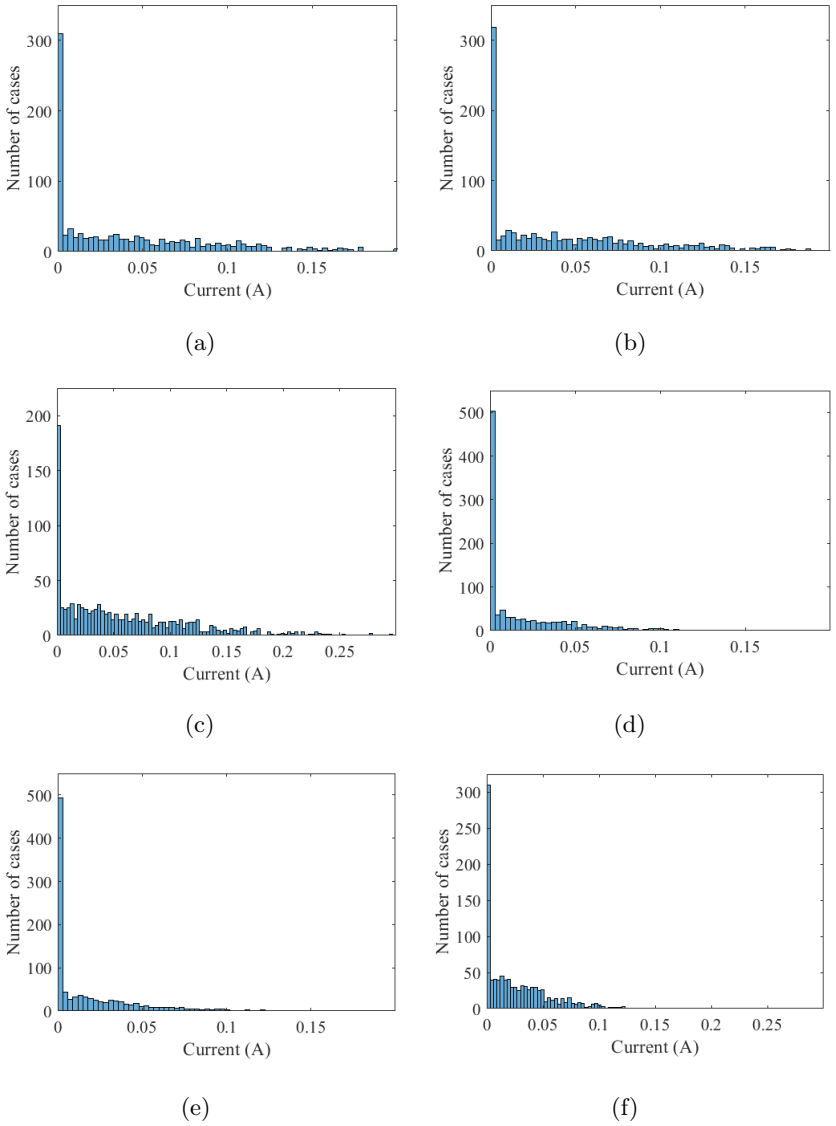

Figure 6.16: Current of phases (a) A, (b) B, and (c) C of the *Type* 1 V/V transformer energized with the proposed method, and phases (d) A, (e) B, and (f) C of the *Type* 1 V/V transformer energized with the method presented in Chapter 5.

6.6.1 Excitation Current Peak Value Determination

The V/V transformer is composed of two 400-VA, 220 V/120 V single-phase transformers, with an excitation current that is 10.62% of the peak value of the nominal transformer current. These single-phase transformers are laboratory-scale transformers

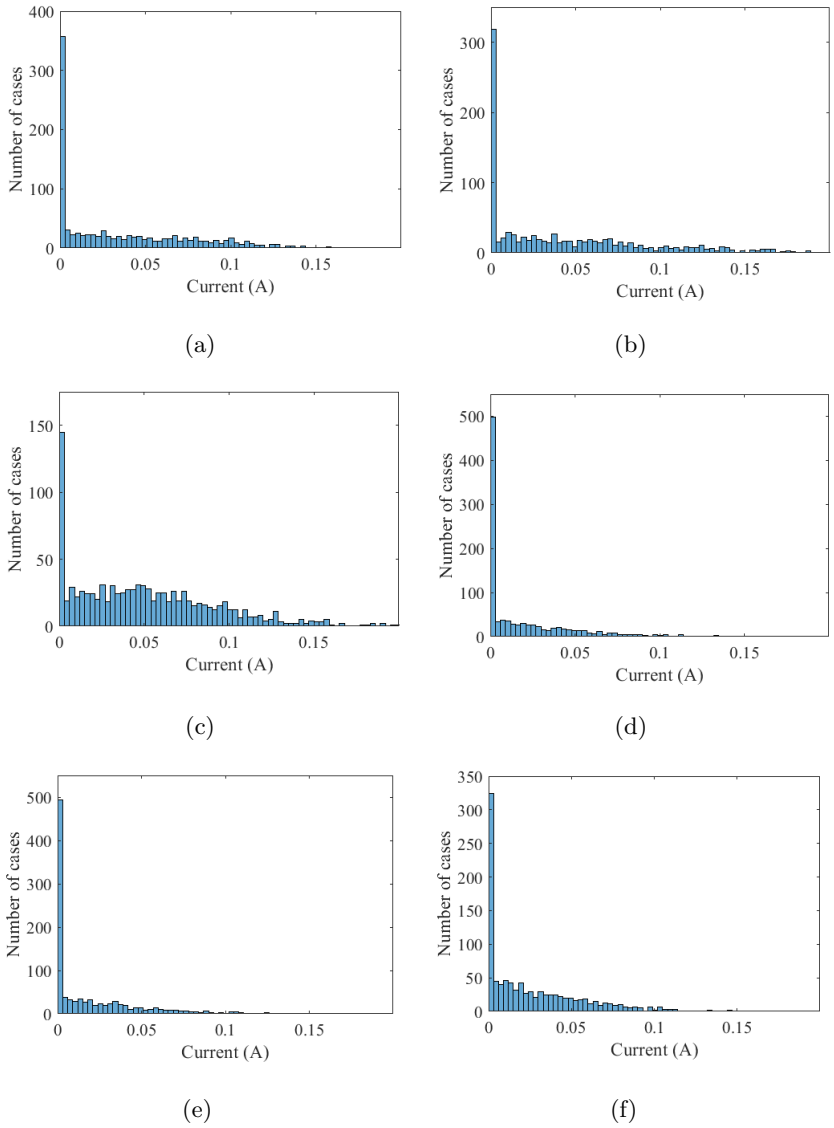

Figure 6.17: Current of phases (a) A, (b) B, and (c) C of the *Type* 3 V/V transformer energized with the proposed method, and phases (d) A, (e) B, and (f) C of the *Type* 3 V/V transformer energized with the method presented in Chapter 5.

with much lower capacity and higher excitation current compared to those typically used in TPSS installations. This explains why their excitation current exceeds 6% of the nominal current, resulting in a longer time to reach the peak value of the excitation current compared to standard traction transformers.

Fig. 6.18 illustrates the process of obtaining the peak excitation current. As shown

in Fig. 6.18(a), a sinusoidal current with a frequency of $f_r = 1$ Hz is injected into the V/V transformer, where the positive direction is considered from the β-side transformer to the α-side transformer. This means this current exactly follows through the β-side transformer, and with the reversed polarity, flows through the α-side transformer. At the start of the injection, the peak current is 4.67 mA (or 0.1% of the transformer's nominal current), with each subsequent step increasing the current by 4.67 mA. Each step lasts for two full cycles, equivalent to two seconds.

Fig. 6.18(b) shows the flux linkage of the β-side transformer (the α-side transformer exhibits the same flux linkage but with reversed polarity) calculated using equation (6.19). As the current magnitude increases, the flux linkage rises correspondingly. In the figure, the red and green dashed lines represent $\pm\lambda^{max}$, where $\lambda^{max} = \frac{220\sqrt{2}}{2\pi\times50} = 0.9903$ Wb.t. At $t = 190.353$ s and $t = 190.758$ s, when the current reaches peak values of 0.4541 A and -0.4541 A, the positive and negative peaks of the flux linkage exceed λ^{max} and $-\lambda^{max}$, respectively. This occurs during the second cycle of current injection, when the current magnitude reaches 0.4541 A, confirming the accuracy of flux estimation via equation (6.19). Once this threshold is reached, no further increase in current magnitude is necessary. It is also important to note that the current frequency, f_r, is maintained at 1 Hz throughout the injection process since this frequency induces voltage on the primary winding which does not exceed the transformer's nominal voltage.

Fig. 6.18(c) illustrates the *B-H* curve plotted using the estimated flux linkage from equation (6.19) and the current injected into the transformer. To better illustrate how the current injection leads to traversing larger minor loops and eventually reaching the major loop, some hysteresis loops are intentionally omitted. An important point to note is that the *B-H* curve starts at the origin, as the results from equation (6.19) are always symmetrical with respect to the x-axis (current axis). Consequently, this curve does not reflect the initial residual flux density. This explains why the injected current continues to increase until it reaches the limits of $\pm\lambda^{max}$— at which point the physical constraints of the transformer core cause the flux density to become symmetrical around the x-axis. At this stage, we can be confident that the flux estimation using equation (6.19) is accurate.

As illustrated in Fig. 6.18, the proposed method successfully determines the peak value of the transformer's excitation current. For the transformer used to validate this method, being a small-scale transformer, its excitation current is higher than that of typ-

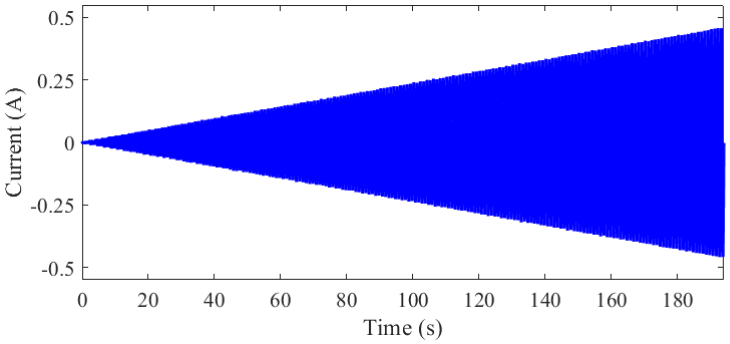

(a)

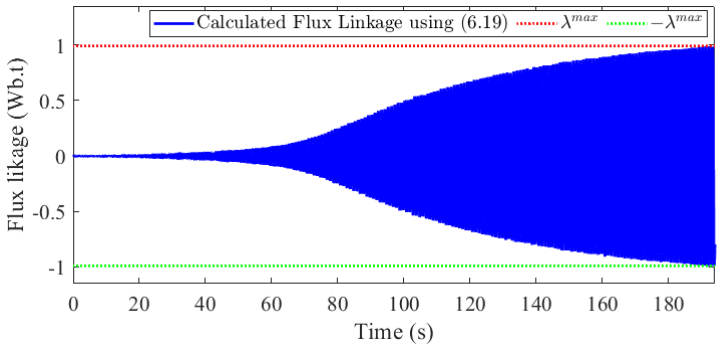

(b)

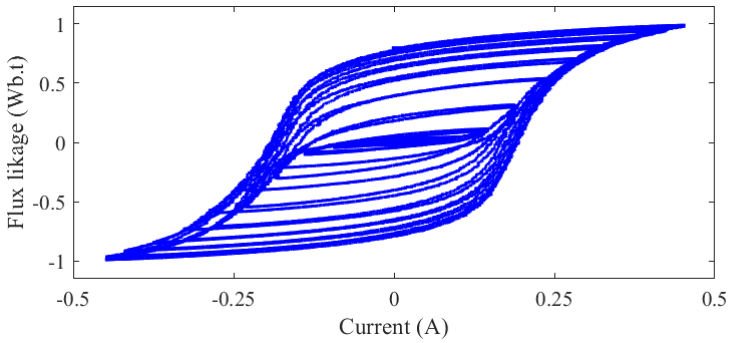

(c)

Figure 6.18: (a) Injected current, (b) flux linkage of the β-side transformer calculated by equation (6.19), and (c) the corresponding B-H curve .

ical traction transformers installed in TPSSs, where excitation current typically ranges from 0.1% to 1% of the transformer's nominal current. For these traction transformers, only a few cycles of current injection are sufficient to reach the peak excitation current.

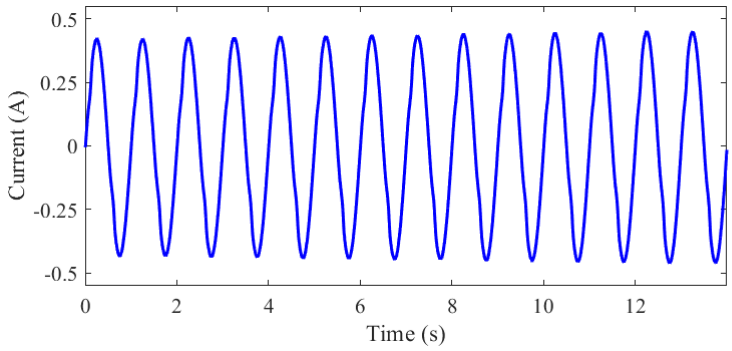

(a)

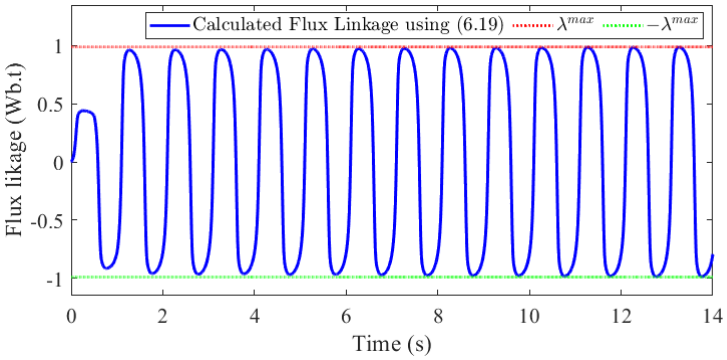

(b)

Figure 6.19: (a) Injected current, and (b) flux linkage of the β-side transformer obtained by equation (6.19).

To evaluate the performance of the proposed method for traction transformers, a current injection is applied, which is shown in Fig. 6.19(a); however, the initial current magnitude is not set at 0.1% of the transformer's nominal current. Instead, the injection begins with a peak value of 0.4261 A (i.e., approximately 9% of the transformer nominal current), and, similar to the previous scenario, the current increases by 4.67 mA per step. As shown in Fig. 6.19(b), after 14 cycles of current injection, when the current magnitude reaches 0.4541 A, the flux linkage peaks—both positive and negative—exceeds λ^{max} and $-\lambda^{max}$ during the second cycle of current injection at $t = 13.25$ s and $t = 13.75$ s, respectively. This indicates that the injected current magnitude closely matches the transformer's peak excitation current, making further increases unnecessary. Additionally, after $t = 13.25$ s, once the flux linkage surpasses λ^{max}, the value of I_c can be determined at $t = 13.5935$ s, where the flux linkage returns to zero. Using this method,

I_c is calculated to be 0.1825 A.

After determining the peak value of the transformer's excitation current, the flux linkage, calculated using equation (6.19), can be used to compute κ via equation (6.20). At $t = 194$ s and $t = 14$ s for the scenarios shown in Figs. 6.18 and 6.19, which correspond to $t = 8T_r$ in Fig. 6.7, the current returns to zero. The corresponding flux linkage is -0.7923 Wb.t, yielding a κ value of 0.8 using equation (6.20). The true κ for this transformer is 0.783, demonstrating that the proposed method estimates κ with acceptable accuracy.

6.6.2 Flux Adjustment

The flux adjustment process, which occurs after determining the peak excitation current, is depicted in Fig. 6.20. For clarity, this figure separates the flux adjustment procedure from the process of obtaining the peak excitation current, assuming the peak value has already been reached. According to equation (6.12), since the value of κ is less than 0.833, the residual flux density in both single-phase transformers is adjusted to $\pm 0.5B_{max}$. To achieve this, the same direction of current injection—from the β-side transformer to the α-side transformer—used to obtain the peak excitation current, is maintained.

In Fig. 6.20(a), the first two cycles of current correspond to the stage where the peak excitation current is obtained. As shown in Fig. 6.20(b), which illustrates the flux linkage of the β-side transformer, during the second cycle between $t = 1$ s and $t = 2$ s, when the current reaches 0.4145 A, both the positive and negative flux linkage values exceed λ^{max} and $-\lambda^{max}$, respectively. After $t = 2$ s, the current magnitude is adjusted for flux adjustment. Initially, the current is reduced by 50%, bringing it to 0.2271 A, and the injection continues for two cycles. Since $0.2271 > I_c$, the current remains at this level. At the zero-crossing point of the second cycle (when the current changes direction at $t = 3.5$ s), the flux linkage falls outside the range of $[0.45\lambda^{max}, 0.55\lambda^{max}]$. Consequently, after $t = 4$ s, the current is modified by half of the previous adjustment (0.1135 A). Since the flux linkage at $t = 3.5$ s is below the lower bound of the target range, 0.1135 A is added to the current, increasing it to 0.3406 A.

The current injection continues for two cycles at a magnitude of 0.3406 A, lasting from $t = 4$ s to $t = 6$ s. At $t = 5.5$ s, the flux linkage exceeds the upper limit of the target range, $[0.45\lambda^{max}, 0.55\lambda^{max}]$, indicating that the injection should continue but with a reduced current. From $t = 6$ s to $t = 8$ s, the current is decreased by 0.0568

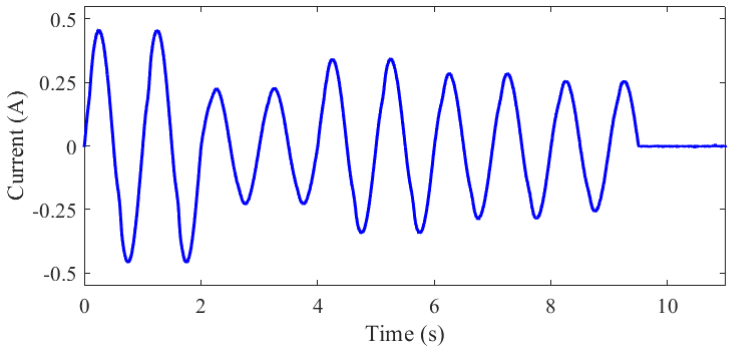

(a)

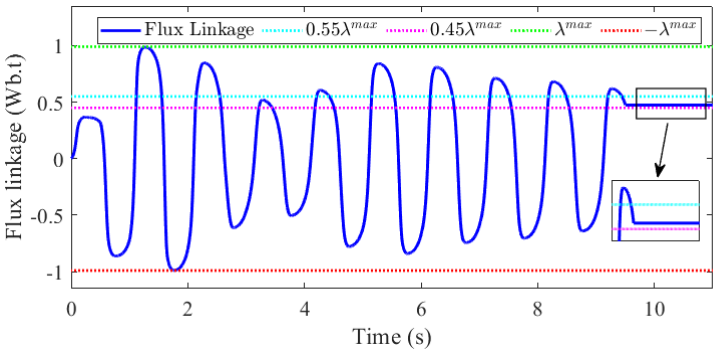

(b)

Figure 6.20: (a) Injected current, and (b) flux linkage of the β-side transformer obtained by equation (6.19).

A—half of the previous adjustment—resulting in a current of 0.2838 A. As seen in Fig. 6.20(b), at $t = 7.5$ s, the flux linkage again exceeds the upper limit of the target range, requiring another reduction. The current is decreased by 0.0284 A (half of the previous adjustment), bringing the current magnitude to 0.2554 A. With this value, as shown in Fig. 6.20(b), the flux linkage reaches 0.4741 Wb.t at $t = 9.5$ s, falling within the range of $[0.45\lambda^{max}, 0.55\lambda^{max}]$. At this point, the current injection can be stopped, as the flux has been successfully adjusted to an acceptable value.

6.6.3 Transformer Energization

After the flux adjustment, the V/V transformer must be energized in such a way that the residual and prospective flux densities match, thus minimizing inrush current. Fig. 6.21 shows the current drawn by the V/V transformer when energized using

both an ideal gang-operated CB and an ideal independent-pole-operated CB. For the independent-pole-operated CB, the transformer is energized following the method proposed in Chapter 5. As illustrated, both methods perform effectively, with the current magnitude limited to the excitation current of the α- and β-side transformers, corresponding to phases A and B. For phase C, the current slightly exceeds the excitation current by approximately 0.5 A; however, it remains well below the transformer's nominal current. The method discussed in this chapter utilizes a gang-operated CB, which is more commonly used in power systems operating at 220 kV or lower, making it a more typical choice for traction transformer energizations in TPSSs. Fig. 6.21 also demonstrates that using the proposed method and energize the V/V tansformer with gang-operated CBs can effectively reduce inrush current to a level comparable to what is expected from methods utilizing independent-pole-operated CBs.

6.7 Summary

This chapter introduces a flux matching method to mitigate the inrush current in V/V traction transformers when energized with a gang-operated CB. For such transformers, two optimal making points can reduce the magnitude of inrush current. The choice between these two points depends on the ratio of B_r^{max}/B^{max}, which is determined by the transformer's B-H curve. The proposed method eliminates the need for prior knowledge of this ratio, as it determines it through current injection. The method introduces a novel approach for estimating the transformer's flux linkage by injecting current and effectively canceling the DC offset present in the output of voltage transducers, which measure the voltage induced on the open-circuited windings. Using this estimated flux linkage, the method accurately calculates the B_r^{max}/B^{max} ratio and performs the necessary flux adjustment. After adjusting the flux density, the optimal closing instant is selected to minimize the difference between the prospective and adjusted residual flux densities, thereby significantly reducing inrush current. This approach mitigates inrush current without relying on impractical tools or unrealistic assumptions.

The results of extensive simulations and experiments confirm that the proposed method performs effectively, regardless of the transformer's core material or initial flux density. Its performance closely matches that of the method described in Chapter 5, which uses independent-pole-operated CBs with greater flexibility. Notably, the proposed method successfully keeps the inrush current well below the nominal current,

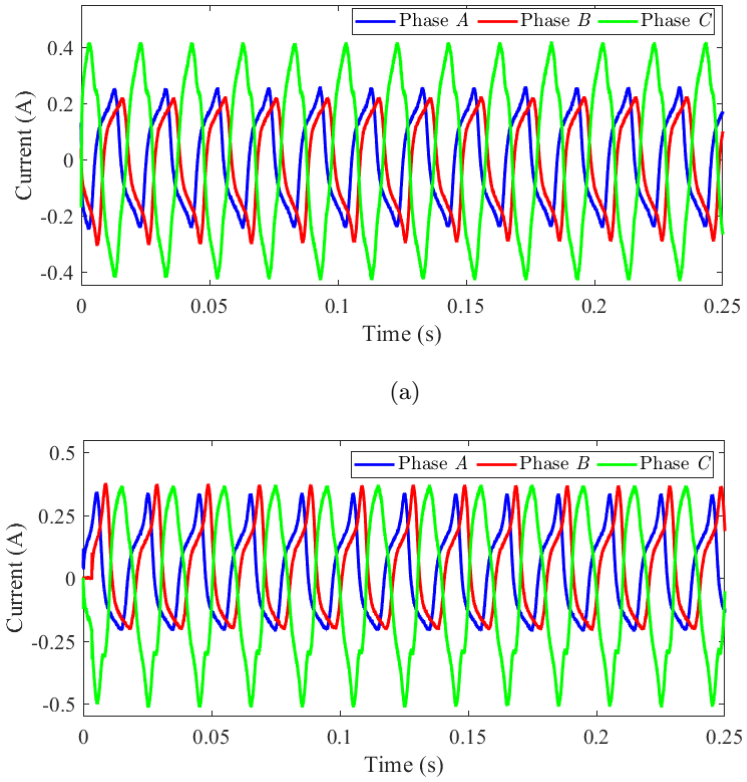

Figure 6.21: Three-phase currents of the V/V transformer energized with (a) proposed method for gang-operated CBs, and (b) the method proposed in the Chapter 5 for independent-pole-operated CBs.

demonstrating a significant improvement despite inherent uncertainties. This method proves that even for V/V traction transformers energized with gang-operated CBs, inrush current can be effectively mitigated—a challenge that may be difficult to overcome with other energization methods.

Chapter 7

Conclusion and Future Works

7.1 Conclusion

In conclusion, this thesis has highlighted key perspectives, introduced novel methodologies, and explored previously underexamined aspects of transformer inrush current mitigation and energization, as summarized below:

Chapter 2 introduced the terminal duality model (TDM), a powerful tool for simulating power transformers, and explained the inverse Jiles-Atherton method, which is used to model the non-linearity of transformer cores. The chapter demonstrated how the TDM, combined with the inverse JA method, can effectively model traction transformers. Two examples were provided: one of a healthy transformer and another with a turn-to-turn fault, illustrating the application of these modeling techniques.

Chapter 3 presented an effective and rapid flux matching energization method for mitigating inrush current in single-phase traction transformers. This method offers exceptional flexibility by allowing the transformer's residual flux density to be adjusted to any desired value within the feasible range, solely through the injection of controlled current into the transformer's winding. The only required input is the magnitude of the transformer's excitation current, which is used to calibrate the injected current, with all other essential data acquired during the flux adjustment process. Additionally, the rate of change of the injected current is carefully controlled to ensure that the induced voltage during flux adjustment does not damage the transformer.

A key concept introduced is the "compatibility flux density range," within which the reference residual flux density is selected. Two factors are considered in choosing this reference value: 1. it must fall within the transformer's feasible range to ensure that the residual flux can be accurately adjusted, and 2. it should minimize the impact of CB closing operation limitations. The chapter also identified the optimal timing for transformer energization, ensuring that the instantaneous steady-state flux density (i.e., prospective flux density) matches with the adjusted residual flux density. Moreover, a technique was introduced for accurately estimating the flux density during the adjustment process, which does not rely on detailed transformer design information. The only requirement for flux estimation is the use of voltage transducers that have been calibrated to eliminate any DC offset in their output.

Chapter 4 introduced advanced pre-fluxing methods designed to effectively mitigate inrush currents in single-phase traction transformers. These methods, termed modified pre-fluxing method 1 (MPFM 1) and modified pre-fluxing method 2 (MPFM 2), address

the shortcomings of traditional pre-fluxing methods. MPFM 1 focuses on estimating the maximum feasible residual flux density relative to the maximum flux density, enabling the determination of optimal energization instants to reduce inrush currents. In contrast, MPFM 2 offers broader capabilities and greater advantages. One significant benefit of MPFM 2 is its minimal reliance on detailed transformer design information. It does not require knowledge of the peak transformer excitation current and relies solely on real-time measurements for flux adjustment.

MPFM 2 is highly efficient, irrespective of transformer size, and can adjust the residual flux to any desired value within the feasible range. It addresses uncertainties in CB closing operations by adjusting the core's residual flux to an appropriate reference value, thereby minimizing negative impacts. Flux adjustment is accomplished using power electronic circuitry, known as the pre-fluxing device, which applies a controlled voltage across the transformer's low-voltage winding. MPFM 2 also estimates flux density during the adjustment process using data from voltage transducers. This method effectively compensates for any DC offset in the transducer output, ensuring reliable flux adjustment. The transformer is then energized at the optimal instant, matching the core's steady-state flux with the adjusted residual flux.

Chapter 5 introduced a flux matching method aimed at mitigating inrush currents in V/V traction transformers, which are widely used in traction systems. This method requires only the nominal voltage and excitation current, eliminating the need for detailed transformer design parameters. Unlike traditional methods such as demagnetization (de-fluxing) or pre-fluxing methods, the proposed flux matching method can adjust the transformer's residual flux density to any desired value within the feasible range.

Inrush current mitigation is accomplished by adjusting the core's residual flux to a carefully chosen reference value and determining the optimal energization instant for independent-pole-operated CBs. This reference flux is selected to ensure adaptability across various transformers, regardless of their core material. The railway power conditioner, typically installed on the low-voltage side of V/V transformers in traction power supply systems, serves as a current source, injecting sinusoidal current into the transformer windings before energization. Notably, this method utilizing existing traction power supply system infrastructure, making it cost-effective by avoiding additional initial and maintenance expenses compared to other energization methods.

For effective flux adjustment, this method estimates flux density during current injection. As with the method proposed in Chapter 3, the method for V/V traction transformers requires voltage transducer measurements that are free from DC offset. After flux adjustment, the precise energization instant is chosen to ensure that the adjusted flux density matches with the steady-state flux corresponding to the applied voltage. By employing this proposed method, inrush current can be significantly mitigated during the energization of V/V transformers, which are typically incompatible with existing energization techniques.

Chapter 6 introduced a flux matching method specifically designed to mitigate inrush current in V/V transformers energized by gang-operated CBs. The mitigation process involves adjusting the core's residual flux to an appropriate reference value and identifying the optimal energization instant. This method, similar to the one proposed for V/V traction transformers energized with independent-pole-operated CBs, uses current injection to adjust the residual flux density. However, unlike the method discussed in Chapter 7, this method does not require prior knowledge of the transformer's peak excitation current. Instead, it calculates the peak excitation current through a step-by-step current injection process. Once the peak value is determined, the method controls the current magnitude to adjust the residual flux density within the feasible range.

The reference residual flux is selected from two optimal points, ensuring it can be achieved regardless of the transformer's core material. To further enhance accuracy, the method incorporates a technique to compensate for the DC offset typically found in voltage measurements from transducers, allowing for precise flux estimation and adjustment. The energization instant is then carefully chosen to ensure that, when a V/V transformer is energized by a gang-operated CB, the adjusted flux density matches with the prospective flux density corresponding to the applied voltage. By employing this method, the energization of V/V traction transformers with gang-operated CBs can be made free of inrush current, a result that is unachievable with other energization methods.

7.2 Future Works

The current research can still be improved and extended. Future recommendations are summarised as follows:

1. This study primarily focused on common transformer types used in traction power systems, specifically single-phase and V/V transformers. However, as noted in Section 1.2.1, other transformer types are also utilized in the electrification of trains. Similar to V/V transformers, conventional energization methods designed for single-phase and three-phase transformers may not be suitable for these other traction transformers. Therefore, future research could explore the effects of standard energization techniques on these transformers and develop specialized energization methods developed for their needs.

2. The methods proposed in this research for single-phase and V/V traction transformers are pioneering in their ability to adjust residual flux density to any value within the feasible range—a capability not addressed by existing energization methods. Future research could investigate the application of these methods to three-phase transformers with three- and five-limb cores. Additionally, given that various types of circuit breakers, such as independent-pole-operated or gang-operated, are used for energizing three-phase transformers, the impact of using different circuit breakers should also be considered in future studies.

3. This research focused solely on mitigating inrush current in traction transformers; however, the proposed methods have potential applications beyond this scope. For instance, inrush current poses a significant threat to the safe and stable operation of distributed energy resources (DERs) connected to distribution systems. The energization methods developed in this study could be expanded and adapted for transformers connected in parallel that integrate DERs, such as those used in wind turbine systems.

4. This research primarily focuses on transformers with cores made of grain-oriented electrical steel, the most common material used for transformer cores. The proposed energization methods have been shown to effectively reduce the magnitude of inrush current in these transformers. However, transformers made of amorphous steel, which have a higher rated flux, a larger linear portion of the magnetization curve, and lower residual flux compared to grain-oriented electrical steel, require further investigation. It is essential to evaluate whether the proposed methods can effectively reduce inrush current in transformers made of amorphous steel. If they prove inadequate, these methods should be adapted to accommodate the

characteristics of this newer material.

5. In this research, current injection methods are used to adjust the residual flux density in transformers by controlling the magnitude of the injected current. Typically, this process takes a few cycles to complete because the precise current magnitude needed for accurate flux adjustment to a specific reference value is not known at the begining of the injection. However, the required current magnitude can be estimated by predicting the transformer's *B-H* curve, which can be determined after a one cycle of current injection with a magnitude equal to the transformer's peak excitation current. Once the *B-H* curve is established, the appropriate current magnitude can be calculated. This approach reduces the time needed for flux adjustment and improves the overall efficiency of the process.

Further research is crucial to addressing the gaps identified above. The flux matching energization methods explored here offer powerful solutions with the potential to significantly reduce inrush currents and address associated challenges in single-phase and V/V traction transformers. Advancing this line of inquiry could lead to the development of more effective inrush current mitigation methods applicable to a broad spectrum of transformer types, particularly those used in transmission and distribution networks.

Appendix A

Conventional and Inverse Jiles-Atherton

A.1 Matlab Code of Inverse Jiles-Atherton

Here is the Matlab code for the inverse JA proposed in [75]:

Listing A.1: Matlab Code for Inverse JA

```
clear; clc;format long;
% Par=[88.789 168.58e-6 1.47e6 .33949 70.017];
Par = [88.498 177.05e-6 1.4552e6 .35049 72.312];

u0 = 4*pi*1e-7;
a=Par(1);
alpha=Par(2);
Ms=Par(3);
c=Par(4);
k1=Par(5);
dt = .001;
t = dt:dt:2;
Bmax = 1.5; % B magnitude
B = Bmax*sin(2*1*pi*t);
Imax = length(B);
Man = zeros(1,Imax);M = zeros(1,Imax);H = zeros(1,Imax);
He = zeros(1,Imax);Mirr = zeros(1,Imax);
dMdB = zeros(1,Imax);dMirrdBe = zeros(1,Imax);dMandHe = zeros(1,Imax);
delta = ones(1,Imax);DB = zeros(1,Imax);
for i = 1 : Imax -1
    DB(i) = B(i+1)-B(i);
    delta(i) = sign(DB(i));
    M(i) = B(i)/u0-H(i);
    He(i) = H(i) + alpha*M(i);
    Man(i) = Ms*(coth(He(i)/a)-a/He(i));
    Mirr(i) = (M(i)-c*Man(i))/(1-c);
    dMandHe(i) = Ms/a*(1-(coth(He(i)/a))^2+(a/He(i))^2);
    dMirrdBe(i) = (Man(i)-Mirr(i))/(u0*k1*delta(i));
```

```
        if dMirrdBe(i) < 0
            dMirrdBe(i) = 0; %% dMirrdBe can not be less than zero
        end

    num = ((1-c)*dMirrdBe(i)+(c/u0)*dMandHe(i));
    den = 1+u0*(1-alpha)*(1-c)*dMirrdBe(i)+c*(1-alpha)*dMandHe(i);
    dMdB(i) = num/den;
    M(i+1) = M(i)+dMdB(i)*DB(i);
    H(i+1) = B(i+1)/u0 - M(i+1);
end

plot(H,B,'-red','LineWidth',2);grid on;
```

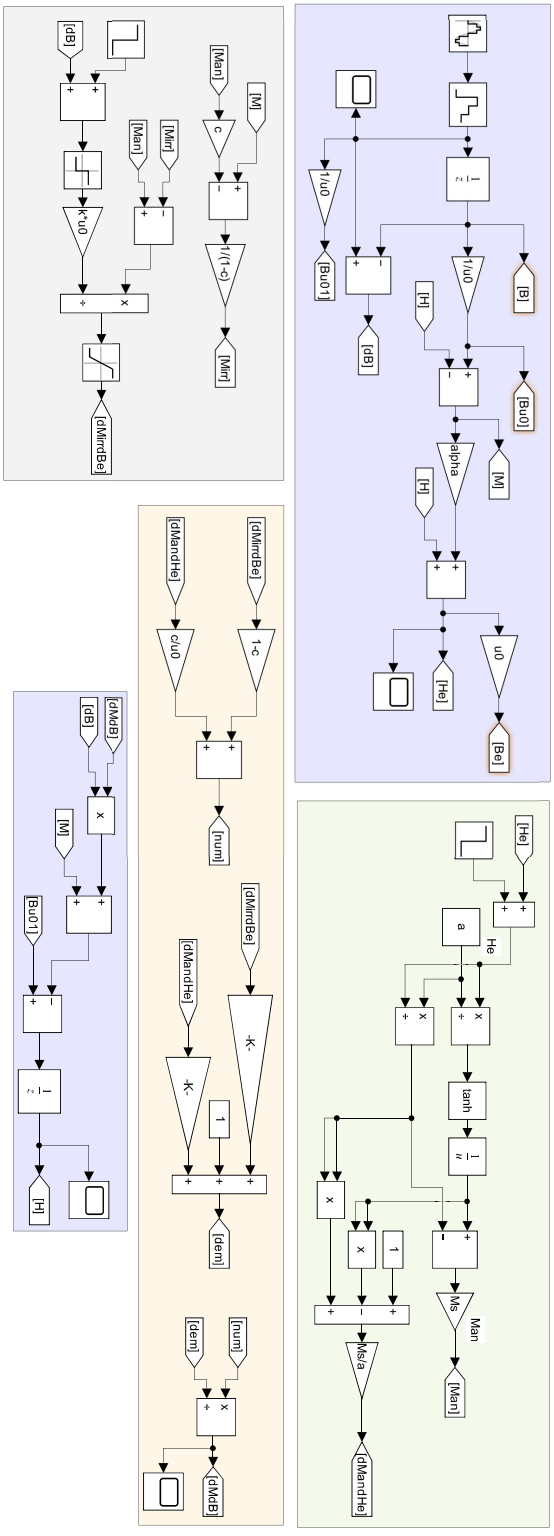

Figure A.1: Implementation of the inverse JA method in Simulink.

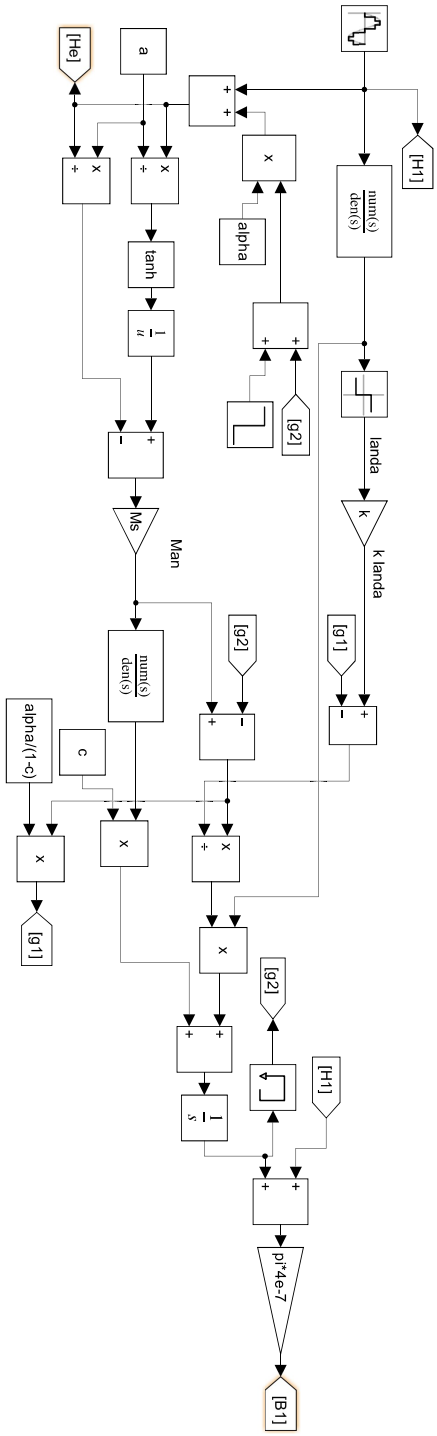

Figure A.2: Implementation of the JA method in Simulink.

Appendix B

TDM of a Single-Phase Transformer with Turn-to-Turn Fault

B.1 Transformer with Turn-to-Turn Fault

In this section, the application of TDM to model a single-phase traction transformer with a turn-to-turn fault is examined. The fault is assumed to occur near the top of one of the high-voltage windings, as indicated by the red regions in Fig. B.1. Due to the turn-to-turn fault, the high-voltage winding is divided into three separate windings. The corresponding inductance circuit of the transformer is depicted in Fig. B.2. This figure shows that the portion of the inductance circuit corresponding to the transformer section with turn-to-turn faults contains inductors with mutual inductances between them. For the section without a turn-to-turn fault, the leakage inductance is equal to 1.47 mH, the same value as for the transformer with no turn-to-turn fault. To determine the values of leakage inductances and corresponding mutual inductances for the section with a turn-to-turn fault, the incidence matrix (considering nodes 1 to 4) should be written first, which is:

$$\boldsymbol{A} = \begin{bmatrix} 1 & -1 & 0 & 0 \\ 1 & 0 & 0 & -1 \\ 0 & -1 & 0 & 1 \\ 0 & 0 & 1 & -1 \\ 0 & -1 & 1 & 0 \end{bmatrix} \tag{B.1}$$

Now, finite element simulation is employed to measure the leakage inductances $\boldsymbol{L_S}$ and the nodal admittance matrices $\boldsymbol{Y_n}$. For this purpose, Maxwell ANSYS software is utilized, and the results are as follows:

$$\boldsymbol{L_S} = 1 \times 10^{-3} \begin{bmatrix} 38 & 0 & 0 & 0 & 0 \\ 0 & 2.32 & 0 & 0 & 0 \\ 0 & 0 & 38.83 & 0 & 0 \\ 0 & 0 & 0 & 39.788 & 0 \\ 0 & 0 & 0 & 0 & 5.14 \end{bmatrix} \tag{B.2}$$

$$\boldsymbol{Y_n} = 25 \times \begin{bmatrix} 0.056 & -2.21 \times 10^{-3} & -9.2 \times 10^{-5} & -0.054 \\ -2.1669 \times 10^{-3} & 0.026 & -0.0239 & 1.63 \times 10^{-4} \\ -9.127 \times 10^{-5} & -0.0239 & 0.0253 & -1.3 \times 10^{-3} \\ -0.054 & 1.6189 \times 10^{-4} & -1.3 \times 10^{-3} & 0.055 \end{bmatrix} \tag{B.3}$$

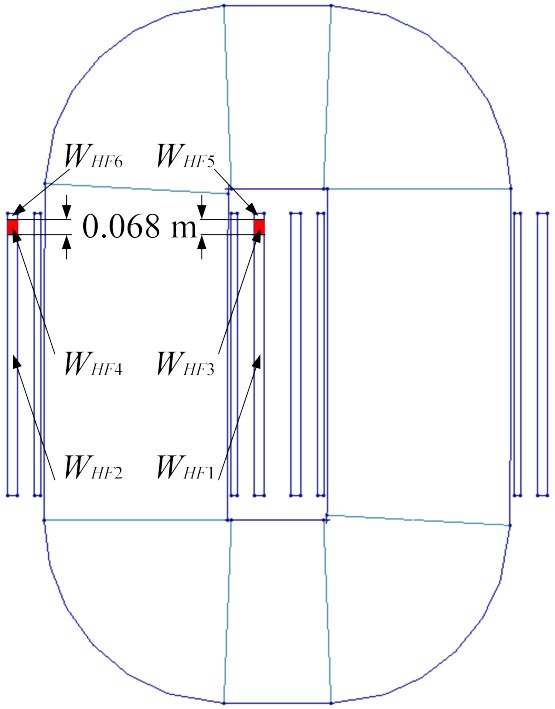

Figure B.1: Transformer front view.

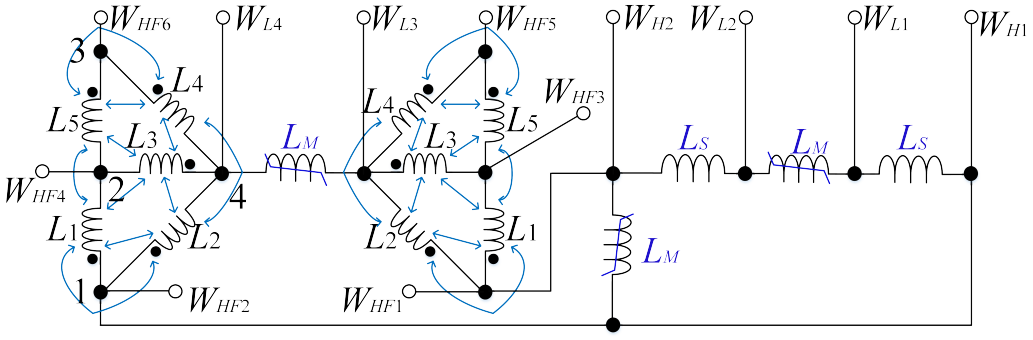

Figure B.2: Inductance circuit.

By replacing $\boldsymbol{L}$ with $\boldsymbol{L_S}$ in equation (2.8), incorporating the value of $\boldsymbol{Y_n}$, and applying the nonlinear least-squares method (with the MATLAB code provided in Appendix C), the impedance matrix $\boldsymbol{L}$ is derived as follows:

$$\boldsymbol{L} = 1 \times 10^{-3} \begin{bmatrix} 38 & 0.8 & 30.3 & -28.9 & 2.1 \\ 0.8 & 2.32 & -1.5 & 1.4 & -0.1 \\ 30.3 & -1.5 & 38.8 & -29.2 & 2.2 \\ -28.9 & 1.4 & -29.2 & 39.8 & 3 \\ 2.1 & -0.1 & 2.2 & 3 & 5.14 \end{bmatrix} \tag{B.4}$$

Similar to the single-phase traction transformer without a turn-to-turn fault, $\boldsymbol{L}$ is divided by two because each winding is represented by two sets of inductors, as shown in Fig. B.2. Consequently, the $\boldsymbol{L}$ for each set of inductors is adjusted as follows:

$$\boldsymbol{L} = 1 \times 10^{-3} \begin{bmatrix} 19 & 0.4 & 15.15 & -14.5 & 1.05 \\ 0.4 & 1.2 & -0.75 & 0.7 & -0.05 \\ 15.15 & -0.75 & 19.4 & -14.6 & 1.1 \\ -14.5 & 0.7 & -14.6 & 19.9 & 1.5 \\ 1.05 & -0.05 & 1.1 & 1.5 & 2.6 \end{bmatrix} \tag{B.5}$$

Fig. B.3 shows the TDM circuit of the single-phase traction transformer with a turn-to-turn fault. Compared to the TDM circuit of the healthy transformer, this circuit includes additional ideal transformers because one high-voltage winding is divided into three windings due to the fault. In this configuration, the $HV01$ transformer is replaced by $HV011$, $HV012$, and $HV013$ transformers. These connect the segments of the high-voltage winding affected by the turn-to-turn fault. The corresponding turn ratios are N_{H1}/N_b, N_{H2}/N_b, and N_{H3}/N_b. Here, N_{H1}/N_b and N_{H3}/N_b represent the number of turns of windings without a turn-to-turn fault, while N_{H2}/N_b represents the number of turns of the winding with the turn-to-turn fault. Additionally, R_f is included in this circuit to model the resistance of the turn-to-turn fault in the transformer winding.

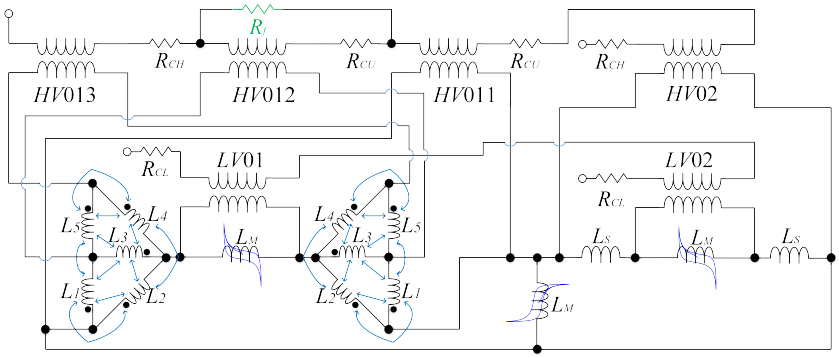

Figure B.3: The TDM circuit of the single-phase tracton transformer with turn-to-turn fault.

Appendix C

Matlab Code of Least-Squares Method

C.1 Matlab Code of Least-Squares Method

Here is the Matlab code for the Least-Squares Method:

Listing C.1: Matlab Code for Least-Squares Method

```
clear;
clc;
options = optimoptions(@lsqnonlin,'Algorithm', ...
    'levenberg-marquardt','FunctionTolerance',1e-12);
f = @(x)parameterfun(x);
[x,resnorm,residual,exitflag,output] = lsqnonlin(f, ...
    x0,[],[],options)
% Define LL matrix with considering the initial values
LL=[38e-3 x(1) x(2) x(3) x(4);...
    x(1) 2.32e-3 x(5) x(6) x(7);...
    x(2) x(5) 38.83e-3 x(8) x(9);...
    x(3) x(6) x(8) 39.788e-3 x(10);...
    x(4) x(7) x(9) x(10) 5.14e-3];
LL2=LL/2;
```

The function of the matlab code of parameterfun is defined as:

Listing C.2: Matlab Code for parameterfun

```
function y = parameterfun(x)
Yn=25*[0.056 -2.21e-3 -9.2e-5 -0.054;...
   -2.21e-3 0.026 -0.0239 1.63e-4;...
  -9.2e-5 -0.0239 0.0253 -1.3e-3;...
    -0.054 1.63e-4 -1.3e-3 0.055];
A=[1 -1 0 0;...
    1 0 0 -1;...
    0 -1 0 1;...
    0 0 1 -1;...
    0 -1 1 0];
B=A.';
w=2*pi*50;
```

```
XX=[38e-3 x(1) x(2) x(3) x(4);...
    x(1) 2.32e-3 x(5) x(6) x(7);...
    x(2) x(5) 38.83e-3 x(8) x(9);...
    x(3) x(6) x(8) 39.788e-3 x(10);...
    x(4) x(7) x(9) x(10) 5.14e-3];
y =B*inv(w*XX)*A-Yn;
```

Appendix D

Matlab Code for Calculating Making Instant

D.1 Matlab Code for Obtaining Making Instant

Here is the Matlab code for obtaining the making instant by using *fzero* function:

Listing D.1: Matlab Code for Obtaining Making Instant

```
clear;
clc;
global tct;
global U;
global RDDS;
global fre;
fre=50; %frequency
T=1/fre;
tCB=40e-3; %the operating time of the circuit-breaker
RDDS_int=20.00e6;
dev=0.1; % RDDS Scatter
DtCB=1.5e-3;
tint=0.1; % the time at which the closing operation is started
U=220e3*sqrt(2);
%%%%%%%%%%%%%%%%%%%%%%%%%%%%%%%%%%%%%%%%%%%%%%%%%%%%%%%%%%%%%%%%%%%%%%%%%%%%%%%
k=round(tCB*fre);
Bradpu=0.87;
RDDS=RDDS_int;
pai=(2*pi/2)-asin(Bradpu);
X=(pai*T)/(2*pi);
tct=tint+X+(abs(U*cos(pai))/(RDDS));
ta=tct;
fun = @pp; % function
x0=tct-(1/fre);
format long
fprintf(['switching WITH THE PROPOSED METHOD for a single-phase' ...
    ' transformer'])
z = fzero(fun,x0)
dd1=z-0.1;
```

```
Bac=sin(2*pi*fre*z-(0*pi/2))
pai*180/(1*pi)
```

The function of the matlab code of is defined as:

Listing D.2: Matlab Code for pp function

```
function y = f(x)
global tct;
global U;
global RDDS;
global fre;
y = abs((U)*cos(2*pi*fre*x))+(RDDS*(x-tct));
```

References

[1] Jin-Maun Ho and Tsung-Ling Tsou. The effect analysis and simulation test of harmonics on differential protection of scott transformers. In *2001 IEEE Porto Power Tech Proceedings (Cat. No. 01EX502)*, volume 4, pages 5–pp. IEEE, 2001.

[2] Sergey E Zirka, Dennis Albert, Yuriy I Moroz, and Herwig Renner. Further improvements in topological transformer model covering core saturation. *IEEE Access*, 10:64018–64027, 2022.

[3] Zhu Lihua, Li Jingjing, Yang Qingxin, Zhu Jianguo, and Chang-Seop Koh. An improved magnetostriction model for electrical steel sheet based on jiles–atherton model. *IEEE Transactions on Magnetics*, 56(3):1–4, 2020.

[4] Zia Emin, Manuel Martinez-Duro, Marta Val Escudero, Robert Adams, Herivelto S Bronzeado, Bruno Caillault, Nicola Chiesa, David Jacobson, Lubomir Kocis, Terrence Martinich, et al. Transformer energization in power systems: A study guide. *CIGRE WG C*, 4, 2014.

[5] Zhengqing Han, Jianzhong Wei, Shuping Liu, and Shibin Gao. Study on protection scheme for traction transformer of high-speed railway. In *2011 Asia-Pacific Power and Energy Engineering Conference*, pages 1–4. IEEE, 2011.

[6] Hamed Dashti, Mahdi Davarpanah, Majid Sanaye-Pasand, and Hamid Lesani. Discriminating transformer large inrush currents from fault currents. *International Journal of Electrical Power & Energy Systems*, 75:74–82, 2016.

[7] Xingjun Tian, Yunhua Li, and Xiaqing Li. Hybrid algorithm for traction transformer differential protection based on intrinsic mode function energy entropy and

correlation dimension. *IET Generation, Transmission & Distribution*, 8(7):1274–1283, 2014.

[8] Johannes Burkard and Jürgen Biela. Transformer inrush current mitigation concept for hybrid transformers. In *2017 19th European Conference on Power Electronics and Applications (EPE'17 ECCE Europe)*, pages P–1. IEEE, 2017.

[9] Hitachi Energy. *Switchsync PWC600 Technical Manual*, 2021. Technical Manual.

[10] Mohamed Tanta, Vítor Monteiro, Tiago JC Sousa, António P Martins, Adriano S Carvalho, and João L Afonso. Power quality phenomena in electrified railways: Conventional and new trends in power quality improvement toward public power systems. In *2018 International Young Engineers Forum (YEF-ECE)*, pages 25–30. IEEE, 2018.

[11] Zhuo Sun, Xinjian Jiang, Dongqi Zhu, and Guixin Zhang. A novel active power quality compensator topology for electrified railway. *IEEE Transactions on power electronics*, 19(4):1036–1042, 2004.

[12] Fujun Ma, An Luo, Xianyong Xu, Huagen Xiao, Chuanping Wu, and Wen Wang. A simplified power conditioner based on half-bridge converter for high-speed railway system. *IEEE transactions on industrial electronics*, 60(2):728–738, 2012.

[13] Zhiwen Zhang, Bin Wu, Jinsong Kang, and Longfu Luo. A multi-purpose balanced transformer for railway traction applications. *IEEE Transactions on Power Delivery*, 24(2):711–718, 2009.

[14] Amir Aghazadeh, Naser Khodabakhshi-Javinani, Solmaz Kahourzadeh, and Amin Mahmoudi. Evaluation and analysis of impedance matching transformer for hbc-power conditioner controller. In *2020 IEEE International Conference on Power Electronics, Drives and Energy Systems (PEDES)*, pages 1–6. IEEE, 2020.

[15] Haiqun Wang, Yingjie Tian, and Qin-chang Gui. Evaluation of negative sequence current injecting into the public grid from different traction substation in electrical railways. In *International Conference on Electricity Distribution*, pages 1–4. IET, 2009.

[16] Bin-Kwie Chen and Bing-Song Guo. Three phase models of specially connected transformers. *IEEE Transactions on Power Delivery*, 11(1):323–330, 1996.

[17] Hiroaki Morimoto, Tetsuo Uzuka, Akira Horiguchi, and Takemi Akita. New type of feeding transformer for ac railway traction system. In *2009 International Conference on Power Electronics and Drive Systems (PEDS)*, pages 800–805. IEEE, 2009.

[18] An Luo, Chuanping Wu, John Shen, Zhikang Shuai, and Fujun Ma. Railway static power conditioners for high-speed train traction power supply systems using three-phase v/v transformers. *IEEE Transactions on Power Electronics*, 26(10):2844–2856, 2011.

[19] Hirofumi Akagi and Ryota Kondo. A transformerless hybrid active filter using a three-level pulsewidth modulation (pwm) converter for a medium-voltage motor drive. *IEEE Transactions on Power Electronics*, 25(6):1365–1374, 2010.

[20] Pee-Chin Tan, Poh Chiang Loh, and Donald Grahame Holmes. A robust multilevel hybrid compensation system for 25-kv electrified railway applications. *IEEE Transactions on Power Electronics*, 19(4):1043–1052, 2004.

[21] R Grunbaum, J-P Hasler, T Larsson, and M Meslay. Statcom to enhance power quality and security of rail traction supply. In *2009 8th International Symposium on Advanced Electromechanical Motion Systems&Electric Drives Joint Symposium*, 2009.

[22] Ning-Yi Dai, Man-Chung Wong, Keng-Weng Lao, and Chi-Kong Wong. Modelling and control of a railway power conditioner in co-phase traction power system under partial compensation. *IET Power Electronics*, 7(5):1044–1054, 2014.

[23] Shuguang Song, Jinjun Liu, Shaodi Ouyang, and Xingxing Chen. A modular multilevel converter based railway power conditioner for power balance and harmonic compensation in scott railway traction system. In *2016 IEEE 8th International Power Electronics and Motion Control Conference (IPEMC-ECCE Asia)*, pages 2412–2416. IEEE, 2016.

[24] Yan Zhao, NingYi Dai, et al. Application of three-phase modular multilevel converter (mmc) in co-phase traction power supply system. In *2014 IEEE Conference and Expo Transportation Electrification Asia-Pacific (ITEC Asia-Pacific)*, pages 1–6. IEEE, 2014.

[25] Mohamed Tanta, José Gabriel Pinto, Vitor Monteiro, Antonio P Martins, Adriano S Carvalho, and Joao L Afonso. Topologies and operation modes of rail power conditioners in ac traction grids: Review and comprehensive comparison. *Energies*, 13(9):2151, 2020.

[26] Mohamed Tanta, Vitor Monteiro, Bruno Exposto, JG Pinto, António P Martins, Adriano S Carvalho, Andrés A Nogueiras Meléndez, and João L Afonso. Simplified rail power conditioner based on a half-bridge indirect ac/dc/ac modular multilevel converter and a v/v power transformer. In *IECON 2017-43rd Annual Conference of the IEEE Industrial Electronics Society*, pages 6431–6436. IEEE, 2017.

[27] Fifth Edition and Stephen J Chapman. Electric machinery fundamentals. 2012.

[28] John H Brunke and Klaus J Frohlich. Elimination of transformer inrush currents by controlled switching. i. theoretical considerations. *IEEE Transactions on power delivery*, 16(2):276–280, 2001.

[29] John H Brunke and Klaus J Frohlich. Elimination of transformer inrush currents by controlled switching. ii. application and performance considerations. *IEEE transactions on power delivery*, 16(2):281–285, 2001.

[30] PS Bimbhra and GC Garg. *Electrical machines-I*. Khanna Publishing House, 2014.

[31] Urmil Parikh and Bhavesh R Bhalja. Mitigation of magnetic inrush current during controlled energization of coupled un-loaded power transformers in presence of residual flux without load side voltage measurements. *International Journal of Electrical Power & Energy Systems*, 76:156–164, 2016.

[32] R Guimarães, AC Delaiba, JC Oliveira, E Saraiva, and AJJ Pereira Rosentino. Electromechanical forces in transformers caused by inrush currents: An analytical, numerical and experimental approach. *Journal of Control, Automation and Electrical Systems*, 24(6):863–872, 2013.

[33] Wellington da S Fonseca, Diorge de S Lima, Adry KF Lima, Newton S Soeiro, and Marcus VA Nunes. Analysis of electromagnetic-mechanical stresses on the winding of a transformer under inrush currents conditions. *International Journal of Applied Electromagnetics and Mechanics*, 50(4):511–524, 2016.

[34] Pedro F Ribeiro, Andreia Leiria, Carlos Cardoso, Luís M Rocha, Miguel Veríssimo, Mário Chaves, Carolina Marques, André Neves, and Miguel Louro. Real case interaction between a sympathetic inrush and a resonant system. In *CIRED 2021-The 26th International Conference and Exhibition on Electricity Distribution*, volume 2021, pages 940–944. IET, 2021.

[35] Mahdi Davarpanah, Majid Sanaye-Pasand, and Reza Iravani. A saturation suppression approach for the current transformer, part i: Fundamental concepts and design. *IEEE transactions on power delivery*, 28(3):1928–1935, 2013.

[36] Randy Hamilton. Analysis of transformer inrush current and comparison of harmonic restraint methods in transformer protection. *IEEE Transactions on Industry Applications*, 49(4):1890–1899, 2013.

[37] Kuniaki Yabe. Power differential method for discrimination between fault and magnetizing inrush current in transformers. *IEEE Transactions on Power Delivery*, 12 (3):1109–1118, 1997.

[38] Bogdan Kasztenny, N Fischer, and Y Xia. A new inrush detection algorithm for transformer differential protection. 2014.

[39] Jawad Faiz and S Lotfi-Fard. A novel wavelet-based algorithm for discrimination of internal faults from magnetizing inrush currents in power transformers. *IEEE Transactions on power delivery*, 21(4):1989–1996, 2006.

[40] AA Hossam Eldin and MA Refaey. A novel algorithm for discrimination between inrush current and internal faults in power transformer differential protection based on discrete wavelet transform. *Electric Power Systems Research*, 81(1):19–24, 2011.

[41] M Rasoulpoor and M Banejad. A correlation based method for discrimination between inrush and short circuit currents in differential protection of power transformer using discrete wavelet transform: theory, simulation and experimental validation. *International Journal of Electrical Power & Energy Systems*, 51:168–177, 2013.

[42] Luis G Perez, Alfred J Flechsig, Jack L Meador, and Zoran Obradovic. Training an artificial neural network to discriminate between magnetizing inrush and internal faults. *IEEE Transactions on Power Delivery*, 9(1):434–441, 1994.

[43] Jože Pihler, B Grcar, and Drago Dolinar. Improved operation of power transformer protection using artificial neural network. *IEEE transactions on power delivery*, 12 (3):1128–1136, 1997.

[44] G Mokryani, M-R Haghifam, H Latafat, P Aliparast, and A Abdollahy. Detection of inrush current based on wavelet transform and lvq neural network. In *IEEE PES T&D 2010*, pages 1–5. IEEE, 2010.

[45] G Mokryani, P Siano, and A Piccolo. Detection of inrush current using s-transform and competitive neural network. In *2010 12th International Conference on Optimization of Electrical and Electronic Equipment*, pages 191–196. IEEE, 2010.

[46] D Bejmert, W Rebizant, and L Schiel. Transformer differential protection with fuzzy logic based inrush stabilization. *International Journal of Electrical Power & Energy Systems*, 63:51–63, 2014.

[47] Jing Ma, Zengping Wang, Qixun Yang, and Yilu Liu. Identifying transformer inrush current based on normalized grille curve. *IEEE Transactions on Power Delivery*, 26(2):588–595, 2011.

[48] Farshid Naseri, Zahra Kazemi, Mohammad Mehdi Arefi, and Ebrahim Farjah. Fast discrimination of transformer magnetizing current from internal faults: An extended kalman filter-based approach. *IEEE Transactions on Power Delivery*, 33(1):110–118, 2017.

[49] Mohammad Ahmadi, Haidar Samet, and Teymoor Ghanbari. Discrimination of internal fault from magnetising inrush current in power transformers based on sine-wave least-squares curve fitting method. *IET Science, Measurement & Technology*, 9(1):73–84, 2014.

[50] Vincent Molcrette, J-L Kotny, J-P Swan, and J-F Brudny. Reduction of inrush current in single-phase transformer using virtual air gap technique. *IEEE Transactions on Magnetics*, 34(4):1192–1194, 1998.

[51] J-F Chen, T-J Liang, C-K Cheng, S-D Chen, R-L Lin, and W-H Yang. Asymmetrical winding configuration to reduce inrush current with appropriate short-circuit current in transformer. *IEE Proceedings-Electric Power Applications*, 152(3):605–611, 2005.

[52] M Tarafdar Hagh and M Valizadeh. Analysis and comparative study of transient inrush current reduction methods. In *2007 International Power Engineering Conference (IPEC 2007)*, pages 287–291. IEEE, 2007.

[53] M Tarafdar Hagh and M Abapour. Dc reactor type transformer inrush current limiter. *IET Electric Power Applications*, 1(5):808–814, 2007.

[54] H-T Tseng and J-F Chen. Voltage compensation-type inrush current limiter for reducing power transformer inrush current. *IET electric power applications*, 6(2): 101–110, 2012.

[55] Seyed Majid Madani, Mehrdad Rostami, GB Gharehpetian, and Reza Hagh Maram. Improved bridge type inrush current limiter for primary grounded transformers. *Electric power systems research*, 95:1–8, 2013.

[56] Hun-Chul Seo, Chul-Hwan Kim, Sang-Bong Rhee, Jae-Chul Kim, and Ok-Bae Hyun. Superconducting fault current limiter application for reduction of the transformer inrush current: a decision scheme of the optimal insertion resistance. *IEEE transactions on applied superconductivity*, 20(4):2255–2264, 2010.

[57] Mohammad Hossein Sadeghi, Yaser Damchi, and Hosseinali Shirani. Improvement of operation of power transformer protection system during sympathetic inrush current phenomena using fault current limiter. *IET Generation, Transmission & Distribution*, 12(22):5968–5974, 2018.

[58] Abbas Ketabi and Ali Reza Hadidi Zavareh. New method for inrush current mitigation using series voltage-source pwm converter for three phase transformer. In *2011 2nd Power Electronics, Drive Systems and Technologies Conference*, pages 501–506. IEEE, 2011.

[59] Yu Cui, Sami G Abdulsalam, Shiuming Chen, and Wilsun Xu. A sequential phase energization technique for transformer inrush current reduction-part i: Simulation and experimental results. *IEEE Transactions on power delivery*, 20(2):943–949, 2005.

[60] Wilsun Xu, Sami G Abdulsalam, Yu Cui, and Xian Liu. A sequential phase energization technique for transformer inrush current reduction-part ii: theoretical analysis and design guide. *IEEE transactions on power delivery*, 20(2):950–957, 2005.

[61] Ramón Cano-González, Alfonso Bachiller-Soler, José Antonio Rosendo-Macías, and Gabriel Álvarez-Cordero. Controlled switching strategies for transformer inrush current reduction: A comparative study. *Electric Power Systems Research*, 145: 12–18, 2017.

[62] Ramón Cano-González, Alfonso Bachiller-Soler, José Antonio Rosendo-Macías, and Gabriel Álvarez-Cordero. Optimal gang-operated switching for transformer inrush current reduction. *Electric Power Systems Research*, 131:80–86, 2016.

[63] Jose C Oliveira, Carlos E Tavares, Roberto Apolonio, Arnulfo B Vasconcellos, and Herivelto S Bronzeado. Transformer controlled switching to eliminate inrush current-part i: Theory and laboratory validation. In *2006 IEEE/PES Transmission & Distribution Conference and Exposition: Latin America*, pages 1–5. IEEE, 2006.

[64] Andreas Ebner, Michael Bosch, and Renato Cortesi. Controlled switching of transformers-effects of closing time scatter and residual flux uncertainty. In *2008 43rd International Universities Power Engineering Conference*, pages 1–5. IEEE, 2008.

[65] Shuhua Fang, Haimiao Ni, Heyun Lin, and Siu Lau Ho. A novel strategy for reducing inrush current of three-phase transformer considering residual flux. *IEEE Transactions on Industrial Electronics*, 63(7):4442–4451, 2016.

[66] Haimiao Ni, Shuhua Fang, and Heyun Lin. A simplified phase-controlled switching strategy for inrush current reduction. *IEEE Transactions on Power Delivery*, 2020.

[67] Douglas I Taylor, Joseph D Law, Brian K Johnson, and Normann Fischer. Single-phase transformer inrush current reduction using prefluxing. *IEEE Transactions on Power Delivery*, 27(1):245–252, 2011.

[68] V Oiring de Castro Cezar, LL Rouve, JL Coulomb, FX Zgainski, O Chadebec, and B Caillault. Elimination of inrush current using a new prefluxing method. application to a single-phase transformer. In *2014 International Conference on Electrical Machines (ICEM)*, pages 1717–1723. IEEE, 2014.

[69] Douglas I Taylor. System, apparatus, and method for reducing inrush current in a three-phase transformer, November 4 2014. US Patent 8,878,391.

[70] Baris Kovan, Francisco De Leon, Dariusz Czarkowski, Zivan Zabar, and Leo Birenbaum. Mitigation of inrush currents in network transformers by reducing the residual flux with an ultra-low-frequency power source. *IEEE Transactions on Power Delivery*, 26(3):1563–1570, 2011.

[71] WG CIGRE. C4. 307 transformer energization in power systems: A study guide. Technical report, CIGRE, Tech. Rep. 568, 2014.

[72] Casimiro Álvarez-Mariño, Francisco De León, and Xosé M López-Fernández. Equivalent circuit for the leakage inductance of multiwinding transformers: Unification of terminal and duality models. *IEEE transactions on power delivery*, 27(1):353–361, 2011.

[73] I Aprd. test code for liquid-immersed distribution, power, and regulating transformers and guide for short-circuit testing of distribution and power transformers.

[74] David C Jiles and David L Atherton. Theory of ferromagnetic hysteresis. *Journal of magnetism and magnetic materials*, 61(1-2):48–60, 1986.

[75] RA Naghizadeh, B Vahidi, and SH Hosseinian. Modelling of inrush current in transformers using inverse jiles–atherton hysteresis model with a neuro-shuffled frog-leaping algorithm approach. *IET electric power applications*, 6(9):727–734, 2012.

[76] M Popov, L Van Der Sluis, GC Paap, and PH Schavemaker. On a hysteresis model for transient analysis. *IEEE Power Engineering Review*, 20(5):53–55, 2000.

[77] Marjan Popov, Leonid Grcev, Lou van der Sluis, and Vladimir V Terzija. An atp-emtp-based model for analysis of shielding properties of ferromagnetic cable sheaths. *IEEE transactions on power delivery*, 20(3):2241–2247, 2005.

[78] Paul M Anderson, Charles F Henville, Rasheek Rifaat, Brian Johnson, and Sakis Meliopoulos. *Power system protection*. John Wiley & Sons, 2022.

[79] Hiroki Ito. *Switching Equipment*. Springer, 2019.

[80] Urmil Parikh and Bhavesh R Bhalja. Challenges in field implementation of controlled energization for various equipment loads with circuit breakers considering diversified dielectric and mechanical characteristics. *International Journal of Electrical Power and Energy Systems*, 87:99–108, 2017.

[81] D Gordon and RE Brown. Recent advances in fluxgate magnetometry. *IEEE Transactions on Magnetics*, 8(1):76–82, 1972.

[82] Stanley Marshall. An analytic model for the fluxgate magnetometer. *IEEE Transactions on Magnetics*, 3(3):459–463, 1967.

[83] Robert Del Vecchio, Robert M Del Vecchio, Bertrand Poulin, Pierre Feghali, Dilipkumar Shah, and Rajendra Ahuja. *Transformer design principles*. CRC press, 2017.

[84] Giorgio Bertotti. *Hysteresis in magnetism: for physicists, materials scientists, and engineers*. Gulf Professional Publishing, 1998.

[85] Akihisa Inoue and Koji Hashimoto. *Amorphous and nanocrystalline materials: Preparation, properties, and applications*, volume 3. Springer Science & Business Media, 2001.

[86] Eric Charles Snelling. Soft ferrites: properties and applications. *(No Title)*, 1969.

[87] Robert C O'handley. *Modern magnetic materials: principles and applications*. 1999.

[88] Parvraj Pachore, Yugal Gupta, Sandeep Anand, Subrata Sarkar, Paresh Mathur, and Pushpendra Kumar Singh. Flux error function based controlled switching method for minimizing inrush current in 3-phase transformer. *IEEE Transactions on Power Delivery*, 36(2):870–879, 2020.

[89] Duehee Lee. Design and implementation of three-phase inverters using a tms320f2812 digital signal processor. 2009.

[90] Texas Instruments. Tms320f2812pgfs texas instruments - dsps, 2021.

[91] Desoer C. A, , and Kuh E. S. *Basic Circuit Theory*. Mcgraw-hill, inc, 1969.

[92] Francisco De Leon, Ashkan Farazmand, and Pekir Joseph. Comparing the t and pi equivalent circuits for the calculation of transformer inrush currents. *IEEE Transactions on Power Delivery*, 27(4):2390–2398, 2012.

[93] Amir Aghazadeh, Kang Li, Vladimir Terzija, and Sadegh Azizi. Modified pre-fluxing method for energization of single-phase transformers. In *2023 IEEE International*

Conference on Energy Technologies for Future Grids (ETFG), pages 1–6. IEEE, 2023.

[94] PS Bimbhra. Electrical machinery. *Khanna Publishers, New Delhi*, 2010.

[95] CIGRE WG3.35. *Guidelines and Best Practices for the Commissioning and Operation of Controlled Switching Projects*, 2019. Available from CIGRE.

[96] Makoto Hagiwara and Hirofumi Akagi. Control and experiment of pulsewidth-modulated modular multilevel converters. *IEEE transactions on power electronics*, 24(7):1737–1746, 2009.

[97] Marc Lacroix, Pierre Taillefer, and André Mercier. Mitigation of transformer inrush current associated with der facilities connected on the distribution grid. In *2015 IEEE Eindhoven PowerTech*, pages 1–5. IEEE, 2015.

[98] Amir Aghazadeh, Ehsan Hajipour, Kang Li, and Sadegh Azizi. Mitigating the inrush current of v/v transformers using railway conditioners. *IEEE Access*, 2024.